Active fluids - Interactions and collective dynamics in phoretic suspensions

Akhil Varma

NNT : 2019SACLX109

Fluides actifs - Interactions et dynamiques collectives dans les suspensions phorétique

Thèse de doctorat de l'Université Paris-Saclay
préparée à École polytechnique

École doctorale n°579: Sciences mécaniques et énergétiques, matériaux et géosciences (SMEMaG)
Spécialité de doctorat: Mécanique des fluides

Thèse présentée et soutenue à Palaiseau, le 14 novembre 2019, par

M. Akhil Varma

Composition du Jury :

M. Bertrand Maury Professeur, Université Paris-Sud, Orsay, France	Président, Examinateur
Mme Salima Rafaï Charge de researche, LiPhy, Grenoble, France	Rapporteur
M. Thomas Bickel Maître de Conférences, LOMA, Talence, France	Rapporteur
M. Holger Stark Professeur, TU Berlin, Berlin, Germany	Examinateur
M. Sébastien Michelin Professeur, École polytechnique, Palaiseau, France	Directeur de thèse

Thèse de doctorat

École polytechnique
Laboratoire d'Hydrodynamique (LadHyX)
Palaiseau, France

Active fluids: Interactions & collective dynamics in phoretic suspensions

Ph.D. Thesis

Akhil Varma

Thèse soutenue le 14 Novembre 2019 devant le jury composé de

Sébastien MICHELIN	Directeur de thèse	LadHyX, Palaiseau, France
Thomas BICKEL	Rapporteur	LOMA, Talence, France
Salima RAFAI	Rapporteur	LiPhy, Grenoble, France
Bertrand MAURY	Examinateur	Université Paris-Sud, Orsay, France
Holger STARK	Examinateur	TU Berlin, Berlin, Germany

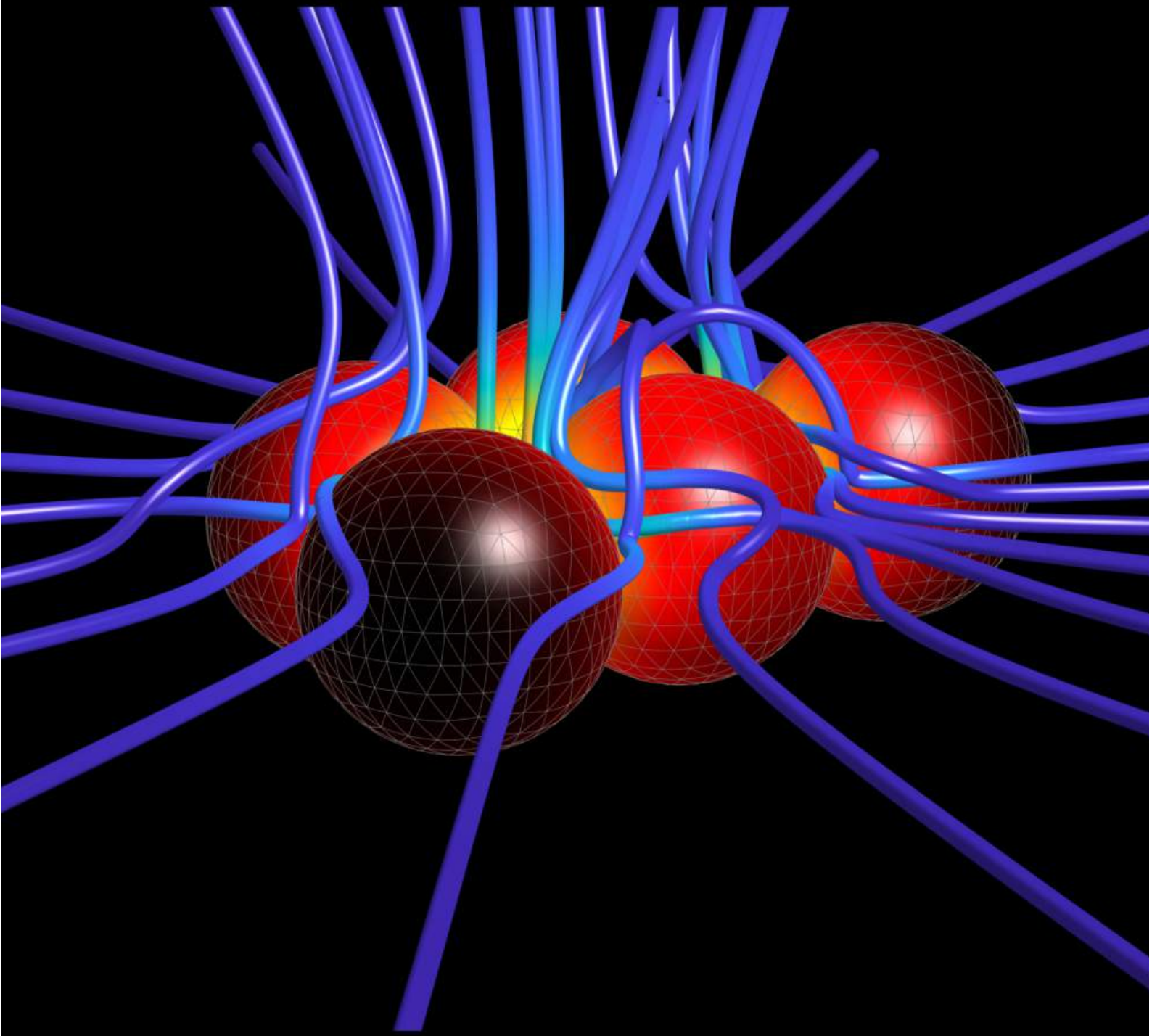

©Backcover *Soft Matter* Issue 35, 2018: 'Clustering-induced self-propulsion of isotropic autophoretic particles' by A. Varma, T. D. Montenegro-Johnson and S. Michelin.

Abstract

Active fluids comprise of self-propelled bodies which expend energy in the fluid to achieve self-propulsion. These are commonly seen in nature - from macroscopic scales such as a group of fish or birds to microscopic scales such as a suspension of swimming microorganisms. The particles, being self-propelled, are in a state of thermal equilibrium and therefore exhibit an interesting collective behavior governed by an non-equilibrium statistical mechanics. Over the past decade, with recent scientific advances, artificial micro-swimmers in the form of colloidal particles have been manufactured which rely on physico-chemical mechanisms for self-propulsion. Here, we will study the collective interactions in the suspensions of a class of these active colloidal particles - called autophoretic particles - which "swim" in the gradients of a self-generated solute concentration field using a mechanism called diffusiophoresis. The surface property of colloids which allows it to respond mechanically to the external surface concentration gradients of a certain species of chemical solute and to swim is called *mobility*. These colloids also have the capacity to catalyze chemical reactions on their surface; this gives them the ability to absorb or emit the chemical solute, thus modifying the concentration field of the surrounding solute. This property is termed surface *activity*. The combined surface properties of chemical activity and mobility can lead to self-propulsion of colloidal particles. This mechanism is exploited by autophoretic particles, which are chemically active synthetic colloids, to achieve self-propulsion.

These particles influence each other's movements through chemical and hydrodynamic interactions and are therefore known for their collective behavior. The modeling of these interactions has been the subject of intense research over the past decades, both from a physical point of view to understand the precise mechanisms of interactions, and from an experimental point of view to explain the observations of formation of large-scale coherent structures. However, exact modeling of is difficult due to multi-body interactions and surface effects. Until now, most efforts have been based on the superimposition of far field approximations for the signature of each particle, which are only valid asymptotically within the limit of dilute suspension. A systematic and unified analytical framework based on the classical method of reflection (MoR) is developed here for Laplace and Stokes problems in order to obtain the multibody interactions and the resulting velocities of the phoretic particles, up to an order of precision of the radius relative to the distance of the particles.

A system comprising only chemically and geometrically isotropic autophoretic particles is then considered in detail. We know that such isotropic particles cannot propel themselves; however, in the presence of other identical particles, the symmetry of the concentration field is broken and the particles spontaneously form packed clusters. Remarkably, these clusters self-propel according to their geometric arrangement. An argument for the origin of this self-propelling behavior of the clusters is explained using the MoR. This result therefore identifies a new way to break the symmetry for the concentration field and for self-propulsion, which is not based on an anisotropic design, but on the collective interactions of identical and homogeneous active particles. In addition, using complete numerical simulations, we characterize the statistical properties such as the maximum, average and most likely self-propelling speeds of the system.

Keywords: Active fluids, self-propulsion, chemo-hydrodynamic interactions, modeling phoretic suspension, collective dynamics

Résumé

Les fluides actifs comprenant des corps autopropulsés qui dépensent de l'énergie dans le fluide pour réaliser l'autopropulsion. Ceux-ci sont couramment observés dans la nature - des échelles macroscopiques comme un groupe de poissons ou d'oiseaux aux échelles microscopiques telles qu'une suspension de micro-organismes nageant. Les particules, étant auto-entraînées, sont dans un état d'équilibre thermique et donc présentent un comportement collectif intéressant régi par une mécanique statistique hors équilibre. Au cours de la dernière décennie, avec les progrès scientifiques récents, des micro-nageurs artificiels sous forme de particules colloïdales ont été fabriqués qui s'appuient sur des mécanismes physico-chimiques pour l'auto-propulsion. Ici, nous étudierons les interactions collectives dans les suspensions d'une classe de ces particules colloïdales actives - appelées particules autophorétiques - qui «nagent» dans les gradients d'un champ de concentration de soluté auto-généré en utilisant un mécanisme appelé diffusiophorèse. La propriété de surface des colloïdes qui lui permet de répondre mécaniquement aux gradients de concentration de surface externe d'une certaine espèce de soluté chimique et de nager est appelée la mobilité de la particule. Ces colloïdes possèdent en outre la capacité de catalyser des réactions chimiques à la surface de leur surface; cela leur donne la capacité d'absorber ou d'émettre le soluté chimique, modifiant ainsi le champ de concentration du soluté environnant. Cette propriété est appelée activité de surface. Les propriétés de surface combinées de l'activité chimique et de la mobilité peuvent donner un nouveau souffle à l'autopropulsion des particules colloïdales. Ce mécanisme est exploité par des particules autophorétiques, qui sont des colloıdes synthétiques chimiquement actifs, pour réaliser une autopropulsion. Ces particules influencent les mouvements des uns et des autres par le biais d'interactions chimiques et hydrodynamiques et sont donc connues pour leur comportement collectif.

La modélisation de ces interactions fait l'objet d'intenses recherches au cours des dernières décennies, tant d'un point de vue physique pour comprendre les mécanismes précis des interactions, que d'un point de vue expérimental pour expliquer les observations de formation de structures cohérentes à grande échelle. Cependant, une modélisation exacte de est difficile en raison des interactions multi-corps et des effets de surface. Jusqu'a présent, la plupart des efforts reposent sur la superposition d'approximations de champ lointain pour la signature de chaque particule, qui ne sont valides que de maniére asymptotique dans la limite de suspension diluée. Un cadre analytique systématique et unifié basé sur la methode classique de reflexion (MoR) est developpe ici pour les problémes de Laplace et de Stokes afin d'obtenir les interactions multicorps et les vitesses résultantes des particules phorétiques, jusqu'a un ordre de précision du rayon rapport à distance des particules .

Un systéme comprenant uniquement des particules autophorétiques chimiquement et geometriquement isotropes est ensuite considéré en détail. On sait que de telles particules isotropes ne peuvent se propulser seules; cependant, en présence d'autres particules identiques, la symétrie du champ de concentration est brisée et les particules forment spontanément des amas tassés. Remarquablement, ces grappes s'auto-propulsent en fonction de leur disposition géométrique. Un argument pour l'origine de ce comportement auto-propulsif des grappes est bas´e sur le MoR. Ce résultat identifie donc une nouvelle voie pour briser la symétrie pour le champ de concentration et pour l^aauto-propulsion, qui ne repose pas sur une conception anisotrope, mais sur les interactions collectives de particules actives identiques et homogénes. De plus, en utilisant des simulations numériques complètes et un modèle théorique de regroupement, nous caractérisons les propriétés statistiques telles que les vitesses maximales, moyennes et les plus probables d'auto-propulsion du système.

Mots clés: fluid actifs, autopropulsion, interactions chimiques et hydrodynamiques, comportement collectif

Acknowledgements

Three years of PhD went by like the blink of an eye, and yet it was a long enough duration to establish strong bonds with people (and projects). Here, I wish to thank these people, who I feel have influenced me significantly, both personally and scientifically. To begin with, I owe this opportunity of conducting my PhD research at LadHyX to my advisor Pr. Sébastien Michelin. I would like to express my deep gratitude and admiration for him for his patient guidance, effective critiques and complete support and involvement in the work which has kept my flame for scientific enquiry alive throughout the 3 years. It is only through his strict adherence to schedule that I've been able to get through some stressful times, especially which overlapped with writing of this thesis. All in all, he has actively spent time to teach me how to think scientifically and act independently with confidence, which I'm forever indebted to him for. On the same academic note, I would also like to thank Pr. Thomas Montenegro-Johnson a.k.a Tom, for assistance with the full numerical simulations used in this thesis, and for being readily available for any queries and for solving technical problems which I still feel the need to understand and master myself.

Science is a social endeavour. The lenient and welcoming atmosphere of LadHyX promotes this idea and it had made me feel quite at home which, I think had also indirectly boosted my confidence and productivity. I would like to acknowledge the often unappreciated over-a-cup-of-coffee conversations with my colleagues, which has helped me many times in gaining new ideas and perspectives about my work, science and academia in general. I would like to thank my colleagues, especially - Matvey, Tullio, Kevin, Francisco, Francesco and Øyvind - for their support and timely guidance! I would also like to extend my thanks to the technicians of the lab for their help with the computing resources as well as the administrative staff for their careful organisation and management of the important administrative and travel documents.

Being a social animal dislocated by an odd 8000 kms from home, I have cherished the company of really good friends over the duration of my stay in Paris. To name all of them would be difficult, but I certainly need to list out some of the very close and important people in my life, who have helped maintain my sanity during tough times and who have also shown me that there is no such thing as "having too much fun" - P Martin, P Seray, P Julie, P Fouad, P Hassan, P Xudong, P Monica, P Katia, P Saurabh, P Ayush and P Disha. These are really kind and smart people going through the same phase of life and as I am, and we have learnt (and are still learning) from each other how to deal with life.

Let me not repeat the same obnoxious mistake as I did in my Masters thesis of omitting to thank my parents and grandparents, without whom I wouldn't even be writing this thesis in the first place. I thank them for encouraging me to go abroad from my home country to pursue my dreams of higher studies in science. It was always a pleasure to attend their daily phone calls which were full of support and unconditional love which I thoroughly embraced and hopefully reciprocated. It is their blessings that has seen me through these years.

Contents

1

Introduction

Motion of microorganisms such as bacteria or microtubules, or microscopic particles such as active colloids produce an activity within a fluid; the microscopic interactions between them can manifest in a macroscopic scale as collective motion and formation of large-scale structures. With synthetic constituents such as autophoretic colloids, one has control over the local interactions and can design these artificial swimmers for a specific task. The objective of the present chapter is to introduce the fundamental physics behind self-propulsion of autophoretic colloids, their collective dynamics dynamics observed in experiments and to describe the current literature on modeling their dynamics in such active matter systems.

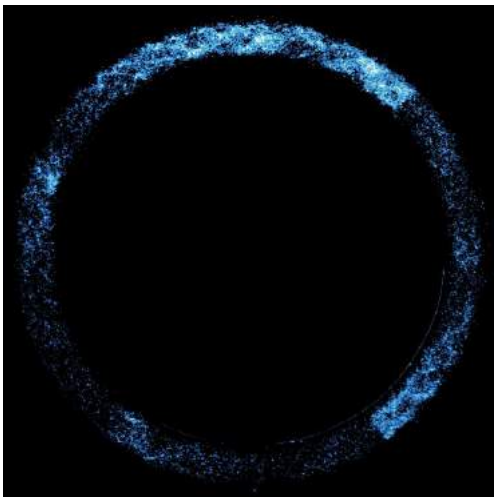

Figure: *Dark-field image of a large population of colloidal rollers confined to a track. They spontaneously form swarms that move in a unique direction. Source: Bricard et. al. 2013 [1]*

Contents

Active matter, as the name suggests, is a physical system in which the constituent elements are in a state of continuous "activity". These include motion of fishes, birds, bees and even human crowds. Their activity comes from their ability to utilise stored energy or convert energy from the surrounding into motion. This broad definition would encapsulate a lot of commonly seen examples in nature spanning multitude of scales. At microscopic scales, bacterial colonies, microtubules and growing tissues display active behaviour. Recent advances in manufacturing of certain artificial self-propelling particles have lead to creation of synthetic active matter with tunable physical properties. Such systems have also shown immense potential for controlled transport at microscopic scales. These two properties make synthetic active matter system attractive for potential engineering applications such as development of meta-materials with desired properties as well as for systems with controlled transport properties for biomedical and therapeutic applications. From a fundamental physical perspective, these systems form a class of internally activated thermodynamic system which is well out of equilibrium.

1.1 A thermodynamic perspective

Thermodynamic equilibrium is a state in which the thermodynamic potential (i.e. the capacity of the system to do work) is minimized. The thermodynamic properties - mechanical, chemical and thermal- of the system in equilibrium remain unchanged unless disturbed by a thermodynamic operation. The operation, which involves injection of energy into the system, pushes the system into an *out-of-equilibrium* state. Thus, a physical system is said to be out-of-equilibrium if its thermodynamic properties vary over time and are also dependent on the spatial location. The spatial difference in properties lead to transport of mass, momentum and energy within the system. Some examples include diffusion, conduction of heat or electricity, pressure/shear-driven flows etc.. The system would eventually decay into a state of thermodynamic equilibrium, unless the source of energy is available. A simple example is a case where the ends of a conducting material are kept in contact with bodies of two different temperatures. The temperature difference drives a heat flux from the hotter to the colder body until all the bodies reach an equilibrium temperature. However, to maintain the non-equilibrium heat flux, external energy has to be supplied to sustain the temperature difference.

In the above situation, the constituent elements of the system experience constant thermodynamic forcing due to an external/ global energy supplied into the system in the form of heat. In another kind of system, the energy consumption or dissipation can be local i.e. the constituent particles are themselves responsible for input of energy into the system to maintain the non-equilibrium nature. This is the defining feature of active matter systems. Due to their continued state of motion, the particles, in low densities, can contribute to enhancing transport within the material [2]. For example, school of fishes swimming in water constitutes an active system in which each creature exerts mechanical energy into the fluid by deforming its body, and in return gets propelled by the fluid.

Non-equilibrium thermodynamic processes are irreversible in nature. The *irreversible fluxes* are coupled to the *thermodynamic forces* and various physical models have been developed to understand this coupling such as Fick's laws for diffusion, Fourier's laws for conduction etc.. It has been observed that simple linear models suffice to explain these thermodynamic processes accurately; non-linear effects are insignificant in most cases [3]. Additionally, since each of the irreversible fluxes are coupled to all the thermodynamic forces, cross-effects can also also exist theoretically; a classical example, observed experimentally as well, is that

of transport of certain colloidal particles resulting from temperature gradients - known as Soret effect / thermophoresis which belongs to a class of mechanism known as *phoresis* - or drift through external gradients [4, 5].

1.1.1 Self-organizing properties

Systems out of thermodynamic equilibrium can exhibit pattern formation behaviour. The local fluctuations in thermodynamic properties of the system, even at the microscopic scales, get amplified due to interactions with the surrounding and lead to mechanical instabilities [4]. These instabilities, under certain circumstances, can develop large-scale coherent structures, even of macroscopic scales. Classical examples of non-equilibrium pattern formation in fluid dynamics are Rayleigh-Bernard convection cells formed due to thermal (convective) instabilities, or shear-flow instabilities such as Kelvin-Helmholtz or Taylor-Couette etc..[6]. Even simple systems such as a mechanical vibrations of a granular media can produce a variety of patterned structures [7]. These are some examples of systems displaying patterns due to external mechanical or thermal excitation. In some processes, for example, Cross-Hohenberg and Belosov-Zhabotinsky reactions(BZ reactions) internal chemical energy is responsible for pattern formation and sustained oscillations [8]. In nature, the interactions between living organisms within the system act as an input of energy to destabilize the system. Commonly observed examples at microscopic scales include bacterial aggregates [7] (figure 1.1d) , kensin-induced patterning of microtubules (figure 1.1c), and various bio-chemical processes. Usually a dynamical systems approach is taken to study these symmetry-breaking bifurcations of transition from equilibrium state and resulting pattern formation.

Systems in thermodynamic equilibrium exhibit time-reversal symmetry i.e. by reversing time, the statistical properties of the equilibrium process remain exactly the same as that when the system advances forward in time. However, the discerning feature of out-of-equilibrium systems is the breakdown of this time-reversal symmetry: A classic example is the case studied by Galajda *et.al.* wherein a preferential aggregation of bacteria were observed in a segregated chamber [11]; reversal of time would cause motion in opposite direction, which breaks the symmetry.

Besides the pattern formation and time irreversibility, there are additionally two features that out-of-equilibrium systems can exhibit viz. (i) Phase separation and (ii) collective directed motion: Many cases of patterning are observed during equilibrium phase transitions, but these are accompanied by non-equilibrium processes. One such example is the formation of dendrites of ice crystals which form regular and similar patterning. Another example is the crystallization of active colloids due to attractive chemical interactions [12, 13, 14]. Secondly, non-equilibrium systems which are internally-driven can exhibit the long-range correlations and directional ordering. The constituent elements exhibit collective directed motion with qualitative feature which are qualitatively quite distinct from individual dynamics. These can be observed at multiple scales: from microscopic interactions between molecular motors and actin filaments, collective migrations of tissue cells as well as bacterial and algal colonies, to collective behaviour of schools of swimming fish, swarms of bees and birds in macroscopic scale (see figure 1.1). By tuning the properties of certain active colloids, the interaction between them can be appropriately controlled which automatically changes the physical behaviour (and properties) of the macroscopic system.

1.1.2 Synthetic active matter

Synthetic active matter comprises of a system wherein the constituent elements have been designed and manufactured to exhibit certain specific behaviour of motion. These elements

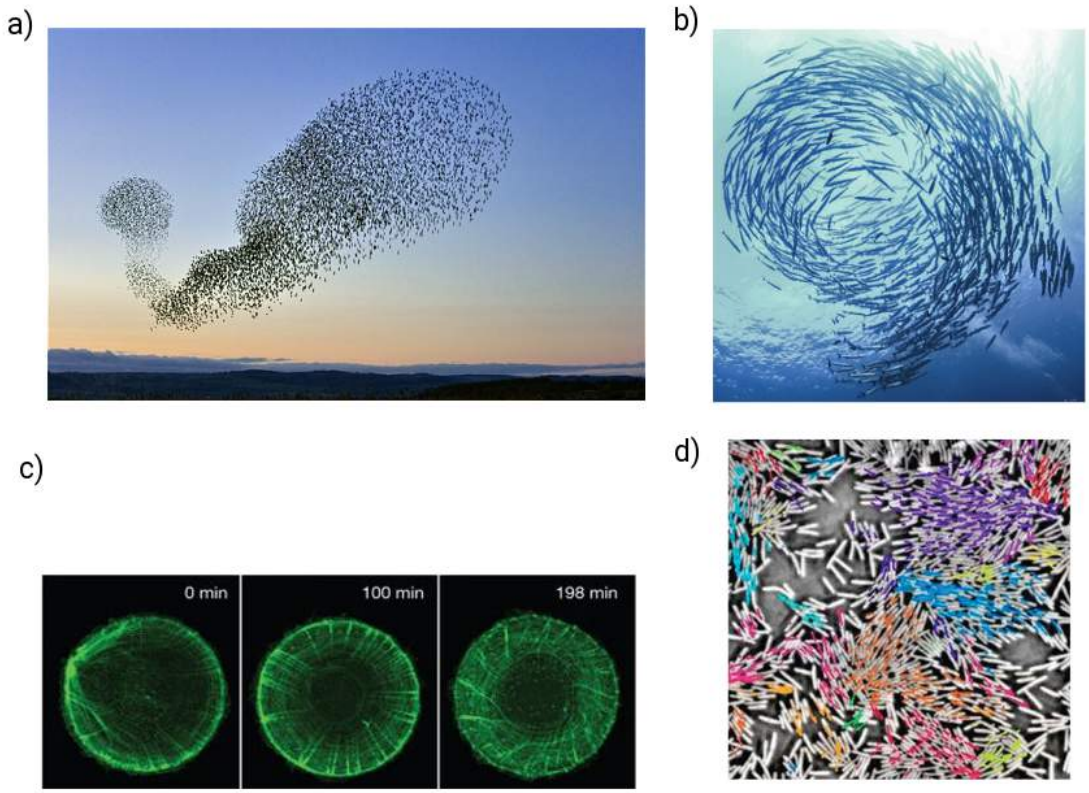

Figure 1.1: Some examples of the two pattern-forming properties exhibited by out-of-equilibrium systems viz. crystallization and long-range collective ordering: a,b) Collective migration of birds (starlings) Daniel Biber© photography (www.worldphoto.org) and fishes c) Actin filaments exhibiting non-equilibrium pattern formation [9] d) Swimming bacterial colonies of bascilus subtilus showing strong polar ordering - Adapted from Zhang *et. al.* [10]

are generally particles of microscopic size. They have been designed to accomplish guided transport at these scales and can serve the purpose of providing a controlled setting to study the physics of active matter such as their collective dynamics [14, 12] or interactions with surroundings [15, 16, 17], as well as acting as engineered "machines" for specific transport applications [18]. There are generally two kinds of synthetic active matter based on the mode of input of energy viz. i) External field driven and ii) driven by an internal mechanism.

1.1.2.1 Externally-driven

In experiments, a wide range of external fields, such as those of magnetic, electric, acoustic, thermal and chemical nature, have been used to induce motion of microscopic particles in a system. Such an external control has the advantage of having the ability to manipulate the propulsion characteristics of the particles by varying the strength and direction of the external field. One class of externally-driven particles propel due to direct forcing from an external oscillating field and move in-sync with it and hence, have excellent tractability. An example is that of a spherical colloid made of a ferromagnetic material (e.g. Nickel) of a given magnetic moment, in an external alternating magnetic field; the colloid traces the rotating field which leads to its rolling motion. Speeds of upto $\sim O(100)\mu$m/s have been achieved in this setup [19, 20, 21].

Another case is when the external (typically non-varying) field itself does not exert the

propulsive force but rather induces the symmetry-breaking mechanism on the particle necessary for its self-propulsion [22, 23, 24]. Although there is less control on the direction, the speed of propulsion is however dependent on the strength of external field [25, 5]. For example, spherical colloids made of dielectric material (such as PMMA) immersed in a conducting fluid achieves self-propulsion in the presence of a constant (DC) electric field using a mechanism called *Quincke rotation*. The electric field induces differential charge on the surface of the colloid; when the strength of the external field $\mathbf{E}_0$ becomes stronger than a threshold value $\mathbf{E}_Q$, an infinitesimal perturbation is sufficient to drive the system out of equilibrium, and leads to rotational motion of the particle with a velocity $\mathbf{U} \propto ((\mathbf{E}_0/\mathbf{E}_Q)^2 - 1)^{1/2}$ [22, 26]. Particles driven by acoustic streaming is another example of this class and have been used for separating particulate matter in a fluid [27].

1.1.2.2 Internally-driven

In certain particles, the symmetry-breaking propulsion is self-induced using internal mechanisms. They are completely self-driven in the sense that their direction and speed depend on the forcing field that they produce by interacting with their immediate surrounding medium. Their dynamics, being dependent only on the instantaneous properties of the local surroundings, restricts the high degree of flexibility for controlled motion which was available for particles driven by external fields.

Mechanically-driven particles which have moving parts that mimic biological swimmers are difficult to manufacture in large numbers and are susceptible to fatigue failure. A popular class of self-driven particles use a mechanism called *autophoresis* where their rigid surface creates chemical/temperature gradients which provide the forcing. For example, silica (SiO_2) colloidal particle half-coated with platinum (Pt) decomposes hydrogen peroxide (H_2O_2) at the platinum end, in its solution; the decreased local concentration of the fuel leads to unbalanced phoretic forcing which drives the particle [28]. This mechanism shall form one of the basis for the rest of the thesis and will be discussed in detail in the proceeding sections. An additional indirect control (i.e. turning the activity ON or OFF or making the activity sensitive to intensity of light) can be achieved by making the surface activity of particle light-sensitive [12].

1.1.3 Why do we need to understand such systems?

Each active matter system is unique with system-specific dynamics prescribed by the self-propulsion characteristics and their complex coupled interactions, both among themselves and with the surrounding medium. The major goal of active matter research is to bring all of these under a common umbrella; this field of research is still quite nascent and many new discoveries are still underway [18]. A proper mathematical and physical foundation for theory of active matter would not only help one to understand and predict the clustering and pattern formation dynamics of non-living systems such as vibrated granular media, self-propelling colloids etc.., but also allow one to distinguish quantitatively, the influence of psychology, biology and physics in the collective behaviour of living active systems. From a biological perspective, the knowledge of the interactions between the various elements of active matter systems such as cells, microtubules, bacteria, algae etc.. would provide an understanding of their growth and organization [29, 30]. Moreover, it provides information regarding their response to environmental stimuli such as external forces. For example, aggregation of biofilaments in cytoskeleton due to influence of motor proteins, growth of human melanocyte cells and their nematic ordering [31] etc..

One of the most prominent engineering application is the use of the self-propelled motion of the constituent elements for controlled transport and for doing work at micron scales. These

active colloids/ catalytic nanomotors have immense potential for targeted drug delivery and therapeutics [32, 18]. They have also been used for operating microscopic mechanical systems such as pumps and ratcheted gears. Some specific examples of their application are described in Section 1.4.3.

Thus, we see that active matter systems show rich dynamics which can be tapped for many potential scientific and engineering applications. Our focus will be on modelling the dynamics of synthetic swimmers; modeling such non-equilibrium systems can become complex with multitude of coupled interactions. However, we shall distill the physics to simple linear models to explain the phenomena. In the coming sections we shall summarize the research on one class of synthetic swimmers that move using forcing from gradients of an external field.

1.2 Motion through surface tension gradients

When a liquid interface is subject to surface tension (γ) gradients, the interface deforms due to the imbalance of forces at the interface. This is the cause for climbing of liquid up a glass of wine and subsequent formation of classical "tears" as the liquid slides down [33]. When the interface is of finite size, such as that of a droplet in emulsions, the droplets can achieve persistent motion because the interface creates non-zero surface forces [34, 35]. Being in a state of non-equilibrium, they form clusters in ordered hexagonal lattice arrangement [36]

If a spherical droplet drifts with a velocity U in a fluid medium of the same viscosity (η), balance between viscous dissipation and the work done by surface tension gradients gives $U \propto \Delta\gamma/\eta$. Here $\Delta\gamma$ is the average variation of surface tension around the drop. In experiments, the viscosity of fluid generally considered is $\eta \sim 10^{-3}$. This shows that even a small surface tension gradient $\sim 10^{-9}$ N/m^2 is sufficient for motion with velocities $U \sim 1$ μm/s. Typically, velocities of tens of micro-meters a second is common [37].

For surfactant adsorption at the interface under thermodynamic equilibrium conditions, the drift velocity of the droplet can be eventually expressed as [34, 33]

$$\mathbf{U}_{\mathrm{m}} = \frac{-akT}{3\bar{\eta} + 2\eta} \left(\frac{\mathrm{d}\gamma}{\mathrm{d}C_\infty} \right)_T \nabla C_\infty \tag{1.1}$$

where a is the drop size, $\bar{\eta}$ and η are the viscosities of fluid within and outside the drop respectively. Note that the direction of propulsion depends on the sign of $\mathrm{d}\gamma/\mathrm{d}C$. Generallly, the presence of a surfactant reduces the local surface tension of the drop i.e. $\mathrm{d}\gamma/\mathrm{d}C$ is negative. Thus, by varying the surfactant concentration in the surrounding fluid, a drop is forced towards a region of higher concentration of surfactant and in doing so, it lowers its interfacial energy [38]. Note that the drift velocity is proportional to the size of the droplet. Marangoni-driven motion has recently gained much attention due to advancements in bio-compatible self-propelling droplets which undergo chemical reaction at the interface to produce the surfactant gradients needed for propulsion.

In Eq. (1.1), when $\bar{\eta} \to \infty$, i.e. the case where the drop is a solid, the drift velocity predicted by equation (1.1) goes to zero, which is a result of the no-slip boundary condition acting on a solid interface subject to internal forcing. However, experiments show that even solid particles undergo drift due to external concentration gradients [39, 40]. But how can this phenomenon be explained? This is what we shall seek to understand in the subsequent sections.

1.3 Phoretic drift of particles

In the current scenario, we try to understand the migratory behaviour of small solid colloidal particles in the presence of external ionic as well as non-ionic compounds. Through only a logical treatment of the problem in section 1.1, it was argued that a thermodynamic forcing could be initiated on a body by any non-equilibrium flux. Thus, by this argument, gradients of a given field could theoretically propel a solid body. The currently accepted model which explains the dynamics was first introduced by Derjaguin *et. al* [41, 40]. They considered the interface of the particle to be diffuse, within which osmotic flows are induced due to local gradients in thermodynamic variables such as concentration / temperature field. This mechanism was later termed as *phoresis* - the Greek word for "bearing" or the act of migrating from one place to another by means of an external agent. By considering only linear phenomenon of interaction of the external field Y_∞, all phoretic effects are seen to induce a surface velocity,

$$\widetilde{\mathbf{u}} = \mathcal{M}\, \nabla Y_\infty \tag{1.2}$$

where $\mathcal{M}$ is termed as the phoretic mobility which is a surface property that determines the behaviour of interaction between the driving field and the surface (also known as the electrokinetic potential or 'Zeta potential' of the surface in case of electrophoresis). It is to be noted that even though this slip velocity in equation (1.2) resembles the Marangoni slip in equation (1.1), it is however starkly different; a Marangoni-driven motion is characterized by a continuous velocity and discontinuous stress across the interface while the phoretic motion exhibits discontinuity in both surface stresses and velocity at the scale of the particle, but are both continuous at the scale of the thickness of the diffuse layer.

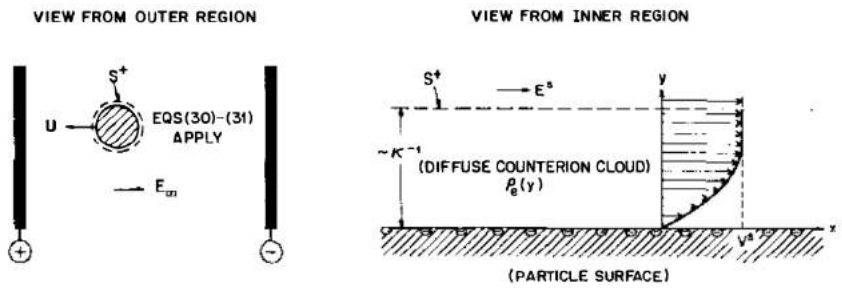

Figure 1.2: Osmotic flow within a diffuse interface during electrophoresis. The velocity field appears discontinuous at the scale of the particle with an effective slip velocity driving the particle (left). However, in the inner region (within diffuse interface) the flow exhibits boundary layer behaviour (right). Figure reproduced from [40]

Phoretic phenomenon is relatively rare in nature (compared to other non-equilibrium thermodynamic processes such as diffusion), but nonetheless present at microscopic scales. Certain bacteria *Dictyostelium Discoidium* exhibit chemotactic behaviour along with phoretic drift [42]. Even enzymes such as catalase shows chemotatic behaviour through direct interaction of its surface to gradients in external chemical field (here, hydrogen peroxide) [43, 44]. In some cases, these natural "motors" have been integrated with microfabricated environment for controlled transport. For example, motor proteins such as Kensin transport vesicles along micro-tubules (at speeds of $O(1)\mu m/s$) have been implemented in controlled pick-up of cargo along artificial rails [45]. These cases inspire as well as emphasize the need for creation of synthetic self-propelling materials that can be tuned and manufactured for the appropriate task.

Over the last decade or more, experimentalists have taken the aid of the above proposed

models for phoretic propulsion mechanism to advance our ability to design and manufacture colloidal particles having controlled propulsion and on-demand transport [20]. Phoretic mechanism is turning out to be one of the leading potential candidates for achieving this and hence, has huge implications in therapeutics such as targeted drug delivery, chemical sensing, cellular separation etc...[18]

1.3.1 Diffusiophoresis

The motion of rigid colloidal particles in a solution containing a concentration gradient of some arbitrary solute is termed as *diffusiophoresis* [40]. The particle may drift either towards or away from higher concentration depending on how its surface interacts with the ionic/ non-ionic solute molecules. The attractive Vander Waals forces compete with repulsive steric effects to decide whether the particle moves towards the higher or lower concentration [40].

1.3.1.1 General mechanism within the double-layer

As mentioned, to explain the phoretic behaviour, the idea of a diffuse interface for the colloid is maintained here; the flow features within this layer determines the macroscopic flow around the particle. Derjaguin *et. al.* argued that the diffusiophoretic effect is a result of differential hydrostatic pressure (exerted by the solute molecules on the surface) acting tangentially along the solid surface within this interaction layer [41]. This results in an osmotic flow within the layer. The interaction of the solute with the solid surface is through i) excluded volume effect: where the solute occupies a finite volume and displaces the fluid near the interface ii) Van der Waal's forces and, iii) Dipole interactions (in the case of ionic solute molecules). Thus, the interface effectively couples fluid mechanics and mass transfer. This interaction is defined by an interaction potential, Φ. The force exerted on the colloid due to absorption/ emission of solute on/from the surface is then, $F = -C\ \nabla\Phi$, where C is the concentration of solute at the interface. Emission of solute occurs when $\Phi > 0$ which creates a fluid flow towards higher concentration of solute thereby creating a motion of the particle to a lower concentration. Diffusiophoretic effect thus also has two different scales of analysis: The flow within the interaction layer and, the flow created in the macroscopic scale due to the interactions in the double-layer. The solute concentration within this layer follows the steady-state diffusion equation

$$\nabla \cdot \mathbf{j} = 0 \qquad \text{where, the flux, } \mathbf{j} = -D\left(\nabla C + \frac{C\ \nabla\Phi}{kT}\right) \tag{1.3}$$

The thickness of the double-layer is considered to be extremely small compared to the size of the particle $\delta/a \ll 1$. Thus, one can think of using results of boundary layer theory within this layer. The flow is thus considered to be parallel to the surface, but variable along y (see figure 1.2). Note that even though the thickness is of $O(10)$Å, a continuum model is used to understand the physical phenomenon within this double-layer. Additionally, the following assumptions are also made for the analysis: (i) the solute-solute interactions are negligible. This assumption however has to be modified in the case of high solute concentrations near the interface (ii) $C(x)$ varies slowly compared to the phoretic forcing $F(x)$.(iii) There is no kinetic barrier to absorption/ desorption of solute on the surface. (iv) There are no polarization effects i.e. the interaction double-layer is so thin that it cannot accumulate any non-zero flux of solute. This is expressed mathematically as

$$D\mathbf{n} \cdot \left(\nabla C + \frac{C\ \nabla\Phi}{kT}\right)\bigg|_{r=a} = 0, \qquad C\Big|_{r\to\infty} = C_\infty \tag{1.4}$$

The flow field within this thin double-layer is dominated by viscous effects and hence, to compute the velocity field within, one can use the Stokes equations

$$-\nabla p + \eta \nabla^2 \mathbf{u} - C\,\nabla\Phi = 0, \qquad \nabla \cdot \mathbf{u} = 0 \tag{1.5}$$

with the no-slip boundary condition at the solid surface,

$$\mathbf{u}\Big|_{r=a} = 0, \qquad \text{and,} \quad \mathbf{u}\Big|_{r\to\infty} = \widetilde{\mathbf{u}} \tag{1.6}$$

It has been shown that the "slip" velocity formed at the boundary of the double-layer is proportional to the local gradient of solute concentration along the surface [46, 41, 47],

$$\widetilde{\mathbf{u}}(x) = \mathcal{M}\left(\frac{\partial C(x)}{\partial x}\right) \tag{1.7}$$

where, as mentioned, $\mathcal{M}$ is the phoretic *mobility*, given by

$$\mathcal{M} = \frac{-kT}{\eta}\int_0^\infty (e^{-\Phi(y)/kT} - 1)y\,\mathrm{d}y \tag{1.8}$$

The above expression was derived using equilibrium thermodynamic relations of solute molecules within the double-layer [40]. The mobility can be either positive or negative depending on how the solute interacts with the solid. It is however not a directly measurable parameter from experiments as it requires detailed knowledge of the surface property $\Phi(y)$. Molecular models have been developed to determine $\mathcal{M}$ in certain special cases such as when the solid surface interacts with solute molecules that have a dipole moment, or the case if we assume rigid solute molecule having steric exclusion [40].

1.3.1.2 Macroscopic flow

The inner region being extremely small behaves as a region where an effective slip velocity is formed which propels the particle. However, within the inner region, the velocity field is continuous but can be variable and satisfying the no-slip boundary condition on the solid. The velocity thus appears discontinuous at the scale of the size of the particle.

Consider the colloid placed in an external concentration field $C_\infty(\mathbf{x})$. The solute molecules are assumed to diffuse (without advection), leading to the Laplace equation

$$\nabla \cdot \mathbf{j} = 0 \quad \implies -D\nabla^2 C_\infty = 0 \tag{1.9}$$

where, D is the diffusvity of the solute in the fluid. The diffuse interface $\mathcal{S}_+$ extends till $r = a$. The interface, being thin ($\delta/a \ll 1$), does not allow any flux into the surface, so that

$$\mathbf{n} \cdot \nabla C_\infty\Big|_{r=a} = 0 \tag{1.10}$$

One can additionally assume the interface to be flat in the scale of δ. At this scale, the velocity and stresses appear discontinuous [40]. Thus, the interface creates an effective slip velocity on the surface of the colloidal particle(from equation 1.7)

$$\mathbf{u}\Big|_{r=a} (= \widetilde{\mathbf{u}}) = \mathcal{M}\,\nabla_{||} C_\infty\Big|_{r=a} \tag{1.11}$$

This slip velocity to the propulsion of the particle. Being in the low Reynolds number regime, the flow field (in the reference frame of the particle) created by the particle obeys

the Stokes equations

$$\nabla^2 \mathbf{u} = \nabla p \quad \text{and} \quad \nabla \cdot \mathbf{u} = 0 \quad \text{with,} \quad \mathbf{u}\Big|_{r\to\infty} = -\mathbf{U}^{\text{self}} - \boldsymbol{\Omega}^{\text{self}} \times \mathbf{r} \tag{1.12}$$

Additionally, the colloidal particle (within the diffuse interface $\mathcal{S}_+$) is both force- and torque-free. This is because the force exerted by the solute gradients is balanced by the drag created by the fluid on the surface of the particle.

$$\int_{\mathcal{S}_+} \boldsymbol{\sigma} \cdot \mathbf{n} = 0, \qquad \int_{\mathcal{S}_+} \mathbf{x} \times (\boldsymbol{\sigma} \cdot \mathbf{n}) = 0 \tag{1.13}$$

The propulsion velocity of the colloid in an external concentration gradient was provided by Smoluchowski in 1921 [40]. For uniform surface mobility,

$$\mathbf{U}_{\text{d}} = \mathcal{M}\, \nabla C_\infty\Big|_{r=0}, \qquad \boldsymbol{\Omega}_{\text{d}} = 0 \tag{1.14}$$

The detailed derivation of this expression is provided in the next chapter. Note that for a given colloid in a solute gradient, the propulsion velocity depends only on the gradient at the center of the particle; it is independent of the shape or the size of the colloid! It needs to be mentioned here that the surface mobility (and hence the slip velocity) is proportional to the thickness of double-layer (δ). When the particles have variable surface mobility, the propulsion velocity is given by [40]

$$\mathbf{U}_{\text{d}} = \left[\langle \mathcal{M} \rangle \mathbf{I} - \frac{1}{2}\langle \mathcal{M}(3\mathbf{nn} - \mathbf{I})\rangle\right] \cdot \nabla C_\infty\Big|_{r=0} \quad \text{and,} \quad \boldsymbol{\Omega}_{\text{d}} = \frac{9}{4a}\langle \mathcal{M}\mathbf{n}\rangle \times \nabla C_\infty\Big|_{r=0} \tag{1.15}$$

When the concentration gradients are uniform, the velocity field created by a particle of uniform mobility is potential flow, decaying as $O(r^{-3})$ [41, 48, 49]. However, when either the gradients are not uniform or if the particle has variable mobility, the flow field created by the particles decay as $O(r^{-2})$. Both these fields decay faster that sedimenting particles. By balancing the surface interaction versus the viscous diffusion of the solute, one can determine the characteristic velocity scale as $U^* = kT\delta^2 c^*/\eta a$, where c^* is the characteristic scale for the concentration field, which depends on the surface activity. If the surface emits a flux at a rate $\mathcal{A}$, then $c^* = \mathcal{A}a/D$. Note that for a phoretic particle having constant rate of flux at the surface, the characteristic velocity $U^* = kT\delta^2\mathcal{A}/\eta D$ is thus independent of the size of the particle, but depends on the size of the interaction layer δ. However, for a two-stage reaction model, the diffusiophoretic velocity is observed to decay with size of the particle (for large particles), in accordance with experimental observations [50]. In Marangoni flows we have seen the propulsion velocity is proportional to the size of the particle a (see equation (1.1)). Thus, since $\delta \ll a$, one can conclude that diffusiophoretic drift velocities are marginal compared to marangoni-driven drift.

1.3.1.3 Diffusiophoresis in electrolyte solutions

Consider an uncharged colloidal particle placed in an electrolyte solution. The surface of the neutral colloid undergoes charge separation (and becomes either positvely or negatively charged) with a cloud of counterions outside which balance the total surface charge. The thickness of the double-layer (ion cloud) in this case is known apriori (known as "Debye screening length") [49, 40]. In a non-uniform electrolyte solution, there are two mechanisms coming into play within the double-layer that propel the charged colloidal particle: (i) the osmotic pressure generated by solute molecules (as in the case of non-electrolyte solute). Both species of solute - the coion and couterion - contribute to propulsion (ii) Force from

an electric field that balances a diffusion current created by charge separation arising from difference in diffusivities of the coion and the counterion in the electrolyte solution [51]. This field creates an electrophoretic propulsive behaviour. For an electrolyte solution, the propulsion velocity,

$$\mathbf{U}_{\mathrm{d}} \propto \nabla \ln C_{\infty}\Big|_{r=0} \tag{1.16}$$

1.3.2 Electrophoresis

Early experiments have observed the phenomenon of movement of ionic solute in the presence of a charged interfaces [49]; some examples include motion of rubber latex particles in electrolyte gradients [52, 53]. The charge on the colloid interface is balanced by counter-ion cloud around it. This cloud is drifted to one direction due to the external electric field, creating more negative charge on one side of the colloid compared to the other, giving rise to spontaneous motion with velocity $\mathbf{U} = \varepsilon\zeta/4\pi\eta\mathbf{E}$, where ϵ is the dielectric constant of the particle, ζ is the zeta potential and $\mathbf{E}$ is the strength of the electric field [48]. Thus the diffuse interface of the colloid actively contributes to structuring the macroscopic flow around it. The interface is of an extremely small thickness within which the stresses and velocity are continuous. Thickness of this region (δ) is much smaller than size of the particle, a (i.e. $\delta/a \ll 1$). Typically, in experiments, the measured double-layer thickness is $\delta \sim O(10^{-9})$m for a particle of size $O(10^{-6})$m [49]. The colloid may have localized charge separation, but it does not have any *net* positive or negative charge. Any stresses generated on the surface of the particle from the interaction of electric field with the local surface charge is balanced by the drag force created by the motion of the particle in surrounding fluid. It is thus interesting to note that unlike sedimentation where the flow field around the sedimenting particle (due to external body force acting on it by the gravitational field) decays as $O(r^{-1})$, the flow field around a particle moving due to an external electric field decays much more rapidly as $O(r^{-3})$ due to absence of any such body forces.

1.3.3 Thermophoresis

Themophoresis is the motion of solid particles in external temperature gradients. This is similar to the phenomenon of *Soret effect* which is the thermal diffusion of fluid mixtures in temperature gradients. Similar to other phoretic mechanisms, a direct microscopic interaction between colloid and surrounding fluid is required to give rise to particle motion; the mechanism of propulsion was proposed using the diffuse interface model by Derjaguin *et.al* [41]. However compared to electrophoresis and diffusiophoresis, thermophoresis has not gained as much popularity because of lack of flexibility and predictability in their dynamics. The propulsion velocity depends on the size of the particle and the solvation forces due to the surrounding medium. Additionally, the effective mobility in thermophoresis is found to be sensitive to the temperature; at high temperatures, the propulsion even reverses direction! [54]. Nonetheless, knowledge of this effect is needed while considering electro-/ diffusiophoretic propulsion at high light intensities. Since we are focusing mainly on diffusiophoretic effects, the reader may consult the review article on thermophoresis in colloidal suspensions by Piazza *et. al* [5] for an extensive review.

1.3.4 Early observations and applications of phoretic drift

In natural and industrial processes where significant gradients in concentration of solute are formed, especially those involving boundary layer phenomena, the diffusiophoretic effects

are expected to play important role. In natural processes, the migration of bacterial colonies have been attributed to electrophoretic effects [49, 55]. The effect is also fairly common in paint coating processes and in porous membrane flows. One such example is the case of manufacture of gloves and other rubberized clothing from latex using coercive dipping/ ionic deposition process [53, 40, 49]. In coating of carbon steel rod, the iron from the surface oxides to form ionic solute that diffuses from the surface of the rod into the solution. This creates migration of the latex particles on to the surface of the rod due to induced electric field as well as diffusiophoretic effects [49]. This has lead to detailed experimental studies of both electrophoretic and diffusiophoretic systems which were focused on measuring the diffusion potential [39, 53], phoretic mobiliteis [39] as well as analysing the collective behaviour of colloidal particles due to these effects [49, 40]. Over the past decade, the mechanism has been heavily applied for controlled transport of colloids and droplets [56, 19].

1.4 Autophoretic self-propulsion

As we have seen in the previous section, a phoretic particle undergoes drift in external gradients of either a scalar field such as concentration or temperature, or vector field like electric or magnetic fields. An *active* phoretic particle has the additional ability to generate their own fields through surface mediated processes; for example, catalytic colloids are a class of active particles that promote chemical reaction at their surface which produces and diffuses a solute around the particle. Moreover, if the colloid is appropriately designed so as to create its own surface field gradients, then it can achieve propulsion through self-induced phoretic forcing. Such self-propelling particles are termed as being *autophoretic*. A common example, is the half coated $SiO_2 - Pt$ Janus colloid which propels in self-generated gradients in concentration of hydrogen peroxide [28]. As the present thesis will be on understanding the collective dynamics of such autophoretic colloids (that employ diffusiophoresis in particular), a theoretical foundation for physics of self-propulsion of individual particles is first required, which shall be detailed in this section.

The solute concentration field created by an active phoretic particle obeys the advection-diffusion equation,

$$\frac{\partial c}{\partial t} = D\,\nabla^2 c - \mathbf{u}\cdot\nabla c \quad \text{with,} \quad c(r\to\infty) = 0, \quad \mathbf{n}\cdot\nabla c|_{\mathcal{S}} = -\mathcal{A} \tag{1.17}$$

Here, $\mathcal{A}$ is the is the solute flux consumed/generated across the surface of the particle, termed as the phoretic *activity*. Note that the reaction considered here is of constant rate-of-flux. However, more complicated situation involving first-order kinetics as well as multiple solute can be additionally incorporated [57]. In the purely diffusive limit, the solute concentration field obeys the steady state diffusion equation,

$$\nabla^2 c = 0 \quad \text{with,} \quad c(r\to\infty) = 0, \quad D\,\mathbf{n}\cdot\nabla c|_{\mathcal{S}} = -\mathcal{A} \tag{1.18}$$

Since advection of the solute by the fluid is neglected here, the solute dynamics is decoupled from the fluid dynamics problem which can then be obtained in a second step using the dimensionless Stokes flow equations.

$$\nabla^2\mathbf{u} = \nabla p, \quad \text{and} \quad \nabla\cdot\mathbf{u} = 0 \tag{1.19}$$

with boundary conditions in the laboratory frame of reference

$$\mathbf{u}|_{\mathcal{S}} = \mathbf{U}^{\text{self}} + \mathbf{\Omega}^{\text{self}}\times\mathbf{x} + \widetilde{\mathbf{u}}, \qquad \widetilde{\mathbf{u}} = \mathcal{M}(\mathbf{I}-\mathbf{nn})\cdot\nabla c, \quad \text{and} \quad \mathbf{u}(r\to\infty)\to 0 \tag{1.20}$$

$\mathbf{x}$ is the position of the center of the particle, and $\mathbf{U}^{\text{self}}$ and $\mathbf{\Omega}^{\text{self}}$ are its translation and rotation velocities. The latter quantities are determined uniquely by imposing that each particle remains force- and torque-free

$$\forall j, \quad \int_{\mathcal{S}_j} \boldsymbol{\sigma} \cdot \mathbf{n} \, \mathrm{d}S = \int_{\mathcal{S}_j} (\mathbf{r} - \mathbf{R}_j) \times (\boldsymbol{\sigma} \cdot \mathbf{n}) \, \mathrm{d}S = 0, \tag{1.21}$$

With these boundary conditions for a phoretic particle, the self-propulsion velocity can be shown to be dependent only on the surface properties and diffusivity of solute; for a particle with uniform mobility $\mathcal{M}$ and only half of the surface active $\mathcal{A}$, the self-propulsion velocity can be computed to be [58],

$$\mathbf{U}^{\text{self}} = \mathcal{A}\mathcal{M}/4D \tag{1.22}$$

1.4.1 Symmetry-breaking propulsion mechanisms

The generation of surface slip velocity is essential for self-propulsion of the particle. Since the slip velocity is linearly dependent on the gradient of the local surface concentration field, a phoretic particle having homogeneous surface activity (and hence produces homogeneous surface concentration field) does not self-propel. Additionally, since the propulsion velocity depends on the surface average of the slip velocity, a symmetrically distributed field does not induce propulsion either, unless the phoretic forcing symmetry is broken by variable surface mobility. Taking these into consideration, some of the common mechanisms used to design self-propelling autophoretic particles are detailed below.

1.4.1.1 Janus and dimer colloids

The most straightforward method to create surface concentration gradients is to spatially vary the surface activity $\mathcal{A}$, and the simplest way to do so is to have an axisymmetric spherical particle having two distinct surface properties - known as the *Janus* particle - as shown in figure 1.3. In experiments, Janus swimmers are usually created by using passive silica bead coated with a reactive metallic cap on one end [58].

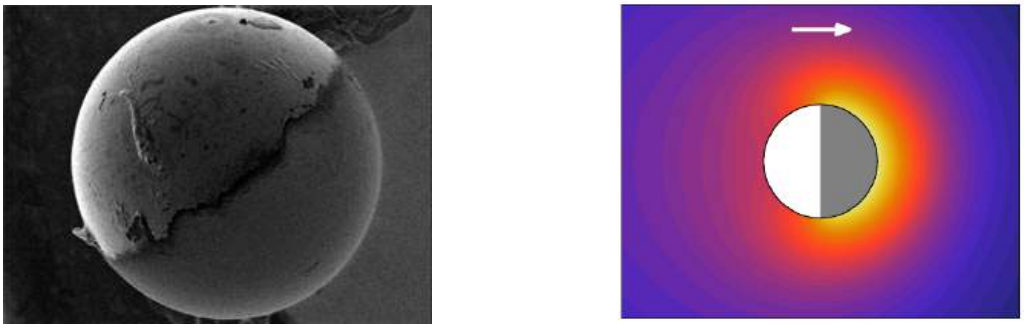

Figure 1.3: a) SEM image of $SiO_2 - Au$ Janus phoretic particle. : adapted from [59] b) The concentration field created by the active surface is determined using diffusion equation for a 1/2 active Janus particle whose polarity is given by $\mathbf{t}$ (white arrow): adapted from [57].

Using the governing equations for solute and fluid dynamics (equations (1.18),(1.20)), the characteristic propulsion velocity of diffusiophoretic swimmers can be obtained as $U \sim \mathcal{A}\mathcal{M}/D$. For a true Janus particle (hemispherical surface coverage) with surface activities $\mathcal{A}_1$ and $\mathcal{A}_2$, and mobilities $\mathcal{M}_1$ and $\mathcal{M}_2$ respectively, the propulsion velocity is computed to be $U^{\text{self}} = (\mathcal{A}_1 - \mathcal{A}_2)(\mathcal{M}_1 + \mathcal{M}_2)/8D$ [58]. The interesting feature of such a

propulsion mechanism is thus that the characteristic velocity is independent of the size of the particle, and depends only on the surface patterning. For a particle with a uniform surface mobility, the half-coated Janus particle shows the highest self-propulsion velocity with $U^{\text{self}} = \mathcal{A}\mathcal{M}/4D$; when solute advective effects are significant, slightly more surface coverage is favoured for higher velocities [57]. Because of its relative ease to manufacture and broader control of phoretic properties by tuning activity and mobility, Janus colloids are considered as prime choice for testing dynamics in experiments. Additional to their flexibility to tune their swimming properties, their axisymmetric nature makes it more tractable for theoretical and numerical computations.

One can also consider the situation where the (non-identical) particles are axisymmetric, but non-spherical; an example is phoretic dimers. Dimers are combinations of two spherical particles with different surface activity (and/or mobility) held together either through phoretic or short-range attractive forces [60]. The difference of near-field structuring of solute concentration as well as flow field from that of Janus particles can create dramatic differences in self-propulsion characteristics [61, 62].

1.4.1.2 Geometric asymmetry

An isotropic distribution of concentration field around a spherical particle having homogeneous surface activity can be modified by distorting the particle geometrically instead of varying surface activity or mobility. The effect of geometric asymmetry can be tested by considering a simple two-sphere system shown in figure 1.4. Both the spheres have uniform surface activity and mobility and are connected by a thin inextensible rod that holds them together.

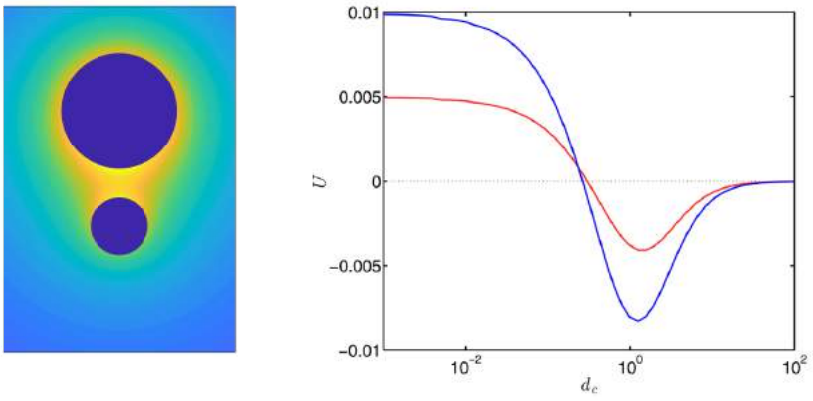

Figure 1.4: Figure on left shows spheres, $R_1 = 1$ and $R_2 = 0.5$ at a contact distance $d_c = 0.5$. The propulsion velocity for the combination $R_2/R_1 = 0.5$ (in dark blue) and $R_2/R_1 = 0.75$ in red. Adapted from Michelin & Lauga, *EPL*, 2015 [61]

The propulsion velocity of such a system at large separation distances, d of the spheres is [63]

$$U^{\text{self}} = \frac{\mathcal{A}\mathcal{M}a_1a_2(a_2 - a_1)}{Dd^2(a_1 + a_2)} \tag{1.23}$$

Thus a non-zero propulsion velocity can be achieved as long as the geometrical symmetry is broken (i.e. $a_2 \neq a_1$). The maximum propulsion velocity was found to be near $a_2/a_1 \approx 0.3 - 0.4$ when the spheres are separated by a unit contact distance. Moreover, note that the characteristic propulsion velocity in equation (1.23) is less than that of Janus particle. As a generalisation, the propulsion velocity of a deformed active particle has also been computed [61, 64].

1.4.1.3 Instability from advection of solute

This is a special case where self-propulsion of the particle is achieved not by introducing non-uniform surface properties, but by the non-linear advection properties of the solute. As the size of the particle increases, the flow-field can create advective effects on the solute. The competition of advection and diffusion is given by the Péclet number, $\mathrm{Pe} = \mathcal{A}\mathcal{M}a/D^2$. At large Péclet numbers, the non-linear coupling between solute concentration and advection induces an instability in the swimming mode that creates a fore-aft asymmetry in the solute distribution, and hence induces phoretic propulsive force as shown in figure 1.5.

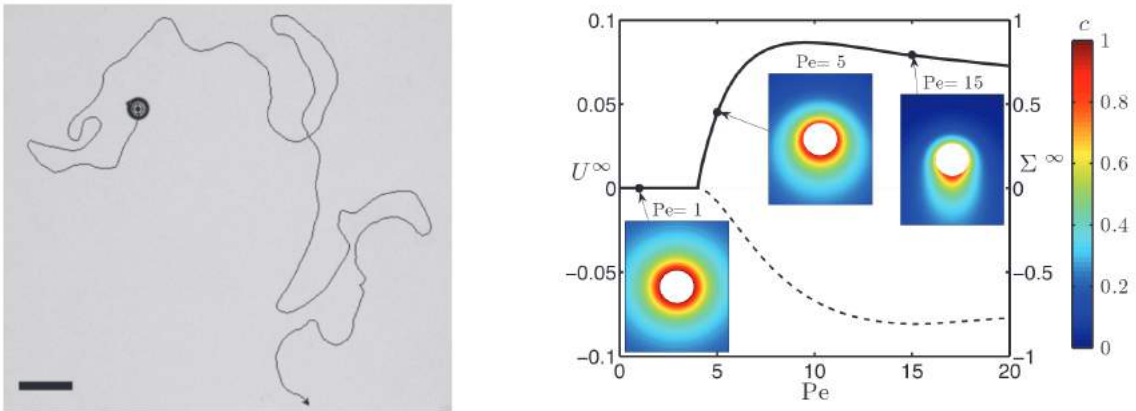

Figure 1.5: a) A spontaneously swimming isotropic active drop [36]. b)Steady-state propulsion velocities of isotropic phoretic particle at various Péclet numbers. The maximum steady swimming velocity is acheived when Pe = 9. Figure is from Michelin *et.al.*, *Phys. Fluids*, 2013 [65].

The particle exhibiting this instability is shown to have a far-field flow resembling a pusher swimmer. This is a universal mechanism of self-propulsion and can be used to explain the dynamics of self-propelling drops [36, 66, 67].

These are some of the mechanisms that have been commonly employed to design and develop active colloids both for understanding the dynamics of active systems but also to open new avenues for engineering applications.

1.4.2 Experiments in autophoretic colloids

The recent advancements in the precision and control over large-scale manufacturing of microscopic phoretic colloids have attracted the attention of many engineers in designing and developing artificial swimmers with characteristics suitable for a particular task [18, 32]. Together with improvements in tools for their visualisation, experimental physicists have started looking into the detailed dynamics of these self-propelling particles in recent years. Some of the active colloid systems have been seen to be more reliable in providing good control of speed and directionality, and relatively better robustness in performance and are slowly becoming a standard test subject for experiments. Some of the commonly used phoretic systems are described below.

One of the early developments in autophoretic particle was on bimetallic cylinders in acid solutions. Platinum-gold ($\mathrm{Pt} - \mathrm{Au}$) bimetallic rods in hydrogen peroxide (H_2O_2) exhibit propulsion due to bipolar electrochemical reactions that induces an electric field within the rod which is responsible for the propulsive force (see figure 1.6a). The concentration gradients thus induce an electrophoretic effect on the rod which propels them at high speeds

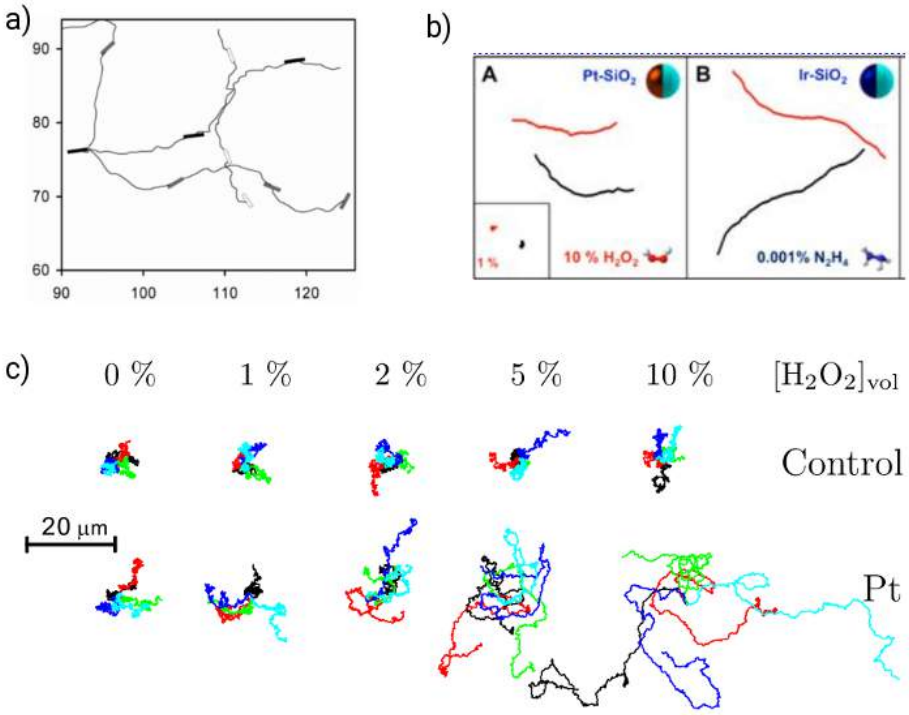

Figure 1.6: a) Trajectories of a bimetallic platinum-gold ($Pt - Au$) rod exhibits direction motion in gradients of hydrogen peroxide (H_2O_2) in its solution through electrophoresis [68]. b) An example (which propels even with very low concentration of fuel $\sim 10^{-5}$ %) is silica-iridium ($SiO_2 - Ir$) Janus particles in hydrazine (N_2H_4) solution. The particle swims with speeds of approximately 20 body lengths per second [69]. c) Non-electrolyte self-diffusiophoresis is silica-platinum ($SiO_2 - Pt$) in H_2O_2 solution. The propulsive speed depends on the amount of fuel (H_2O_2) in the solution [28].

of around 10 body lengths/sec [68]. An example of *non-electrolyte* self-diffusiophoresis is polystyrene ($PS - Pt$) in H_2O_2 solution (see figure 1.6c). The platinum end catalyses the chemical reaction that decomposes hydrogen peroxide at the surface of the particle; the reduced availability of the fuel at this end creates local concentration gradients which induces diffusiophoretic propulsion. Speeds upto a few diameters are achieved [19]. *Electrolyte diffusiophoresis* can be observed in $SiO_2 - TiO_2$ Janus particles immersed in H_2O_2 solution when the particles are illuminated with UV light [70]. The above experiments have partial electrophoretic effects acting on the particle; a purely diffusiophoretic propulsion has only been observed on polymerization driven self-propulsion [71].

The above mentioned setups consider colloids which are activated by a light source. A special case of a thermally activated diffusiophoretic system is when one uses paramagnetic $SiO_2 - Au$ in a binary mixture of water and 2,6-lutidine [72]. A homogeneous illumination will locally heat the metallic half beyond the critical temperature causing local de-mixing. This causes the water molecules to approach the hydrophilic (gold) cap. The mechanism of propulsion is hence not due to thermophoresis but due to the differential adsorption of water (or lutidine) and water-lutidine mixture which creates a *diffusiophoretic* forcing in the diffuse interface of the particle [73]. The advantage of using the binary-mixture setup is the need for only low intensities of light to propel the particle compared to that needed for thermophoresis. Another advantage of such a system is that the binary-mixture does not promote long-range chemical interactions between the particles thus, allowing one to experimentally observe clustering dynamics resulting purely from mobility of the particles.

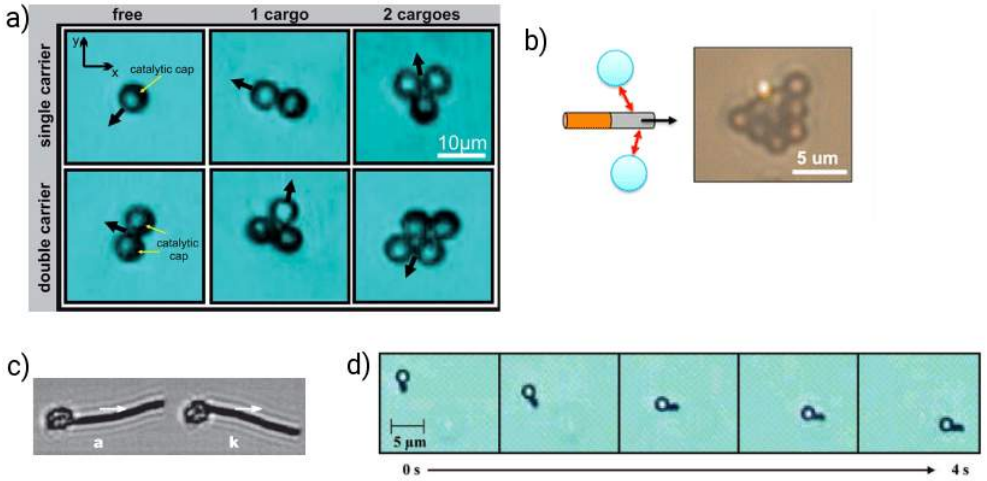

Figure 1.7: a) Janus particle and their collective can be used for transport of passive colloids such as silica [77]. b,d) Electrostatic interaction between $Pt - Au$ nanomotors and charged polystyrene colloids have been used to capture the passive colloids and, transport and deliver it at a desired location [78, 68]. Such model swimmers have been used to attach themselves to passive particles and transport cargo in a desired direction in a highly controlled fashion [79] c) Swimming motion of artificial flagella mimicking spermatozoa is driven by an external magnetic field and is used to transport cargo.

Additionally one can tune the approach length of these particles to control the particles through complex environments [72].

1.4.3 Some applications

From a fundamental physical perspective, one of the primary applications for which such phoretic systems have shown application for, is controlled and directed transport. This property is much sought-after because of potential applications in therapeutic, and medicine. Self-propelled particles such as Janus colloids create chemical and hydrodynamic fields as they swim through the fluid. These fields (which are characteristic signature of the particle) introduce long-range interactions which can be used for gathering certain cargo. One such example is that of diffusiophoretic Janus particles which couple with passive particles can be used for combined transport. Attractive magnetic interactions of $Pt - Ni - Au$ micromotor with colloids having a ferromagnetic core have also been used for similar purpose. Externally driven particles such as magnetic micro and nano-swimmers can be used to mimic the motion of biological swimmers like bacteria and spermatozoa [74, 75, 76] (see figure 1.7c). Some examples of internally and externally driven particles particles displaying cargo transport is shown in figure 1.7.

In thermal equilibrium, the passive particles exert equal forces regardless of the geometry of the system it is acting on. However, for active systems, a clear preference can be observed for clustering in confined regions - known as "ratchet effect" [56, 80, 11]. From a thermodynamic perspective, the observation implies that the pressure does not satisfy the equation of state and depends on the interaction of bacteria with the walls; the excess pressure in confined region, which when left unbalanced can lead to propulsion (see figure 1.8). This thus shows that at a macroscopic scale, the internal energy possessed by a collection of these active self-propelling particles in suspensions can be channelled to perform a macroscopic operation collectively.

Another potential field of application is in active sensing and directional delivery using

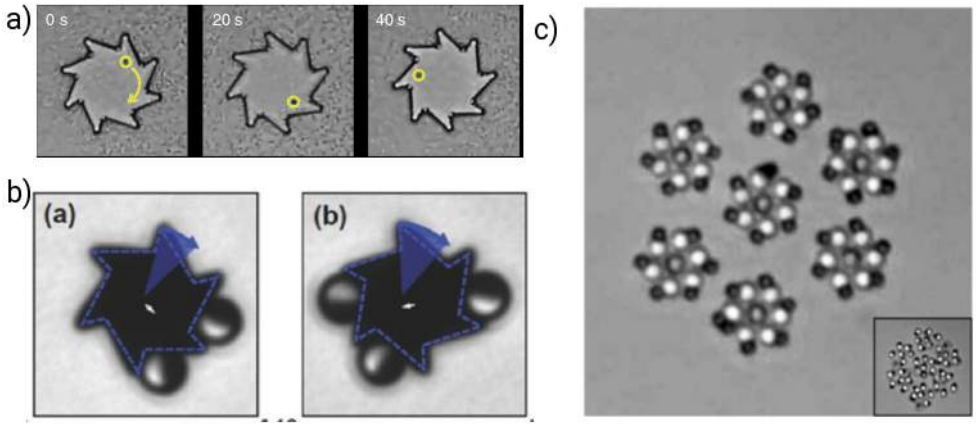

Figure 1.8: a) swimming bacteria can be used to power a ratchet geared assembly [81]. b,c) Active matter suspensions comprising of light-activated colloids have been used to create self-assembling rotating micro-motors; the asymmetric diffusiophoretic interactions create net rotation of the motors with angular velocity $\sim O(0.1)$ rpm [82, 83]. Such engineering feats show potential for developing controlled machines in micron scales;

the property of artificial chemotaxis. Particles which are driven using internal mechanism such as autophoresis cannot maintain their direction of propulsion for long time; being in microscopic scales, they are subject to thermal noise in the background causing them to have a Brownian motion which reduces control over their directed motion [28]. However, one can create external gradients of the activating field to create a chemotactic behaviour [77]: the particle reorients itself to align parallel or anti-parallel to the local concentration gradient [84, 85]. The mechanism is independent for phoresis in that chemotaxis is due to differential diffusivities of the particle in the external field; the diffusivities could either be enhanced or suppressed depending on the concentration of solute. Even in the absence of external fields, the self-generated fields by surrounding particles can behave as local sources of chemotaxis. This chemotactic property can be used for sensing and calibrating external fields. Such systems also naturally display a variety of pattern-forming dynamics such as schooling, waves and oscillatory behaviour of particles [84, 86, 87].

Stationary autophoretic boundaries act as osmotic pump at microscopic scales [70]. The concentration gradients along the active walls of the micron-size pipe, created either from asymmetrical chemical patterning or from asymmetrical geometry, create the phoretic forcing and hence, transport of the fluid. [63, 88].

1.5 Collective dynamics of active particles

Elements of active matter display self-organisation and collective behaviour. Understanding the fundamental mechanism of interactions is insightful in predicting this collective dynamics. From an engineering perspective, the self-organisation of active mater can be useful for tuning active materials.

1.5.1 Clustering through short-range interactions

For systems in thermodynamic equilibrium, the steady state is independent of kinematic parameters and the particles obey equilibrium statistics. However, active particles are far-

from-equilibrium systems. Even in the absence of any long-range interactions, self-propelling particles still form dense clusters. The non-equilibrium nature of the system can be shown through the collective clustering of active particles near wedges (obstacle) [56, 89]. For an isotropic processes, the steady-state density of a particulate system is inversely related to the velocity at that point. When the system is in thermodynamic equilibrium, the velocity is a random distribution that is independent of the position (depends only on the system temperature). However, for self-propelled particles, which are out-of-equilibrium, the short-range steric interactions between particles reduce their swimming velocity, which hence increases their packing density. This feedback loop creates an instability that leads to local clustering, known as *motility-induced phase separation (MIPS)*. Numerical simulations of system of passive particles driven by a mobile point force creates crystallization of the particles into ordered hexagonal lattices [90]. Such enhanced cluster formation purely because of the non-equilibrium nature of the system is seen commonly in dense biological suspensions [91].

1.5.2 Collective dynamics through long-range interactions in phoretic suspensions

There are two main long-range interactions arising in phoretic suspensions: (i) chemical interactions between particles due to self-generated concentration field gradients in the bulk fluid and (ii) the hydrodynamic flow field created due to motion from the concentration field gradients. Thus, there is a dynamical coupling between the chemical and hydrodynamic fields, and the motion of the particles. In this section we shall look at some of the instances where the chemical and hydrodynamic interactions play a crucial role in the collective behaviour of active phoretic systems.

1.5.2.1 Effect of chemical interactions

Particles align towards or away from external concentration gradients. If the interactions are attractive in nature, clusters are formed even in dilute suspensions. This gives rise to Attractive K-S type interactions exist when particles align with the external concentration gradient regardless of its mobility. These clusters vary in shape and size over time through constant dynamic interactions with other clusters, and is hence termed 'dynamic clustering' [87, 92]. Multiple experiments have shown the existence of long-range chemical (as well as hydrodynamic) interactions between particles in a phoretic suspension. Theurkauff *et.al.* compared the density of a suspension of sedimenting $Au - Pt$ Janus colloids when they were active and inactive [93]. When inactive, the particles formed a monolayer at the bottom of the setup; however, when active, they observed that the collective chemotactic attraction between the particles formed clusters of intermediate densities, creating a less dense system (gel-like state). The mean cluster size was observed to be proportional to the particle velocity (more precisely, to the particle Péclet number) [94, 12, 93, 95].

The steady-state concentration field created by a point source of chemical that purely diffuses into a fluid decays as $\sim 1/r$ (r being the radial distance from the point source). The chemotactic drift velocity created by phoretic interaction with the gradient (and proportional to it) is thus expected to create velocities $\sim 1/r^2$. Exhibited in nature by *Dictyostelium* cells which aggregate using a positive feedback loop of chemical generation and chemo-attraction; the clustering allows them to survive long periods of starvation.

A Janus particle when exposed to external field responds to both the self-generated and the external gradients. By properly tuning the surface mobilities of the particle, a group of Janus particles can attain collective polarity (against random background reorientations)

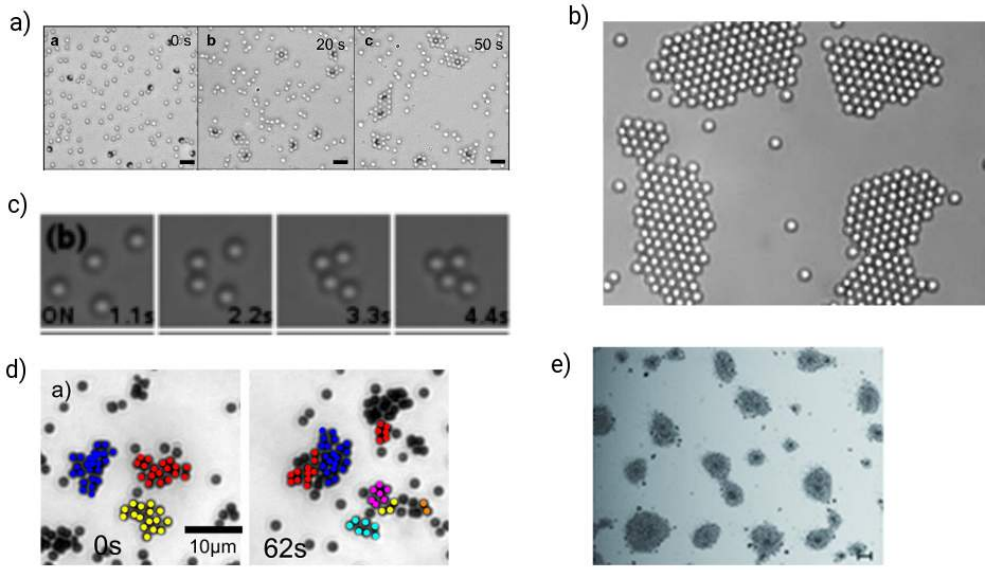

Figure 1.9: Clustering due to long-range interactions between active colloids: a) Janus colloid attracts passive colloids. b) Anti-ferromagnetic hematite cubes are chemically activated under blue-violet light. When embedded in silica colloidal particle, the colloids are observed to form clusters in an ordered lattice [12] c) Thermophoretic colloids (silica) in in glycerol-water mixture is sensitive to temperature gradients and are spontaneously are attracted [96] d) Chemotactic Janus colloids form clusters thus reducing of sedimenting Janus colloids [93] e) When gold particles are immersed in H_2O_2, addition of N_2H_4 causes coagulation of the gold particles [97]. This is attributed to the decomposition of N_2H_4 due to surface catalysis which generates the necessary electrolyte gradients for phoresis.

and hence, can be guided towards a prescribed direction using external field such a laser light intensity [98]. Janus colloids cluster even with a packing fraction of $3 - 10\%$ [86, 87, 92]; for particles that are not chemically active, phase separtion purely due to their motility requires a packing fraction $> 30\%$ [99]. In a binary mixture of active and passive particles, the properties of clusters formed depend on the difference in motility of the colloids and, their number ratio; more fraction of faster particles promote jamming and clustering. These clusters are themselves active and can self-propel [62].

Complex swarming behaviour of Janus colloids can be observed by appropriately tuning their translational and rotational response to external gradients. To be more precise, these two responses are governed by the parameters: their chemotactic alignment rate and their surface mobility. These two parameters decide the particle Péclet number − a small value creates a chemotactic collapse of the particles to a single cluster; large values create gas-like dynamic clusters [87, 86]. Using phenomenological models, Liebchen *et.al.* [87] showed that repulsive interactions can also form loose clusters, but additionally, they also display a wide range of complex dynamic patterns such as travelling waves in random directions which collapse into intermediate clusters. If additional considerations such as that of first-order reaction kinetics are made, at high solute concentrations, multiple diffusion-driven instabilities including formation of asters, microphase separation etc.. are formed [84]. Recently, the long-term dynamics and properties of such a system, generalized for reactant-solute driven propulsion, was computed using generalized Taylor dispersion theory [85].

1.5.2.2 Effect of hydrodynamic interactions

In biological systems, which generally constitutes living organisms immersed in water, the fluid medium plays a crucial role in long-range transfer of information; the consequence being that the microscopic interactions extend over the macroscopic scale, creating large swirling flows (such as in 'bacterial turbulence') in suspensions [100]. These interactions are essential for the collective transport of microfilaments and tubules in cytoskeletons [31]. Microswimmers in suspensions interact with each other using long-range hydrodynamic interactions. The hydrodynamic effect created by each swimmer decays at infinity and hence has little influence in dilute suspensions. Thus, in dilute suspensions a gas-like state is formed with no long-lived clusters [90]. However, for denser suspensions, hydrodynamic interactions play a crucial role in creating polar positional as well as orientational ordering [101, 90, 102]. Far-field interactions are not sufficient in this case to predict polar ordering [101]. It is observed that spherical *puller* swimmers have polar order that display time periodic aggregation and band formation [102, 103, 104]. Spherical pushers however do not form such ordered state. For self-propelled rods which have considerably different near-field dynamics, polar order emerges for pushers rods instead. Simha & Ramaswamy [105] showed using mean-field theory that nematic alignment is always unstable in long wavelengths and hence creates orientational disorder. This is evident in experiments of pusher bacteria [100]. Detailed calculations using slender body theory has elucidated the mechanism of interaction [106].

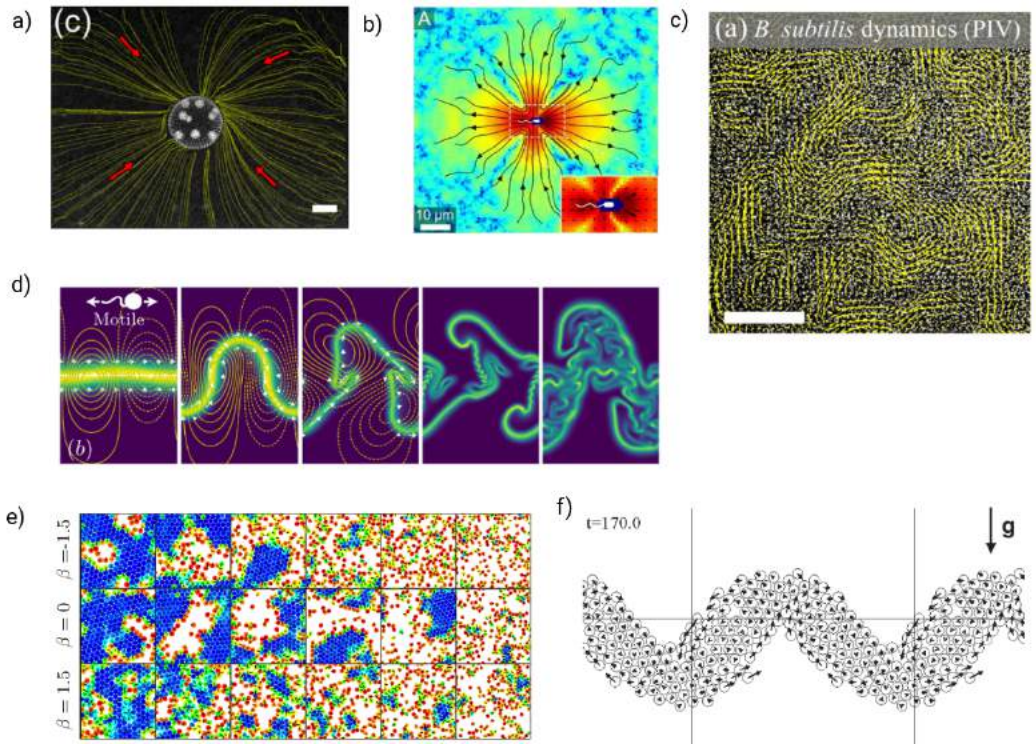

Figure 1.10: Flow -field around each micro-swimmer induces long-range hydrodynamic interactions which can create macro-scale coherent structures a) PIV of hydrodynamic field created by a swimming *Volvox* [107]. b) PIV of flow signature of a swimming *E.coli* bacterium near a bottom boundary [79] c) Large-scale structures observed in *B. subtilis* bacterial suspension [108]. d) Destabilisation of a line of pusher swimmers. [109] e) Simulations of collective dynamics of polar disks which display different clustering densities based on their hydrodynamic signature. [90] f) Destabilisation of a line of bottom-heavy pullers which form band-like structures. [102]

Yoshinaga *et.al.* [101] were able to identify the formation of gel-like states of suspensions of squirmers by additionally taking into account lubrication effects for short-range interactions between the squirming particles. Moreover, denser suspensions show formation of clusters which form and breaks apart periodically [110]. Large-scale polar alignment of active particles arising from hydrodynamic and magnetic interactions can be observed, which can create unstable fronts at large particle velocities [1, 22, 23]. It is observed that by modeling without the influence of hydrodynamic interactions, active particles accumulate at the boundaries. However, in agreement with experiments, by including hydrodynamic effects, some swimmers are shown to avoid/ attract towards obstacles and boundaries [72, 111, 79, 112].

1.6 Modeling the collective dynamics of phoretic particles

Emergence of collective motion is arises from the velocity-alignment interactions between self-propelled point particles and its extensions [113, 114, 115]. Viscek model takes into account of these aligning interactions with neighbouring particles by using an alignment potential; the dynamics of a particle i is given by [113],

$$\dot{\mathbf{r}}_i = U_i \mathbf{p}_i \tag{1.24}$$

$$\dot{\theta}_i = \frac{K}{\pi R_i^2} \sum_{j \neq i} f_{ij} + \sqrt{2D_r}\, \boldsymbol{\xi}_r(t) \tag{1.25}$$

where the alignment interaction between the particles j and i within a circular region of radius R_i around particle i is of strength Γ and whose behaviour is defined by the function f_{ij}; generally, in the absence of any prescribed physical mechanism of interaction between the particles, the function is often chosen as $f_{ij} = \sin(\theta_j - \theta_i)$ [113]. In the continuum limit, the Viscek interactions form the basis of what is known as the Toner and Tu model [114]. A salient feature of this non-equilibrium dynamics is the spontaneous formation of large-scale structures.

1.6.1 Phenomenological models

1. *Active Brownian Particle (ABP)* model: The ratio of angular coupling strength to the Brownian realignment is given by $K/8\pi a^2 D_r$ [116]. If this ratio is small the alignment interactions between particles are negligible, one obtains the ABP model. It does not take into account interactions with any external field (besides thermal noise).

$$\dot{\mathbf{r}}(t) = U\mathbf{p} + \sqrt{2D}\, \boldsymbol{\xi}_t(t) \tag{1.26}$$

$$\dot{\theta}(t) = \sqrt{2D_r}\, \boldsymbol{\xi}_r(t) \tag{1.27}$$

   One may add an interactive potential gradient between the particles in equation (1.26): for example, this can be a simple short-range steric repulsion between the particles to prevent inter-particle overlap in simulations [117]. These repulsive interactions surprisingly contributes positively to the clustering [118, 119, 120].

2. *Active Attractive Alignment* (AAA) model: The particles, in isolation, translate with a velocity U in the direction $\mathbf{p}$. In the presence of a background chemical field $c(\mathbf{r})$ created by the surrounding particles as well as due to the thermal noise (given by the Gaussian white noise of strength ξ) in the system. The particles have aligning

interactions with the local chemical gradients. The dynamics of the particles is thus modeled using the following equations

$$\dot{\mathbf{r}}(t) = U\mathbf{p} + \beta_t \nabla c(\mathbf{r}, t) + \sqrt{2D}\, \boldsymbol{\xi}_t(t) \tag{1.28}$$

$$\dot{\theta}(t) = \beta_r \mathbf{p} \times \nabla c(\mathbf{r}, t) + \sqrt{2D_r}\, \boldsymbol{\xi}_r(t) \tag{1.29}$$

where β_t and β_r are the translational and rotational response to the external field respectively. The ABP model predicts short lived clusters whose size distribution decays exponentially with size; using AAA model, cluster size is found to decrease more slowly (algebraically) as seen in experiments [121, 122].

3. *Phoretic Brownian Particle*(PBP) model: Setting $\beta_r = 0$ gives isotropic attraction model. Setting the translational drift, $\beta_t = 0$ in equation (1.28) gives the PBP model. It has been used to simulate the variety of pattern-forming dynamics of a large number of phoretic particles [87, 116]. However, this model does not predict chemotactic clustering of particles in dilute suspensions, as seen in experiments [12, 93].

Phenomenological models however do not capture the exact physics of the problem of interacting phoretic particles.

1.6.2 Physical models

One class of modelling approach builds from known physical principles relevant to the problem. For example, the fundamental solutions to Stokes equations form the basis for modelling swimming and hydrodynamic interactions at low Reynolds numbers. For phoretic problems, physical principles of hydrodynamics, solute diffusion as well as their coupled interactions with the solid active body are used to model the complex dynamics of the system. In the case of modelling the collective dynamics of self-propelling phoretic particles, there are two possibilities based on the desired resolution of the dynamics: i) Discrete particle models where the microscopic interactions between discrete phoretic particles are used to study their dynamics ii) Continuum models where continuum models based on microscopic interactions approximate the physics at a much larger scale .

Hydrodynamic interactions have received far less attention than chemical interactions even though they can be significant in any cases. The simplest physical model that takes into account both the chemical and hydrodynamic interactions at the leading order is the *far-field model*. The far-field chemical (phoretic) interaction between particles create drift velocity that scales as $\sim 1/r^2$. For half-active Janus particle with uniform mobility, the leading order flow-field is a potential dipole which creates a hydrodynamic drift velocity that scales as $\sim 1/r^3$; this approximation may also be made for Janus particles with slight asymmetry in surface activity or mobility. But under strong asymmetry, the stresslet flow-field $\sim 1/r^2$ cannot be neglected [122]. the propulsion velocity created by both the chemical and hydrodynamic fields scale as a^2/d^2 (a being the size of the particle and d being the separation between their centers with, $a \ll d$) [112, 123]. The far-field model invariably considers only pairwise interactions between particles; nonetheless, they have shed light on our understanding of their dynamics in dilute suspensions. [124, 112, 125, 36, 85, 84, 126, 123]. More accurate models have been obtained by extending the the far-field model to include higher-order terms [127], or by considering additional near-field interactions [128, 129]. In dense suspensions, the distance between particles are less than their characteristic size; the interactions between the particles are thus, in the near-field. This requires one to take into account the sharp gradients of solute created by wedge effect. Lubrication theory must be employed to study the hydrodynamic interactions [101, 130].

Continuum modelling/ mean field theory approach do not consider point particles individually, rather by considering their dynamics averaged over all degrees of freedom i.e. it gives a statistical approximation of the exact dynamics. This allows one to avoid computing multi-body dynamics of large populations of particles in a system as they can effectively be expressed in one or two statistical quantities; such reduction is nonetheless valuable to compute the stability of phoretic suspensions. The computational power can be used for computing long-term dynamics of the system. However, the continuum approximation comes at the expense of loss of accuracy.

The focus of this thesis will be on studying the microscopic interactions and collective dynamics at the particle scale using discrete particle models.

1.6.3 Numerical simulations

The nature of motion of active particles in a fluid is obtained by solving the relevant governing equations along with the boundary conditions that impose fluid-structure interactions. In many situations, for example in systems where multiple particles are present, exact analytical solutions do not exist. A detailed and accurate description of the dynamics of particles can be determined by solving for the spatially and temporally discretized governing equations using various numerical techniques.

Certain class of simulations take a bottom-up approach where the fluid is itself considered to be composed of discrete fluid elements which are modelled using molecular dynamics. These discrete algorithms have shown to recover N-S equations in the continuum limit. Lattice Boltzmann Methods (LBM) is one such example where the fluid is discretized into a regular lattice [131]. Fluid density within each lattice is simulated using streaming and collision processes which are governed by Boltzmann equations. Mass and momentum of fluid are conserved within each lattice. However, LBM does not inherently account for thermal fluctuations. Multi-particle Collision Dynamics (MPCD) model, on the other hand, the fluid molecules maintain continuous phase-space and velocity [132, 133]. Hence, MPCD exhibits good numerical stability. The spatial domain of fluid is discretized into "cells" within which multi-particle collisions happen. Mass and momentum are conserved in each cell. MPCD models account for thermal fluctuations. Both MPCD and LBM have been shown to provide accurate description of the dynamics of self-propelling particles and polymer chains in fluid suspensions. Although they capture even the molecular description of fluid dynamics, MPCD and LBM are suitable for parallel computational architecture and require large computational resources.

In the continuum limit, the fluid dynamics is governed by Navier-Stokes equations. A common approach is to "immerse" the discretized solid in a stationary discretized fluid domain and then use Finite Element or Finite Volume methods to solve the fluid-structure interactions. This computational technique is called *Immersed Boundary Methods* (IBM) [134, 135, 136]. In IBM, the body-conforming grid has adequate local resolution of the boundary with minimum grid points. However, the grid sizes may vary for both fluid and solid domain and alignment issues can arise which create inaccuracies; thus, IBM are not suitable for complex geometries. IBM has been used to solve for problems involving fluid-structure interactions at low as well as high Reynolds numbers. An attractive alternative for phoretic problems is using *Boundary Element Methods* (BEM). BEM is based on the boundary integral representations of Stokes (for hydrodynamic field) and Laplace equations (for solute concentration field). The velocity and pressure fields (concentration field respectively) at any point in the domain can be computed by distributing point forces (chemical sources respectively) on the discretized surface of the solid body. By having the boundary conditions prescribed on the surface of the body, one can avoid computations in the bulk;

this is of major advantage for solving phoretic problems which have surface chemical and hydrodynamic boundary conditions. BEM has been used to model low Reynolds number hydrodynamics in suspensions of squirmers, cilia, phoretic colloids etc.. [129, 137, 17, 138]. These simulations are however computationally expensive and hence are performed on a few particles.

An alternative to full numerical simulations, with lesser computational cost at the expense of accuracy, is *Stokesian dynamics* (SD) modified for mobility problems [102, 139]. SD uses a truncated multipolar expansion about the center of each particle in the boundary integral representation of the flow field. All interactions corresponding to a particular multipole between all particles (i.e. infinite reflections) are taken into account [140]. FCM considers the particles to be point particles of regularised force multipoles [141, 23] and their propulsion velocities are obtained by averaging the computed flow velocity within this 'blob' domain. In recent works, Singh et. al [13, 142] have developed framework to compute iterative corrections to surface slip velocity arising from multi-body interactions of active particles. Although the above mentioned methods incorporate multi-body interactions, they do not derive solution systematically to a desired order of accuracy.

1.7 Conclusions

Studies of active matter systems have focused on two important aspects viz. to study the physical dynamics of out-of-equilibrium systems and, to design and implement the active elements as agents for controlled transport which has potential for engineering and biomedical applications. Phoretic Janus particles are a classic example of active colloids that use phoresis - transport through self-generated chemical gradients - for controlled transport. In a system containing multiple phoretic particles, the particles interact via chemical and hydrodynamic fields created by each. We have seen in this chapter that both chemical and hydrodynamic fields can have significant influenceon the collective dynamics of the particles.

The current physical modelling approach for dynamics of phoretic particles in suspensions consider only the far-field interactions between the particles. This approach is valid only for dilute suspensions (generally with particle densities $< 0.5\%$) However in denser suspensions, the higher-order interactions can become significant. Using numerical methods in such situations can provide accurate solutions to the dynamics, however are computationally intensive. What we search for is a theoretical modelling approach which can be used to understand the multi-body dynamics of phoretic particles to a degree of accuracy beyond the far-field models. Thus, such a model would take into account the and could predict or explain some new physics, which are not captured by simply considering the leading-order interactions. In the subsequent chapters we shall discuss the theoretical foundations that are used to develop this method for phoretic problems.

In Chapter 2, a fluid mechanics perspective of swimming at microscopic scales is described. Some commonly used mathematical tools for determining the flow velocities and stresses in flows at low Reynolds numbers will be outlined. This gives insight into developing physical modeling swimming of phoretic particles. We shall also detail the mathematical foundations of the *Boundary Integral formulation*, which forms the backbone of a powerful numerical technique for simulations of phoretic problems known as *Boundary Element Methods* (BEM). In Chapter 3 we develop a generalized framework based on the classical *Method of reflections*(MoR) for modeling both the chemical and hydrodynamic interactions between Janus phoretic colloids in their suspensions and, subsequently determine the multi-body dynamics of the particles. The dynamics of a system comprising of isotropic phoretic particles is

determined in Chapter 4. Full numerical simulations using BEM show that the individually-non-swimming particles break each others' concentration field symmetry to spontaneously form clusters which can propel. We characterize the properties of this newly identified route of self-propulsion arising from clustering. A summary as well as conclusions of this thesis are drawn out in Chapter 5. An outlook into the possible applications of the MoR framework developed here for modeling dynamics of phoretic particles is also provided.

2

Modeling transport at microscopic scales

The resistance to motion for micro-swimmers is predominantly due to viscosity of the fluid. In this chapter we shall describe the fundamental fluid mechanics principles governing motion in microscopic scales and how micro-swimmers, both organic and synthetic, achieve self-propulsion. We shall detail useful mathematical tools and techniques which are commonly used to evaluate the governing equations of motion as well as the hydrodynamic signature of the moving body. Boundary integral formulation for the Stokes and Laplace equations are presented which allows one to compute the stress and velocity fields (solute concentration respectively) on the surface without evaluating the fields in the bulk.

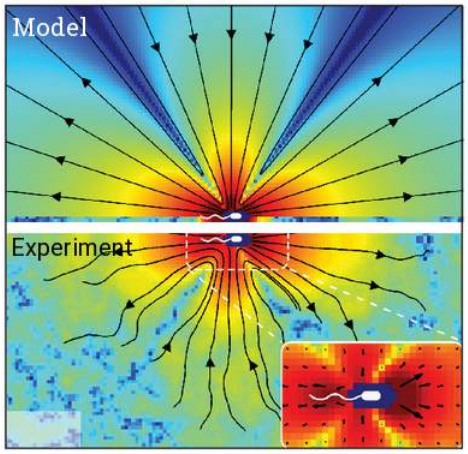

Figure: *Hydrodynamic flow field around a swimming E.coli bacterium predicted from theoretical models show good agreement with measurements made using PIV. Source: Drescher et. al. 2011 [123]*

Contents

Active fluids are fluid suspensions containing microscopic self-propelled bodies. They form a majority of living organisms such as bacterial suspensions, cells, spermatozoa, biofilaments in cytoskeleton, actin filaments etc.. Many biological processes including reproduction, marine life-cycle, growth of infections and so on rely on motility of these swimming organisms at micron and sub-micron scales in a viscous fluid. In recent years, artificial miro-swimmers are being developed for creating active fluids with desired physical properties and for transport applications at microscopic scales. Figure 2.1 gives the readers a sense of the size and speed of some common organic and artificial swimmers in active suspensions.

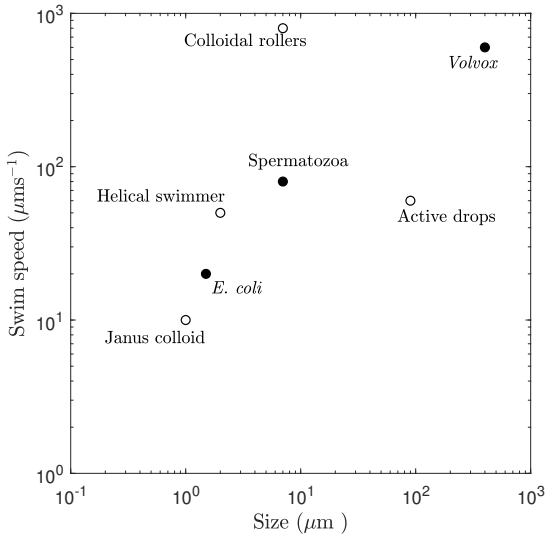

Figure 2.1: The size and speed spectrum of active swimmers commonly found in nature (shaded) as well as their synthetic counterparts commonly used in experiments. Janus particle ($Au - SiO_2$ colloid in H_2O_2) use diffusiophoresis mechanism to attain typical speeds of for a few tens of body-lengths per second [19]; Helical/ chiral swimmers [143] and colloidal rollers [22] use external magnetic field to transport goods; Active drops use gradients in surfactant concentration to have Marangoni-driven propulsion [144]; In nature, bacteria such as *E.coli* use flagella to achieve swim speeds of a few body lengths/ sec [145]. Spermatozoa use flexible oar while green algae like *Volvox* use biflagellatic somatic cells on their surface to swim at speeds orders of magnitude more than their body sizes [29]. Figure motivated from [16].

To determine the origins of the mechanical and statistical properties of fluid suspensions of these active particles, one requires a thorough understanding of their individual dynamics and their interactions with the surrounding medium. The goal of this chapter is thus to lay the foundations for physical modeling of transport at microscopic scales using the principles of mechanics of motion in viscous fluids. This forms a bottom-up approach for modeling collective dynamics of self-swimming particles. By capturing the nature of motion and interactions of swimming micro-organisms, these modeling tools can aid in tailoring the behaviour of synthetic suspensions, such as that of self-propelling colloids for controlled transport or, for designing materials with tunable physical properties.

In Section 2.1, a description of the different methods of transport at microscopic scale is provided. Section 2.2 details the fundamental mathematical framework derived from the Navier-Stokes equations for motion of a body in a fluid where viscous effects dominate over inertia (Stokes flow). In the process, we shall understand the consequences of motion in the viscous-dominated regime such as time independence and reversibility. This framework provides an insight into the hydrodynamic interactions between moving bodies in a fluid. In Section 2.4, we use the principles to quantify how swimmers exploit fluid-surface interactions

to produce net propulsive motion. As a special case, the propulsion of Janus phoretic colloid is considered. And finally, in Section 2.5, the different mathematical representations of the flow field created by the swimming body is detailed. This includes description of the general spherical harmonic decomposition of the field as well as the Green's function solution for the Stokes flow problem. The Green's function solution forms the basis of a powerful numerical tool known as the *Boundary Integral Methods* (BIM) for computing the dynamics of particles, which are governed entirely by the surface boundary conditions without need for computations of the flow in the bulk. The mathematical foundations behind BIM for the phoretic problem i.e. for both solute diffusion as well as Stokes flow are detailed in Section 2.6

2.1 Transport in fluids at microscopic scales

From a thermodynamic perspective transport process in a system is an irreversible process involving displacement of thermodynamic properties within the system. When a system is in a state of non-equilibrium, it tries to reach equilibrium through transport of mass, momentum and energy. For example, chemical diffusion, fluid flow are examples of mass and momentum transfer; heat transfer is an example of energy transport. We shall now consider the various means of mass transport within fluids.

2.1.1 Advection-diffusion of molecules

At molecular scales, an imbalance in volume density of certain solute molecules of a substance between two systems which can exchange mass and momentum, leads to transport of the solute from higher to a lower density. This process is known as *diffusion*. Diffusion is one of the predominant modes of transport of material such as amino acids within cell bodies [146]. The rate of transport was found to depend on the temperature, viscosity of fluid and size of solute molecules; a continuum model for diffusion was proposed by Fick in 1855 to exlain this phenomenon [147]. The steady-state mass flux of the substance occurs from a higher concentration to a lower one and the rate is proportional to the gradient of the concentration field. If the solute molecules are large enough, the external motion of fluid can advect the molecules along with the flow.

$$\mathbf{j} = -D\ \nabla c + \mathbf{u}\ c \tag{2.1}$$

The constant of proportionality is known as the diffusivity (denoted here by D), and has the units of m^2/s. As an example, diffusivity of carbon dioxide in water at room temperature is $O(a0^{-9})\mathrm{m}^2/\mathrm{s}$. Note that the linear phenomenological model of equation (2.1) is observed to agree well for a large range of experimental observations. Fick's second law of diffusion is the mass conservation equation, and is often called the advection-diffusion equation,

$$\frac{\partial c}{\partial t} + \nabla \cdot \mathbf{j} = 0 \tag{2.2}$$

In dimensionless terms (denoted by $*$),

$$\mathrm{Pe}\left(\frac{\partial c^*}{\partial t^*} + \mathbf{u}^* \cdot \nabla^* c^*\right) - \nabla^{*2} c = 0 \tag{2.3}$$

where Pe is known as the Péclet number defined as

$$\mathrm{Pe} = \frac{\text{Diffusion time}}{\text{Advection time}} = \frac{a^2/D}{a/U} = \frac{aU}{D} \tag{2.4}$$

Low Péclet number ($\mathrm{Pe} \ll 1$) implies that the physics is diffusion dominated and the governing equation simplifies to Laplace equation for diffusion at steady-states,

$$\nabla^2 c = 0 \tag{2.5}$$

Advective effects can be neglected when the solute molecules are extremely small so that they diffuse through the system almost instantaneously.

2.1.2 Brownian diffusion

Diffusion within a fluid is observed even beyond molecular scales, where rigid micron-sized bodies are subject to a variety of stochastic background processes such as thermal noise which continuously alter their motion. Such an irregular motion was observed by the botanist Robert Brown in experiments during 1827 of small pollen [148] and later observed for small soot particles in air. A theoretical description relating this observed "Brownian" motion with kinetic theory of gases were given by W. Sutherland [149] in 1904, A. Einstein in 1905 [150] and M. Smoluchowski in 1906 [151], all independently. The general form of this constitutive relation is given in terms of an effective particle diffusivity,

$$D_p = \mu k T \qquad \text{where,} \quad \mu = \frac{\text{Drift velocity}}{\text{Applied force}} \tag{2.6}$$

μ is known as the thermal mobility of the particle, k is the Boltzmann constant and T is the absolute temperature. For a spherical particle, mobility can be determined by using the Stokes relation $\mu = 1/6\pi\eta a$; a stationary bacteria in a fluid has as diffusivity of $D_p \sim O(10^{-9}) - O(10^{-10})$ m^2/s. The Brownian diffusion times are much larger compared to molecular diffusion time scales. The Brownian motion characterized by zero mean displacement which is induced by random fluctuating *forces* exerted on the body by the fluid, and can be described by Langevin dynamics viz. $\mathbf{F}_B + \mathbf{F} = 0$, $\langle \mathbf{F}_B(t) \rangle = 0$, and $\langle \mathbf{F}_B(t)\mathbf{F}_B(t') = 2kT\mathbf{R}\delta(t-t') \rangle$, where $\mathbf{R}$ is the resistance tensor that determines the drag force on the body due to its motion; it depends on the geometry of the body.

2.1.3 Self-propulsion

Unlike advection and diffusion, which are forms passive transport within fluids, swimming requires expenditure of energy by the body into the fluid. At the scale of the size of a human being, the dynamics of fluids are determined by inertia. This is why swimming (or flying, when the fluid is air) in these fluids require thrust force generally through swift motion of the body in water. However, at microscopic scales, viscous effects far outweigh inertail effects. Let us consider the transport of fluid of viscosity η with a velocity U within a characteristic length scale a. The strength of inertial and viscous forces can be compared using a dimensionless parameter called the *Reynolds number* (denoted by Re):

$$\mathrm{Re} = \frac{\text{Inertial force}}{\text{Viscous force}} = \frac{\rho U^2/a}{\eta U/a^2} = \frac{\rho U a}{\eta} \tag{2.7}$$

If we look at swimming bacteria or sperm, their size is of the order of $a \sim 10^{-6}$ m; these organisms then swim at a velocity of a few body-lengths a second ($U \sim 10^{-5}$ m/s) in wa-

ter (at 25 °C, $\nu = 8.9 \times 10^{-7}\text{m}^2/\text{s} \approx 10^{-6}\text{m}^2/\text{s}$). Thus the Reynolds number associated with the motion of fluid around these organisms (from equation 2.7) is $\text{Re} \sim O(10^{-5}) \ll 1$. This implies that the flow at microscopic scales are dominated by viscosity. The effect of swimming would be equivalent to a human swimmer in a pool of honey. Due to the completely different physics at play, swimming at microscopic scales is contrastingly different; the thrusting of fluid, commonly observed in swimmers at our scales are ineffective as the inertial forces generated contribute negligibly to swimming at these scales.

2.2 Motion at low Reynolds numbers

As a body moves through a fluid, the displaced fluid conserves two physical properties: Mass and momentum. In the continuum limit, which is the scale of analysis we shall employ throughout, the mass balance for an incompressible fluid is given by the continuity equation

$$\nabla \cdot \mathbf{u} = 0 \tag{2.8}$$

Here, ρ is the density and $\mathbf{u}$ is the velocity of the fluid. Note that here we assume the fluid to be Newtonian. We let $\boldsymbol{\sigma}$ be a second-order stress tensor that represents the normal and shear stresses acting on a fluid element. In its dimensionless form,

$$\boldsymbol{\sigma} = -p\mathbf{I} + 2\eta\mathbf{E} \quad \text{where,} \quad \mathbf{E} = \frac{1}{2}(\nabla\mathbf{u} + (\nabla\mathbf{u})^T) \tag{2.9}$$

where p is the magnitude of isotropic stress i.e. the pressure and $\mathbf{E}$ is a symmetric second-order tensor known as the *strain-rate tensor*. Now let us consider a body of size a moving steadily through the fluid (of viscosity η and density ρ) with a velocity U. The momentum conservation law within a fluid is represented by the Cauchy's momentum equation.

$$\frac{1}{\rho}(\nabla \cdot \boldsymbol{\sigma}) = \frac{\partial \mathbf{u}}{\partial t} + (\mathbf{u} \cdot \nabla)\mathbf{u} \tag{2.10}$$

The body has to overcome the viscous dissipation to maintain its propulsive speed. By non-dimensionalizing equation (2.9), using a and U as the characteristic length and velocity scales respectively, one obtains the characteristic (viscous) stress as $\eta U/a$. The characteristic time scale for microscale swimming problem is a bit more complex; it depends on two properties, diffusion of particle through the medium or its advection (through external or internal forces). If the body was purely diffusing through the medium (Browian motion), the characteristic time-scale would then be a^2/D, with D being the diffusivity of the body in the fluid. Since here we consider the self-propelling motion of the particle, the characteristic time scale of the motion is a/U. Non-dimensionalizing the equation (2.10) using these characteristic scales, we get

$$\nabla^* \cdot \boldsymbol{\sigma}^* = \text{Re}\left(\frac{\partial \mathbf{u}^*}{\partial t} + (\mathbf{u}^* \cdot \nabla^*)\mathbf{u}^*\right), \quad \text{and,} \quad \nabla^* \cdot \mathbf{u}^* = 0 \tag{2.11}$$

where the $*$ denotes dimensionless parameters. We however drop the $*$ notation hereafter for convenience. Using the above equation (2.9) (after non-dimensionalizing), one can rewrite the equations in (2.11) at vanishing Reynolds number ($\text{Re} \to 0$) as

$$-\nabla p + \nabla^2\mathbf{u} = 0 \quad \text{and,} \quad \nabla \cdot \mathbf{u} = 0 \tag{2.12}$$

which forms the governing equation, known as the *Stokes equations*, for all bodies moving

through an incompressible fluid at low Reynolds numbers.

In the absence of inertia at low Reynolds numbers, the swimmer is both force- and torque-free. Thus, if a body is acted upon by an external force $\mathbf{F}$ (or torque $\mathbf{T}$), the body moves with a velocity such that the drag force (and torque) by the fluid on the body balances the applied force. One can compute the hydrodynamic force and torques on the body from the surface stress distribution using,

$$\mathbf{F} = \int_{\mathcal{S}} \boldsymbol{\sigma} \cdot \mathbf{n} \, d\mathcal{S} \quad \text{and,} \quad \mathbf{T} = \int_{\mathcal{S}} \mathbf{r} \times \boldsymbol{\sigma} \cdot \mathbf{n} \, d\mathcal{S} \tag{2.13}$$

where $\mathbf{r}$ is the position vector on the surface $\mathcal{S}$ of the body.

There are a few properties of low Reynolds swimming that can be understood from equation (2.11),

1. Time-independence of the equations. The pressure, viscous and the body forces acting on a fluid element balance each other at all times even if the flow is unsteady. This means that the instantaneous flow depends only on the boundary configuration as well as the boundary conditions prescribing the flow, and not on the history of motion. The absence of the unsteady term also implies that how fast or slow you change your swimming configuration does not affect the flow field and hence your motion.

2. Kinematic reversibility : Replacing the pressure and velocity, $\mathbf{u}$, p by $-\mathbf{u}$ and $-p$ would still satisfy the same equations i.e. any reversed flow is also a valid solution and that by flipping the direction of velocity, the stresses are exactly reversed. This property is called the *kinematic reversibility* of Stokes flows. By reversing the sequence of motions, the streamlines (given by ψ = constant) remain the same, but the flow direction is reversed. A popular testable experiment is when a blob of dye is placed in a viscous fluid and slowly sheared. By retracing the motion, the dye that was presumably mixed within the viscous fluid reforms into the blob.

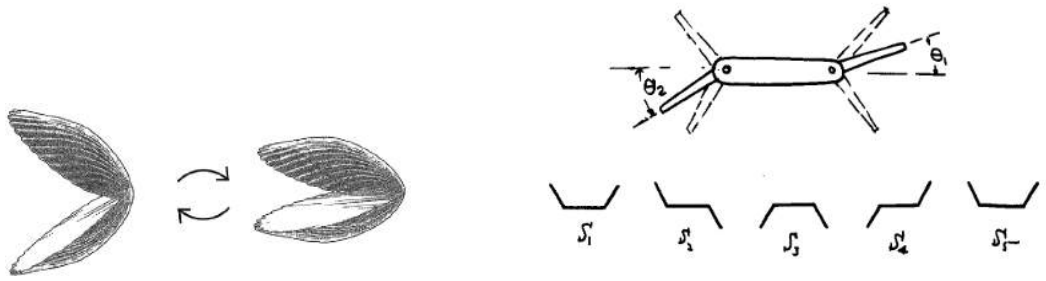

Figure 2.2: (left) The lack of inertia at low Reynolds number prevents a scallop from swimming using its quick reciprocal strokes. This is a result of the principle that a single-hinged swimmer cannot propel; a reconfigurable combination with variable drag is necessary, such as a minimal 2-hinged swimmer shown in the right. Figure reused from [152].

This property has some interesting consequences to the motion of bodies in the Stokes limit. A swimmer exhibiting reciprocal swimming stroke would not be able to achieve a net displacement: the forces in the forward stroke would be balanced by the forces acting in the opposite direction in the reverse stroke. This property is popularly known as the *Scallop theorem* [152]. This comes from the fact that a scallop that swims by squirting out fluid though the back of its shell through oscillatory motion of its body would find it difficult to swim in a highly viscous fluid because of the absence of inertia and that any reciprocal movement of its body results in reciprocal motion with zero net displacement.

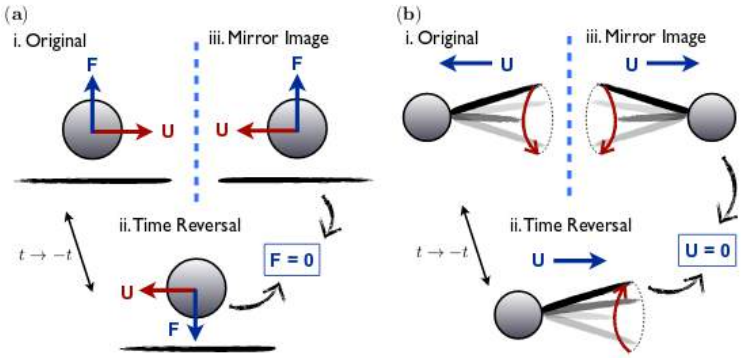

Figure 2.3: Figure from [145]. An example is the fact that a sphere moving parallel to a wall should maintain its motion at the same distance from the wall [153, 154]. One can test this reasoning by considering a sphere moving parallel to a wall being acted upon by a (upward normal) force. By reversing the time, both the forces and velocity are are reversed. However, in the mirror image, which also satisfies the Stokes equations, the velocity is reversed but not the force. Since the boundary conditions are the same in both cases, it can only imply that the net force on the sphere is zero. A similar argument based on the mismatch of mirror image and time-reversed strokes can be made about the inability of an organism to swim by a constant rotation of its tail in a conical fashion.

These examples show the need for symmetry-breaking for propulsion in low Reynolds numbers. The simplest example is a Purcell type swimmer [152] which is a simple two-hinged body that, two a series of non-reciprocal movements, can achieve locomotion. In the biological world, the simplest example is bacteria like *E.coli* which have a rotating helical tail; the chirality of the tail allows for symmetry-breaking when under continuous rotation. Sperms have a flexible oar in its rear which create travelling waves along its length that provides the net non-zero thrust [155]. Metachronal waves along the flagella of certain algae and along the cilia of paramecium are generate a net directional slip velocity on the surface that leads to effective propulsion [30, 156]. For a helical swimmer (or any swimmer with a chirality), the torques and velocities of both the time-reversed and mirror image are exactly the same showing that the net propulsion velocity for a given torque is non-zero. Autophoretic swimmers produce local surface concentration gradients − through asymmetries in chemical patterning or in their geometry − which provides them with the phoretic forcing necessary for self-propulsion [58].

3. Linearity of the equations. The linearity of the Stokes equations extends to the linear relation between the forces and the velocity on the body [154, 157]

$$\begin{bmatrix} \mathbf{F} \\ \mathbf{T} \end{bmatrix} = \eta \begin{bmatrix} \mathbf{A} & \mathbf{B} \\ \mathbf{B} & \mathbf{C} \end{bmatrix} \begin{bmatrix} \mathbf{U} \\ \boldsymbol{\Omega} \end{bmatrix} \tag{2.14}$$

where the square matrix is known as the *resistance matrix*. Note that the matrix is symmetric, which is a consequence of the reciprocal theorem (discussed in next section). The elements $\mathbf{A}$, $\mathbf{B}$ and $\mathbf{C}$ are each second-order tensors and have the characteristic dimensions (in powers of length) of a, a^2 and a^3 respectively. Thus, in a given fluid, the drag on a rigid body swimming in the viscous regime depends only on the shape and orientation of the body with regard to the flow, and the swimming velocity. For an axisymmetric achiral body, the resistance matrix is diagonal; for a sphere, $\mathbf{A} = 6\pi a\mathbf{I}$, $\mathbf{B} = \mathbf{0}$ and, $\mathbf{C} = 8\pi a^3\mathbf{I}$. The matrix is not known apriori

for all geometries. For manufactured geometries, such as a helix of known weight, sedimentation experiment can be performed to calculate the coefficients [152]. However for more complex systems and biological organisms, these coefficients can only be approximately estimated using theoretical methods such as slender body theory [158].

2.3 Hydrodynamic signature of a moving body

As a body moves through a viscous fluid, momentum is transmitted to the fluid and the flow created is a characteristic of the kinematics of the body; Let the particles move along the direction $\mathbf{t}$. For ease of expression, we note $\mu = \mathbf{t} \cdot \mathbf{r}/r$ with $r = |\mathbf{r}|$.

2.3.1 Passive particles subject to body force

When a sphere subjected to a body force F along the direction $\mathbf{t}$ in a viscous fluid, the body moves at a constant velocity $\mathbf{U} = F/6\pi\eta a\ \mathbf{t}$. The streamfunction of the flow created by the moving sphere is given by [159],

$$\Psi(r, \mu) = U(1 - \mu^2)\left(\frac{3a}{4r} - \frac{a^3}{4r^3}\right) \tag{2.15}$$

where, $\mu = \mathbf{t} \cdot \mathbf{n}$. The velocity and pressure fields can then be derived as,

$$\mathbf{u} = -\frac{\mathbf{U}}{4}\left(\frac{3a}{r} + \frac{a^3}{r^3}\right) + \frac{3\mathbf{U}}{4} \cdot \left(\frac{-a\mathbf{rr}}{r^3} + \frac{a^3\mathbf{rr}}{r^5}\right) \cdot \tag{2.16}$$

$$p = \frac{-3a\eta\mathbf{U} \cdot \mathbf{r}}{2r^3} \quad \text{and so,} \quad \boldsymbol{\sigma} \cdot \mathbf{n}|_{r=a} = \frac{3\eta\mathbf{U}}{2a} \tag{2.17}$$

This is the case of a sedimenting sphere where the body is subjected to a constant gravitational force (see figure 2.4). The body force acting on the sphere by gravity is balanced by the drag force created by the fluid.

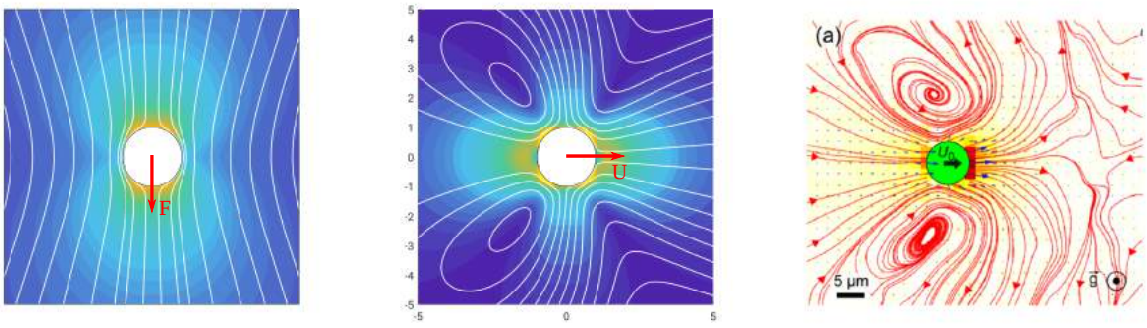

Figure 2.4: a) Flow field created by a rigid sphere sedimenting at a fixed velocity. b) Flow field created by a spherical swimmer with surface slip velocity. The parameters used here (in equation 2.20) are $\alpha_1 = 0.01, \alpha_2 = 0.5$. c) PIV of Flow field produced by green algae *Chlamydomonas reinhardtii* swimmig by generating surface veocity in a background flow-adapted from [29].

2.3.2 Axisymmetric squirmers

When a body expends energy to swim through the fluid at low Reynolds numbers, the particle however is force- and torque-free. A particular type of swimmer that uses only tangential surface velocity to achieve self-propulsion is known as a squirmer. The streamfunction for the flow created by an axisymmetric squirmer is classically given by Lighthill [160] and later corrected by Blake [161],

$$\Psi(r,\mu) = \sum_{m\geq 1} \frac{2m+1}{m(m+1)} \alpha_m \psi_m (1-\mu^2) L'_m(\mu) \tag{2.18}$$

where $L_m(\mu)$ are the Legendre polynomials of order m,

$$\psi_1 = \frac{1-r^3}{3r}, \qquad \psi_{m\geq 2} = \frac{1}{2}\left(\frac{1}{r^n} - \frac{1}{r^{n-2}}\right) \tag{2.19}$$

and, for all $m \geq 1$,

$$\alpha_m = \frac{1}{2}\int_{-1}^{1} \sqrt{1-\mu^2}\; L'_m(\mu)\; \widetilde{\mathbf{u}} \cdot \mathbf{e}_\theta \; d\mu. \tag{2.20}$$

The complete axisymmetric hydrodynamic flow field (in the reference frame of the swimmer) is further obtained from the streamfunction solution as [161, 162, 57]:

$$\begin{aligned}\mathbf{u}(\mathbf{r}) = {} & \frac{\alpha_1}{2r^3}\left(\frac{3\mathbf{rr}}{r^2} - \mathbf{I}\right)\cdot\mathbf{t} \\ & - \sum_{m\geq 2} \frac{(2m+1)\alpha_m}{2m(m+1)} \Bigg\{ \left(m(m+1) L_m(\mu) \left[\left(\frac{a}{r}\right)^{m+2} - \left(\frac{a}{r}\right)^{m} \right] \right) \frac{\mathbf{r}}{r} \\ & \qquad + L'_m(\mu) \left[(m-2)\left(\frac{a}{r}\right)^m - m\left(\frac{a}{r}\right)^{m+2} \right] \left(\mathbf{I} - \frac{\mathbf{rr}}{r^2}\right)\cdot\mathbf{t} \Bigg\}\end{aligned} \tag{2.21}$$

2.3.3 Autophoretic particles

Chemically active particles have two signatures viz. their 1) chemical signature and 2) their hydrodynamic signature. This axisymmetric particle is characterized by its orientation $\mathbf{t}$ indicating the direction of its axis of symmetry, and along which self-propulsion occurs. The activity of the particle is modeled as a spatially-dependent production (resp. consumption) of solute with a fixed rate $\mathcal{A}(\mu) > 0$ (resp. $\mathcal{A}(\mu) < 0$) which may vary along the surface. Denoting the characteristic surface activity, $\mathcal{A}^*$, one can write the dimensionless surface activity as $A(\mu) = \mathcal{A}(\mu)/\mathcal{A}^*$. The concentration field of the solute within the fluid is governed by the steady-state diffusion equation (in dimensionless form),

$$\nabla^2 c = 0, \tag{2.22}$$

with boundary conditions in the far-field and on the particle's surface,

$$c(r\to\infty,\mu) = 0 \qquad \text{and} \qquad \mathbf{n}\cdot\nabla c\Big|_{r=a} = -A(\mu). \tag{2.23}$$

The general solution to the Laplace problem in equations (2.22)–(2.23) is obtained as an

harmonic series [58, 57, 138, 124],

$$c(\mathbf{r}) = \sum_{m=0}^{\infty} \frac{A_m}{m+1} \left(\frac{a}{r}\right)^{m+1} L_m(\mu) \qquad \text{with} \quad A_m = \frac{2m+1}{2} \int_{-1}^{1} A(\mu)\, L_m(\mu) d\mu, \tag{2.24}$$

The concentration field is thus decomposed into the superposition of an infinite number of azimuthal modes of increasing order and spatial decay rate: $m = 0$ represents a *point source* ($\sim r^{-1}$), $m = 1$ a *source dipole* ($\sim r^{-2}$), $m = 2$ a *source quadrupole* ($\sim r^{-3}$) and so on. The strength of each mode, A_m, is obtained by a simple projection along $L_m(\mu)$ of the activity distribution, Eq. (2.24). For a hemispheric Janus particle with $A(\mu) = 1$ for $\mu \in [0, 1]$ and $A(\mu) = 0$ otherwise, the mode amplitudes A_m can be obtained analytically as $A_0 = 1/2$, $A_1 = 3/4$, $A_2 = 0$, $A_3 = -7/16$, etc..

Following the classical continuum framework [57, 58], the surface of the particle generates an effective slip velocity in response to local concentration gradients along the surface.

$$\tilde{\mathbf{u}}(r, \mu) = M \nabla_{||} c = M \sqrt{1-\mu^2} \frac{\partial \widetilde{c}}{\partial \mu} \tag{2.25}$$

where $\widetilde{c}$ represents the surface concentration.

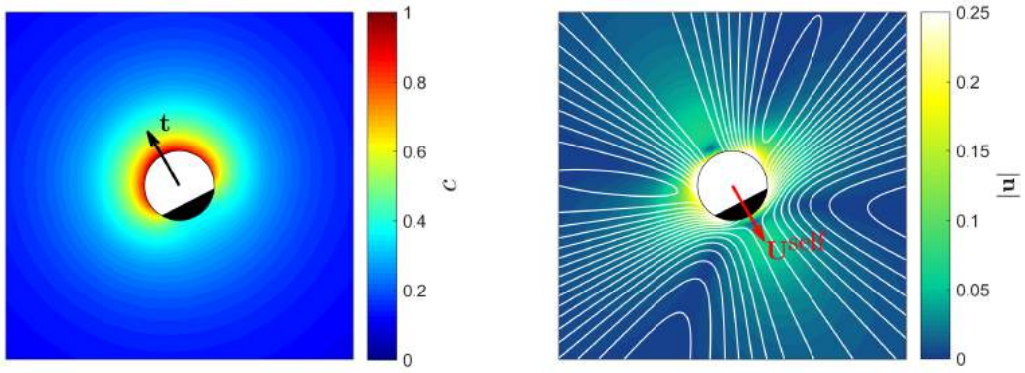

Figure 2.5: Janus swimmer with $3/4^{\text{th}}$ of its surface active with $A = 1$ (in white) a) Chemical field b) Hydrodynamic field

This surface velocity creates the flow signature of the particle. Substituting the above expression in equation (2.20) gives,

$$\alpha_m = -\frac{M}{2} \int_{-1}^{1} (1-\mu^2) L'_m(\mu) \frac{\partial \widetilde{c}}{\partial \mu} d\mu. \tag{2.26}$$

Integrating by parts,

$$\alpha_m = \frac{M}{2} \int_{-1}^{1} \left[(1-\mu^2) L''_m(\mu) - 2\mu L'_m(\mu)\right] \widetilde{c}\, d\mu = -\frac{M}{2} \int_{-1}^{1} m(m+1) L_m(\mu) \widetilde{c}\, d\mu \tag{2.27}$$

The above simplification was possible by utilizing the Legendre equation. Using equation (2.24) to obtain $\widetilde{c} = c(r = a) = \sum_{n \geq 0} A_n L_n(\mu)/(n+1)$, and substituting in the above

equation and simplifying using the integral properties of Legendre polynomial,

$$\alpha_m = \frac{-M}{2} \sum_{n\geq 0} \int_{-1}^{1} m(m+1) \frac{A_n}{n+1} L_n(\mu) L_m(\mu) \tag{2.28}$$

$$\implies \alpha_m = -\frac{mMA_m}{2m+1} \tag{2.29}$$

Thus, we come to an important conclusion that for phoretic swimmers with uniform surface mobility and a fixed rate of flux activity, one can establish a one-to-one relation between the chemical and the hydrodynamic modes [57].

2.4 Propulsion through surface effects

Why is swimming difficult at microscopic scales? The absence of inertial forces to propel the body makes it difficult to swim a microscopic scales; energy is continuously dissipated by viscosity. By stopping the propulsion, the swimming body is thus brought to rest immediately. And, by continuously balancing the viscous drag on the body creates very low swimming efficiency $\sim O(1)\%$ i.e. the scaling laws limit the maximum power obtainable from the motor [152].

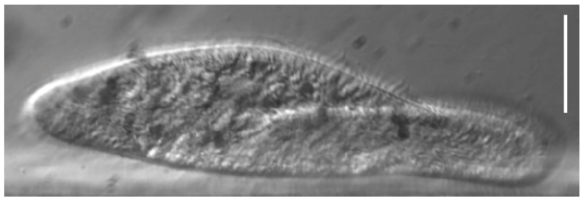

Figure 2.6: Paramecium swims through deformation of cilia on its surface to generate transverse wave that create surface velocity. Figure adapted from [163].

Directed swimming is even more difficult: the swimming micro-organism is continuously subjected to background thermal noise i.e. the external Brownian forces which reorient their swimming trajectory. Thus, the swimmer not only has to exert constant propulsive power, which in itself is less efficient, but also has to continuously modify its orientation to reach its target.

In the previous section, we have seen that a body can propel within a fluid by implementing effective velocities on their surface. Here, we shall mathematically provide the condition in which these effective slip velocites on the surface lead to net motion of the body.

The linearity of the Stokes flows allows for interesting features relating the work done in a fluid. In this section, a brief review of the formulation of Lorentz's reciprocal theorem for fluids in the Stokes limit is derived.

2.4.1 Reciprocal theorem for Stokes flows

Consider a fluid domain of volume V, enclosed within a surface $\mathcal{S}$. Let a velocity and stress field (given by $\mathbf{u}$ and $\boldsymbol{\sigma}$) satisfy the Stokes equations. Let another field given by $\hat{\mathbf{u}}$ and $\hat{\boldsymbol{\sigma}}$ also satisfy the Stokes equations within the same fluid domain. The second solution, denoted by the hat, is known as the *auxillary* flow field.

We know that the stress in the fluid at any point in the domain is given by,

$$\boldsymbol{\sigma} = -p\mathbf{I} + 2\eta\mathbf{E} \quad \text{where,} \quad \mathbf{E} = \frac{1}{2}(\nabla\mathbf{u} + (\nabla\mathbf{u})^T) \tag{2.30}$$

Note here that the strain-rate tensor $\mathbf{E}$ is fully symmetric and deviatoric in nature. Thus, by implementing the reduction $\boldsymbol{\sigma} : \hat{\mathbf{E}}$, we see that

$$\boldsymbol{\sigma} : \hat{\mathbf{E}} = 2\eta\mathbf{E} : \hat{\mathbf{E}} \tag{2.31}$$

In a similar fashion, one can show the identical result that $\hat{\boldsymbol{\sigma}} : \mathbf{E} = 2\eta\mathbf{E} : \hat{\mathbf{E}}$. Thus, we obtain the relation,

$$\boldsymbol{\sigma} : \hat{\mathbf{E}} = \hat{\boldsymbol{\sigma}} : \mathbf{E} \tag{2.32}$$

Furthermore, by using the expansion for strain-rate tensor from equation (2.30), we can derive the following result:

$$\nabla \cdot (\boldsymbol{\sigma} \cdot \hat{\mathbf{u}}) = \nabla \cdot (\hat{\boldsymbol{\sigma}} \cdot \mathbf{u}) \tag{2.33}$$

Summing up the stresses in the bulk fluid gives,

$$\int_V \nabla \cdot (\boldsymbol{\sigma} \cdot \hat{\mathbf{u}}) \mathrm{d}V = \int_V \nabla \cdot (\hat{\boldsymbol{\sigma}} \cdot \mathbf{u}) \mathrm{d}V \tag{2.34}$$

Thus, by implementing the divergence theorem within the fluid domain, we have

$$\int_{\mathcal{S}} \mathbf{n} \cdot (\boldsymbol{\sigma} \cdot \hat{\mathbf{u}}) \mathrm{d}\mathcal{S} - \int_V \hat{\mathbf{u}} \cdot (\nabla \cdot \boldsymbol{\sigma}) \mathrm{d}V = \int_{\mathcal{S}} \mathbf{n} \cdot (\hat{\boldsymbol{\sigma}} \cdot \mathbf{u}) \mathrm{d}\mathcal{S} - \int_V \mathbf{u} \cdot (\nabla \cdot \hat{\boldsymbol{\sigma}}) \mathrm{d}V. \tag{2.35}$$

Stokes flows have zero divergence of stress, thus reducing the above equation to

$$\int_{\mathcal{S}} \mathbf{n} \cdot (\boldsymbol{\sigma} \cdot \hat{\mathbf{u}}) \mathrm{d}\mathcal{S} = \int_{\mathcal{S}} \mathbf{n} \cdot (\hat{\boldsymbol{\sigma}} \cdot \mathbf{u}) \mathrm{d}\mathcal{S} \tag{2.36}$$

The above equation thus relates the virtual work done by two flow fields. To consider external flows, one can let the surface $\mathcal{S}$ to be composed of the region outside a surface $\mathcal{S}_1$ of a solid body and within $\mathcal{S}_\infty$. But letting $\mathcal{S}_\infty$ extend to infinity, where the flow velocity is zero, one can apply the reciprocal theorem for the region outside a swimming body's surface $\mathcal{S}$ of any arbitrary shape. As it will be seen from the subsequent sections, this reciprocal theorem is a powerful tool as it can be used to evaluate the kinematics of the swimmer without computing the flow field in the bulk fluid.

2.4.1.1 Self-propulsion velocity of swimmers

We shall now utilise the Lorentz reciprocal theorem derived above to derive a simple expression for the swimming velocities of microscopic swimmers which propel through surface distortions without the need for computing the bulk flow field. This powerful technique is a way of obtaining "something from nothing" [164]. The swimmer creates a surface disturbance flow $\widetilde{\mathbf{u}}$ which exerts stresses on the fluid. The fluid, being inertialess, balances the net force exerted on it by the body by creating a drag force on it; this is possible through a relative motion between the body and fluid. If the body is pinned at its location, the fluid is pumped on the surface to balance the force, or in case of the swimmer, the net force is balanced by the motion of the swimmer in the fluid.

The flow around the swimmer obeys the Stokes equations given in equation (2.12). If we consider the laboratory frame of reference for the flow field, we have, on the surface of the

body,

$$\mathbf{u}(t) = \widetilde{\mathbf{u}} + \mathbf{U} + a\,\boldsymbol{\Omega} \times \mathbf{n} \tag{2.37}$$

where $\widetilde{\mathbf{u}}$ represents the surface slip velocity, $\mathbf{U}$ the translational velocity of the swimmer and $\boldsymbol{\Omega}$, its angular velocity. Far away from the body, the flow field decays to zero

$$\mathbf{u} = 0 \quad \text{when} \quad \mathbf{r} \to \infty \tag{2.38}$$

The dual problem involves the field $(\hat{\mathbf{u}}, \hat{\boldsymbol{\sigma}})$ where the rigid body is being driven by an external force $\hat{\mathbf{F}}(t)$ and an external torque $\hat{\mathbf{T}}(t)$ which creates a motion of the body with a translational velocity $\hat{\mathbf{U}}(t)$ and rotational velocity $\hat{\boldsymbol{\Omega}}(t)$; if the body is spherical, then it is well known that $\hat{\mathbf{F}} = 6\pi\eta a\hat{\mathbf{U}}$ and $\hat{\mathbf{T}} = 8\pi\eta a^3\hat{\boldsymbol{\Omega}}$. Implementing the boundary condition of equation 18 in the reciprocal theorem derived in equation 17,

$$\hat{\mathbf{U}} \cdot \int_{\mathcal{S}} \boldsymbol{\sigma} \cdot \mathbf{n}\, \mathrm{d}\mathcal{S} = \int_{\mathcal{S}} \mathbf{n} \cdot (\hat{\boldsymbol{\sigma}} \cdot \widetilde{\mathbf{u}})\, \mathrm{d}\mathcal{S} + \hat{\mathbf{F}} \cdot \mathbf{U} \tag{2.39}$$

The force-free boundary condition in the true (swimming) problem gives

$$-\hat{\mathbf{F}} \cdot \mathbf{U} = \int_{\mathcal{S}} \mathbf{n} \cdot (\hat{\boldsymbol{\sigma}} \cdot \widetilde{\mathbf{u}})\, \mathrm{d}\mathcal{S} \implies -6\pi\eta a\hat{\mathbf{U}} \cdot \mathbf{U} = \int_{\mathcal{S}} \frac{3\eta\hat{\mathbf{U}}}{2a} \cdot \widetilde{\mathbf{u}}\, \mathrm{d}\mathcal{S} \tag{2.40}$$

$$\implies \mathbf{U} = -\frac{1}{4\pi a^2}\int_{\mathcal{S}} \widetilde{\mathbf{u}}\, \mathrm{d}\mathcal{S} = -\langle \widetilde{\mathbf{u}} \rangle \tag{2.41}$$

The angle brackets is just to represent the surface average. Thus, from the knowledge of surface distribution of velocity, the propulsion velocity of the swimmer can be computed by simply determining surface averages. Substituting the velocity field equation of (2.21) (on the surface of the body, $r = a$) in the above equation (2.41), one can show that the propulsion velocity simply depends only on the first mode and is given by,

$$\mathbf{U} = -\alpha_1 \mathbf{t} \tag{2.42}$$

In a similar manner, one can find the angular velocity due to surface distortions as,

$$-\hat{\mathbf{T}} \cdot \boldsymbol{\Omega} = \int_{\mathcal{S}} \mathbf{n} \cdot (\hat{\boldsymbol{\sigma}} \cdot \widetilde{\mathbf{u}})\, \mathrm{d}\mathcal{S} \implies \boldsymbol{\Omega} = -\frac{3}{8\pi a^3}\int_{\mathcal{S}} \mathbf{n} \times \widetilde{\mathbf{u}}\, \mathrm{d}\mathcal{S} = -\frac{3}{2a}\langle \mathbf{n} \times \widetilde{\mathbf{u}} \rangle \tag{2.43}$$

For an axisymmetric Janus particle having a uniform surface mobility M, the intensity of the first swimming mode α_1 relates to the activity A_1 using equation (2.29) and hence, the self-propulsion velocity, computed using equation (2.41), turns out to be:

$$\mathbf{U}^{\text{self}} = -\alpha_1 \mathbf{t} = -(MA_1/3)\mathbf{t}, \qquad \boldsymbol{\Omega}^{\text{self}} = 0 \tag{2.44}$$

The remaining modes for the non-swimming modes which contribute to the hydrodynamic signature of the particle. For a hemispherically active Janus colloid uniform surface mobility ($M = 1$), the first mode of surface activity $A_1 = 3/4$; thus, the self-propulsion velocity becomes $\mathbf{U}^{\text{self}} = -\mathbf{t}/4$.

2.4.1.2 Motion due to external flow-field: Faxen's laws

Faxen's laws determine the drift velocity created on a body resting in an external fluid flow $\mathbf{u}_\infty$. Let us consider a sphere within an external flow $\mathbf{u}_\infty$. Let $\mathbf{u}_+$ be the net flow created due to the presence of the particle in this background field. Thus, once can say the disturbance

field,

$$\mathbf{u}_1 = \mathbf{u}_+ - \mathbf{u}_\infty \tag{2.45}$$

Since the body moves at low Reynolds numbers, it does not experience any net force in an external flow and simply and drifts along with the flow; thus, we shall denote the force $\mathbf{F}_1 = 0$. Also note that the disturbance flow decays at infinity $\mathbf{u}_1(r \to \infty) = 0$. We shall define the case of a rigid sphere translating with a velocity $\mathbf{U}_2$ in a viscous fluid to be the dual problem. The particle would create a flow field $\mathbf{u}_2$ and a stress $\boldsymbol{\sigma_2}$. Thus, using the reciprocal theorem, one can write,

$$\int_{\mathcal{S}} \mathbf{u}_1 \cdot \boldsymbol{\sigma}_2 \cdot \mathbf{n}\, d\mathcal{S} = \int_{\mathcal{S}} \mathbf{u}_2 \cdot \boldsymbol{\sigma}_1 \cdot \mathbf{n}\, d\mathcal{S} \tag{2.46}$$

$$\implies -\frac{3\eta \mathbf{U}_2}{a} \cdot \int_{\mathcal{S}} \mathbf{u}_1\, d\mathcal{S} = \mathbf{U}_2 \cdot \int_{\mathcal{S}} \boldsymbol{\sigma}_1 \cdot \mathbf{n}\, d\mathcal{S} \tag{2.47}$$

The above evaluation is made using the property that the viscous stress on a rigid sphere moving with a velocity $\mathbf{U}$ is $\boldsymbol{\sigma} \cdot \mathbf{n} = 3\eta \mathbf{U}/a$ (as derived in equation 2.17). Applying equation (2.45),

$$-\frac{3\eta \mathbf{U}_2}{a} \cdot \int_{\mathcal{S}} (\mathbf{u}_+ - \mathbf{u}_\infty)\, d\mathcal{S} = \mathbf{U}_2 \cdot \mathbf{F}_1 \tag{2.48}$$

However, being in low Reynolds number regime, the body is force-free, $\mathbf{F}_1 = 0$. Additionally, noting that the drift velocity of the body,

$$\mathbf{U}_d = -\langle \mathbf{u}_+ \rangle = -\frac{1}{4\pi a^2} \int_{\mathcal{S}} \mathbf{u}_+\, d\mathcal{S}, \tag{2.49}$$

the above equation (2.49) reduces to

$$\mathbf{U}_d = \frac{1}{4\pi a^2} \int_{\mathcal{S}} \mathbf{u}_\infty\, d\mathcal{S} = \langle \mathbf{u}_\infty \rangle \tag{2.50}$$

$\langle\rangle$ represents surface average over the sphere. Now, expanding the surface velocity near the center of the body using a Taylor series expansion,

$$\mathbf{u}_\infty|_{r=a} = \mathbf{u}_\infty\Big|_{r=0} + a\mathbf{n} \cdot \nabla \mathbf{u}_\infty\Big|_{r=0} + \frac{a^2 \mathbf{nn}}{2} : \nabla\nabla \mathbf{u}_\infty\Big|_{r=0} + \dots \tag{2.51}$$

The expansion in equation (2.51) is used in equation (2.50) and noting that odd modes vanish,

$$\mathbf{U}_d = \mathbf{u}_\infty\Big|_{r=0} + \nabla\nabla \mathbf{u}_\infty\Big|_{r=0} : \frac{a^2 \mathbf{I}}{6} + \nabla\nabla\nabla\nabla \mathbf{u}_\infty\Big|_{r=0} \overset{4}{\odot} \frac{a^4(\mathbf{II} + (\mathbf{II})^{T_{23}} + (\mathbf{II})^{T_{24}})}{720} + \dots \tag{2.52}$$

$$= \left(1 + \frac{a^2}{6}\nabla^2 + \frac{a^4}{240}\nabla^4 + \dots \nabla^{2n}\text{terms}\right) \mathbf{u}_\infty\Big|_{r=0} \tag{2.53}$$

Since the pressure field satisfies $\nabla^2 p = 0$, one can obtain from the Stokes equations that $\nabla^{2n}\mathbf{u} = 0$ for all $n \geq 2$. Thus, equation (2.53) reduces to

$$\mathbf{U}_d = \left(1 + \frac{a^2}{6}\nabla^2\right) \mathbf{u}_\infty\Big|_{r=0} \tag{2.54}$$

Similar procedure may be followed for determining the angular drift velocity $\boldsymbol{\Omega}_d$ due to

background flow.

$$\boldsymbol{\Omega}_d = \frac{1}{2}\nabla \times \mathbf{u}_\infty\Big|_{r=0}. \tag{2.55}$$

2.4.2 Influence of Brownian motion

As mentioned in Section 2.1, besides motion from self-swimming and drift from external flows, bodies immersed in a fluid are subject to random collisions from surrounding fluid molecules leading to Brownian diffusion which produces both translation as well as reorientation of the body. For bodies of microscopic sizes, these effects are non-negligible and are evident in experiments involving swimming bacteria as well as active colloidal particles. These active particles thus have a net displacement with continuous reorientation of the direction of propulsion, thus exhibiting diffusive behaviour in long time scales [72, 25]. The thermal reorientation time scale is $\tau = \eta a^3/k_B T$, where k_B is the Boltzmann constant and T is the temperature of the fluid in kelvin. This random reorientation is known to produce effective diffusion of the particles in the fluid with a diffusivity, $D = mK_B T$, where m is the mobility of the body in the fluid; for a sphere, $m = 1/6\pi\eta a$. For a body swimming with a given velocity U in the fluid, the diffusivity is effective diffusivity is enhanced due to the motion, $D_e = U^2\tau$. For a bacteria swimming at $U \sim O(10^{-5})$, the enhanced diffusivity $D_e \sim O(100)$. Such enhanced diffusion is surprisingly also observed in systems where the particle undergoes reciprocal swimming motion [165].

The dynamics thus involves overdamped motion as well as their thermal reorientation [125, 25]. However, to reduce the complexity of converting the acting forces into velocity of the particle, commonly employed minimal models, called *Active Brownian Particles* describe the essential dynamics by imposing the fluctuations on the *velocity* of the body, thus assuming the particles to be isotropic, and act independently from each other. In the absence of inertia, the evolution of the position $\mathbf{R}_j^{(b)}(t)$ of a spherical particle j under the effect of background noise is given by the overdamped Langevin equation:

$$\frac{\mathrm{d}\mathbf{R}_j^{(b)}(t)}{\mathrm{d}t} = \mathbf{U}_j(t) + \boldsymbol{\xi}_j(t), \tag{2.56}$$

where $\mathbf{U}_j(t)$ is its deterministic velocity in tha absence of any background fluctuations. An external Gaussian white noise, $\boldsymbol{\xi}_j(t)$, has

$$\text{zero mean }, \langle \boldsymbol{\xi}_i(t) \rangle = 0 \tag{2.57}$$

$$\text{and a variance }, \sigma^2 \mathbf{I} = \langle \boldsymbol{\xi}_i(t)\, \boldsymbol{\xi}_j(t') \rangle = 2D\delta(t-t')\delta_{ij}\mathbf{I} \tag{2.58}$$

where D is the diffusivity of each particle in the fluid.

2.5 Other representations of flow-fields

Consider a spherical coordinate system where the zenith angle is denoted by θ and the azimuthal angle by ϕ. We also denote the projection as $\mu = \cos\theta$. Let a spherical particle be represented by $r = a$ in this coordinate system. The particle has a surface slip velocity $\widetilde{\mathbf{u}}$ and moves with a velocity $\mathbf{U}$ and angular velocity $\boldsymbol{\Omega}$. The surface velocity is then given by

$$\mathbf{u}|_{r=a} = \widetilde{\mathbf{u}} + \mathbf{U} + a\, \boldsymbol{\Omega} \times \mathbf{n} \tag{2.59}$$

2.5.1 Spherical harmonic decomposition

The flow field of an axisymmteric swimmer in a fluid is given by the Lamb's general solution [166] for Stokes equation. Since the pressure field obeys the Laplace equation, the general solution for can be written as a harmonic series ,

$$p = \sum_{n=-\infty}^{\infty} p_n, \quad \text{where} \quad p_n = \sum_{m=0}^{n} r^n L_n^m(\mu)(a_{mn}\cos m\phi + \widetilde{a}_{mn}\sin m\phi) \tag{2.60}$$

where $L_n^m(\mu)$ is the n^{th} order Legendre polynomial of degree m. Solving for the coefficients a_{mn} and $\widetilde{a}_{mn}$ in the pressure field requires knowledge of the boundary conditions. In addition to this particular solution, the flow field also comprises of the homogeneous solution to the Stokes equations, given by

$$\mathbf{u}_H = \nabla\phi + \nabla \times \mathbf{r}\chi \tag{2.61}$$

where ϕ_n and χ_n are solid spherical harmonics i.e. $\nabla^2\phi = 0$ and $\nabla^2\chi = 0$. This implies that,

$$\phi = \sum_{n=-\infty}^{\infty} \phi_n, \quad \text{where} \quad \phi_n = \sum_{m=0}^{n} r^n L_n^m(\mu)(b_{mn}\cos m\phi + \widetilde{b}_{mn}\sin m\phi) \tag{2.62}$$

$$\chi = \sum_{n=-\infty}^{\infty} \chi_n \quad \text{where} \quad \chi_n = \sum_{m=0}^{n} r^n L_n^m(\mu)(c_{mn}\cos m\phi + \widetilde{c}_{mn}\sin m\phi) \tag{2.63}$$

Using the above harmonic expansions, the general solution of the Stokes equations, attributed to Lamb [166], can be written as,

$$\mathbf{u} = \sum_{\substack{n=-\infty \\ n\neq -1}}^{\infty} \left[\frac{(n+3)r^2\nabla p_n}{2\eta(n+1)(2n+3)} - \frac{n\mathbf{r}p_n}{\eta(n+1)(2n+3)}\right] + \sum_{n=-\infty}^{\infty} [\nabla\phi_n + \nabla \times (\mathbf{r}\chi_n)] \tag{2.64}$$

The case $n = -1$ is not considered here because the flows correspond to sources (and sinks) which violate the mass conservation for moving solid bodies in a fluid. The flow-field can be thus decomposed into constituent physical parts such as 1) Potential flow contribution from ϕ which decays as r^{-n-2} 2) Rotational flow contribution from χ which decays as r^{-n-1} and 3) pressure driven flow contribution from p which decays as r^{-n}. However, for solid bodies moving through a fluid the pressure field decays at $r \to \infty$; thus, only the negative modes of the series expansion are valid solutions to the problem. Hence, the general solution becomes,

$$\mathbf{u} = \sum_{n=1}^{\infty} \left[\frac{-(n-2)r^2\nabla p_{-n-1} + 2(n+1)\mathbf{r}p_{-n-1}}{2\eta n(2n-1)}\right] + \sum_{n=1}^{\infty} [\nabla\phi_{-n-1} + \nabla \times (\mathbf{r}\chi_{-n-1})] \tag{2.65}$$

For axisymmetric swimmers, $m = 0$ in equations (B.5), (2.62) and (2.63). Thus, the coefficients in the above expansion become (for $n \geq 1$),

$$p_{-n-1} = a_n r^{-n-1} L_n(\mu), \quad \phi_{-n-1} = b_n r^{-n-1} L_n(\mu), \quad \chi_{-n-1} = c_n r^{-n-1} L_n(\mu) \tag{2.66}$$

Here L_n are the Legendre polynomials of order n. We shall henceforth denote the coefficients as n instead of $(-n-1)$ for ease of expression. Expansion of this form suggests the general

expansion for the solution of Lapalce equation

$$\begin{bmatrix} p_n \\ \phi_n \\ \chi_n \end{bmatrix} = \begin{bmatrix} \mathbf{P}_n \\ \mathbf{\Phi}_n \\ \mathbf{X}_n \end{bmatrix} \overset{n}{\odot} \frac{\overset{n}{\otimes} \mathbf{r}}{r^{2n+1}} \tag{2.67}$$

where $_n$, $\mathbf{\Phi}_n$ and $\mathbf{X}_n$ are fully symmetric and deviatoric tensors of order n. If the velocity boundary conditions $\mathbf{u} = \widetilde{\mathbf{u}}$ on a spherical surface $r = a$ is given, then the coefficients can be obtained using the following relation [157]

$$\begin{bmatrix} p_n \\ \phi_n \\ \chi_n \end{bmatrix} = \frac{1}{n+1} \begin{bmatrix} -\eta(2n-1)(n+2)/a & -\eta(2n-1)/a & 0 \\ a\ n/2 & a/2 & 0 \\ 0 & 0 & 1/n \end{bmatrix} \begin{bmatrix} \mathcal{P}_n(\widetilde{\mathbf{u}} \cdot \mathbf{n}) \\ \mathcal{P}_n(-a\nabla_{||} \cdot \widetilde{\mathbf{u}}) \\ \mathcal{P}_n(a\mathbf{n} \cdot \nabla_{||} \times \widetilde{\mathbf{u}}) \end{bmatrix} + \begin{bmatrix} 3a\eta \mathbf{U} \cdot \mathbf{n}/2\ \delta_{n,1} \\ a^3 \mathbf{U} \cdot \mathbf{n}/4\ \delta_{n,1} \\ a^3 \mathbf{\Omega} \cdot \mathbf{n}\ \delta_{n,1} \end{bmatrix} \tag{2.68}$$

Here $\nabla_{||}$ represents the surface gradients.

$[\mathcal{P}_q(f)]_q$ is thus the unique set of fully symmetric and deviatoric tensors of order q such that the expansion of scalar field $f(\mathbf{x})$ into spherical harmonics at the surface of particle k writes as

$$f(\mathbf{x})\Big|_{r=a} = \sum_{q \geq 0} \mathcal{P}_q[f] \overset{q}{\odot} [\mathbf{n}_k \overset{q}{\odot} \mathbf{n}_k]. \tag{2.69}$$

In Eq. (2.67), each term corresponds to flow singularities of increasing order [161, 157, 154], namely (i) source/potential multipoles, ($\mathbf{\Phi}_q$), with a flow field decaying as $1/r^{q+2}$, (ii) symmetric force multipoles ($\mathbf{P}_q$), with a flow field decaying as $1/r^q$ and (iii) rotlet (torque) multipoles ($\mathbf{X}_q$), with a flow field decaying as $1/r^{q+1}$. For instance, $\mathbf{\Phi}_1$ corresponds to a source dipole of intensity $-4\pi\mathbf{\Phi}_1$ while $\mathbf{P}_2$ corresponds to a stresslet of intensity $-4\pi\mathbf{P}_2/3$.

2.5.2 Far-field description of a swimmer

The force and torque on a body moving through the fluid is given by [157]

$$\mathbf{F} = -4\pi\nabla(r^3 p_1) = -4\pi\mathbf{P}_1 \tag{2.70}$$

$$\mathbf{T} = -8\pi\eta\nabla(r^3\chi_1) = -8\pi\eta\mathbf{X}_1 \tag{2.71}$$

The first mode $n = 1$ contributes to the translation and rotation of the particle.

2.5.2.1 Translating passive sphere

For example consider a sphere of radius a moving with a velocity U along the direction $\mathbf{e}_z$. The surface velocity on the sphere $\widetilde{\mathbf{u}} = U\mathbf{e}_z$. Using equation (2.68) with $n = 1$, we get

$$\begin{bmatrix} p_1 \\ \phi_1 \\ \chi_1 \end{bmatrix} = \begin{bmatrix} 3a\eta \mathbf{U} \cdot \mathbf{n}/2\ \delta_{n,1} \\ a^3\eta \mathbf{U} \cdot \mathbf{n}/4\ \delta_{n,1} \\ a^3 \mathbf{\Omega} \cdot \mathbf{n}\ \delta_{n,1} \end{bmatrix} \tag{2.72}$$

Thus, $p_1 = -3\eta U\mathbf{e}_z \cdot \mathbf{n}/2a$. Moreover, using equation (2.67), the first mode, $p_1 = \mathbf{P}_1 \cdot \mathbf{n}/a^2$. Equating these two terms give $\mathbf{P}_1 = -3\eta aU\mathbf{e}_z/2$. Using the expression for force on the body (from equation (A.27)) force on the sphere, one retrieves the well known expression $\mathbf{F} = -4\pi\mathbf{P}_1 = 6\pi\eta aU\mathbf{e}_z$.

One can compute the subsequent modes ($n > 1$), which are the non-swimming modes that decide the flow signature of the particles. The slowest decaying non-swimming mode ($n = 2$)

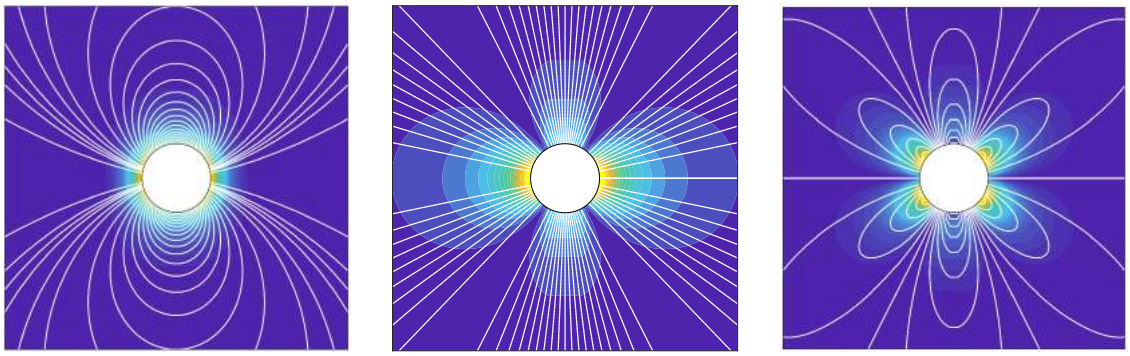

Figure 2.7: a) Potential dipole of strength $\mathbf{\Phi}_1$ b) Stresslet of strength $\mathbf{P}_2$ and c) force quadrupole (which includes a rotlet-dipole flow field)

is called the *stresslet*, which decays as $1/r^2$. This is the symmetric part of the flow created by a force dipole; the flow is radial in nature. The direction of the applied forced dipole $\mathbf{P}_2$ decides the nature of flow and the stresses generated in the fluid: an inward force dipole is a *puller* while an outward force-dipole is called a *pusher*. The leading order potential flow is a point source dipole that decays as $1/r^3$. It's strength depends on the magnitude of $\mathbf{\Phi}$ term. When the swimming particle is non-axisymmetric, the flow field created has a net vorticity. The strength of the rotational flows, with leading order as $1/r^3$ i.e. a rotlet dipole, which is the (anti-symmetric part of point force dipole) are determined by the magnitude of $\mathbf{X}$ term.

2.5.2.2 Phoretic swimmer

For phoretic swimmers, the surface velocity is related to the concentration gradients via equation (2.25) i.e. $\widetilde{\mathbf{u}} = M(\mathbf{I} - \mathbf{nn}) \cdot \nabla c$. Note that here we consider the case where the particle has a uniform surface mobility M. Thus, we have the following properties,

$$\widetilde{\mathbf{u}} \cdot \mathbf{n} = 0, \qquad -a\nabla_s \cdot \widetilde{\mathbf{u}} = -M\mathbf{nn} : \nabla\nabla c \quad \text{and,} \quad a\mathbf{n} \cdot \nabla_s \times \widetilde{\mathbf{u}} = 0 \tag{2.73}$$

Furthermore, one can expand the concentration field in terms of Legendre polynomials to obtain,

$$-a\nabla_s \cdot \widetilde{\mathbf{u}} = -M \sum_{m \geq 1} \frac{A_m a^{m+1}}{m+1} L_m(\mu) \tag{2.74}$$

where $\mu = \mathbf{t} \cdot \mathbf{n}$, with $\mathbf{t}$ being the axis of symmetry and defines the direction of propulsion. Substituting in equation (2.68),

$$\begin{bmatrix} p_n \\ \Phi_n \\ \chi_n \end{bmatrix} = -M \begin{bmatrix} -\frac{\eta(2n-1)(n+2)}{a(n+1)} & -\frac{\eta(2n-1)}{a(n+1)} & 0 \\ \frac{an}{2(n+1)} & \frac{a}{2(n+1)} & 0 \\ 0 & 0 & \frac{1}{n(n+1)} \end{bmatrix} \begin{bmatrix} 0 \\ \frac{A_n a^{n+1}}{n+1} L_n(\mu) \\ 0 \end{bmatrix} + \begin{bmatrix} 3Ua\mu/2\ \delta_{n,1} \\ Ua^3\mu/4\ \delta_{n,1} \\ 0 \end{bmatrix} \tag{2.75}$$

Since the particle is force-free and torque-free, p_1, ϕ_1 and χ_1 zero. Thus, for $n = 1$, which represents the mode contribution to self-propulsion,

$$-M \begin{bmatrix} -3\eta/2a & -\eta/2a & 0 \\ a/4 & a/4 & 0 \\ 0 & 0 & 1/2 \end{bmatrix} \begin{bmatrix} 0 \\ A_1 a^2/2 \\ 0 \end{bmatrix} = \begin{bmatrix} 3a\eta U/2 \\ Ua^3/4 \\ 0 \end{bmatrix} \tag{2.76}$$

from which one can deduce back the result obtained in equation (2.44): $U = A_1 M/3$.

2.5.3 Green's function solutions Stokes flows

Consider a point force $\mathbf{F}$ acting on a fluid at a fixed point $\mathbf{x}_0$. This, for example, is the case of a point object settling in a viscous fluid under the effect of gravity. The Stokes equations for the velocity and pressure at any point $\mathbf{x}$ in the fluid is then,

$$\nabla^2\mathbf{u}(\mathbf{x}) - \nabla p(\mathbf{x}) = -\mathbf{F}\,\delta(\mathbf{x},\mathbf{x}_0) \quad \text{and,} \quad \nabla\cdot\mathbf{u}(\mathbf{x}) = 0 \tag{2.77}$$

where $\delta(\mathbf{x},\mathbf{x}_0)$ is the delta function. Taking divergence of equation 2.77 gives an independent expression for the pressure field,

$$\nabla^2 p(\mathbf{x}) = \nabla\cdot\mathbf{F}. \tag{2.78}$$

The velocity, pressure and stress fields being harmonic, are written in terms of the Green's functions as

$$\mathbf{u}(\mathbf{x}) = \frac{1}{8\pi\eta}\mathbf{S}(\mathbf{x},\mathbf{x}_0)\cdot\mathbf{F}, \quad p(\mathbf{x}) = \frac{1}{8\pi}\mathbf{Q}(\mathbf{x},\mathbf{x}_0)\cdot\mathbf{F}, \quad \text{and,} \quad \boldsymbol{\sigma}(\mathbf{x}) = \frac{1}{8\pi}\mathbf{T}(\mathbf{x},\mathbf{x}_0)\cdot\mathbf{F} \tag{2.79}$$

respectively. Here $\mathbf{S}$, $\mathbf{Q}$, and $\mathbf{T}$ are Green's function tensors of order two, one and three respectively. Note that these functions depend on both the point of disturbance $\mathbf{x}_0$ as well as the point of observation $\mathbf{x}$. By determining the expressions for these functions, one can determine the properties of flow at any point $\mathbf{x}$ in the domain created by point forcing at $\mathbf{x}_0$. Re-writing the Stokes equation (2.77) using equations (2.79), we get

$$\frac{1}{8\pi\eta}\nabla^2\mathbf{S}(\mathbf{x},\mathbf{x}_0)\cdot\mathbf{F} - \frac{1}{8\pi}\nabla\mathbf{Q}(\mathbf{x},\mathbf{x}_0)\cdot\mathbf{F} = -\mathbf{F}\delta(\mathbf{x},\mathbf{x}_0). \tag{2.80}$$

Now, let $\mathbf{G}(\mathbf{x})$ be the Green's function solution of Laplace equation i.e.

$$\nabla^2\mathbf{G}(\mathbf{x}-\mathbf{x}_0) = \delta(\mathbf{x},\mathbf{x}_0) \tag{2.81}$$

whose solution is well known to be

$$\mathbf{G}(\mathbf{x}-\mathbf{x}_0) = -\frac{1}{4\pi|\mathbf{x}-\mathbf{x}_0|} \tag{2.82}$$

By substituting equation (2.79) in equation (2.78), one obtains

$$\frac{1}{8\pi}\nabla^2\mathbf{Q}(\mathbf{x},\mathbf{x}_0)\cdot\mathbf{F} = \nabla\cdot\mathbf{F} \implies \mathbf{Q}(\mathbf{x},\mathbf{x}_0) = 8\pi\nabla\mathbf{G}(\mathbf{x}-\mathbf{x}_0) \tag{2.83}$$

Using equation (2.82) in the above equation (2.83), we finally obtain

$$\mathbf{Q}(\mathbf{x},\mathbf{x}_0) = \frac{2\mathbf{r}}{r^3} \tag{2.84}$$

where $\mathbf{r} = \mathbf{x}-\mathbf{x}_0$ and $r = |\mathbf{r}|$. Substituting equation (2.84) in equation (2.80) and solving,

$$\mathbf{S}(\mathbf{x},\mathbf{x}_0) = \frac{\mathbf{I}}{r} + \frac{\mathbf{rr}}{r} \tag{2.85}$$

The Green's function in equation (2.85) is known as a *Stokeslet*. Substituting Eqs.(2.84) and (2.85) in Eq. (2.79), one obtains the flow and pressure fields created by a point force $\mathbf{F}$ as,

$$\mathbf{u}(\mathbf{r}) = \frac{1}{8\pi\eta}\left(\frac{\mathbf{F}}{r} + \frac{(\mathbf{F}\cdot\mathbf{r})\mathbf{r}}{r^3}\right), \qquad p(\mathbf{r}) = \frac{\mathbf{F}\cdot\mathbf{r}}{4\pi r} \tag{2.86}$$

Note that the Stokeslet flow field decays as $1/r$ and is the slowest decaying flow field. By computing the stress field $\boldsymbol{\sigma}(\mathbf{x})$ from the velocity and pressure fields, one can subsequently

deduce using equation (2.79) that

$$\mathbf{T}(\mathbf{x}, \mathbf{x}_0) = \frac{-6\mathbf{rrr}}{r^5} + \frac{3(\mathbf{rI} + (\mathbf{rI})^{T_{12}} + (\mathbf{rI})^{T_{13}})}{r^3} \tag{2.87}$$

Derivatives of the Green's functions can be used to represent flows from higher-order modes such as force and torque multipoles; because of the linearity of the Stokes equations, these derivatives are also indeed solutions. Taking the derivative of Stokeslet, one obtains,

$$\nabla\mathbf{S}(\mathbf{x}, \mathbf{x}_0) = \left(\frac{-\mathbf{Ir} + (\mathbf{Ir})^{T_{23}} + \mathbf{rI}}{r^3} - \frac{3\mathbf{rrr}}{r^5}\right) \tag{2.88}$$

This is a fundamental singularity comprising of a symmetric as well as an anti-symmeteric component. The fully symmetric and deviatoric part of this Green's solution is known as the *Stresslet*. If the strength of a point force dipole is considered to be $\mathbf{F}_d$, then the the stresslet flow field is,

$$\mathbf{u}(\mathbf{x}) = \frac{1}{8\pi\eta}\mathbf{F}_d : \nabla\mathbf{S} \tag{2.89}$$

For a $\mathbf{d}$ directed force dipole F_d, the gradient along $\mathbf{d}$ direction gives a stresslet flow field,

$$\mathbf{u}(\mathbf{r}) = \frac{1}{8\pi\eta}\left[-\frac{(\mathbf{F}_d \cdot \mathbf{d})\mathbf{r}}{r^3} + 3\frac{(\mathbf{F}_d \cdot \mathbf{r})(\mathbf{d} \cdot \mathbf{r})\mathbf{r}}{r^5}\right] \tag{2.90}$$

The anti-symmetric part of the tensor is called a *rotlet* and physically describes the flow field created by a point torque dipole. The flow-field of the rotlet is thus given by

$$\mathbf{R} = \frac{(\mathbf{d} \times \mathbf{F}) \times \mathbf{r}}{8\pi\eta r^3} \tag{2.91}$$

Note that both the stresslet and rotlet decay as $1/r^2$. For force and torque-free swimmers in Stokes flow, the leading order decay of flow field is a stresslet. Taking subsequent gradients give the higher order terms that represent force multipoles.

2.5.4 Flows due to point source and its derivatives

The flow field created by a point source of strength m is given by,

$$\mathbf{u}(\mathbf{r}) = \frac{m}{4\pi}\mathbf{H} \tag{2.92}$$

where $\mathbf{H}$ is the Green's function solution, given by

$$\mathbf{H} = \frac{\mathbf{r}}{r^3} \tag{2.93}$$

For a swimmer in an incompressible fluid, there is no source of flow ($m = 0$. Thus, the leading order contribution comes from a *source dipole*, (also known as a *potential dipole*). For a given dipole strength $\mathbf{D}$, one can compute the flow field by taking gradients of the Green's function solution i.e.,

$$\mathbf{u}(\mathbf{r}) = -\frac{\mathbf{D} \cdot \nabla\mathbf{H}}{4\pi} = \frac{1}{4\pi}\mathbf{D} \cdot \left(\frac{-\mathbf{I}}{r^3} + \frac{3\mathbf{rr}}{r^5}\right) \tag{2.94}$$

Thus, the leading order decay of flow field for a micro-swimmer is $1/r^3$. Higher order flows due point source multipoles may be computed by taking subsequent derivatives of the

Green's function.

2.6 Boundary integral formulation

The divergence-free nature of the flow as well as the stress field in the case of Stokes flows allows one to express the flows as surface integrals. The idea of boundary integral formulation is that, in the case of Stokes flow of incompressible fluids, one can Boundary element methods are especially useful for phoretic problems because the boundary conditions are described on the surface of the body. The computations for the flow field in the the bulk are not necessary.

2.6.1 Boundary integral formulation for Stokes equations

Consider a body B immersed in a fluid and let $(\mathbf{u}, \boldsymbol{\sigma})$ represent the velocity and stress field velocity and stress fields around this body. As an auxilliary problem, let us consider the fluid containing a point forcing $\mathbf{F}^*$ at a point $\mathbf{x}_0$ in the fluid domain. One can then write equation (2.77) in its index notation as,

$$\frac{\partial}{\partial r_k}[u_i^*(\mathbf{x})\sigma_{ik}(\mathbf{x}) - u_i(\mathbf{x})\sigma_{ik}^*(\mathbf{x})] = u_j(\mathbf{x})\ F_j^*\delta(\mathbf{x}, \mathbf{x}_0) \tag{2.95}$$

Using the Green's function solution for Stokes flow from equation (2.79) for the auxilliary flow field, we obtain

$$\frac{\partial}{\partial r_k}[S_{ij}^*(\mathbf{x}, \mathbf{x}_0)\sigma_{ik}(\mathbf{x}) - \eta u_i(\mathbf{x})\ T_{ijk}^*(\mathbf{x}, \mathbf{x}_0)] = u_j(\mathbf{x})\delta(\mathbf{x}, \mathbf{x}_0) \tag{2.96}$$

Now, let us choose a control volume V in the exterior of the body B and extends spherically outwards such that it completely encloses it. The volume integral of the above equation gives

$$\int_V \frac{\partial}{\partial r_k}[S_{ij}^*(\mathbf{x}, \mathbf{x}_0)\sigma_{ik}(\mathbf{x}) - \eta u_i(\mathbf{x})\ T_{ijk}^*(\mathbf{x}, \mathbf{x}_0)]\mathrm{d}V = \int_V u_j(\mathbf{x})\delta(\mathbf{x}, \mathbf{x}_0)\mathrm{d}V \tag{2.97}$$

which has singular kernals S^* and T^*. Using Gauss divergence theorem, the volume integral can be converted into a surface integral over the closed surface $\partial\mathcal{S}$. If the outer sphere approaches infinity, the surface integral reduces only to the surface of the body B

$$\int_{\partial B}[S_{ij}^*(\mathbf{x}, \mathbf{x}_0)\sigma_{ik}(\mathbf{x}) - \eta u_i(\mathbf{x})T_{ijk}^*(\mathbf{x}, \mathbf{x}_0)]n_k(\mathbf{x})\ dS(\mathbf{x}) = \int_V u_j(\mathbf{x})\delta(\mathbf{x}, \mathbf{x}_0)\mathrm{d}V \tag{2.98}$$

which implies [153]

$$u_j(\mathbf{x}_0) = -\frac{1}{8\pi\eta}\int_{\partial\mathcal{B}} S_{ij}^*(\mathbf{x}, \mathbf{x}_0)\ f_i(\mathbf{x})\ d\mathcal{S}(\mathbf{x}) + \frac{1}{8\pi}\int_{\partial\mathcal{B}} u_i(\mathbf{x})\ T_{ijk}^*(\mathbf{x}, \mathbf{x}_0)\ n_k(\mathbf{x})dS(\mathbf{x}) \tag{2.99}$$

where one can expresses the traction on the surface, $\boldsymbol{\sigma}\cdot\mathbf{n} = \mathbf{f}$. The first term on the RHS of equation (2.99) is known as the *single layer potential* whereas the second term is called the *double layer potential*. In situation where the body is non-deformable, it can be shown that there is no contribution from the double-layer potential in the expression equation (2.99) [141, 167]. The equation 2.99 needs to be closed with the force- and torque-free boundary

condition for bodies moving in the viscous regime, i.e.

$$\int_{\partial B} \mathbf{f}(\mathbf{x}) \mathrm{d}\mathcal{S} = 0 \quad \text{and} \quad \int_{\partial B} (\mathbf{x} - \mathbf{x}_c) \times \mathbf{f}(\mathbf{x}) \mathrm{d}\mathcal{S} = 0 \tag{2.100}$$

These equations are sufficient to compute the velocity and traction on the surface of the particle. In the need for estimating the flow velocity and stresses in the bulk fluid, one can project from the known surface values of these quantities.

2.6.2 Boundary integral formulation for diffusion equation

Phoretic particles produce a solute concentration field in the fluid through surface chemical reactions. Here, we assume a particle to emit/ absorb a certain solute at a constant rate from the surface. The advective effects of the solute are taken to be negligible and, additionally, we shall assume the solute to diffuse instantaneously into the fluid. This lets one consider a quasi-steady state of diffusion process. Summing up briefly the diffusion equation and the surface boundary conditions,

$$\nabla^2 c = 0, \qquad \text{with,} \quad \left.\frac{\partial c}{\partial n}\right|_{\mathcal{S}} = -A \quad \text{and} \qquad c \to 0 \text{ as } r \to \infty \tag{2.101}$$

The fundamental solutions to the Laplace equation (2.101) is given by the Green's functions representing a *point sink* and a *point source dipole*.

$$J(\mathbf{x}, \mathbf{x}_0) = -\frac{1}{4\pi r} \quad \text{and} \quad \mathbf{K}(\mathbf{x}, \mathbf{x}_0) = \frac{\mathbf{r}}{4\pi r^3} \tag{2.102}$$

The boundary integral equation for the concentration field in response to the flux forcing on the active particles [137, 17]

$$\lambda\, c(\mathbf{x}_0) = \int_{\mathcal{S}} \Big[c(\mathbf{x})\, \mathbf{K}(\mathbf{x}, \mathbf{x}_0) \cdot \mathbf{n}(\mathbf{x}) - \frac{\partial c(\mathbf{x})}{\partial n}\, J(\mathbf{x}, \mathbf{x}_0) \Big] \mathrm{d}\mathcal{S}(\mathbf{x}) \tag{2.103}$$

where $\mathbf{x}$ is any point on the surface $\mathcal{S}$ of the particle with local normal $\mathbf{n}(\mathbf{x})$. Here, $\lambda = 0,\ 1/2$ or, 1 depending on whether the point of evaluation, $\mathbf{x}_0$ is inside, on or outside the surface of the body.

2.7 Conclusions

In this chapter, we explain the physical features of mechanics of fluid flow at low Reynolds numbers as well as its influence on rigid bodies immersed in the fluid. Beginning from the fundamental Stokes equations, we have established the requirements of self-propulsion in this regime. Due to lack of inertia the active bodies require spending continuous supply of energy to maintain the drag-asymmetry needed for propulsion. For rigid bodies, their propulsion velocities depend only on the distribution of instantaneous surface velocities; biological organisms use appendages on their surface while artificial phoretic swimmers use surface concentration gradients of a solute to generate the slip velocity. When subjected to external flow field, the advective response of the bodies is determined using Faxen's laws. Additionally, Brownian dynamics is used to explain the random drift and reorientation of bodies in the fluid.

The swimming bodies generate a flow field around them as the move through the fluid, the

features of which are a characteristic of the surface forcing of the swimmer. This flow signature can be understood analytically for an axisymmetric swimmer through decomposition of the field into its spherical harmonic components; these are essentially point force and source multipoles. In a system with multiple particles, the field from each acts as a disturbance on the others. The harmonic decomposition of the field however assumes the bodies to behave as point particles. To determine exact solution to bodies with finite volume, boundary integral methods are introduced whereby the surface stresses and propulsion velocities of the bodies can be determined by appropriate distribution of the singular Green's functions solutions on the surface of the body. Its numerical implementation, known as Boundary Element Methods (BEM), is a powerful numerical technique for solving Stokes flow problems; the advantage being that the surface dynamics of the body can be determined without computations of the flow-field in the bulk fluid.

in this chapter, we have laid the mathematical foundations needed to explain transport of a *single* active or passive body in microscopic scales. In the rest of the thesis, we shall implement the analytical as well as numerical methods (BEM) proposed here to develop physical models to understand the interactions between multiple particles in a system and to study their ensuing collective dynamics. We shall however restrict our attention to phoretic micro-swimmers alone, where both chemical and hydrodynamic effects play a role in the multi-particle interactions.

3

Modeling chemical and hydrodynamic interactions in phoretic suspensions

Autophoretic colloids exploit local self-generated chemical gradients to achieve self-propulsion at the microscopic scales. Understanding the collective dynamics of a large number of such particles is currently the focus of intense research efforts. Thus far, most efforts for modelling the dynamics rely on simple superposition of far-field approximations, which are only valid asymptotically in the dilute suspension limit. A systematic and unified analytical framework based on the classical Method of Reflections (MoR) is developed here for both Laplace and Stokes' problems to obtain the higher-order interactions and the resulting velocities of multiple phoretic particles, up to any order of accuracy in the radius-to-distance ratio ε of the particles. This model allows us to account for the generic chemo-hydrodynamic couplings as well as N-particle interactions ($N \geq 3$). The ε^5-accurate interaction velocities are then explicitly obtained and the resulting implementation of this MoR model is discussed and validated quantitatively against exact solutions of a few canonical problems.

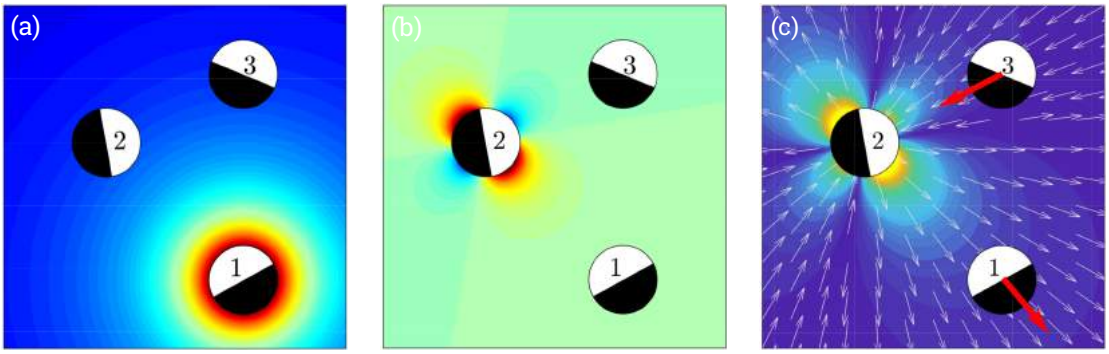

Figure: *Three-body chemo-hydrodynamic interactions between janus phoretic particles using Method of reflections: A chemical source field from particle 1 (a) creates a reflected source quadrupole on particle 2 (b) which induces a hydrodynamic field that drifts the surrounding particles (c).*

Contents

This chapter contains a modified version of article "Modeling chemo-hydrodynamic interactions of phoretic particles: a unified framework" by A. Varma and S. Michelin, submitted to *Physical Review Fluids*.

In this Chapter, we shall derive an analytical framework to compute the chemical and hydrodynamic fields created by phoretic particles in a suspension, and their resulting multi-body dynamics. The method involves developing the spherical harmonic expansions of both the chemical and hydrodynamic fields created by each particle as described in Chapter 2; the presence of other similar chemically and hydrodynamically active particles in the system modifies this field and hence their dynamics. For a particle with a finite volume, the chemical and hydrodynamic flux boundary conditions on the surface are not met if one simply superimposes the field created by the particles in isolation. This situation was encountered by Smoluchowski (1911) while studying the dynamics of settling passive spheres [168]. The technique he implemented involves an iterative procedure known as *Method of reflections* wherein at each stage the spurious hydrodynamic field created by each particle is corrected for by appropriate modification of the strength of field generated by the particle till the previous stage. Here, we shall implement this technique to determine the corrected propulsion velocities of autophoretic particles due to chemical and hydrodynamic interactions between them.

3.1 Swimming in external fields

To understand the chemical and hydrodynamic interactions created by the surrounding particles and their influence on the dynamics of a particular particle, a first step is to understand how the particle responds to any arbitrary background concentration (and hydrodynamic) field. The advective effects on the solute are considered negligible (Pe $\ll 1$).

3.1.1 Phoretic drift in an external chemical field

We analyze here the drift generated on a spherical inert particle ($A(\mathbf{r}) = 0$) placed in a spatially non-uniform background concentration field $c_\infty(\mathbf{r})$ of a solute. The diffusivity of the solute is considered to be much larger than the particle, making the process quasi-static; additionally, the solute dynamics is considered to be diffusion driven (advective effects are negligible). Thus, due to the linearity of the chemical problem, the net concentration field when the particle is present can be written as the superposition of (i) the background field in the absence of the particle, $c_\infty(\mathbf{r})$, and (ii) a perturbation $c'(\mathbf{r})$ due to the presence of the particle in the background field.

$$c(\mathbf{r}) = c_\infty(\mathbf{r}) + c'(\mathbf{r}) \tag{3.1}$$

To satisfy the no penetration boundary condition at the particle's surface, the perturbation field c' must satisfy

$$\nabla^2 c'(\mathbf{r}) = 0 \qquad \text{with the boundary conditions,} \tag{3.2}$$

$$\mathbf{n}\cdot\nabla c'\Big|_{r=a} = -\mathbf{n}\cdot\nabla c_\infty\Big|_{r=a} \qquad \text{and,} \quad c'(\mathbf{r}\to\infty) = 0, \tag{3.3}$$

whose generic solution can be expressed uniquely as

$$c'(\mathbf{r}) = \sum_{q\geq 0} \frac{a^{q+1}}{r^{2q+1}} \mathbf{C}_q \overset{q}{\odot} \mathbf{r}\ldots\mathbf{r} \tag{3.4}$$

where $\overset{q}{\odot}$ denotes q successive tensor contractions and $\mathbf{C}_q$ is a tensor of order q which is fully symmetric and deviatoric. Determining c' is therefore equivalent to finding the set $(\mathbf{C}_q)_q$.

Near the particle, the background field c_∞ can be expanded in Taylor series as,

$$c_\infty(\mathbf{r}) = \sum_{q\geq 0} \frac{1}{q!} \overset{q}{\nabla} c_\infty \Big|_{r=0} \overset{q}{\odot} \mathbf{r}\dots\mathbf{r} = c_\infty\Big|_{r=0} + \mathbf{r}\cdot\nabla c_\infty\Big|_{r=0} + \frac{\mathbf{rr}}{2!} : \nabla\nabla c_\infty\Big|_{r=0} + \dots \quad (3.5)$$

where $\overset{q}{\nabla} c$ denotes the q-th gradient of c. This background field creates a normal flux on the surface of the particle,

$$\mathbf{n}\cdot\nabla c_\infty\Big|_{r=a} = \sum_{q\geq 1} \frac{a^{q-1}}{(q-1)!} \overset{q-1}{\nabla} c_\infty\Big|_{r=0} \overset{q}{\odot} \mathbf{n}\dots\mathbf{n} = \mathbf{n}\cdot\nabla c_\infty\Big|_{r=0} + a\mathbf{nn} : \nabla\nabla c_\infty\Big|_{r=0} + \dots \quad (3.6)$$

The perturbation field $c'(\mathbf{r})$ must cancel out this spurious external surface flux exactly (as described in equation (3.3)). Taking the gradient of Eq. (3.4), its normal component at the surface is given by

$$\mathbf{n}\cdot\nabla c'\Big|_{r=a} = -\frac{1}{a}\sum_{q\geq 0}(q+1)\mathbf{C}_q \overset{q}{\odot} \mathbf{n}\dots\mathbf{n} = -\frac{C_0}{a} - \frac{2\mathbf{C}_1}{a}\cdot\mathbf{n} - \frac{3\mathbf{C}_2 : \mathbf{nn}}{a} + \dots \quad (3.7)$$

Identification between equations (3.6) and (3.7) provides

$$\mathbf{C}_q = \frac{qa^q}{(q+1)!} \overset{q}{\nabla} c_\infty\Big|_{r=0}. \quad (3.8)$$

As a result, the concentration field due to the presence of a passive particle in an external field is finally obtained as,

$$\begin{aligned} c'(\mathbf{r}) + c_\infty(\mathbf{r}) &= \sum_{q\geq 0}\frac{1}{q!}\left(\overset{q}{\nabla} c_\infty\Big|_{r=0} \overset{q}{\odot} \mathbf{r}\dots\mathbf{r}\right)\left[1 + \frac{q}{q+1}\left(\frac{a}{r}\right)^{2q+1}\right] \\ &= c_\infty\Big|_{r=0} + \mathbf{r}\cdot\nabla c_\infty\Big|_{r=0}\left(1+\frac{a^3}{2r^3}\right) + \frac{\mathbf{rr}}{2} : \nabla\nabla c_\infty\Big|_{r=0}\left(1+\frac{2a^3}{3r^5}\right) + \dots \end{aligned} \quad (3.9)$$

Taking the tangential gradient of this field on the surface,

$$\begin{aligned} (\mathbf{I}-\mathbf{nn})\cdot\Big[\nabla c'(\mathbf{r}) + \nabla c_\infty(\mathbf{r})\Big]_{r=a} &= (\mathbf{I}-\mathbf{nn})\cdot\sum_{q\geq 1}\frac{q(2q+1)a^{q-1}}{(q+1)!}\left(\overset{q}{\nabla} c_\infty\Big|_{r=0} \overset{q-1}{\odot} \mathbf{n}\dots\mathbf{n}\right) \\ &= (\mathbf{I}-\mathbf{nn})\cdot\left[\frac{3}{2}\nabla c_\infty\Big|_{r_k=0} + \frac{5a}{3}\nabla\nabla c_\infty\Big|_{r_k=0}\cdot\mathbf{n}\dots\right]. \end{aligned} \quad (3.10)$$

The chemical drift velocities $(\mathbf{U}^\chi, \mathbf{\Omega}^\chi)$, resulting from the presence of the particle in the external field c_∞, are then obtained using the reciprocal theorem for low-Re locomotion [169]:

$$\mathbf{U}^\chi = -\left\langle M(\mathbf{n})(\mathbf{I}-\mathbf{nn})\cdot\Big[\nabla c'(\mathbf{r}) + \nabla c_\infty(\mathbf{r})\Big]_{r=a}\right\rangle = -M\,\nabla c_\infty\Big|_{r=0} \quad (3.11)$$

$$\mathbf{\Omega}^\chi = \frac{3}{2a}\left\langle\left\{M(\mathbf{n})(\mathbf{I}-\mathbf{nn})\cdot\Big[\nabla c'(\mathbf{r}) + \nabla c_\infty(\mathbf{r})\Big]_{r=a}\right\}\times\mathbf{n}\right\rangle = \mathbf{0} \quad (3.12)$$

where the last equality of each equation holds when the mobility of the particle, $M(\mathbf{n})$ is spatially uniform. Note that in the case of uniform surface mobility, the only non-zero

surface average of slip velocity is the term with $\mathbf{C}_1$ (i.e. ∇c_∞) and is the sole contribution for the chemical drift of the particle. Note that when the particles have a uniform mobility, the external fields do not contribute to any rotational effects; this is hence a reduced influence on the chemotactic behaviour where particle aligns towards or away from the concentration gradients.

3.1.2 Hydrodynamic drift of an inert particle

The last contribution to the active particle motion in external fields is the effect of an external disturbance flow $\mathbf{u}_\infty$, which is analyzed here by computing the hydrodynamic drift on a rigid particle exposed to a non-uniform background hydrodynamic field $\mathbf{u}_\infty(\mathbf{r})$. This is a classical Faxén's laws [154] that were briefly derived in Chapter 2 (section 2.4.1.2).

$$\mathbf{U}^h = \mathbf{u}_\infty\Big|_{r=0} + \frac{1}{6}\nabla^2\mathbf{u}_\infty\Big|_{r=0} \quad \text{and} \quad \mathbf{\Omega}^h = \frac{1}{2}\nabla\times\mathbf{u}_\infty\Big|_{r=0}. \tag{3.13}$$

3.2 Far-field interactions

In this section we shall study the leading order interactions between active phoretic particles. Note that here we shall examine the case of spherical phoretic particles having an axis of symmetry of their surface activity; the surface activity (solute flux) is additionally considered to be constant i.e. the reaction kinetics is first-order and is independent of the surrounding concentration field. Thus the governing equations of the solute concentration field generated by an arbitrary isolated phoretic particle j is summarized from Chapter 2 as,

$$\nabla^2 c_j = 0, \quad \mathbf{n}_j\cdot\nabla c_j = -A_j(\mu_j) \quad \text{and,} \quad c_j(r_j\to\infty) = 0 \tag{3.14}$$

where $\mu_j = \mathbf{t}_j\cdot\mathbf{r}_j/r_j$. The general solution is given by equation (2.24) as

$$c_j(\mathbf{r}_j) = \sum_{m=0}^{\infty}\frac{A_{j,m}}{m+1}\left(\frac{a_j}{r_j}\right)^{m+1} L_m(\mu_j) \qquad \text{with} \quad A_{j,m} = \frac{2m+1}{2}\int_{-1}^{1} A_j(\mu)\, L_m(\mu)d\mu, \tag{3.15}$$

with the leading-order decay being a chemical source which decays as $\sim 1/r$

$$c_j = \frac{A_{j,0}\, a_j}{r_j} \tag{3.16}$$

Similarly, the hydrodynamic field produced by the particle j obeys the Stokes equations

$$\nabla\cdot\mathbf{u}_j = 0, \quad \nabla^2\mathbf{u}_j = \nabla p_j \tag{3.17}$$

with boundary conditions on the surface of the particle and at infinity,

$$\mathbf{u}_j\Big|_{r_j=a_j} = \widetilde{\mathbf{u}}_j + \mathbf{U} + a\,\mathbf{\Omega}\times\mathbf{n} \quad \text{and,} \quad \mathbf{u}_j(r_j\to\infty) = 0 \tag{3.18}$$

The surface slip velocity is related to the concentration gradients as $\widetilde{\mathbf{u}}_j = M(\mathbf{I}-\mathbf{n}_j\mathbf{n}_j)\cdot\nabla c_j$. The general solution for a force- and torque-free particle in given by Blake (as described in

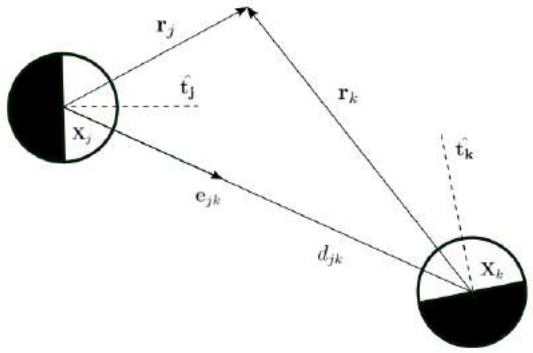

Figure 3.1: Notations used for geometric description of the arrangement of any two Janus particles j and k. The Janus particles comprise active (white) and inert (black) caps.

Chapter 2, equation (2.21)),

$$\mathbf{u}_j(\mathbf{r}_j) = -\frac{A_{j,1}M_j}{6r_j^3}\left(\frac{3\mathbf{r}_j\mathbf{r}_j}{r_j^2} - \mathbf{I}\right)\cdot\mathbf{t}_j \tag{3.19}$$

$$- \sum_{m\geq 2}\frac{-M_j A_{j,m}}{2(m+1)}\Bigg\{\left(m(m+1)L_m(\mu_j)\left[\left(\frac{a_j}{r_j}\right)^{m+2} - \left(\frac{a_j}{r_j}\right)^{m}\right]\right)\frac{\mathbf{r}_j}{r_j}$$

$$+ L'_m(\mu_j)\left[(m-2)\left(\frac{a_j}{r_j}\right)^{m} - m\left(\frac{a_j}{r_j}\right)^{m+2}\right]\left(\mathbf{I} - \frac{\mathbf{r}_j\mathbf{r}_j}{r_j^2}\right)\cdot\mathbf{t}_j\Bigg\} \tag{3.20}$$

with the leading-order field being a stresslet whose flow field (decaying as $\sim 1/r^2$) is obtained as,

$$\mathbf{u}_j(\mathbf{r}_j) = \frac{a_j^2 M_j A_{j,2}}{2}(3\mathbf{t}_j\mathbf{t}_j - \mathbf{I}) : \left(\frac{\mathbf{r}_j\mathbf{r}_j\mathbf{r}_j}{r_j^5}\right) \tag{3.21}$$

The interaction between multiple active particles may now be understood by considering the particles to be immersed in a chemical and hydrodynamic field produced by the surrounding particles. An approximation of the dynamics between particles can be made by assuming only the far-field interactions between the particles. It assumes that the background concentration and hydrodynamic fields experienced by a given particle k results from the superposition of the chemical and hydrodynamic signatures of each of its neighbours (noted $j \neq k$) *as if these particles were themselves isolated.* The far-field models consider the particles to be point particles and thus neglect the presence and the influence of the solid surface of the particles on the chemical and hydrodynamic fields they generate. Further, in the dilute limit (i.e. when the particles are asymptotically far away from each other), only the slowest decaying contribution to each signature is to be retained to obtain the dominant chemical and hydrodynamic drifts.

The position of particle k is noted $\mathbf{x}_k$, its radius is a_k, and its orientation is given by a unit vector $\mathbf{t}_k$. For any two particles j and k, d_{jk} and $\mathbf{e}_{jk}$ respectively denote their center-to-center distance and the unit vector joining the centre of particles j to k, i.e. $d_{jk}\mathbf{e}_{jk} = \mathbf{x}_k - \mathbf{x}_j$, as shown in figure 3.1. We further denote $\mathbf{r}_j$ the position vector measured with respect to particle j, i.e. $\mathbf{r}_j = \mathbf{r} - \mathbf{x}_j$.

The concentration and hydrodynamic fields created by isolated particles (equations (3.15) and (3.20) respt.) can be expanded as series of chemical and hydrodynamic singularities

whose effect on neighbouring particles scale like increasing powers of $\varepsilon = a/d$ (where a and d denote here the typical values of particle radius a_j and interparticle distance d_{jk}, respectively). When sufficiently far apart (i.e. $\varepsilon \ll 1$), the phoretic particles behave, at the leading order, as the slowest decaying chemical and hydrodynamic singularities, i.e. a *chemical point source* and a *hydrodynamic force-dipole*.

As mentioned previously, each particle is considered isolated from the others. Thus, the concentration field produced by each particle (say j) obeys equation (3.15). At the leading order, each particle behaves as a chemical source (equation (3.16)) and the net field produced in the system is a simple superposition of the individual fields. Thus,

$$c(\mathbf{r}_j) = \sum_j \frac{A_{j,0} a_j}{r_j} \tag{3.22}$$

When a particle k is placed in this field, the external concentration field $c_{\infty,k}$ experienced by particle k (and its gradient) at the particle's center ($r_k = 0$) are obtained as

$$c_{\infty,k} = \sum_{j\neq k} \frac{A_{j,0} a_j}{r_j} \quad \Rightarrow \quad \nabla c_{\infty,k}\Big|_{r_k=0} = -\sum_{j\neq k} \frac{A_{j,0}\, a_j^2}{d_{jk}^2} \mathbf{e}_{jk}. \tag{3.23}$$

The drift velocity induced on a particle placed in an external concentration field $c_{\infty,k}$ is thus given by equation (3.11) as,

$$\mathbf{U}_k^{\chi} = M_k \sum_{j\neq k} \frac{A_{j,0}\, a_j^2}{d_{jk}^2} \mathbf{e}_{jk}, \quad \text{and} \quad \mathbf{\Omega}_k^{\chi} = \mathbf{0}. \tag{3.24}$$

Each neighbouring particle j thus induces on particle k a chemical drift along their line of centers (with an order of magnitude $O(\varepsilon^2)$), but without any rotation (for uniform mobility).

Similarly, retaining only the leading-order flow field created by particle j (i.e. that of a stresslet in equation (3.21)), the background hydrodynamic field experienced by particle k is given by

$$\mathbf{u}_{\infty,k}(\mathbf{r}) = \sum_{j\neq k} \frac{a_j^2 M_j A_{j,2}}{2} (3\mathbf{t}_j\mathbf{t}_j - \mathbf{I}) : \left(\frac{\mathbf{r}_j \mathbf{r}_j \mathbf{r}_j}{r_j^5} \right), \tag{3.25}$$

and the hydrodynamic drifts are obtained from Eqs. (3.13), keeping only leading order contributions, as

$$\mathbf{U}_k^h = \sum_{j\neq k} \frac{M_j A_{j,2}}{2} \left(\frac{a_j}{d_{jk}} \right)^2 (3\mathbf{t}_j\mathbf{t}_j - \mathbf{I}) : \mathbf{e}_{jk}\mathbf{e}_{jk}\mathbf{e}_{jk}, \tag{3.26}$$

$$\mathbf{\Omega}_k^h = \sum_{j\neq k} \frac{3 a_j^2 M_j A_{j,2}}{2 d_{jk}^3} (\mathbf{t}_j \cdot \mathbf{e}_{jk})(\mathbf{e}_{jk} \times \mathbf{t}_j). \tag{3.27}$$

In non-dimensional units, the self-propulsion velocity of the particles is $O(1)$, while the chemical and hydrodynamic drifts introduced by the presence of other particles, Eqs (3.11) and (3.26)–(3.27) are both of the same order, $O(\varepsilon^2)$.

The resulting framework, termed *far-field interaction model*, is fundamentally based on neglecting (i) higher order contributions to the chemical and hydrodynamic signatures of individual particles which would contribute to $O(\varepsilon^3)$ or smaller drift velocities and, (ii) modifications of the field production by each particle due to the presence of others. Note that in the above analysis, by restricting to far-field modeling, we are able to obtain solutions that

provide pairwise interaction between the particles. Additionally, to maintain consistency of the asymptotics, far-field models must also ignore higher order corrections as the Laplacian term in Faxen's law (in equation (3.13)) which would contribute an $O(\varepsilon^4)$ to the particles' velocities.

The higher-order interactions ($O\left(a^n/d^n\right),\ n>2$) however become increasingly influential on the dynamics when the separation d between particles decreases. This substantiates the need for more accurate estimates of the propulsion velocities $\mathbf{U}_k$ and $\mathbf{\Omega}_k$ which requires taking into account explicitly these faster-decaying terms. In doing so, multiple interdependent interactions between the particles would be taken into account and this property is at the heart of the classical *Method of Reflections* for both chemical and hydrodynamic problem, which we exploit in the following section.

3.3 Method of Reflections (MoR)

The objective is to construct analytically consistent estimates of the velocities with increasing order of accuracy.

3.3.1 MoR for chemical problem

The method is initiated by considering the superposition of the chemical field created by isolated particles, noted c_k^0, which was obtained explicitly in equation (3.15). When isolated, c_k^0 satisfies the correct constant flux boundary condition on particle k, but, if it is introduced to a system consisting of similar active particles, a spurious flux is introduced on its surface from the diffuse flux created by others; the particle k itself would then create spurious chemical flux on the surface of others. The objective of MoR is to sequentially eliminate this spurious flux so that the correct boundary condition is closely reached.

At each subsequent stage ($r \geq 1$), known as a "reflection", a correction c_k^r to the concentration field created by a particle k is introduced in order to correct the spurious normal flux introduced on the boundary of particle k during the previous reflection at the other particles (e.g. c_k^1 must correct for the spurious flux introduced by $\sum_{j\neq k} c_j^0$). c_k^r is therefore the unique solution to the following Laplace problem

$$\nabla^2 c_k^r = 0 \quad \text{for } r_k \geq a_k, \qquad \mathbf{n}_k \cdot \nabla c_k^r\Big|_{r_k=a_k} = -\sum_{j\neq k} \mathbf{n}_k \cdot \nabla c_j^{r-1}\Big|_{r_k=a_k}, \qquad c_k^r(r_k \gg a_k) \longrightarrow 0. \tag{3.28}$$

and can be written as

$$c_k^r(\mathbf{r}_k) = \sum_{q\geq 0} \frac{a_k^{q+1}}{r_k^{2q+1}} \mathbf{C}_{k,q}^r \overset{q}{\odot} [\mathbf{r}_k \overset{q}{\otimes} \mathbf{r}_k], \tag{3.29}$$

where $(\mathbf{C}_{k,q}^r)_q$ is a unique set of q^{th} order fully symmetric and deviatoric tensors. In the previous equation $\mathbf{r}_k \overset{q}{\otimes} \mathbf{r}_k$ denote the tensorial product of vector $\mathbf{r}_k$ by itself repeated q times, while $\mathbf{A} \overset{q}{\odot} \mathbf{B}$ denotes the q-fold contraction of tensors $\mathbf{A}$ and $\mathbf{B}$. Expanding c_j^{r-1} in Taylor

series near the center of particle k,

$$c_j^{r-1}(\mathbf{r}_j) = \sum_{q\geq 0} \frac{1}{q!} \overset{q}{\nabla} c_j^{r-1}\Big|_{r_k=0} \overset{q}{\odot} [\mathbf{r}_k \overset{q}{\otimes} \mathbf{r}_k] = c_j^{r-1}\Big|_{r_k=0} + \mathbf{r}_k \cdot \nabla c_j^{r-1}\Big|_{r_k=0} + \frac{\mathbf{r}_k \mathbf{r}_k}{2!} : \nabla\nabla c_j^{r-1}\Big|_{r_k=0} + \ldots, \tag{3.30}$$

the flux boundary condition in Eq. (3.28) together with Eqs. (3.29)–(3.30) imposes:

$$\mathbf{C}_{k,q}^r = \sum_{j\neq k} \frac{q a_k^q}{(q+1)!} \overset{q}{\nabla} c_j^{r-1}\Big|_{r_k=0}. \tag{3.31}$$

Substituting Eq. (3.29) for particle j at reflection $r-1$ into Eq. (3.31) provides the recursive relation

$$\mathbf{C}_{k,q}^r = \sum_{j\neq k} \sum_{s\geq 0} \mathbf{C}_{j,s}^{r-1} \overset{s}{\odot} \boldsymbol{\mathcal{F}}_{\boldsymbol{jk}}^{\boldsymbol{\chi}}(q,s), \qquad \text{with,} \tag{3.32}$$

$$\boldsymbol{\mathcal{F}}_{\boldsymbol{jk}}^{\boldsymbol{\chi}}(q,s) = \frac{q a_k^q a_j^{s+1}}{(q+1)!} \left[\overset{q}{\nabla} \left(\frac{\mathbf{r}_j \overset{s}{\otimes} \mathbf{r}_j}{r_j^{2s+1}} \right) \right]_{r_k=0} = O(\varepsilon^{q+s+1}). \tag{3.33}$$

$\boldsymbol{\mathcal{F}}_{\boldsymbol{jk}}^{\boldsymbol{\chi}}(q,s)$ is the transfer function, which is a tensor of order $(q+s)$ that relates the q^{th} order tensor coefficient of particle k ($\mathbf{C}_{k,q}^r$) with the s^{th} order tensor coefficient of particle j ($\mathbf{C}_{j,s}^r$). Note that the formulation above corresponds to a *parallel* form of the method of reflections (it relates the new concentration multipole on particle k to that of other particles at the previous reflection). A *sequential* approach of the method (i.e. obtaining $\mathbf{C}_{k,q}^r$ for each particle k successively) would correspond to splitting the sum on j in Eq. (3.33) (respectively for $j<k$ and $j>k$) in order to exploit that for $j<k$, the new concentration multipole $\mathbf{C}_{j,s}^r$, being already available, would be used to compute $\mathbf{C}_{k,q}^r$.

Also, it should be noted that $\boldsymbol{\mathcal{F}}_{\boldsymbol{jk}}^{\boldsymbol{\chi}}(q=0,s)=0$ for all s; this implies that the reflections induce no net source because the boundary condition to be met is a balance of the concentration gradients. The isotropic mode (source term) do not contribute to generating directed surface gradients. It is to be noted that only the fully symmetric and deviatoric part of the transfer function $\boldsymbol{\mathcal{F}}_{\boldsymbol{jk}}^{\boldsymbol{\chi}}(q,s)$ with respect to its first s indices contribute since $\mathbf{C}_{j,s}^{r-1}$ is fully symmetric and deviatoric. The lowest order transfer functions are thus obtained as:

$$\boldsymbol{\mathcal{F}}_{\boldsymbol{jk}}^{\boldsymbol{\chi}}(1,0) = -\frac{a_j a_k\, \mathbf{e}_{jk}}{2d_{jk}^2} = O(\varepsilon^2), \tag{3.34}$$

$$\boldsymbol{\mathcal{F}}_{\boldsymbol{jk}}^{\boldsymbol{\chi}}(2,0) = \frac{a_k^2 a_j (3\mathbf{e}_{jk}\mathbf{e}_{jk} - \mathbf{I})}{3d_{jk}^3} = O(\varepsilon^3), \tag{3.35}$$

$$\boldsymbol{\mathcal{F}}_{\boldsymbol{jk}}^{\boldsymbol{\chi}}(3,0) = \frac{3a_k^3 a_j}{8d_{jk}^4} \left(\mathbf{I}\mathbf{e}_{jk} + \mathbf{e}_{jk}\mathbf{I} + (\mathbf{I}\mathbf{e}_{jk})^{T_{23}} - 5\mathbf{e}_{jk}\mathbf{e}_{jk}\mathbf{e}_{jk} \right) = O(\varepsilon^4) \tag{3.36}$$

$$\boldsymbol{\mathcal{F}}_{\boldsymbol{jk}}^{\boldsymbol{\chi}}(1,1) = -\frac{a_k a_j^2 (2\mathbf{e}_{jk}\mathbf{e}_{jk} - \mathbf{I})}{3d_{jk}^3} = O(\varepsilon^3) \tag{3.37}$$

$$\boldsymbol{\mathcal{F}}_{\boldsymbol{jk}}^{\boldsymbol{\chi}}(2,1) = -\frac{a_k^2 a_j^2}{d_{jk}^4} \left(\mathbf{I}\mathbf{e}_{jk} + \mathbf{e}_{jk}\mathbf{I} + (\mathbf{I}\mathbf{e}_{jk})^{T_{23}} - 5\mathbf{e}_{jk}\mathbf{e}_{jk}\mathbf{e}_{jk} \right) = O(\varepsilon^4) \tag{3.38}$$

$$\boldsymbol{\mathcal{F}}_{\boldsymbol{jk}}^{\boldsymbol{\chi}}(1,2) = \frac{3a_k a_j^3}{2d_{jk}^4} \left(\mathbf{I}\mathbf{e}_{jk} + \mathbf{e}_{jk}\mathbf{I} + (\mathbf{I}\mathbf{e}_{jk})^{T_{23}} - 5\mathbf{e}_{jk}\mathbf{e}_{jk}\mathbf{e}_{jk} \right) = O(\varepsilon^4). \tag{3.39}$$

The recursive relation in Eq. (3.33) is initiated by noting that the tensors $\mathbf{C}_{k,q}^0$ are obtained

from the activity distribution coefficients $A_{k,n}$ (equation 3.15) of the individual particle as

$$C^0_{k,0} = A_{k,0}, \qquad \mathbf{C}^0_{k,1} = \frac{A_{k,1}\,\mathbf{t}_k}{2}, \qquad \mathbf{C}^0_{k,q\geq 2} = \frac{(2q-1)!\,A_{k,q}}{2^{q-1}(q-1)!\times(q+1)!}\overline{\mathbf{t}_k \overset{q}{\otimes} \mathbf{t}_k}, \tag{3.40}$$

with $\overline{\mathbf{B}}$ denoting the fully symmetric and deviatoric part of any given tensor $\mathbf{B}$ [127]. For example, using the index notation, it can be shown that

$$\overline{t_i t_j} = \frac{1}{2}(t_i t_j + t_j t_i) - \frac{1}{3}t_s t_s \delta_{ij} = t_i t_j - \delta_{ij}/3, \tag{3.41}$$

$$\begin{aligned}\overline{t_i t_j t_k} = &\frac{1}{6}(t_i t_j t_k + t_i t_k t_j + t_j t_i t_k + t_j t_k t_i + t_k t_i t_j + t_k t_j t_i)\\ &- \frac{1}{15}\left((t_s t_s t_i + t_s t_i t_s + t_i t_s t_s)\delta_{kj} + (t_s t_s t_j + t_s t_j t_s + t_j t_s t_s)\delta_{ik} + (t_s t_s t_k + t_s t_k t_s + t_k t_s t_s)\delta_{ij}\right)\end{aligned} \tag{3.42}$$

$$= t_i t_j t_k - \frac{1}{5}(t_i\delta_{jk} + t_j\delta_{ik} + t_k\delta_{ij}). \tag{3.43}$$

It should be stressed here that the method is presented for axisymmetric particles (i.e. the successive moments $\mathbf{C}^0_{k,q}$ are function of the axis of the particle $\mathbf{t}_k$ only), yet could easily be extended to particles of arbitrary coverage [170] by modifying Eq. (3.40) accordingly.

The change in surface concentration of particle k introduced at reflection $r \geq 1$, noted $\tilde{c}^r_k$, is obtained within this framework as the sum of c^r_k and of the contributions c^{r-1}_j of all the other particles ($j \neq k$) evaluated at $r_k = a_k$:

$$\tilde{c}^r_k = c^r_k\Big|_{r_k=a_k} + \sum_{j\neq k} c^{r-1}_j\Big|_{r_k=a_k} = \sum_{q\geq 1}\frac{2q+1}{q}\mathbf{C}^r_{k,q} \overset{q}{\odot} [\mathbf{n}_k \overset{q}{\otimes} \mathbf{n}_k]. \tag{3.44}$$

For $r = 0$, the surface concentration is similarly obtained as

$$\tilde{c}^0_k = c^0_k\Big|_{r_k=a_k} = \sum_{q\geq 0}\mathbf{C}^0_{k,q} \overset{q}{\odot} [\mathbf{n}_k \overset{q}{\otimes} \mathbf{n}_k]. \tag{3.45}$$

Equation (3.44) provides an interpretation of the tensorial coefficients $\mathbf{C}^r_{k,q}$ as the fully symmetric and deviatoric moment of order q of the surface concentration introduced at reflection r,

$$\mathbf{C}^r_{k,q} = \frac{q}{2q+1}\langle \tilde{c}^r_k\, \overline{\mathbf{n}_k \overset{q}{\otimes} \mathbf{n}_k}\rangle. \tag{3.46}$$

Finally, after all the desired reflections have been performed, the surface concentration $\tilde{c}_k$ of particle k is obtained by superimposing all the different contributions $\tilde{c}^r_k$,

$$\tilde{c}_k = C^0_{k,0} + \sum_{q\geq 1}\left[\mathbf{C}^0_{k,q} + \sum_{r\geq 1}\frac{(2q+1)}{q}\mathbf{C}^r_{k,q}\right] \overset{q}{\odot} [\mathbf{n}_k \overset{q}{\otimes} \mathbf{n}_k]. \tag{3.47}$$

3.3.2 MoR for hydrodynamic problem

A similar framework can be formulated for the hydrodynamic problem. At each stage p, for a given particle k, we seek the unique solution of Stokes equation around particle k that decays in the far-field,

$$\nabla^2 \mathbf{u}^p_k = \nabla p^p_k, \qquad \nabla\cdot\mathbf{u}^p_k = 0, \qquad \mathbf{u}^p_k(r_k \gg a_k) \to 0, \tag{3.48}$$

and further satisfies the following Dirichlet condition on the particle's surface

$$\mathbf{u}_k^p\Big|_{r_k=a_k} = \mathbf{v}_k^p + \mathbf{U}_k^p + \mathbf{\Omega}_k^p \times \mathbf{n}_k, \tag{3.49}$$

where $\mathbf{U}_k^p$ and $\mathbf{\Omega}_k^p$ are the translation and rotation velocity corrections for particle k at reflection p (determined by enforcing the linear and angular momentum balances on particle k), and $\mathbf{v}_k^0$ (initialization) corresponds to the phoretic slip resulting from the concentration distribution at the particle's surface, while $\mathbf{v}_k^p$ with $p \geq 1$ (subsequent reflections) balances the spurious flow created at stage $p-1$ by all the other particles.

As described in detail in Chapter 2 (Section 2.5.1), the general solution to Stokes equations in (3.48) is clasically written in terms of three sets of spherical harmonics [157, 166],

$$\mathbf{u}_k^p = \sum_{q=1}^{\infty} \left[\nabla \phi_{k,q}^p + \nabla \times \left(\chi_{k,q}^p \mathbf{r}_k \right) + \frac{2(q+1)p_{k,q}^p \mathbf{r}_k - (q-2) r_k^2 \nabla p_{k,q}^p}{2q(2q-1)} \right] \tag{3.50}$$

with,

$$\begin{bmatrix} p_{k,q}^p(\mathbf{r}_k) \\ \phi_{k,q}^p(\mathbf{r}_k) \\ \chi_{k,q}^p(\mathbf{r}_k) \end{bmatrix} = \begin{bmatrix} \mathbf{P}_{k,q}^p \\ \mathbf{\Phi}_{k,q}^p \\ \mathbf{X}_{k,q}^p \end{bmatrix} \overset{q}{\odot} \left(\frac{\mathbf{r}_k \overset{q}{\otimes} \mathbf{r}_k}{r_k^{2q+1}} \right), \tag{3.51}$$

and $(\mathbf{\Phi}_{k,q}^p)_q$, $(\mathbf{P}_{k,q}^p)_q$ and $(\mathbf{X}_{k,q}^p)_q$ are three sets of fully-symmetric and deviatoric tensors of order q:

$$\mathbf{\Phi}_{k,q}^p = \frac{a_k^{q+2}}{2(q+1)} \left(q \mathcal{P}_q^k[\mathbf{n}_k \cdot \mathbf{v}_k^p] + \mathcal{P}_q^k[-a_k \nabla_s \cdot \mathbf{v}_k^p] \right) + \frac{\delta_{q,1} a_k^3}{4} \mathbf{U}_k^p \tag{3.52}$$

$$\mathbf{P}_{k,q}^p = \frac{(2q-1)a_k^q}{q+1} \left((q+2) \mathcal{P}_q^k[\mathbf{n}_k \cdot \mathbf{v}_k^p] + \mathcal{P}_q^k[-a_k \nabla_s \cdot \mathbf{v}_k^p] \right) + \frac{3\delta_{q,1} a_k}{2} \mathbf{U}_k^p \tag{3.53}$$

$$\mathbf{X}_{k,q}^p = \frac{a_k^{q+1}}{q(q+1)} \mathcal{P}_q^k[a_k \mathbf{n}_k \cdot (\nabla_s \times \mathbf{v}_k^p)] + \delta_{q,1} a_k^3 \mathbf{\Omega}_k^p, \tag{3.54}$$

As detailed in Chapter 2, $\mathcal{P}_q^k[f(\mathbf{x})]$ represents the fully symmetric and deviatoric part of the q^{th} order tensor of the spherical harmonic decomposition of the scalar field $f(\mathbf{x})$. The conservation of linear and angular momentum for each particle imposes two further conditions that uniquely determine $\mathbf{U}_k^p$ and $\mathbf{\Omega}_k^p$. For example, for force- and torque-free particles, $\mathbf{X}_{k,1}^p = \mathbf{P}_{k,1}^p = 0$ (there is no rotlet or stokeslet contribution to particle k's hydrodynamic signature).

3.3.2.1 Initialization from the phoretic slip distribution ($p = 0$)

In the context of the present work, i.e. the collective dynamics of phoretic particles, the hydrodynamic problem is initiated by considering the flow field generated by a single isolated particle ($p = 0$) with a phoretic slip distribution $\mathbf{v}_k^0$ at its surface. By definition, $\mathbf{v}_k^0 = M(\mathbf{n}_k)\nabla_s C$ is purely tangential. Also, $a_k \mathbf{n}_k \cdot (\nabla_s \times \mathbf{v}_k^p) = a_k \mathbf{n}_k \cdot (\nabla_s M \times \nabla_s \tilde{c}_k)$ which is strictly zero for particles of uniform mobility. Finally, the surface divergence of $\mathbf{v}_k^0$ is obtained from the spherical harmonic decomposition of the surface concentration on that

particle, Eq. (3.47). For particles of uniform mobility M_k, we finally obtain

$$\mathbf{n}_k \cdot \mathbf{v}_k^0 = 0, \qquad -a_k \nabla_s \cdot \mathbf{v}_k^0 = M_k \sum_{q\geq 1} (q+1) \left[q\mathbf{C}_{k,q}^0 + \sum_{r\geq 1} (2q+1)\mathbf{C}_{k,q}^r \right] \overset{q}{\odot} [\mathbf{n}_k \overset{q}{\otimes} \mathbf{n}_k] \quad \text{and,} \tag{3.55}$$

$$a_k \mathbf{n}_k \cdot (\nabla_s \times \mathbf{v}_k^p) = 0. \tag{3.56}$$

The last equation above imposes that $\mathbf{X}_{k,q}^0 = 0$ for all q, so that there is no self-rotation associated with phoretic slip for torque-free particles of uniform mobility. For force- and torque-free particles of uniform mobility, we finally obtain

$$\mathbf{U}_k^0 = -\frac{2M_k}{3} \left[\mathbf{C}_{k,1}^0 + \sum_{r\geq 1} 3\mathbf{C}_{k,1}^r \right], \qquad \mathbf{\Omega}_k^0 = 0, \qquad \mathbf{\Phi}_{k,1}^0 = -\frac{a_k^3 \mathbf{U}_k^0}{2}, \tag{3.57}$$

$$\mathbf{\Phi}_{k,q\geq 2}^0 = \frac{a_k^2 \mathbf{P}_{k,q}^0}{2(2q-1)} = \frac{a_k^{q+2} M_k}{2} \left[q\mathbf{C}_{k,q}^0 + \sum_{r\geq 1} (2q+1)\mathbf{C}_{k,q}^r \right], \qquad \mathbf{X}_{k,q\geq 1}^0 = 0. \tag{3.58}$$

For an isolated particle, one can use equations (3.58) and (3.40) to determine that $\mathbf{U}_k^0 = 2M_k \mathbf{C}_{k,1}^0/3 = -A_{k,1} M_k/3$ as expected from equation (2.75).

It should be noted that the mobility distribution at the surface of the particles only impacts the initialization of the hydrodynamic problem ($p = 0$), and not the recursive relations for $p \geq 1$ which are completely general. Although Eqs. (3.57)–(3.58) are only valid for particles of uniform mobility, they can be generalized straightforwardly to particles of non-uniform mobility (e.g. Janus particles with different activities and mobilities on both hemispheres), by performing a tensor reduction process to rewrite the modified Eqs. (3.56) in terms of fully-symmetric and deviatoric tensors. This would potentially introduce a non-zero surface vorticity in Eq. (3.56).

3.3.2.2 Recursive relations for the hydrodynamic singularities ($p \geq 1$)

When $p \geq 1$, $\mathbf{v}_k^p$ must exactly cancel the flow introduced at the surface of particle k by the previous reflection at all the other particles $j \neq k$; using a Taylor series expansion of those flow fields near the center of particle k,

$$\mathbf{v}_k^p = -\sum_{j\neq k} \mathbf{u}_j^{p-1}\Big|_{r_k = a_k} = -\sum_{q\geq 1} \left[\sum_{j\neq k} \frac{a_k^{q-1}}{(q-1)!} \overset{q-1}{\nabla} \mathbf{u}_j^{p-1}\Big|_{r_k=0} \right] \overset{q-1}{\odot} [\mathbf{n}_k \overset{q-1}{\otimes} \mathbf{n}_k], \tag{3.59}$$

and the surface normal velocity, divergence and vorticity are obtained as

$$\mathbf{v}_k^p \cdot \mathbf{n}_k = -\sum_{q\geq 1}\left[\sum_{j\neq k}\frac{a_k^{q-1}}{(q-1)!}\left(1+\frac{a_k^2}{2(2q+3)}\nabla^2\right)\overline{\nabla^{q-1}\mathbf{u}_j^{p-1}}\Big|_{r_k=0}\right]\overset{q}{\odot}[\mathbf{n}_k\overset{q}{\otimes}\mathbf{n}_k], \tag{3.60}$$

$$-a_k\nabla_s\cdot\mathbf{v}_k^p = -\sum_{q\geq 1}\left[\sum_{j\neq k}\frac{a_k^{q-1}}{(q-1)!}\left(q-1+\frac{(q+1)a_k^2}{2(2q+3)}\nabla^2\right)\overline{\nabla^{q-1}\mathbf{u}_j^{p-1}}\Big|_{r_k=0}\right]\overset{q}{\odot}[\mathbf{n}_k\overset{q}{\otimes}\mathbf{n}_k], \tag{3.61}$$

$$a_k\mathbf{n}_k\cdot[\nabla_s\times\mathbf{v}_k^p] = -\sum_{q\geq 1}\left[\sum_{j\neq k}\frac{a_k^q}{q!}\overline{\nabla^{q-1}\boldsymbol{\omega}_j^{p-1}}\Big|_{r_k=0}\right]\overset{q}{\odot}[\mathbf{n}_k\overset{q}{\otimes}\mathbf{n}_k], \tag{3.62}$$

where $\overline{\nabla^{q-1}\mathbf{u}_j^{p-1}}$ denotes the fully symmetric and deviatoric part of the $(q-1)$-th velocity gradient. For force- and torque-free particles, $\mathbf{P}_{k,1}^p = \mathbf{X}_{k,1}^p = 0$,

$$\mathbf{U}_k^p = \sum_{j\neq k}\left(1+\frac{a_k^2}{6}\nabla^2\right)\mathbf{u}_j^{p-1}\Big|_{r_k=0},\qquad \boldsymbol{\Omega}_k^p = \frac{1}{2}\sum_{j\neq k}\boldsymbol{\omega}_j^{p-1}\Big|_{r_k=0},\qquad \boldsymbol{\Phi}_{k,1}^p = -\frac{a_k^5}{30}\sum_{j\neq k}\nabla^2\mathbf{u}_j^{p-1}\Big|_{r_k=0}, \tag{3.63}$$

which recovers Faxen's laws exactly, and for $q\geq 2$,

$$\boldsymbol{\Phi}_{k,q}^p = -\frac{2q-1}{2(q+1)}\frac{a_k^{2q+1}}{(q-1)!}\sum_{j\neq k}\left(1+\frac{(2q+1)a_k^2}{2(2q-1)(2q+3)}\nabla^2\right)\overline{\nabla^{q-1}\mathbf{u}_j^{p-1}}\Big|_{r_k=0}, \tag{3.64}$$

$$\mathbf{P}_{k,q}^p = -\frac{2q+1}{2(q+1)}\frac{a_k^{2q-1}}{(q-1)!}\sum_{j\neq k}\left(1+\frac{a_k^2}{2(2q+1)}\nabla^2\right)\overline{\nabla^{q-1}\mathbf{u}_j^{p-1}}\Big|_{r_k=0}, \tag{3.65}$$

$$\mathbf{X}_{k,q}^p = -\frac{1}{q(q+1)}\frac{a_k^{2q+1}}{q!}\sum_{j\neq k}\overline{\nabla^{q-1}\boldsymbol{\omega}_j^{p-1}}\Big|_{r_k=0}. \tag{3.66}$$

Computing the required gradients at the center of particle k provides recursive definitions of the flow singularities $(\boldsymbol{\Phi}_{k,q}^p, \mathbf{P}_{k,q}^p, \mathbf{X}_{k,q}^p)_q$ and particles' velocities $(\mathbf{U}_k^p, \boldsymbol{\Omega}_k^p)$ at reflection p as linear functions of those at reflection $p-1$, thus obtaining transfer functions that are independent of $p\geq 1$ (see Appendix D). For force- and torque-free particles, these write:

$$\mathbf{U}_k^p = \sum_{j\neq k}\sum_{s\geq 1}\left[\boldsymbol{\Phi}_{j,s}^{p-1}\overset{s}{\odot}\boldsymbol{\mathcal{F}}_{\boldsymbol{jk}}^{\mathbf{1}}(1,s) - \mathbf{X}_{j,s}^{p-1}\overset{s}{\odot}\boldsymbol{\mathcal{F}}_{\boldsymbol{jk}}^{\mathbf{2}}(1,s) + \mathbf{P}_{j,s}^{p-1}\overset{s}{\odot}\left(\boldsymbol{\mathcal{F}}_{\boldsymbol{jk}}^{\mathbf{3}}(1,s)+\frac{a_k^2}{6}\boldsymbol{\mathcal{F}}_{\boldsymbol{jk}}^{\mathbf{1}}(1,s)\right)\right], \tag{3.67}$$

$$\boldsymbol{\Omega}_k^p = -\frac{1}{2}\sum_{j\neq k}\sum_{s\geq 1}\left[\mathbf{P}_{j,s}^{p-1}\overset{s}{\odot}\boldsymbol{\mathcal{F}}_{\boldsymbol{jk}}^{\mathbf{2}}(1,s) + s\mathbf{X}_{j,s}^{p-1}\overset{s}{\odot}\boldsymbol{\mathcal{F}}_{\boldsymbol{jk}}^{\mathbf{1}}(1,s)\right], \tag{3.68}$$

$$\boldsymbol{\Phi}_{j,1}^p = -\frac{a_k^5}{30}\sum_{j\neq k}\sum_{s\geq 1}\left[\mathbf{P}_{j,s}^{p-1}\overset{s}{\odot}\boldsymbol{\mathcal{F}}_{\boldsymbol{jk}}^{\mathbf{1}}(1,s)\right], \tag{3.69}$$

and for $q \geq 2$:

$$\boldsymbol{\Phi}^p_{k,q} = \sum_{j\neq k}\sum_{s\geq 1}\left[\boldsymbol{\Phi}^{p-1}_{j,s} \overset{s}{\odot} \boldsymbol{\mathcal{F}}^{\boldsymbol{\Phi}\to\boldsymbol{\Phi}}_{\boldsymbol{jk}}(q,s) + \mathbf{P}^{p-1}_{j,s} \overset{s}{\odot} \boldsymbol{\mathcal{F}}^{\boldsymbol{P}\to\boldsymbol{\Phi}}_{\boldsymbol{jk}}(q,s) + \mathbf{X}^{p-1}_{j,s} \overset{s}{\odot} \boldsymbol{\mathcal{F}}^{\boldsymbol{X}\to\boldsymbol{\Phi}}_{\boldsymbol{jk}}(q,s)\right], \tag{3.70}$$

$$\mathbf{P}^p_{k,q} = \sum_{j\neq k}\sum_{s\geq 1}\left[\boldsymbol{\Phi}^{p-1}_{j,s} \overset{s}{\odot} \boldsymbol{\mathcal{F}}^{\boldsymbol{\Phi}\to\boldsymbol{P}}_{\boldsymbol{jk}}(q,s) + \mathbf{P}^{p-1}_{j,s} \overset{s}{\odot} \boldsymbol{\mathcal{F}}^{\boldsymbol{P}\to\boldsymbol{P}}_{\boldsymbol{jk}}(q,s) + \mathbf{X}^{p-1}_{j,s} \overset{s}{\odot} \boldsymbol{\mathcal{F}}^{\boldsymbol{X}\to\boldsymbol{P}}_{\boldsymbol{jk}}(q,s)\right], \tag{3.71}$$

$$\mathbf{X}^p_{k,q} = \sum_{j\neq k}\sum_{s\geq 1}\left[\boldsymbol{\Phi}^{p-1}_{j,s} \overset{s}{\odot} \boldsymbol{\mathcal{F}}^{\boldsymbol{\Phi}\to\boldsymbol{X}}_{\boldsymbol{jk}}(q,s) + \mathbf{P}^{p-1}_{j,s} \overset{s}{\odot} \boldsymbol{\mathcal{F}}^{\boldsymbol{P}\to\boldsymbol{X}}_{\boldsymbol{jk}}(q,s) + \mathbf{X}^{p-1}_{j,s} \overset{s}{\odot} \boldsymbol{\mathcal{F}}^{\boldsymbol{X}\to\boldsymbol{X}}_{\boldsymbol{jk}}(q,s)\right], \tag{3.72}$$

with $\boldsymbol{\mathcal{F}}^{\boldsymbol{\Phi}\to\boldsymbol{X}}_{\boldsymbol{jk}}{}_{jk}(q,s) = 0$ and the other transfer functions above defined in Eqs. (D.16)–(D.25). Of utmost importance to truncate the reflection process at a fixed order in ε consistently, they respectively scale as:

$$\boldsymbol{\mathcal{F}}^{\boldsymbol{P}\to\boldsymbol{\Phi}}_{\boldsymbol{jk}}(q,s) = O(\varepsilon^{s+q-1}), \tag{3.73}$$
$$\boldsymbol{\mathcal{F}}^{\boldsymbol{P}\to\boldsymbol{P}}_{\boldsymbol{jk}}(q,s) = (\varepsilon^{s+q+1}), \tag{3.74}$$
$$\boldsymbol{\mathcal{F}}^{\boldsymbol{X}\to\boldsymbol{\Phi}}_{\boldsymbol{jk}}(q,s) = O(\varepsilon^{s+q}), \tag{3.75}$$
$$\boldsymbol{\mathcal{F}}^{\boldsymbol{X}\to\boldsymbol{P}}_{\boldsymbol{jk}}(q,s) = O(\varepsilon^{s+q}), \tag{3.76}$$
$$\boldsymbol{\mathcal{F}}^{\boldsymbol{X}\to\boldsymbol{X}}_{\boldsymbol{jk}}(q,s) = O(\varepsilon^{s+q}), \tag{3.77}$$
$$\boldsymbol{\mathcal{F}}^{\boldsymbol{P}\to\boldsymbol{X}}_{\boldsymbol{jk}}(q,s) = O(\varepsilon^{s+q}), \tag{3.78}$$
$$\boldsymbol{\mathcal{F}}^{\boldsymbol{\Phi}\to\boldsymbol{\Phi}}_{\boldsymbol{jk}}(q,s) = O(\varepsilon^{s+q+1}), \tag{3.79}$$
$$\boldsymbol{\mathcal{F}}^{\boldsymbol{\Phi}\to\boldsymbol{P}}_{\boldsymbol{jk}}(q,s) = O(\varepsilon^{s+q+1}). \tag{3.80}$$

As an example, using the results of Appendix D,

$$\begin{aligned}\boldsymbol{\mathcal{F}}^{\boldsymbol{P}\to\boldsymbol{P}}_{\boldsymbol{jk}}(2,2) = &-\frac{5a_k^3}{12d_{jk}^3}\left[\frac{(\mathbf{I}\mathbf{e}_{jk}\mathbf{e}_{jk})^{T_{24}} + (\mathbf{I}\mathbf{e}_{jk}\mathbf{e}_{jk})^{T_{23}} + (\mathbf{e}_{jk}\mathbf{I}\mathbf{e}_{jk})^{T_{34}} + \mathbf{e}_{jk}\mathbf{I}\mathbf{e}_{jk}}{2} + \mathbf{e}_{jk}\mathbf{e}_{jk}\mathbf{I} - 5\mathbf{e}_{jk}\mathbf{e}_{jk}\mathbf{e}_{jk}\mathbf{e}_{jk}\right] \\ &-\frac{a_k^5}{12d_{jk}^5}\left[\frac{(\mathbf{II})^{T_{23}} + (\mathbf{II})^{T_{24}} + \mathbf{II}}{5} - \mathbf{I}\mathbf{e}_{jk}\mathbf{e}_{jk} - (\mathbf{I}\mathbf{e}_{jk}\mathbf{e}_{jk})^{T_{23}} - (\mathbf{I}\mathbf{e}_{jk}\mathbf{e}_{jk})^{T_{24}} - (\mathbf{e}_{jk}\mathbf{I}\mathbf{e}_{jk})^{T_{34}}\right. \\ &\left. - \mathbf{e}_{jk}\mathbf{I}\mathbf{e}_{jk} - \mathbf{e}_{jk}\mathbf{e}_{jk}\mathbf{I} + 7\mathbf{e}_{jk}\mathbf{e}_{jk}\mathbf{e}_{jk}\mathbf{e}_{jk}\right]\end{aligned} \tag{3.81}$$

and the stresslet induced during reflection p on particle k by the stresslet signature of all the other particles at the previous reflection is:

$$\mathbf{P}^p_{k,2} = -\sum_{j\neq k}\frac{5a_j^3}{12d_{jk}^3}\left[(\mathbf{P}^{p-1}_{j,2}\cdot\mathbf{e}_{jk})\mathbf{e}_{jk} + \mathbf{e}_{jk}(\mathbf{P}^{p-1}_{j,2}\cdot\mathbf{e}_{jk}) + (\mathbf{P}^{p-1}_{j,2} : \mathbf{e}_{jk}\mathbf{e}_{jk})(\mathbf{I} - 5\mathbf{e}_{jk}\mathbf{e}_{jk})\right] + O(\varepsilon^5\,\mathbf{P}^{p-1}_{j,2}). \tag{3.82}$$

The results above provide an explicit approach to obtain the successive reflections for the hydrodynamic flow field and to truncate them to a required degree of approximation in ε. Note that the method is completely general and could be applied formally to any low-Re problem involving a suspension of spherical particles.

3.3.3 Chemical vs. hydrodynamic vs. chemo-hydrodynamic interactions

Performing successive reflections as described in the previous sections then provides a systematic framework to obtain the velocity and rotation rate $(\mathbf{U}_k, \mathbf{\Omega}_k)$ in terms of the position and orientation of the different particles $(\mathbf{R}_k, \mathbf{t}_k)$ in the form of a series of terms in increasing powers of $O(\varepsilon)$. Truncating to a particular degree of accuracy provides a computationally-efficient and asymptotically-consistent approach to determine the collective dynamics of N particles.

This convenient framework also provides a clear understanding of the different interactions routes between the particles, and an explicit way to analyse only certain components of the coupling. Formally, we show below that the particles' velocity includes four different contributions [142]:

1. *Self-propulsion velocity*: velocity of the isolated particle in an unbounded fluid (no chemical and no hydrodynamic reflections).

2. *Chemical interactions*: modification of the particle velocity resulting from the perturbation of its own surface chemical concentration by the presence of the other particles (i.e. chemical reflections with $r \geq 1$ in Sec. 3.3.1) but solving for its swimming velocity as if it was hydrodynamically-isolated (i.e. no hydrodynamic reflections). At the leading-order for first reflection of concentration field is a source dipole of strength $O(\varepsilon^2)$ (and hence propulsion velocity of $O(\varepsilon^2)$). Using equation (3.33) it can be shown that subsequent r reflections create source dipoles of strength $O(\varepsilon^{3r})$. Thus, the leading-order propulsion velocity resulting from gradients of field created after r chemical reflections is $O(\varepsilon^{3r+2})$.

3. *Hydrodynamic interactions*: modification of the particle velocity resulting from the hydrodynamic influence of the other particles (i.e. performing hydrodynamic reflections with $p \geq 1$ in Sec. 3.3.2.2) but neglecting any chemical influence of the other particles (i.e. no chemical reflections). The leading-order hydrodynamic field is a stresslet which creates a drift velocity of $O(\varepsilon^2)$. The strength of reflected stresslet is known from equation (3.80) to be $O(\varepsilon^{3p})$. Thus, after p hydrodynamic reflections, the propulsion velocity due to drift of particles from the resulting flow field is of $O(\varepsilon^{3p+2})$.

4. *Chemo-hydrodynamic interactions*: modification to the particle velocity resulting from the hydrodynamic influence of the particles (hydrodynamic reflections with $p \geq 1$) and forced by the modification in surface concentration distribution due to the presence of other particles (chemical reflections with $r \geq 1$). Since chemo-hydrodynamic interactions are a combination of effects from chemical and hydrodynamic effects, the propulsion velocity expected after p chemo-hydrodynamic reflections is also $O(\varepsilon^{3p+2})$.

In the present framework, it is therefore particularly easy to analyse the effect of one interaction route over another, by simply including or not any chemical and/or hydrodynamic reflections of order $r, p \geq 1$. It can be shown that by including the above mentioned interactions in p reflections, one can compute the propulsion velocities to an accuracy of $O(\varepsilon^{3p+2})$ (i.e. within an error of $O(\varepsilon^{3(p+1)})$).

It should also be noted that the classical view on phoretic particles' interactions is that of two distinct and independent routes, namely chemical and hydrodynamic couplings. While this dichotomy may be relevant for far-field (dilute) interactions which essentially are limited to two-particle interactions (i.e. the chemical or hydrodynamic influence of particle i on particle j's velocity), the present results emphasize that this does not hold in general and instead reveal the more intricate nature of the particles' coupling: in fact, a third coupling

occurs as a result of the dual influence of the chemical and hydrodynamic of particles on each other. This third route, termed here "chemo-hydrodynamic" interactions, is fundamentally a three-particle coupling as its simplest occurence involves the chemical influence of particle i on particle j's surface concentration, resulting in a modified flow field near particle k (note that particles i and k may be identical). As a result such interactions only arise at higher order of accuracy and are therefore sub-dominant in the far-field limit.

3.4 An ε^5-accurate framework for phoretic particles

In this section, we apply the previous formalism explicitly and systematically determine the particles' velocity and rotation rate resulting from the different interaction routes described in the previous section, up to an order of accuracy of ε^5, i.e. with the largest asymptotic errors for large distances scaling as $O(\varepsilon^6)$. This choice of truncature order is motivated by the inclusion at that order of the dominant 3-particle interactions (i.e. the interaction between two particles due to the presence of a third one) and chemo-hydrodynamic coupling. In principle however, the framework of Section 3.3 can be repeated to any number of reflections and hence, achieve any stated degree of accuracy.

3.4.1 Self-propulsion ($p = 0$)

The leading order contribution to the particles' velocities corresponds to the self-generated concentration gradients at its surface (i.e. self-propulsion). It is obtained by neglecting any chemical or hydrodynamic interaction with other particles. Hence, no reflection should be performed and using the results of Eqs. (3.57), the propulsion velocities are obtained as,

$$\mathbf{U}_k^{sp} = -\frac{2M_k}{3}\mathbf{C}_{k,1}^0 = -\frac{A_1 M_k}{3}\mathbf{t}_k \qquad \text{and} \quad \mathbf{\Omega}_k^0 = 0. \tag{3.83}$$

3.4.2 Chemical interactions between particles

As for self-propulsion, the hydrodynamic effect of other particles is neglected, hence no hydrodynamic reflections are performed. The chemical interactions correspond to the contributions in the surface concentration moments $\mathbf{C}_{k,1}^r$ with $r \geq 1$:

$$\mathbf{U}_k^{\chi} = -2M_k \sum_{r\geq 1} \mathbf{C}_{k,1}^r, \qquad \mathbf{\Omega}_k^{\chi} = 0, \tag{3.84}$$

and $\mathbf{C}_{k,r}^1$ with $r \geq 1$ are obtained using the recursive relations, Eq. (3.33). Chemical reflections with $r \geq 3$ (i.e. 4-particle interactions) do not contribute to the $O(\varepsilon^5)$ approximation of the velocity and are therefore ignored. The contribution to the chemical interaction velocity $\mathbf{U}_k^{\chi}$ can therefore be decomposed into two main groups whether (i) they involve the gradient of the concentration field near a given particle and created individually by all its neighbours (2-particle interactions, $r = 1$) or (ii) they involve the gradient near the particle of interest of the correction to the concentration field introduced by a second particle due to the presence of a third one (3-particle interactions, $r = 2$).

3.4.2.1 2-particle chemical interactions

We focus first on the contribution of $r = 1$ to Eq. (3.84), i.e. the concentration gradient created directly by other particles, which is obtained from Eq. (3.33). The induced velocity $\mathbf{U}_k^{\chi,r=1}$ is of order $O(\varepsilon^{s+2})$ where, $s \geq 0$ represents the s^{th} chemical mode. Hence, truncating terms smaller than ε^5,

$$\mathbf{C}_{k,1}^1 = \sum_{j\neq k} \left[C_{j,0}^0 \boldsymbol{\mathcal{F}}_{\boldsymbol{jk}}^{\boldsymbol{\chi}}(1,0) + \mathbf{C}_{j,1}^0 \cdot \boldsymbol{\mathcal{F}}_{\boldsymbol{jk}}^{\boldsymbol{\chi}}(1,1) + \mathbf{C}_{j,2}^0 : \boldsymbol{\mathcal{F}}_{\boldsymbol{jk}}^{\boldsymbol{\chi}}(1,2) + \mathbf{C}_{j,3}^0 \overset{3}{\odot} \boldsymbol{\mathcal{F}}_{\boldsymbol{jk}}^{\boldsymbol{\chi}}(1,3) \right]. \quad (3.85)$$

Using the expression for the transfer function $\boldsymbol{\mathcal{F}}_{\boldsymbol{jk}}^{\boldsymbol{\chi}}(q,s)$ provided in Eq. (3.33), the resulting chemical drift velocity is

$$\begin{aligned} \mathbf{U}_k^{\chi,r=1} = M_k \sum_{j\neq k} \Bigg[& \frac{a_j a_k C_{j,0}^0 \mathbf{e}_{jk}}{d_{jk}^2} + \frac{a_k a_j^2 (3\mathbf{e}_{jk}\mathbf{e}_{jk} - \mathbf{I}) \cdot \mathbf{C}_{j,1}^0}{d_{jk}^3} + \frac{a_k a_j^3}{d_{jk}^4} (\mathbf{C}_{j,2}^0 \cdot \mathbf{e}_{jk}) \cdot (5\mathbf{e}_{jk}\mathbf{e}_{jk} - 2\mathbf{I}) \\ & + \frac{a_k a_j^4}{d_{jk}^5} [\mathbf{C}_{j,3}^0 : (\mathbf{e}_{jk}\mathbf{e}_{jk})] \cdot (-3\mathbf{I} + 7\mathbf{e}_{jk}\mathbf{e}_{jk}) \Bigg], \end{aligned} \quad (3.86)$$

with $\mathbf{C}_{j,s}^0$ given in terms of the particles' orientation $\mathbf{t}_j$ in Eq. (3.40). One recognizes the successive contribution of the first four chemical singularities contributing to the signature of particle j (monopole $C_{j,0}^0$, dipole $\mathbf{C}_{j,1}^0$, quadrupole $\mathbf{C}_{j,2}^0$ and octopole $\mathbf{C}_{j,3}^0$) to the concentration gradient near particle k and its resulting chemical drift. Also note that the leading order term proportional to $C_{j,0}^0$ is the velocity obtained from the far-field model (Section 3.2).

3.4.2.2 3-particle chemical interactions

Proceeding now with the second reflection (3-particle interactions), we note that the concentration moments satisfy $\mathbf{C}_{j,q}^1 = O(\varepsilon^{q+1})$ (i.e. the velocity induced by 3-particle chemical interactions are $O(\varepsilon^{2q+s+3})$ with $q \geq 1$ and $s \geq 0$). This reflection is not necessary to be computed as one can determine the drift velocity of remaining particles from the gradients of the first reflected field at the center of each particle. Using the expression for the transfer function $\boldsymbol{\mathcal{F}}_{\boldsymbol{jk}}^{\boldsymbol{\chi}}(q,s)$ given in Eq. (3.33), the gradient of concentration $\mathbf{C}_{k,1}^2$ near particle k responsible for its chemical drift includes a single $O(\varepsilon^5)$-contribution, namely

$$\mathbf{C}_{k,1}^2 = \sum_{j\neq k} \mathbf{C}_{j,1}^1 \cdot \boldsymbol{\mathcal{F}}_{\boldsymbol{jk}}^{\boldsymbol{\chi}}(1,1) = \sum_{j\neq k} \sum_{l\neq j} C_{l,0}^0 \boldsymbol{\mathcal{F}}_{\boldsymbol{lj}}^{\boldsymbol{\chi}}(1,0) \cdot \boldsymbol{\mathcal{F}}_{\boldsymbol{jk}}^{\boldsymbol{\chi}}(1,1), \quad (3.87)$$

and the resulting 3-particle chemical interaction drift velocity of particle k is obtained as

$$\mathbf{U}_k^{\chi,r=2} = -M_k \sum_{l} \sum_{j\neq(k,l)} C_{l,0}^0 \frac{a_k a_j^3 a_l (3\mathbf{e}_{jk}\mathbf{e}_{jk} - \mathbf{I}) \cdot \mathbf{e}_{lj}}{2 d_{jl}^2 d_{jk}^3}. \quad (3.88)$$

Note that in the previous equation $l = k$ is possible, i.e. this also provides the interaction of particle k with itself due to the presence of a second particle j. The sole contribution to the 3-particle chemical interaction drift is therefore the gradient of concentration generated near particle k by the dipolar correction near particle j due to the source field (Figure 3.2). The total velocity induced through purely chemical reflections is hence obtained from Eq. (3.86) and Eq. (3.88).

$$\mathbf{U}_k^{\chi} = \mathbf{U}_k^{\chi,r=1} + \mathbf{U}_k^{\chi,r=2}. \quad (3.89)$$

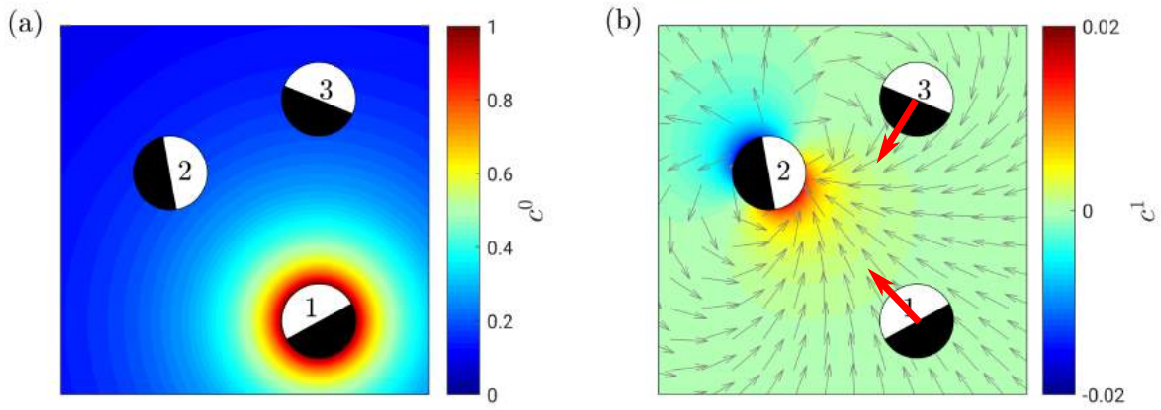

Figure 3.2: Illustration of 3-particle chemical interactions arising from a single reflection of the concentration field. The chemical source from particle 1 (left) induces a chemical dipole (right) at the surface of particle 2. In turn, this corrected field and its gradient (arrows) induce a drift of particles 1 and 3.

We further note from the considerations above that the leading 4-particle interactions ($r = 3$) would be at most $O(\varepsilon^8)$ and all such 4-particle interactions are therefore ignored here.

3.4.3 Drift from purely hydrodynamic interactions

We turn now to the hydrodynamic drift of particles arising from the flow fields created by their neighbours. For purely hydrodynamic interactions, the flow forcing applied by each particle on the surrounding fluid is that resulting from its own chemical signature (i.e. no chemical reflections): hydrodynamic reflections are thus initiated with Eqs. (3.57)–(3.58) using $\mathbf{C}^q_{k,0}$ defined in Eqs. (3.40), and recursive relations in Eqs. (4.29)–(3.72) are used to obtain the hydrodynamic drifts $\mathbf{U}^h_k$ and $\mathbf{\Omega}^h_k$:

$$\mathbf{U}^h_k = \sum_{p\geq 1} \mathbf{U}^p_k \quad \text{and,} \quad \mathbf{\Omega}^h_k = \sum_{p\geq 1} \mathbf{\Omega}^p_k \tag{3.90}$$

where $\mathbf{U}^p_k$ an $\mathbf{\Omega}^p_k$ are defined in Eqs. (4.29)–(4.30); the transfer functions are given in Appendix D.

3.4.3.1 2-particle hydrodynamic interactions

For 2-particle interactions ($p = 1$), the correction to propulsion velocity induced by a force multipole $\mathbf{P}^0_{j,s}$ of order s is $O(\varepsilon^s)$ for the translational velocity and of $O(\varepsilon^{s+1})$ for the angular velocity (with $s \geq 2$ in both cases). Similarly, the correction to propulsion velocity from a potential multipole $\mathbf{\Phi}^0_{j,s}$ of order s is $O(\varepsilon^{s+2})$ (with $s \geq 1$), and there are no rotlet multipoles in the signature of an isolated phoretic particle of uniform mobility ($\mathbf{X}^0_{j,s} = 0$). $\mathbf{\Phi}^0_{j,s}$ and $\mathbf{P}^0_{j,s}$ are $O(1)$ quantities, and using Eqs. (3.74)–(3.80), the drifts with $p = 1$ in Eq. (3.90)

are obtained by retaining terms that are $O(\varepsilon^5)$ or larger:

$$\begin{aligned}\mathbf{U}_k^{h,p=1} = \sum_{j\neq k}\Bigg[&\boldsymbol{\Phi}_{j,1}^0\cdot\boldsymbol{\mathcal{F}}_{\boldsymbol{jk}}^{\mathbf{1}}(1,1)+\boldsymbol{\Phi}_{j,2}^0:\boldsymbol{\mathcal{F}}_{\boldsymbol{jk}}^{\mathbf{1}}(1,2)+\mathbf{P}_{j,2}^0:\left(\boldsymbol{\mathcal{F}}_{\boldsymbol{jk}}^{\mathbf{3}}(1,2)+\frac{a_k^2}{6}\boldsymbol{\mathcal{F}}_{\boldsymbol{jk}}^{\mathbf{1}}(1,2)\right)\\&+\boldsymbol{\Phi}_{j,3}^0\overset{3}{\odot}\boldsymbol{\mathcal{F}}_{\boldsymbol{jk}}^{\mathbf{1}}(1,3)+\mathbf{P}_{j,3}^0\overset{3}{\odot}\left(\boldsymbol{\mathcal{F}}_{\boldsymbol{jk}}^{\mathbf{3}}(1,3)+\frac{a_k^2}{6}\boldsymbol{\mathcal{F}}_{\boldsymbol{jk}}^{\mathbf{1}}(1,3)\right)\\&+\mathbf{P}_{j,4}^0\overset{4}{\odot}\boldsymbol{\mathcal{F}}_{\boldsymbol{jk}}^{\mathbf{3}}(1,4)+\mathbf{P}_{j,5}^0\overset{s}{\odot}\boldsymbol{\mathcal{F}}_{\boldsymbol{jk}}^{\mathbf{3}}(1,5)\Bigg],\end{aligned}\tag{3.91}$$

$$\boldsymbol{\Omega}_k^{h,p=1} = -\frac{1}{2}\sum_{j\neq k}\left[\mathbf{P}_{j,2}^0:\boldsymbol{\mathcal{F}}_{\boldsymbol{jk}}^{\mathbf{2}}(1,2)+\mathbf{P}_{j,3}^0\overset{3}{\odot}\boldsymbol{\mathcal{F}}_{\boldsymbol{jk}}^{\mathbf{2}}(1,3)+\mathbf{P}_{j,4}^0\overset{3}{\odot}\boldsymbol{\mathcal{F}}_{\boldsymbol{jk}}^{\mathbf{2}}(1,4)\right].\tag{3.92}$$

As expected, only force multipoles contribute to the rotation of the particles (potential flows do not create any vorticity). The strength of the different multipoles in the previous equations are directly related to the multipoles of concentration using Eqs. (3.58) (e.g. $\Phi_{j,1}^0 = a_j^3 M_j \mathbf{C}_{j,1}^0/3$, $\mathbf{P}_{j,2}^0 = 6a_j^2 M_j \mathbf{C}_{j,2}^0$ and so on). Using the definition of the transfer functions provided in Appendix D, the ε^5-accurate 2-particle hydrodynamic interaction velocities are finally obtained as

$$\begin{aligned}\mathbf{U}_k^{h,p=1} = \sum_{j\neq k}\Bigg[&\frac{M_j a_j^3}{3d_{jk}^3}\mathbf{C}_{j,1}^0\cdot(\mathbf{I}-3\mathbf{e}_{jk}\mathbf{e}_{jk})+M_j(\mathbf{C}_{j,2}^0\cdot\mathbf{e}_{jk})\cdot\left(\frac{3a_j^2}{d_{jk}^2}\mathbf{e}_{jk}\mathbf{e}_{jk}+\frac{a_j^2(a_j^2+a_k^2)}{d_{jk}^4}(2\mathbf{I}-5\mathbf{e}_{jk}\mathbf{e}_{jk})\right)\\&+M_j(\mathbf{C}_{j,3}^0:\mathbf{e}_{jk}\mathbf{e}_{jk})\cdot\left(-\frac{3a_j^3}{2d_{jk}^3}(\mathbf{I}-5\mathbf{e}_{jk}\mathbf{e}_{jk})+\frac{a_j^3(3a_j^2+5a_k^2)}{d_{jk}^5}(3\mathbf{I}-7\mathbf{e}_{jk}\mathbf{e}_{jk})\right)\\&-\frac{3a_j^4M_j}{d_{jk}^4}(\mathbf{C}_{j,4}^0\overset{3}{\odot}\mathbf{e}_{jk}\mathbf{e}_{jk}\mathbf{e}_{jk})\cdot(\mathbf{I}+4\mathbf{e}_{jk}\mathbf{e}_{jk})-\frac{15a_j^5M_j}{2d_{jk}^5}(\mathbf{C}_{j,5}^0\overset{4}{\odot}\mathbf{e}_{jk}\mathbf{e}_{jk}\mathbf{e}_{jk}\mathbf{e}_{jk})\cdot(\mathbf{I}-3\mathbf{e}_{jk}\mathbf{e}_{jk})\Bigg],\end{aligned}\tag{3.93}$$

$$\begin{aligned}\boldsymbol{\Omega}_k^{h,p=1} = \sum_{j\neq k}\Bigg[&\frac{3a_j^2M_j}{d_{jk}^3}\Big(\mathbf{e}_{jk}\times[\mathbf{C}_{j,2}^0\cdot\mathbf{e}_{jk}]\Big)-\sum_{j\neq k}\frac{15a_j^3M_j}{2d_{jk}^4}\Big(\mathbf{e}_{jk}\times[\mathbf{C}_{j,3}^0:\mathbf{e}_{jk}\mathbf{e}_{jk}]\Big)\\&-\frac{14a_j^4M_j}{d_{jk}^5}\Big(\mathbf{e}_{jk}\times[\mathbf{C}_{j,4}^0\overset{3}{\odot}\mathbf{e}_{jk}\mathbf{e}_{jk}\mathbf{e}_{jk}]\Big)\Bigg].\end{aligned}\tag{3.94}$$

3.4.3.2 3-particle hydrodynamic interactions

The slowest decaying transfer function listed in Eqs. (3.74)–(3.80) corresponds to the stresslet induced by a stresslet on another particle (equivalent to the transfer function $\boldsymbol{\mathcal{F}}^{\boldsymbol{P}\rightarrow\boldsymbol{P}}{}_{lj}(2,2)$) at the previous reflection and scales as ε^3. The slowest-decaying 3-particle interaction therefore corresponds to the hydrodynamic drift of particle k associated with the stresslet induced by particle j after reflection of the flow field generated by the stresslet of particle l (Figure 3.3), and its dominant contribution scales as ε^5:

$$\mathbf{U}_k^{h,p=2} = \mathbf{P}_{j,2}^1:\boldsymbol{\mathcal{F}}_{\boldsymbol{jk}}^{\mathbf{3}}(1,2) = \sum_{l\neq j}(\mathbf{P}_{l,2}^0:\boldsymbol{\mathcal{F}}^{\boldsymbol{P}\rightarrow\boldsymbol{P}}{}_{lj}(2,2)):\boldsymbol{\mathcal{F}}_{\boldsymbol{jk}}^{\mathbf{3}}(1,2),\tag{3.95}$$

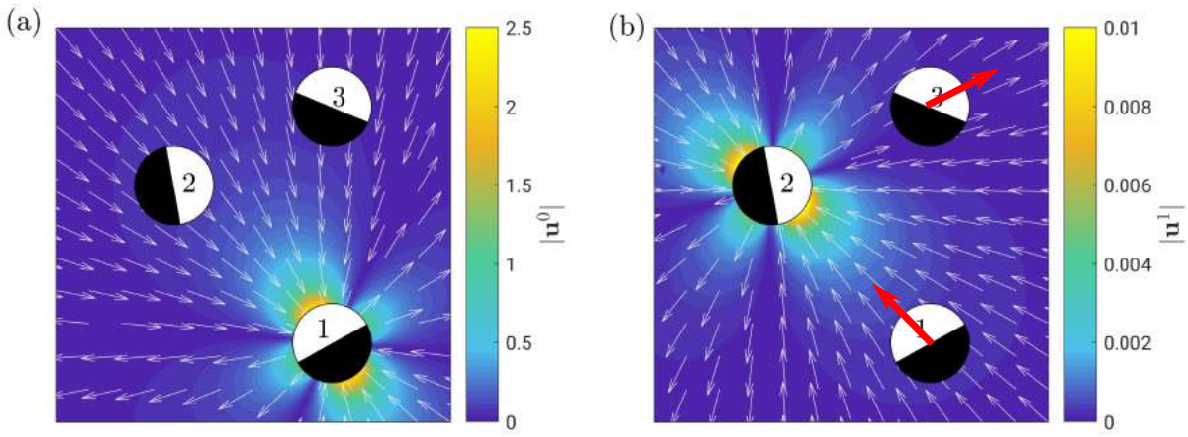

Figure 3.3: Illustration of 3-particle hydrodynamic interactions resulting from a single hydrodynamic reflection: The stresslet induced by the self-propulsion of particle 1 (a) induces a reflected stresslet at particle 2 (b). In turn, this modifies the hydrodynamic environment of particle 1 and 3 and induces their hydrodynamic drift (red arrow). The velocity magnitude (color) and direction (white arrow) are shown. Note that a rotation is also induced but scales as $O(\varepsilon^6)$ and is neglected here.

Knowing $\boldsymbol{\mathcal{F}}^{\boldsymbol{P}\to\boldsymbol{P}}{}_{lj}(2,2)$ from equation 3.82 and remembering $\mathbf{P}^0_{l,2} = 6a_l^2 M_l \mathbf{C}^0_{l,2}$

$$\mathbf{U}_k^{h,p=2} = -\sum_l \sum_{j\neq(k,l)} \frac{5a_j^3 a_l^2 M_l}{2d_{lj}^3 d_{jk}^2}\Big[2(\mathbf{e}_{jk}\cdot\mathbf{C}^0_{l,2}\cdot\mathbf{e}_{lj})(\mathbf{e}_{jk}\cdot\mathbf{e}_{lj}) + (\mathbf{e}_{lj}\cdot\mathbf{C}^0_{l,2}\cdot\mathbf{e}_{lj})(1-5(\mathbf{e}_{lj}\cdot\mathbf{e}_{jk})^2)\Big]\mathbf{e}_{jk}. \tag{3.96}$$

An illustration of the drift created by this 3 particle hydrodynamic interaction is shown in figure 3.3. The induced rotation from 3-particle hydrodynamic interactions scales as $O(\varepsilon^6)$ and is therefore ignored here. Indeed, rotational effects of the stresslet $\mathbf{P}^1_{j,2}$ considered above is $O(\varepsilon^6)$. The only other singularity that can contribute to Ω_k^2, namely the rotlet dipole $\mathbf{X}^1_{j,2}$, has an $O(\varepsilon^3)$ intensity (see Eqs. (3.74)–(3.80)) and the associated rotation rate is therefore $O(\varepsilon^7)$.

3.4.4 Drift from chemo-hydrodynamic interactions

A third type of interactions arise when accounting for reflections both in the hydrodynamic and chemical problems between at least 3 particles. These are *chemo-hydrodynamic interactions*, which are the hydrodynamic drifts generated by a given particle on its neighbors as a result of their chemical signature. Such interactions are completely absent in the far-field model (Section 3.2) as these frameworks solely focused on pairwise and direct interactions of particles. They also correspond to higher-order corrections of the particles' velocity and therefore become particularly important in not-so-dilute regimes. In the following, we show that the leading-order chemo-hydrodynamic interactions is $O(\varepsilon^5)$.

From a practical point of view, hydrodynamic reflections are initiated with Eqs. (3.57)–(3.58) using $\mathbf{C}^{r\geq 1}_{k,q}$ (chemical reflections), and recursive relations in Eqs. (4.29)–(3.72) are used to obtain the hydrodynamic drifts $\mathbf{U}_k^{\chi h}$ and $\mathbf{\Omega}_k^{\chi h}$. The dominant such contribution involves three particles (one chemical reflection, $r = 1$, and one hydrodynamic reflection, $p = 1$. A force multipole of order $q \geq 2$, $\mathbf{P}^0_{j,q}$, generated by the reflected $O(\varepsilon^{q+1})$ concentration multipole $\mathbf{C}^1_{j,q}$, Eq. (3.58), results in a $O(\varepsilon^{2q+1})$ drift velocity $\mathbf{U}_k^{\chi h}$ on a third particle.

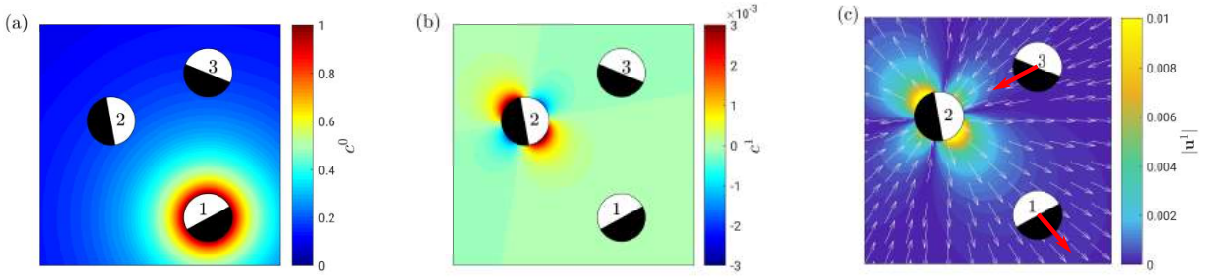

Figure 3.4: Illustration of one of the dominant chemo-hydrodynamic interactions resulting from a single reflection of the concentration field: (a) the chemical source from particle 1 induces a quadrupolar correction of the concentration field near particle 2 (b). This source quadrupole induces a hydrodynamic stresslet (c) which is responsible for the drift of particles 1 and 3 (red arrows). In (a) and (b), the concentration fields are shown, while (c) shows the velocity magnitude (color) and direction (white arrows).

Similarly, a potential multipole of order $q \geq 1$, $\mathbf{\Phi}^0_{j,q}$, generated by the $O(\varepsilon^{q+1})$ reflected concentration multipole $\mathbf{C}^1_{j,q}$, Eq. (3.58), results in a $O(\varepsilon^{2q+3})$ drift velocity $\mathbf{U}^{\chi h}_k$. The two dominant interactions, which scale as $O(\varepsilon^5)$, therefore correspond to (i) the drift on particle k induced by the potential dipole of particle j created by the chemical dipole of particle l, and (ii) the drift on particle k induced by the stresslet of particle j resulting from the chemical quadrupole of particle l (Figure 3.4), all other interactions being subdominant. Using Eqs. (4.29), (3.69), (3.57) and (3.58), the dominant chemo-hydrodynamic drift is obtained as

$$\mathbf{U}^{\chi h}_k = \sum_{j\neq k}\left[\mathbf{\Phi}^0_{j,1}\cdot\boldsymbol{\mathcal{F}}^{\mathbf{1}}_{\boldsymbol{jk}}(1,1) + \mathbf{P}^0_{j,2} : \boldsymbol{\mathcal{F}}^{\mathbf{3}}_{\boldsymbol{jk}}(1,2)\right], \qquad \text{with } \mathbf{\Phi}^0_{j,1} = M_j a_j^3 \mathbf{C}^1_{j,1}, \qquad \mathbf{P}^0_{j,2} = 15 M_j a_j^2 \mathbf{C}^1_{j,2}. \tag{3.97}$$

which is finally obtained explicitly using Eq. (3.33)

$$\mathbf{U}^{\chi h}_k = \sum_l \sum_{j\neq(l,k)} M_j C^0_{l,0}\left[\frac{a_l a_j^4}{2d_{jk}^3 d_{lj}^2}\mathbf{e}_{lj}\cdot[3(\mathbf{e}_{jk}\cdot\mathbf{e}_{lj})\mathbf{e}_{jk} - \mathbf{e}_{lj}] + \frac{5a_l a_j^4}{2d_{jk}^2 d_{lj}^3}[3(\mathbf{e}_{lj}\cdot\mathbf{e}_{jk})^2 - 1]\mathbf{e}_{jk}\right]. \tag{3.98}$$

It should be noted that any rotation induced by 3-particle chemo-hydrodynamic interactions is at most $O(\varepsilon^6)$ and is therefore ignored.

Assembling the contributions to the interactions velocities provided in Eqs. (3.83) (self-propulsion), Eqs. (3.86) and (3.88) (purely chemical interactions), Eqs. (3.93), (3.94) and (3.96) (purely hydrodynamic interations and Eq. (3.98) (chemo-hydrodynamic interactions) provide a consistent asymptotic approximation of the particles' dynamics with a ε^5 accuracy. It should be noted that a similar approach can be used to obtain velocities with a prescribed arbitrary accuracy of ε^n with $n \geq 6$.

3.5 Examples of dynamics of multiple Janus particles

In this section, the ε^5-accurate framework based on the Method of Reflections proposed in the previous section (thereafter referred to as MoR) is used to compute the dynamics of multiple active Janus particles, and its predictions are compared with the exact solution of the full interaction problem (obtained either analytically or numerically depending on the problem's symmetries) and simple far-field approximations (Section 3.2). This provides both a validatation of these results as well as the opportunity to analyze the accuracy gained in the description of the collective dynamics by accounting for higher-order interactions (in particular, 3-particle and chemo-hydrodynamic interactions).

Note that the present framework, in its long-range asymptotic formulation, is expected to be particularly accurate for large particle distances but does not include intrinsically a description of the lubrication interactions of particles. Further, phoretic interactions may be attractive in the near-range [171]. To prevent particles' overlapping each other, steric repulsion is accounted for by implementing an additional repulsive velocity between any pair of particles (j, k),

$$\mathbf{u}_{jk}^{\text{rep}} = -A\left[1 - \tanh\left(\frac{d_{c_{jk}}}{\delta_{\text{rep}}}\right)\right], \tag{3.99}$$

with $d_{c_{jk}} = d_{jk} - a_j - a_k$ the contact distance between particles j and k. In the following, we use $A = 35$ and $\delta_{\text{rep}} = 0.04$, so that this repulsion velocity is sufficient to prevent the particles' overlap but is only significant when the particles' surfaces are distant by less than about a tenth of their radii [138].

3.5.1 Axisymmmetric relative translation of two Janus particles

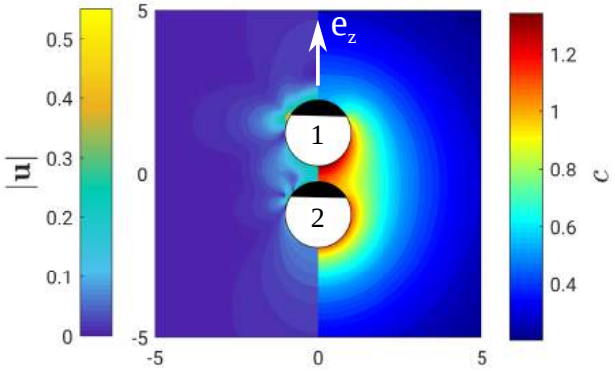

Figure 3.5: Interactions of two aligned Janus particles: (left) flow velocity magnitude obtained using BEM and (right) concentration field obtained analytically (Appendix A). Both Janus particles have positive mobility ($M = 1$) and equal unit radius, with 3/4th of their surface releasing solute at a fixed rate ($A = 1$, white region) while the rest of their surface is inert ($A = 0$, black region). The particles have a contact distance $d_c = d - 2 = 0.5$, and swim toward their inert cap when isolated (i.e. along $+\mathbf{e}_z$).

We first consider the case of two Janus particles arranged axisymmetrically, both aligned in the same direction as shown in Figure 3.5. Both particles have unit radius ($a = 1$) and uniform and positive mobility ($M = 1$); 3/4-th of their surface is active ($A = 1$), the rest being inert ($A = 0$). In isolation, each particle would hence swim with a velocity $\mathbf{U}^{\text{self}} = 3/16\ \mathbf{e}_z$. A 3/4-th active Janus is chosen here so as to test the framework with the

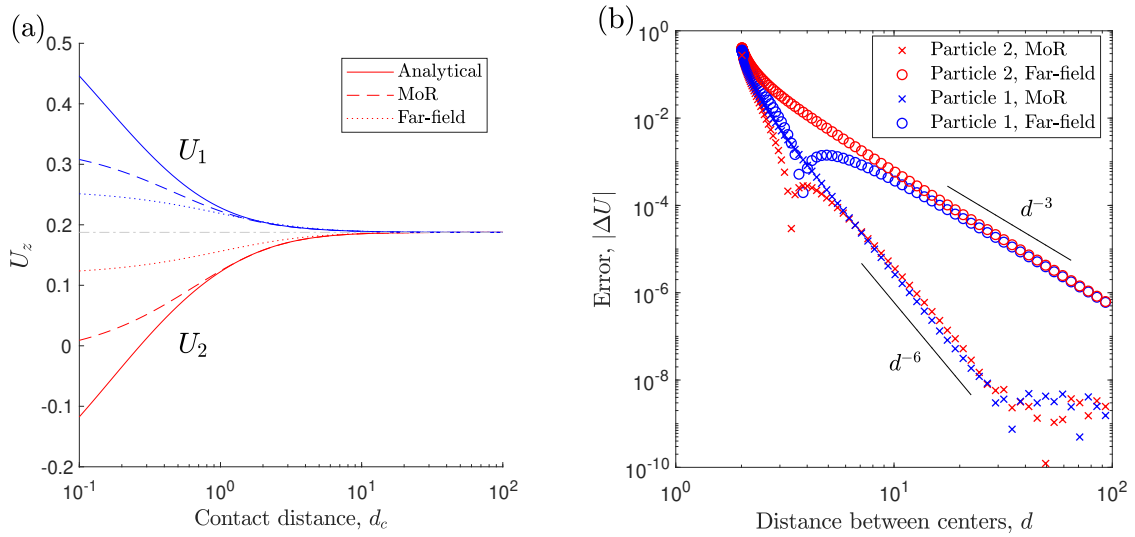

Figure 3.6: Translation of two aligned Janus particles (see Figure 3.5): (a) Swimming velocities of particle 1 (blue) and particle 2 (red) as a function of their contact distance $d_c = d - 2$, as obtained analytically (solid) or using MoR (dashed) or far-field models (dotted). The reference self-propulsion velocity of an isolated particle, $U^{\text{self}} = 0.1875$ is also shown (dot-dashed). (b) Error magnitude $|\Delta U|$ in the velocity prediction of far-field and MoR models with respect to the analytical solution.

most generic chemical and hydrodynamic reflections computed in Section 3.4 (hemispheric Janus particles of uniform mobility have no intrinsic stresslet).

In this highly-symmetric setting, the chemical and hydrodynamic fields as well as the particles' velocities can be obtained analytically for an arbitrary distance using bispherical coordinates [61, 138] (Appendix A). The resulting flow and concentration fields are reported on Figure 3.5. In the gap between the particles, the diffusion of the solute emitted from particle 1's active cap is limited by the confining effect of particle 2's proximity, leading to increased levels of concentration and modified slip velocity at the particles' surface in this region. The resulting hydrodynamic field is further modified by lubrication effects at close contact.

Due to this confinement-induced modification of the concentration field, the contrast between the front and back of the leading particle 1 is enhanced, while it is reduced for the trailing particle 2, leading to an increased velocity of the former and a reduced velocity for the latter (see Figure 3.6). In fact, the trailing particle is brought to rest at contact distance $d_c = 0.27$, and further reduction in contact distance leads to reversal in its swimming direction. Moreover, since $U_2 \leq U_1$ for all d_c, particles drift away from each other.

As seen in Figure 3.6, the reduction (resp. enhancement) of the velocity of the trailing particle (resp. leading particle) is captured by the far-field and MoR models. Moreover, both underestimate the velocity of particle 1 and overestimate that of particle 2 when the particles are close ($d_c < 1$). The propulsion velocity predicted using only far-field model deviate from analytical solution below contact distances of a few radii while that predicted using MoR provides a good estimate even for contact distances slightly smaller than a particle radius. Asymptotically, when $\varepsilon = 1/d \ll 1$, the expected error scalings are observed, i.e. $O(\varepsilon^3)$ for the far-field approximation and $O(\varepsilon^6)$ for the MoR model (Figure 3.6b).

The previous considerations focused on instantaneous velocity predictions (for a fixed geometry). We now evaluate the far-field and MoR models performance in predicting the

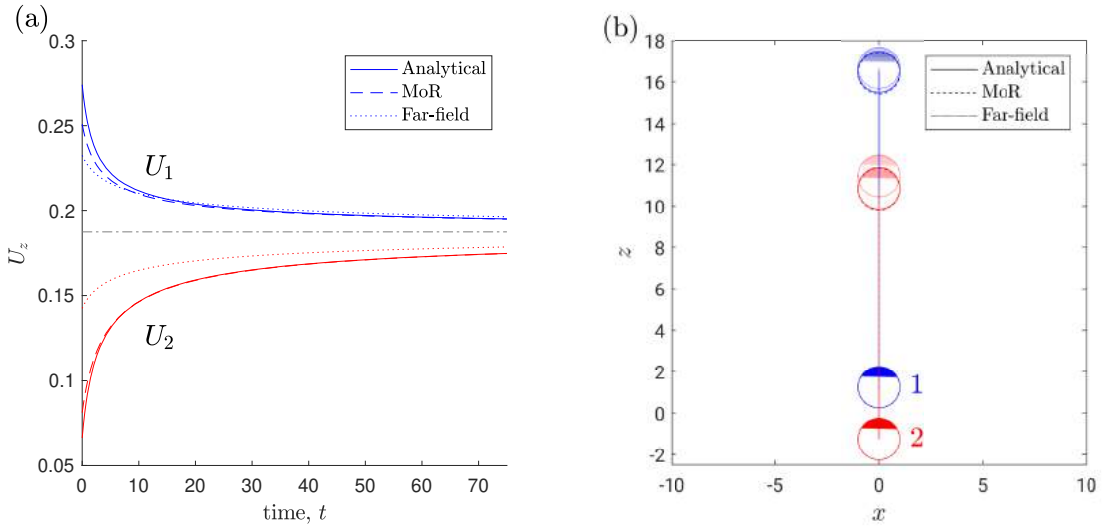

Figure 3.7: Translation of two aligned Janus particles (see Figure 3.5): (a) Evolution in time of the particles' velocity for an initial separation distance $d_c = 0.5$. The predictions for MoR and far-field modes are computed at the relative positions described analytically. (b) Trajectories of the particles. Positions of particles at $t = 0$ and $t = 75$ are shown.

long-term dynamics of two particles initially positioned at $d_c = 0.5$ (Figure 3.7). The particles swim in the same direction but drift apart as $U_1 > U_2$. As time progresses, their relative influence and resulting relative drift reduces, and both particles approach their self-propulsion velocity asymptotically (Figure 3.7a). Even for small separation (e.g. $d_c = 0.5$), MoR-predicted propulsion velocities have a good accuracy (the error for particle 2 when $d_c = 0.5$ is $\left|\frac{U_2^{\text{mor}} - U_2^{\text{analytical}}}{U_2^{\text{self}} - U_2^{\text{analytical}}}\right| \times 100 \approx 15\%$), while errors introduced by the far-field model are large ($\approx 60\%$). The cumulated error in position over time (when the particles are far away from each other) is essentially negligible for MoR, while it is of the order of the particle radius for the far-field model (Figure 3.7b).

3.5.2 Co-planar translation and rotation of 2 Janus particles

We next focus on the coplanar and non-axisymmetric motion of two Janus particles. In contrast with the previous highly-symmetric situation, a critical element for the prediction of the particles' trajectory lies in the correct estimation of their rotation velocities (which arise from interactions with their neighbours as particles with homogeneous mobility do not rotate when isolated). The axisymmetry of a pair of Janus particles is lost as soon as they are not aligned with their relative position, and while a solution in bispherical coordinates remains available in principle, it becomes rapidly cumbersome [172]. Instead, the particles' velocities are obtained here numerically using the regularized Boundary Element Methods framework for phoretic particles (regBEM), a versatile numerical technique developed by Montenegro-Johnson *et. al.* [137, 138].

The long-term dynamics of a pair of Janus particles is considered, which are initially aligned along $\mathbf{e}_x$, i.e. orthogonally to their relative distance which is along $\mathbf{e}_z$ (Figure 3.8). The particles have uniform mobility $M = 1$ and hemispherical activity distribution. When isolated, these particles swim with a velocity $\mathbf{U}^{\text{self}} = \mathbf{e}_x/4$ and are neutral squirmers (i.e. $A_2 = 0$, no stresslet signature).

In such an arrangement, the particle pair attract and contact in finite time [172], which is

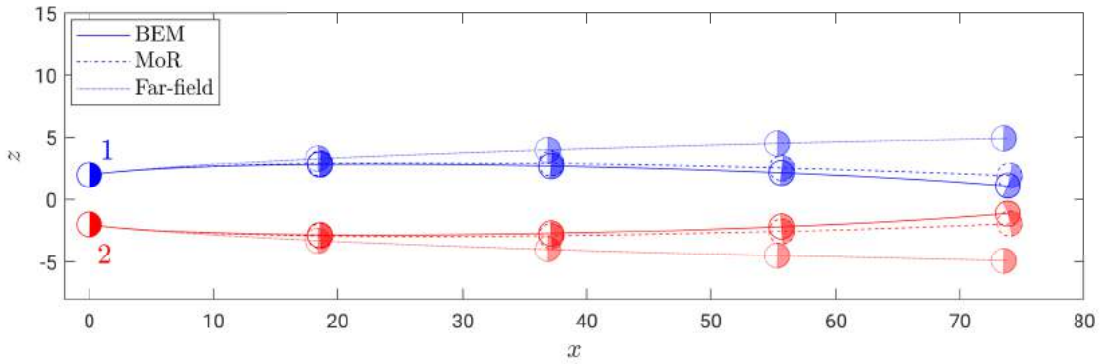

Figure 3.8: Co-planar trajectories of two Janus particles obtained using BEM (solid), MoR (dashed) and far-field (dotted). The particles' center-to-center distance is initially $d = 4a$. Particles have uniform mobility $M = 1$ and hemispherical activity with $A = 1$ on their active half (black) and $A = 0$ on their inert cap (white). Particle locations and their orientations as obtained from BEM simulations are also shown at equal intervals of time. Note that y-axis is directed into the plane of the paper.

indeed observed in the trajectories obtained from BEM simulations (see figure 3.8), where the particles, exhibiting mirror symmetrical motion, first drift apart while rotating to swim toward each other at a later stage. The initial drift of the particles away from each other is easily understood by their anti-chemotactic nature: they drift and swim down the concentration gradient created by the other particle. Their rotation solely results from hydrodynamic and chemo-hydrodynamic interactions since purely chemical interaction cannot induce rotation (for uniform mobility).

Instantaneous translational and angular velocities of particle 1 are shown in Figure 3.9. The particles' interaction results in a slight increase of their propulsion velocities (but only by a few percent). Particle 1 monotonically rotates clockwise, with a sharp increase in angular velocity arising before the particles contact. Once the particles form a cluster, they adopt a fixed tilted orientation that balances chemical, hydrodynamic and chemo-hydrodynamic interactions as well as steric repulsion; a steady co-propulsion velocity is achieved in this case.

The far-field model predicts the translational velocities reasonably well when the particles are a few radii apart but deviates strongly towards the final stages of clustering (when $d_c < 1$). It however does not predict any rotation as a result of the absence of a self-generated stresslet and resulting hydrodynamic interactions for a hemispheric Janus particle of uniform mobility. It should be emphasized here that even if the particles were to have non-zero intrinsic stresslets (e.g. for non-hemispheric coverage), the angular velocities predicted using the far-field model would still be zero in this highly-symmetric setting: this is the result of the stresslet flow-field produced by each Janus particle having a plane of symmetry passing through the center of the other particle, which creates no effective shear-induced rotation. Thus, in this configuration, the force-quadrupole is the leading order term responsible for the particles' reorientation. As a result, the far-field model, limited to only a force dipole, is unable to capture the qualitative trajectory (see figure 3.8), in particular to obtain the long-term dynamics. On the other hand, Figure 3.9 demonstrates that the MoR model provides very accurate estimates of the translation velocities throughout the dynamics; the predicted angular velocities, accurate to $O(\varepsilon^5)$ are adequate, except for close contact where higher order corrections are necessary to fully capture lubrication effects.

Thus, it is clearly seen from figure 3.8 that the trajectories predicted by MoR are much more accurate than far-field models both quantitatively and qualitatively. MoR further provides

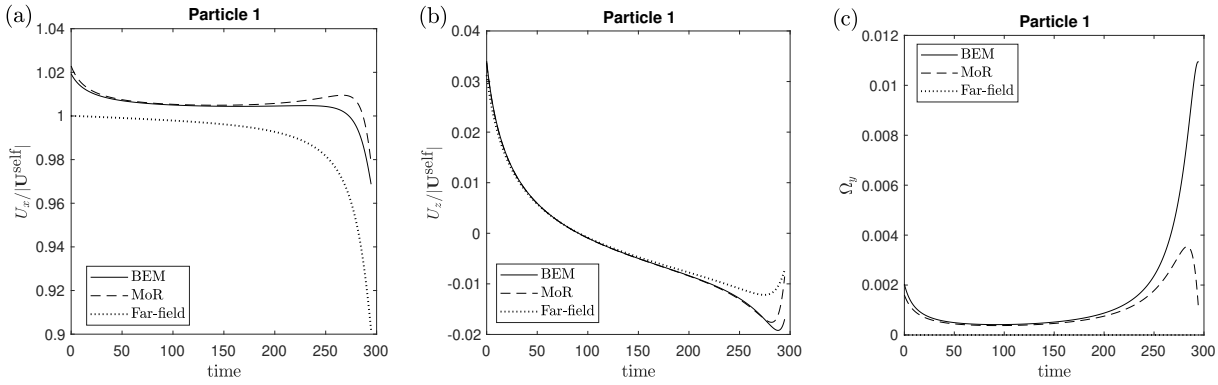

Figure 3.9: (a) Horizontal, (b) vertical and (c) rotation velocity of Janus particle 1 for two coplanar particles (see Fig 3.8), as obtained from BEM (solid), MoR(dashed) and the far-field model. At each time, the comparison between the prediction of the different models is performed for the same geometric configuration of the particles (i.e. that obtained from BEM simulations). The translation velocity is scaled by the self-propulsion velocity of an isolated Janus particle. Note that there is no angular velocity in the far-field model for all separations. The corresponding velocities of particle 2 are obtained using the planar symmetry of the problem with respect to $z = 0$.

a good compromise between accuracy and computational performance: while BEM simulations took about 6 hours of computational time, the simulation using MoR approximation was performed in milliseconds and still captured the dynamics within an error of a particle radius.

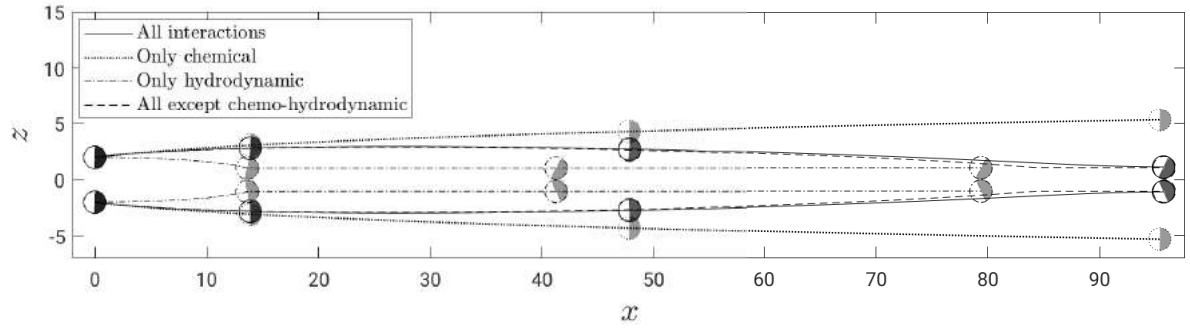

Figure 3.10: Comparison of the effects of the different interactions on the trajectory of 2 co-planar particles using the ε^5-accurate MoR model. The trajectories obtained with all interactions (solid), purely chemical interactions only (dotted), purely hydrodynamic interaction only (dash-dotted) and chemical and hydrodynamic interactions (i.e. without chemo-hydrodynamic interactions, dashed) are shown. Particles' location and their orientation at various instances of time are shown graphically.

Additionally, MoR clearly distinguishes chemical, hydrodynamic and chemo-hydrodynamic interactions, thus allowing us to analyse their relative and respective role in the particles' coupling by simply including or removing the appropriate interactions (Figure 3.10). This conclusively shows that the chemical interactions are predominantly responsible for the lateral drift. As expected, purely chemical interactions do not induce any particle reorientation and the particles drift apart laterally down the chemical gradient created by their neighbor. Hydrodynamic interactions, on the other hand, do no create any significant lateral drift but play a crucial role in reorienting the self-propelling particles toward each other, thus inducing their clustering. Chemo-hydrodynamic interactions, in the present case, are effectively

repulsive but, their sharp asymptotic decay $O(\varepsilon^5)$ makes them almost non-influential in the long-term dynamics here. It is thus the competing chemical and hydrodynamic interactions that primarily gives rise to the unusual dynamics in this particular case.

3.5.3 Dynamics of randomly-arranged co-planar particles

In this section, we test the ability of the $O(\varepsilon^5)$-accurate MoR model to predict the dynamics of a larger number of particles ($N > 2$). For simplicity of analysis and visualization, we consider here a system of 5 Janus particles initially distributed randomly in a plane (see figure 3.11), in relatively close proximity (average contact distances of the order of a few radii) . Due to the small density of particles, we restrict the choice of their random initial orientations along the plane to only within a quadrant to favour their interactions as would be expected in denser situations (i.e. with more particles). The exact dynamics are first obtained using BEM simulations and then compared with the MoR and far-field models (figure 3.11). Using a coarse mesh, BEM simulations required around 12 hrs of computational time while MoR results were obtained in 5 seconds.

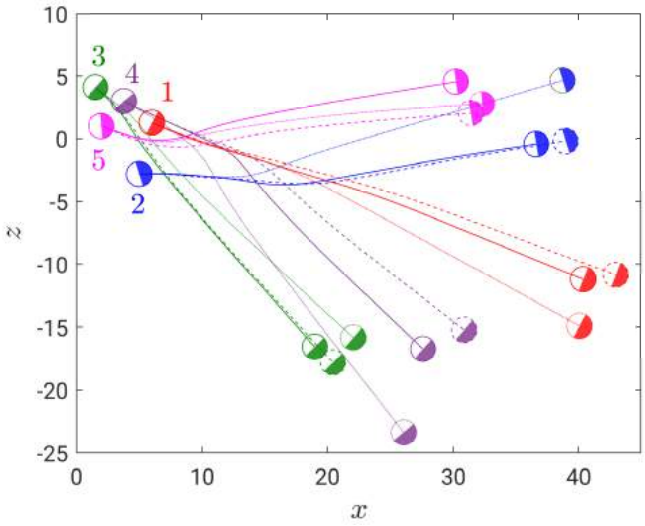

Figure 3.11: Comparison of the trajectories of 5 Janus particles predicted by BEM (solid), MoR (dashed) and far-field models (dotted). The initial positions (at $t = 0$) of the numbered particles and their predicted positions at $t = 117$ are shown as well. Note that y-axis is directed into the plane of the paper.

Each particle self-propels along a straight line when isolated. Any slight change of their orientation has a drastic effect on their long-term positions. Yet, Figure 3.11 shows that the MoR $O(\varepsilon^5)$-accurate model is sufficient for estimating these long-term trajectories to a reasonable accuracy and performs significantly better in that regard than the simpler far-field model. Note that the particles do not come in contact at any point in time.

Focusing on the instantaneous dynamics of particles 2 and 5, the MoR model is seen to capture the qualitative trend of the velocities much more accurately than the far-field model (Figure 3.12). Quantitatively, the magnitudes and the errors in estimation of the translational velocities by MoR model are quite comparable with far-field model. Hence, the net displacement of the particles are of the same orders. However, the major advantage of the MoR model over far-field models lies is in its ability to account accurately for the particles' reorientation. Indeed, far-field models are unable to produce any change in orientation as chemical interactions do not produce any rotational effects.

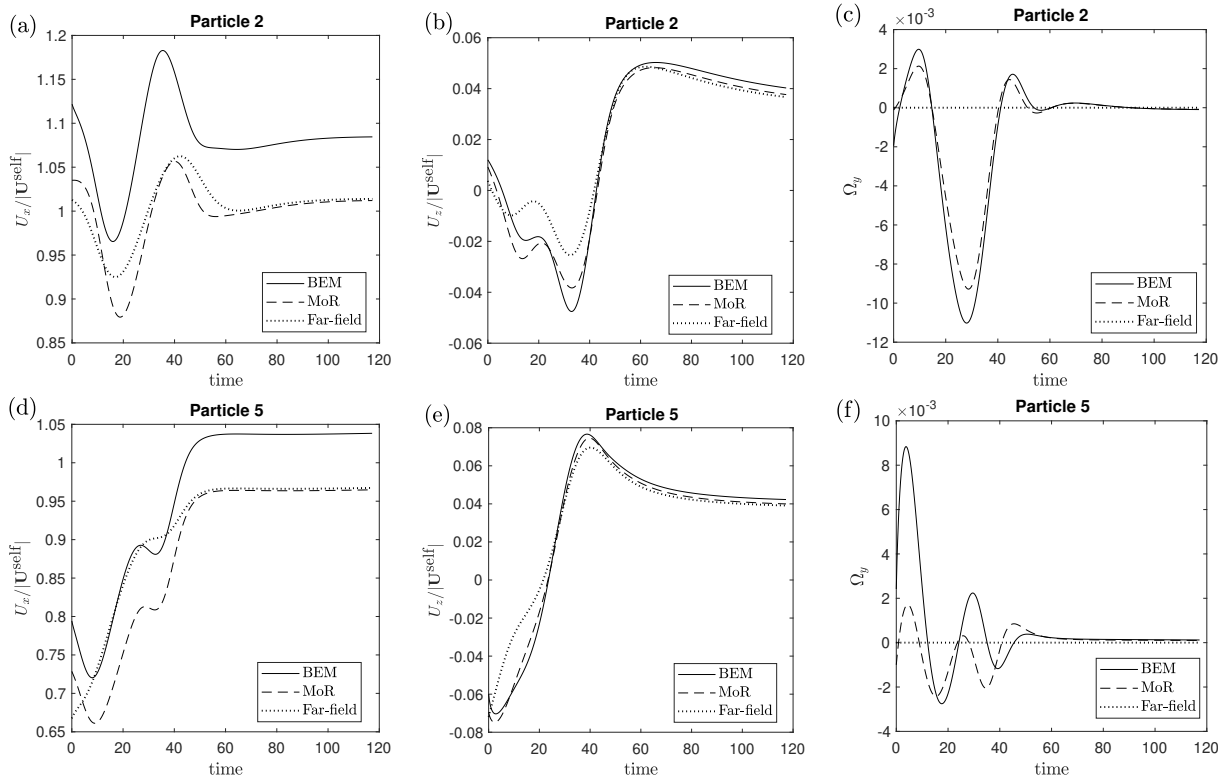

Figure 3.12: Evolution of the particles' velocities during the planar interactions of five Janus particles (Figure 3.11): (a,d) Horizontal, (b,e) vertical and (c,f) rotation velocties of particles 2 (top) and 5 (bottom) predicted by BEM (solid), MoR(dashed) and far-field models. The same particles' positions (obtained from the BEM simulations) are considered for all three models.

MoR model correctly predicts the transient peak in angular velocity and captures the dynamics generated by its hydrodynamic interaction with other particles (Figures 3.11 and 3.12). This is much less the case for particle 5, for which the prediction of MoR for its angular velocity, while qualitatively correct, exhibits large errors that can be attributed to strong lubrication effects from close contact with neighbouring particles (especially particles 3 and 4). For this particle, although the oscillatory trend in angular velocity is reproduced by MoR, the performance in terms of position predictions is significantly reduced.

3.6 Conclusions

In this work, we propose a general framework based on the method of reflections (MoR) to systematically determine the velocities of interacting autophoretic particles up to any order of accuracy in the particle density, under the combined influence of their chemical and hydrodynamic signatures on their environment. The explicit implementation of this framework with an ε^5-accuracy demonstrated its ability to capture not only the instantaneous velocity but also essential features of the long-term dynamics of phoretic particles. The performance of the predictions are significantly better, qualitatively and quantitatively, than classical far-field models which can be seen as ε^2-truncations of the present framework. Such far-field models are widely used due to their simplicity [122, 125, 124]; yet, as they focus solely on pairwise particle interactions through the slowest-decaying hydrodynamic and chemi-

cal signatures, they fundamentally overlook more complex chemo-hydrodynamic interaction routes as well as many-body interactions. The analysis presented here demonstrate that these models become fundamentally inaccurate in not-so-dilute suspensions where particles are separated by a few radii or less. In contrast, the MoR model proposed here is observed to correctly predict the particles' velocities with a comparable computational cost, even when the particles have contact distances of the order of a single particle radius. Further, it is able to capture quantitatively the reorientation of the self-propelled particles, an element that is critical to predict and understand their long-term trajectories and interactions. As such, the MoR model offers a promising alternative to far-field models in order to analyse dynamics of suspensions that are not asymptotically dilute. These predictions are furthermore obtained at a computational cost that is orders of magnitude smaller than a direct numerical simulation using classical approaches such as Boundary Elements or Immersed Boundary Methods.

The complete analytical framework was presented as well as a practical application to $O(\varepsilon^5)$ accuracy for particles of uniform mobility. Yet, it could easily be extended to obtain more precise estimates, by identifying which combination of reflections (both for the Laplace and Stokes problems) lead to interactions of greater asymptotic order than the requested accuracy. The chosen accuracy is motivated here as the smallest order at which 3-particle interactions become significant and combine both chemical and hydrodynamic coupling, in contrast with far-field models that simply superimpose pairwise interactions that involve solely chemical or hydrodynamic effects. The uniformity of the particles' mobility significantly simplifies the final expression of the interaction velocities as there is a direct mapping between the concentration multipole intensities and the velocity field singularities used for initializing the hydrodynamic reflections. Yet the entire framework presented here is directly applicable to particles of arbitrary mobility distribution, provided this initialization step is modified by adding a tensorial reduction process as discussed in Section 3.3.2.2.

Besides its rapid convergence, the MoR method is also surprisingly accurate as it is able to capture many of the particles' dynamics and predict their velocity even for inter-particle contact distances of the order of their radius.

The presentation of the framework followed here, for simplicity, is that of a *parallel* implementation of the method of reflections [173], i.e. a Jacobi-type iteration where corrections near a given particle are based on the information from all the other particles at the previous iteration. An alternative approach is the historical *sequential* approach [168, 174], for which the newest correction near any particle is used as soon as it becomes available in a Gauss-Seidel-type iteration (i.e. even during the same reflection near the subsequent particles). The present framework can be straightforwardly implemented sequentially rather than in parallel (see the discussion of Eq. (3.33)), and a similar remark holds for the hydrodynamic reflection sequence, Eqs. (4.29)–(3.72). Mathematically, when truncating at a given number of reflections, the sequential method is proved to converge exponentially for the *mobility problem* considered here, where the forces on particles are prescribed [174] (it wouldn't be the case for a resistance problem where particles' velocities are imposed [175]). In contrast, mathematical convergence of the parallel implementation is still an open question. However, this does not impact the implementation of the method proposed here, which is based on a truncation of the series approximation based on a fixed maximum order of the different terms in powers of $\varepsilon = a/d$ rather than a fixed number of reflections: with this physically-based approach, both the sequential and parallel methods then lead to retaining the same contributions.

An important feature and fundamental interest of this approach, from a physical point of view, is to clearly identify the physical mechanisms resulting in the different components of the particles' interaction velocities, as demonstrated in Section 3.4. The interaction of phoretic particles are indeed commonly and perhaps short-sightedly considered

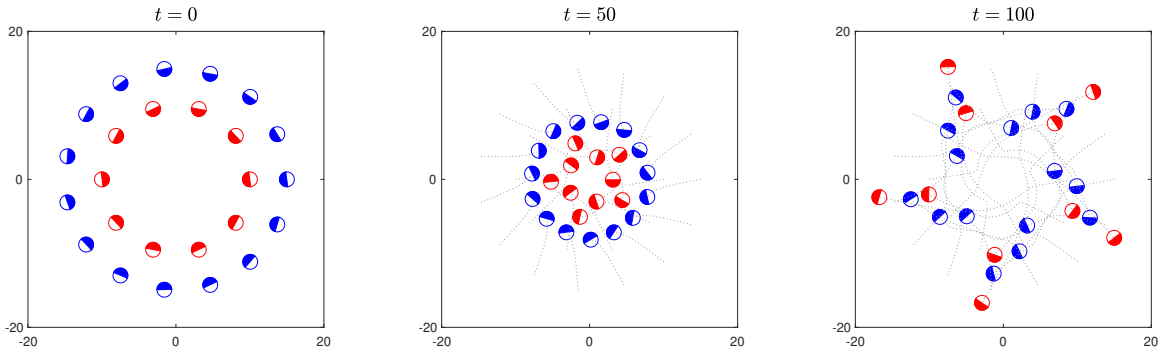

Figure 3.13: Collective dynamics of 25 Janus particles with uniform positive mobility and hemispherical activity. A set of 10 particles (in red) are arranged on a circle of radius 10 units, aligned offset from the radial direction by an angle 0.05π and 15 particles (in blue) are arranged on a circle of radius 15 units with the same angular offset from the radial direction. Particles' position computed using the MoR framework of Section 3.4 are shown for various instances of time, t.

as the juxtaposition of two independent and fundamentally different physical mechanisms, namely the effect of their non-uniform chemical signature and the hydrodynamic flow they create while swimming, and the question of their relative weight is attracting much debate [62, 122, 124, 125]. This picture, inherited implicitly from far-field models is misleading: in essence, the only physical mechanism leading to the particles' displacement is hydrodynamics as particles do not have any direct chemical or physical interactions (i.e. so-called chemical interactions are in fact due to the hydrodynamic slip generated by the neighbouring particles' chemical effect). It further overlooks the intricate coupling of the hydrodynamic and chemical problems, and the most generic interactions are in fact chemo-hydrodynamic and involve many particles, rather than being simply pairwise. The present framework in fact provides a unique opportunity to analyse rigorously the relative weight of different interaction routes, as each interaction type can be turned on or off easily in the model (a feature that is much more difficult to implement on a full numerical simulation for example).

The MoR model was implemented and tested here in the limit of a small number of particles, to enable quantitative comparisons with direct numerical simulations. However, it can straightforwardly be applied to analyse complex dynamics of larger systems. As an illustration, Figure 3.13 shows the interactions and scattering dynamics of 25 Janus particles initially distributed regularly. Its low computational cost makes this method particularly well-suited for analysing the dynamics of a very large number of particles and of suspensions. For a large number of particles, N in the system, a $O(N^2)$-computational cost makes it a compelling candidate to obtain quantitative insights in the behavior of large active suspensions.

4

Self-propulsion induced by clustering of isotropic autophoretic particles

In isolation, a chemically- and geometrically-isotropic autophoretic particle cannot swim; we show that it can however achieve self-propulsion through phoretic and hydrodynamic interactions with other identical particles by spontaneously forming clusters. This result thus identifies a new route to symmetry-breaking for the concentration field and to self-propulsion, that is not based on an anisotropic design, but on the collective interactions of identical and homogeneous active particles. Using full numerical simulations as well as theoretical modelling of the clustering process, the statistical properties of the propulsion are obtained. The robustness of these results to the effect of Brownian motion is also discussed.

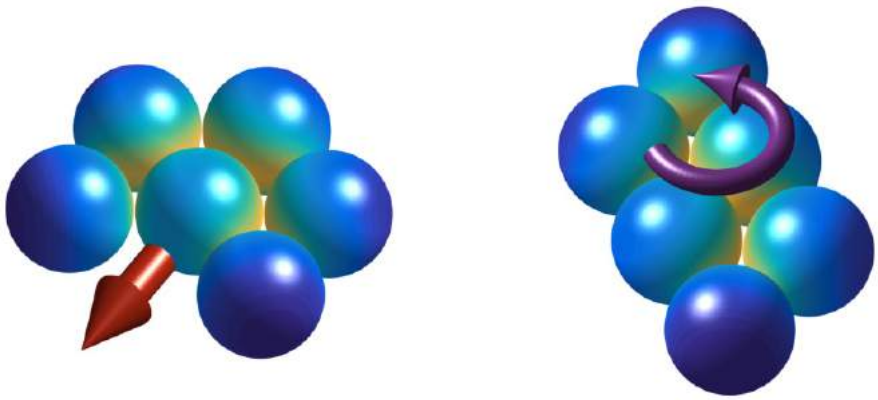

Figure: *Two different configurations of 6-particle clusters formed from isotropic autophoretic particles, that can self-propel (translate/rotate) based on the asymmetry of cluster geometry.*

Contents

This chapter contains a modified version of article "Clustering-induced self-propulsion of isotropic autophoretic particles" by A. Varma, T. D. Montenegro-Johnson and S. Michelin, published in *Soft Matter*, 2018 (DOI:10.1039/C8SM00690C).

To achieve self-propulsion, autophoretic colloids must set the surrounding fluid into motion which fundamentally requires an asymmetric distribution in the solute concentration at their surface. So far, three different mechanisms have been identified to achieve such symmetry-breaking of the concentration field: (i) an asymmetric chemical patterning of the surface (e.g. Janus particles, [28, 58]) (ii) an asymmetric shape of the chemically-homogeneous colloid [176, 177] and (iii) an instability resulting from the non-linear advective coupling between the solute dynamics and the flow motion [65, 144]. The former two are fundamentally associated with the particle design, and are built into its architecture. The latter, in contrast, arises spontaneously from the destabilization of a non-motile isotropic state.

The purpose of the present chapter is to introduce and characterize a fourth route to symmetry-breaking of the concentration field and self-propulsion, wherein geometrically- and chemically-isotropic particles interacting with diffusive solutes do not propel on their own but instead gain locomotion from forming asymmetric clusters. All particles are identical here, which is a fundamentally different situation from the assembly of chemically-inhomogeneous molecules from a mixture of two different types of particles [62]. Identical isotropic phoretic particles which can attract (for $\mathcal{A}$ and $\mathcal{M}$ of opposite signs) each other because they generate radial concentration gradients which induce a phoretic drift on the other particles. This phoretic attraction combined with steric constraints enable only a discrete set of stable configurations that may display a geometric asymmetry, which is a sufficient ingredient for self-propulsion of this assembly [61].

This collective self-propulsion is therefore intimately linked to the exact geometry of the particle assembly, which itself results from the dynamic phoretic clustering of the particles. An essential goal of the present work is therefore to characterize the statistical properties of the particle arrangement arising from the clustering process, and therefore requires a careful modelling of this dynamics. Note that self-propulsion and collective dynamics of chemically-isotropic and individually non-motile particles was also observed for colloidal particles trapped at a fluid-fluid interface [178]; then fluid motion resulted from the Marangoni stresses at the free surface rather than a direct hydrodynamic forcing by each particle as considered here.

A single geometrically- and chemically-isotropic particle is shown to be non-propelling in Section 4.1. In Section 4.2, the collective dynamics of two identical isotropic particles is considered in detail and their relative motion is computed analytically. Such analytic solutions are not available for larger number of particles. A reduced-order model, validated with full numerical solution using a regularized Boundary Element Method (BEM), is then used in Appendix C to determine the statistics of formation of different clusters, their velocity and the resulting mean properties and their evolution with N. Finally, Section 4.7 analyses the effect of noise and Brownian motion on these results and conclusions are finally drawn in Section 4.8.

4.1 Single isotropic particle

A particle j with uniform surface activity (say, A_j) produces an isotropic concentration field through diffusion. Since the steady-state field is symmetrical, no phoretic forcing is expected, and so, the particle should not self-propel in the fluid at low Reynolds regime. To put more formally, let us recapitulate the governing equations for the concentration field,

$$\nabla^2 c = 0 \tag{4.1}$$

with the boundary conditions,

$$c(r_j \to \infty) = 0, \quad \text{and on the surface,} \quad \mathbf{n}_j \cdot \nabla c|_{r_j=a_j} = -A_j \tag{4.2}$$

The solution to the above Laplacian is simply,

$$c = \frac{A_j a_j}{r_j} \tag{4.3}$$

The gradient of the field,

$$\nabla c = -\frac{A_j a_j^2}{r_j^3}\mathbf{r}_j \tag{4.4}$$

The slip velocity generated on the surface due to the local concentration gradients for a particle of uniform mobility, M,

$$\widetilde{\mathbf{u}}_j = M_j \, \nabla_{||} c|_{r_j=a_j} = \frac{-A_j M_j}{a_j}(\mathbf{I} - \mathbf{n}_j\mathbf{n}_j) \cdot \mathbf{n}_j = \mathbf{0} \tag{4.5}$$

Thus, a homogeneously active spherical particle does not generate any flow field around it. As a consequence of the zero surface slip velocity, the force- and torque-free particle additionally does not achieve self-propulsion.

$$\mathbf{U}_j^{\text{self}} = -\langle \widetilde{\mathbf{u}}_j \rangle = \mathbf{0} \quad \text{and,} \quad \mathbf{\Omega}_j^{\text{self}} = -\frac{3}{2a_j}\langle \mathbf{n}_j \times \widetilde{\mathbf{u}}_j \rangle = \mathbf{0} \tag{4.6}$$

Thus, it is formally shown that the homogeneously coated particle does not propel. But let us now consider the situation where a similar particle is introduced in the system.

4.2 Dynamics of two isotropic particles

Let the position vector of any particle j be given by $\mathbf{R}_j$. The distance between any two particles j and k is denoted by $d = |\mathbf{R}_j - \mathbf{R}_k|$.

4.2.1 Far-field model

To first have an intuitive grasp of the dynamics, we analyse a simple far-field interaction between the particles. The gradients of the field created by one particle creates a drift velocity on the second. If the two particles are separated by a distance d, the drift velocity of particle 2 due to particle 1 is given by,

$$\mathbf{U}_2 = -M_2 \, \nabla c_1|_{r_2=0} = \frac{A_1 M_2 a_1^2}{d^2}\mathbf{e}_{12} \quad \Omega_2 = \mathbf{0} \tag{4.7}$$

If we let the two particles be identical spheres of radius a with activity A and mobility M, aligned along the axis $\mathbf{e}_z$ as shown in figure 4.1, the propulsion velocities of the particles can thus be written as,

$$\mathbf{U}_1 = \frac{AMa^2}{d^2}\mathbf{e}_z \quad \mathbf{U}_2 = -\frac{AMa^2}{d^2}\mathbf{e}_z \tag{4.8}$$

The particles break each other's symmetry of concentration field to create equal magnitude of propulsion velocity but in opposite directions i.e. they exhibit an action-reaction symmetry.

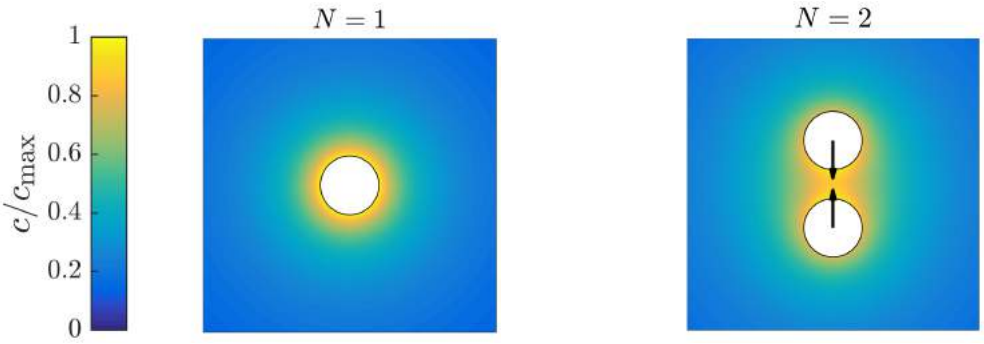

Figure 4.1: Relative concentration field around (a) a single isotropic phoretic particle and (b) two identical isotropic phoretic particles ($A = 1$ and $M = -1$). In (a), the isotropic concentration field leads to no fluid motion nor propulsion. In (b), the asymmetric concentration field around each particle leads to a mutual attraction.

When the particles are sufficiently far apart $a/d \ll 1$ they swim with velocities scaling as a^2/d^2. The activity A and the mobility M can be tuned to make the particles swim towards or away from each other; in our analysis, we are interested in the case where the particles cluster towards each other and thus, the particles need to satisfy the criteria: $AM = -1$. Note that this is equivalent to chemotactic behaviour of the particles.

4.2.2 Exact solution for the dynamics

Note that, due to action-reaction symmetry, this mutual attraction/repulsion velocity U depends only on the distance d between the particles. It is convenient to express the distance between the particles in terms of the separation between their surfaces along the line joining their centers- known as the contact distance $d_c = d - 2a$. The velocity is hence computed at various separation, d_c (using semi-analytical solution of the problem in bispherical coordinates presented in Appendix A) and is plotted in Figure 4.2.

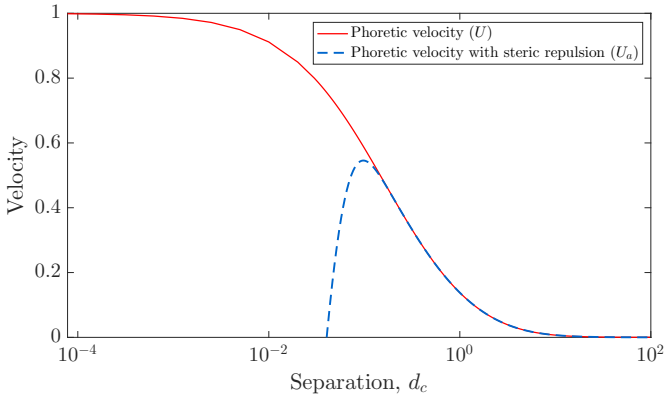

Figure 4.2: Clustering velocity of each particle as a function of the contact distance d_c between the two particles. A short-ranged repulsion potential is added to prevent overlap of the particles given by equation (4.9) with $C = 35$, $\delta = 25$ and $d^* = 1.95$

4.2.3 Langevin dynamics of the system

When the particles are extremely close to each other, i.e. when $d_c/a \ll 1$, the short-range repulsive interactions between the molecules on the surface of the two particles become significant. These intermolecular repulsive forces prevent the overlap of the particles (steric effect). To preserve the previous velocity formulation, this repulsive effect is therefore included as an additional repulsive velocity to mimic this behaviour, in the form of a smoothed step-function. The complete expression for the clustering velocity is hence given by

$$U_a(d) = U(d) - C\,(1 - \tanh(\delta\,(d - d^*))), \tag{4.9}$$

where C, δ and d^* are chosen appropriately so that the particles have negligible separation after clustering. For our simulations, we use $C = 35$, $\delta = 25$ and $d^* = 1.95$ and the velocity function is shown in figure 4.2. This clustering velocity U_a is a function solely of the particles' distance d, shown in Figure 4.2. The dynamics of the two particles can therefore be described by an over-damped deterministic Langevin dynamics within an interaction potential:

$$\frac{\mathrm{d}\mathbf{R}_j}{\mathrm{d}t} = -\frac{\partial \mathcal{E}}{\partial \mathbf{R}_j}, \quad \text{with } \mathcal{E}(\mathbf{R}_1, \mathbf{R}_2) = \mathcal{E}_{2p}(|\mathbf{R}_1 - \mathbf{R}_2|), \tag{4.10}$$

and

$$\frac{\partial \mathcal{E}_{2p}}{\partial d} = -U_a(d). \tag{4.11}$$

This potential $\mathcal{E}_{2p}$ is a measure of the stability of the two-particle cluster. In the absence of any external noise in the system, the system evolves at each instant down the direction of its steepest gradient. When the particles are spaced infinitely apart, they do not influence each other (i.e. their velocities are zero); their interaction potential is zero. When spaced at a finite distance, the system is in non-equilibrium and the potential of the system drops over time as the particles approach each other. The potential is in a (minimal) stable equilibrium when the particles are in contact i.e. when the steric repulsion balances the phoretic attraction.

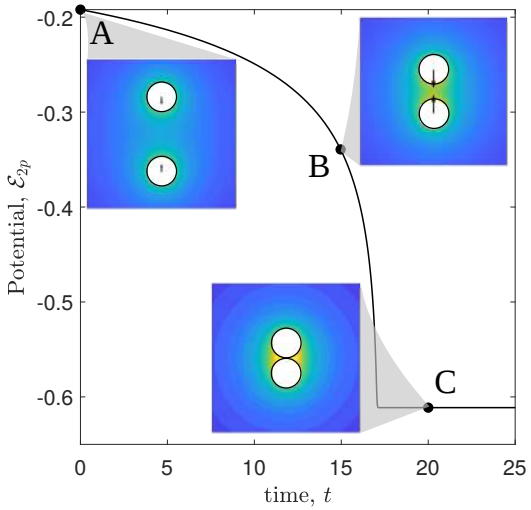

Figure 4.3: Evolution of the interaction potential of the two particles during clustering. The concentration field distribution and the relative velocities of both the particles are shown. Three positions in particular, **A**- where particles are initially at $d = 5a$, **B**- at $d = 3a$ after which the cluster rapidly collapses and, in **C** when the particles are stationary held at $d = 2.04a$.

Note that for two particles, hydrodynamic and phoretic interactions introduce an asymmetry

in the system that enables the motion of individual particles. Yet, the center of mass of the arrangement remains stationary for identical particles due to action-reaction symmetry that is present and, creates a final cluster (i.e. dimer) that is front-back symmetric. This symmetry would exist only if the particles are identical and, so it would be broken if the particles are of different sizes or activity, which would lead to net motion of the center of mass.

4.3 Dynamics of N-particle system

An analytical solution can no longer be determined exactly for the phoretic and hydrodynamic problem for $N(\geq 2)$ particles.

4.3.1 Boundary element method

Boundary element methods (BEM), based on the classical boundary integral formulation of Stokes flows provide accurate numerical solution to flow field. The computational technique is shown to give good accuracy even when there exists strong near-field hydrodynamic interactions between particles [179, 167]. Boundary Element Methods solve the Laplace equation for the concentration field and Stokes equations for the flow-field outside a set of rigid particles by using the fundamental integral representation of the solutions to these harmonic and bi-harmonic equations, in terms of their values and normal gradients on the bounding surfaces only. Such methods are therefore particularly well-suited for phoretic problems in Stokes flows since the coupling of the concentration and velocity fields occurs only on the particles' surfaces. The details of the boundary integral formulation and their discretisation into BEM scheme have been detailed in Chapter 2 and in Appendix C. We validate the BEM for the mesh form described above, for the case of a two-sphere swimmer that propels due to geometric asymmetry [61] in Appendix C. Using the above mentioned meshing, an accuracy of about 1% was obtained on the swimming velocity of the cluster even for particles near contact with $d_c = 0.01$ and $d_c = 0.02$ (about 10 times the local element size in the adapted mesh).

4.3.2 Clustering dynamics

Under the effect of phoretic attractions, complex non-equilibrium clustering dynamics are observed leading to the formation of a stable rigid planar assembly, held together by the balance between phoretic attraction and short-ranged repulsive forces. These clusters are stable in the classical sense that any slight perturbation would return them back to their original configuration. For a given number of particles in the system, multiple stable configurations can be imagined. Since each particle attracts the other, the

We analyse the case where the particles are initially distributed in a plane. As mentioned, this choice is simply for the ease of analysis of the different cluster configurations; the problem is solved however, for 3D solute and hydrodynamics and hence, the present formalism can be readily applied to 3D clustering. As an example, let us consider a 5-particle system where the particles are initially randomly distributed. The detailed kinematics of the particles is marched in time using an adaptive two-step Adam-Bashforth method, where the time step is determined on the smallest-separation between the particles. To prevent particle overlap, a soft repulsive potential is introduced akin to that leading to the corrective relative velocity for the two-particle system. A relatively coarse (512 nodes per sphere) is

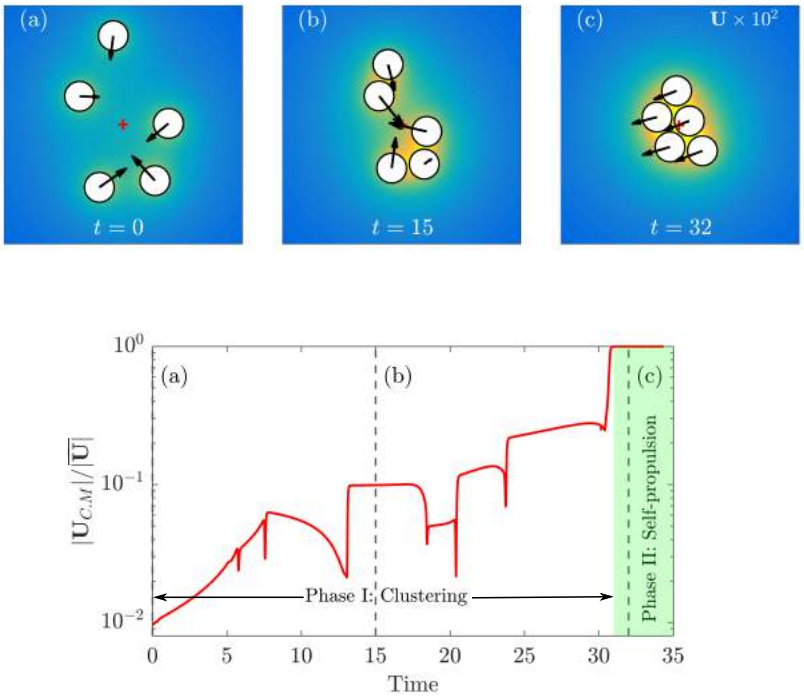

Figure 4.4: (Top) Clustering dynamics of 5 isotropic particles ($A = 1, M = -1$). The velocity of each particle is shown by black arrows and the color indicates the concentration field. The red cross indicates the position of the center of mass. (Bottom) Ratio of the magnitude of the center of mass velocity to the average individual velocity magnitude of the 5 particles. A stable cluster is formed when there is no relative motion between the center of mass and individual particles (green shade). The vertical dashed lines correspond to the three snapshots above.

used here to compute the velocities of the particles. The computations for the clustering phase for 5 particles in the described example took about 10 hrs of computational time.

The concentration field generated around each particle is asymmetric in nature due to the influence of the fields created by the surrounding identical particles. This creates a chemotactic drift of the particles towards each other. The general direction of each particle hence tends to be towards the instantaneous geometric center of the assembly; the highest attractive influence is however, towards their nearest neighbour because the concentration field gradients that create the chemotatic drift decay quickly away from each particle. Up until the particles form a rigid stable cluster, the velocity of the center of mass of the particles is noticeably at least one order of magnitude smaller than the velocity of individual particles (see Figure 4.4). It can be inferred from this that the center of mass of the system remains effectively stationary during that phase. This is somewhat unsurprising given the opposite (attractive) velocities induced by the particles on each other as observed in the 2-sphere case.

Once a stable cluster is formed, the particles do not experience any relative motion as the phoretic force binds them together. However, it is observed that the global velocity is interestingly non-zero i.e. the particles begin to swim as a cluster! This transition clearly decomposes the dynamics of N phoretic particles into two different regimes, that differ fundamentally in the relative magnitude of the mean and relative velocities of the particles. We can classify the entire process into two phases viz. (i) Phase I which is characterized by a global velocity (i.e. velocity of their geometric center) that is negligible in front of

individual motion and (ii) Phase II which has a significantly enhanced global velocity when the particles are rigidly-bound in a cluster. This difference is expected to be attributed to the fact that in the clustering phase (Phase I), the particles are individually force-free hydrodynamically. In the self-propulsion phase (Phase II), they are rigidly-bound by the balance of phoretic attraction and repulsive internal forces that prevent their overlap, and the hydrodynamic force on each particle is now non-zero, although the cluster as a whole is. As will be seen, this change in boundary condition profoundly modifies each particle's hydrodynamic signature.

4.3.3 Self-propulsion of clusters

Since it is observed that in stable clusters, the particles are arranged on a regular hexagonal lattice, the computational accuracy of the cluster dynamics is expected to be improved significantly by using a finer mesh of the nodes in regions of closest contact. Additional mesh refinement is hence performed in the clustering plane near the positions of particles' contact on hexagonal lattices (see figure 4.5). This meshing provides an efficient framework to compute the translation and rotational velocities of clustered particles.

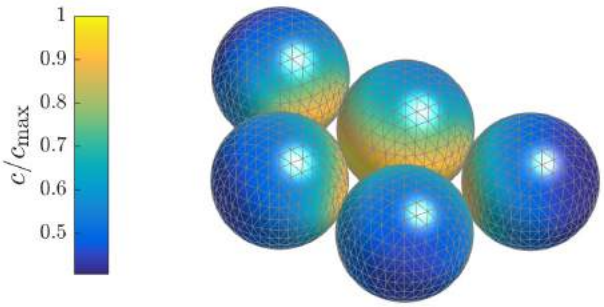

Figure 4.5: The accurate meshing used for computing the propulsion velocity of 5 particle cluster. The cluster swims with a speed $U = 8.5 \times 10^{-4}$ along its symmetry plane.

Numerically, the particle assembly is considered as rigid, and the resulting velocity of these stable clusters is computed with inter-particle separation, $d_c = 0.01$ and $d_c = 0.02$; a Taylor series expansion of the global swimming velocity of the cluster in terms of contact distance around $d_c = 0$ is then used to extrapolate the true self-propulsion velocities of clusters when particles are in actual contact. To achieve sufficient accuracy on the global motion of the cluster (in particular resolving properly the flow field around the particles in the lubrication regions), a finer mesh is used with 1538 nodes and refinement near the regions of contact as described previously. Computation of the cluster velocity for $N = 13$ yet requires ≈ 28 GB of allocated memory, but only two computations are performed for each cluster shape. The simplest self-propelling cluster is of size $N = 5$; for $N < 5$, the clusters form symmetric geometry which do not provide the effective phoretic forcing. A detailed mathematical understanding of the origin of self-propulsion is made in the next section using the method of reflections.

4.4 Origin of self-propulsion

The far-field model regards each phoretic particle a as point chemical source and point stresslet. The interactions between these point particles are inherently pairwise in nature

i.e. the multi-body interactions are omitted. Hence, by using the far-field model, the global velocity of a system containing identical isotropic phoretic particles would be predicted to be zero. However, we notice from BEM simulations (see figure 4.4) that the global velocity is non-zero and exhibits complex behaviour even during the clustering phase. This can be attributed to the fact that these simulations take into account surface effects of the particles as well as the multi-body interactions between them. These two effects, at large particle separations ($\varepsilon = a/d \ll 1$), can be accounted for in a theoretical model by implementing the *Method of Reflections* (MoR) framework developed in chapter 3; our analysis is restricted to within propulsion velocity of $O(\varepsilon^5)$ which include three-body chemical, hydrodynamic as well as chemo-hydrodynamic interactions. Thus, by evaluating the global velocities of the system of particles at asymptotically large distances between the particles in both clustering and self-propulsion phases, we shall to rationalize the self-propulsion behaviour of clusters.

4.4.1 Chemical interactions

Let us consider an isotropic phoretic particle (say, j) having a uniform surface activity A_j and a surface mobility M_j. As described in chapter 3, the concentration field around the particle j can be decomposed into into spherical harmonics as,

$$c_j = \sum_{p\geq 1} \frac{a_j^{q+1}}{r_j^{2q+1}} \mathbf{C}^p_{j,q} \overset{q}{\odot} \mathbf{r}_j \overset{q}{\otimes} \mathbf{r}_j \tag{4.12}$$

Since the isotropic particle behaves as a point source of chemical solute, one can directly obtain from equation (3.40),

$$C^0_{j,0} = A_j \quad \text{and,} \quad \mathbf{C}^0_{j,q\geq 1} = 0 \tag{4.13}$$

By using the expression for propulsion velocity resulting from concentration gradients given by equation (3.59), we find that $\mathbf{U}^0_j = -2M_j\mathbf{C}^0_{j,1}/3 = 0$; this justifies the fact that an isotropic particle, in isolation, does not self-propel due to zero concentration gradients of the chemical solute that create phoretic forcing.
The spherical harmonic coefficients of the reflected concentration field on the surface of particle k is obtained from equation (3.31) as an asymptotic expansion in $\varepsilon = a/d$,

$$\mathbf{C}^r_{k,q} = \mathbf{C}^{r-1}_{j,s} \overset{s}{\odot} \boldsymbol{\mathcal{F}}^{\chi}_{jk}(q,s) \quad \text{where,} \tag{4.14}$$

$$\boldsymbol{\mathcal{F}}^{\chi}_{jk}(q,s) = \frac{q a_k^q a_j^{s+1}}{(q+1)!} \left[\overset{q}{\nabla} \left(\frac{\mathbf{r}_j \overset{s}{\otimes} \mathbf{r}_j}{r_j^{2s+1}} \right) \right] = O(\varepsilon^{s+q+1}) \tag{4.15}$$

The first few coefficients of the modes of the first reflection thus become,

$$\mathbf{C}^1_{k,1} = \sum_{j\neq k} C^0_{j,0}\, \boldsymbol{\mathcal{F}}^{\chi}_{jk}(1,0) = -\sum_{j\neq k} \frac{A_j a_j a_k}{2d_{jk}^2} \mathbf{e}_{jk}, \tag{4.16}$$

$$\mathbf{C}^1_{k,2} = \sum_{j\neq k} C^0_{j,0}\, \boldsymbol{\mathcal{F}}^{\chi}_{jk}(2,0) = -\sum_{j\neq k} \frac{A_j a_k^2 a_j}{3d_{jk}^3} (\mathbf{I} - 3\mathbf{e}_{jk}\mathbf{e}_{jk}) \tag{4.17}$$

and so on. Note that the reflected source term, $C^r_{k,0} = 0$ for all $r \geq 1$. At the leading-order, the reflected field is a source dipole ($s = 1$). The propulsion velocity arising only from the concentration field of r^{th} reflection on particle k (i.e. ignoring any hydrodynamic

interactions presently) is given by equation(3.59),

$$\mathbf{U}_k^{\chi,r} = -2M_k \sum_{r\geq 1} \mathbf{C}_{k,1}^r = -2M_k \sum_{j\neq k} \sum_s \mathbf{C}_{j,s}^r \overset{s}{\odot} \boldsymbol{\mathcal{F}}_{jk}^{\chi}(1,s) \tag{4.18}$$

Thus, the propulsion velocity of particle k from *first* reflection ($r=1$) of the concentration field is determined using equation (4.16) in (4.18),

$$\mathbf{U}_k^{\chi,r=1} = -2M_k \mathbf{C}_{k,1}^1 = M_k \sum_{j\neq k} \frac{A_j a_j a_k}{d_{jk}^2} \mathbf{e}_{jk} \tag{4.19}$$

The leading-order mode of *second* reflection is a source dipole ($q=1$) created from the first reflection of source dipole (equation (4.16)) induced by a chemical source. This is thus a three-body chemical interaction with the coefficient of the leading-order mode,

$$\mathbf{C}_{k,1}^2 = \sum_{j\neq k} \mathbf{C}_{k,1}^1 \cdot \boldsymbol{\mathcal{F}}_{jk}^{\chi}(1,1) = \sum_{j\neq k} \sum_{l\neq j} C_{l,0}^0 \, \boldsymbol{\mathcal{F}}_{lj}^{\chi}(1,0) \cdot \boldsymbol{\mathcal{F}}_{jk}^{\chi}(1,1) \tag{4.20}$$

$$= -\sum_{j\neq k} \sum_{l\neq j} \frac{A_l a_l a_j^3 a_k}{4 d_{lj}^2 d_{jk}^3} \mathbf{e}_{lj} \cdot (\mathbf{I} - 3\mathbf{e}_{jk}\mathbf{e}_{jk}) \tag{4.21}$$

Note that this coefficient is of magnitude $O(\varepsilon^5)$. The next order term would be a source dipole ($q=1$) created from a source quadrupole ($q=2$) i.e. $\mathbf{C}_{k,1}^2 = \sum_{j\neq k} \mathbf{C}_{k,2}^1 : \boldsymbol{\mathcal{F}}_{jk}^{\chi}(1,2)$ which is of $O(\varepsilon^7)$. Since we limit our analysis to $O(\varepsilon^5)$, we shall neglect this as well as reflection of subsequent modes. Thus, the leading-order propulsion velocity from second reflection is,

$$\mathbf{U}_k^{\chi,r=2} = -2M_k \mathbf{C}_{k,1}^2 = M_k \sum_{j\neq k} \sum_{l\neq j} \frac{A_l a_l a_j^3 a_k}{2 d_{lj}^2 d_{jk}^3} \mathbf{e}_{lj} \cdot (\mathbf{I} - 3\mathbf{e}_{jk}\mathbf{e}_{jk}) \tag{4.22}$$

It should be noted here that the propulsion velocity is of $O(\varepsilon^5)$. The propulsion velocity, limited to $O(\varepsilon^5)$ accuracy, resulting from chemical drift can now be determined from equations (4.19) and (4.22),

$$\mathbf{U}_k^{\chi,\text{free}} = \mathbf{U}_k^{\chi,r=1} + \mathbf{U}_k^{\chi,r=2} \tag{4.23}$$

$$= M_k \sum_{j\neq k} \left(\frac{A_j a_j a_k}{d_{jk}^2} \mathbf{e}_{jk} + \sum_{l\neq j} \frac{A_l a_l a_j^3 a_k}{2 d_{lj}^2 d_{jk}^3} \mathbf{e}_{lj} \cdot (\mathbf{I} - 3\mathbf{e}_{jk}\mathbf{e}_{jk}) \right) + O(\varepsilon^7) \tag{4.24}$$

4.4.2 Chemo-hydrodynamic interactions: force-free particles

Similar to the chemical problem, the flow field produced by a particle can be decomposed into its spherical harmonic parts, given by equation (D.8) as,

$$\mathbf{u}_j^p = \sum_{s=1}^{\infty} \left\{ \boldsymbol{\Phi}_{j,s}^p \overset{s}{\odot} \nabla \left(\frac{\mathbf{r}_j \overset{s}{\otimes} \mathbf{r}_j}{r_j^{2s+1}} \right) - \mathbf{X}_{j,s}^p \overset{s}{\odot} \left[s \left(\frac{\mathbf{r}_j \overset{s-1}{\otimes} \mathbf{r}_j}{r_j^{2s+1}} \right) \otimes (\boldsymbol{\varepsilon} \cdot \mathbf{r}_j) \right] \right.$$
$$\left. + \frac{\mathbf{P}_{j,s}^p}{2(2s-1)} \overset{s}{\odot} \left[\frac{\mathbf{r}_j \overset{s-1}{\otimes} \mathbf{r}_j}{r_j^{2s-1}} \otimes \left((2s-1)\frac{\mathbf{r}_j \mathbf{r}_j}{r_j^2} - (s-2)\mathbf{I} \right) \right] \right\}, \tag{4.25}$$

where, $\mathbf{P}_{j,s}$, $\mathbf{\Phi}_{j,s}$ and $\mathbf{X}_{j,s}$ represent symmetric force multipoles, potential multipoles and rotlet multipoles respectively. Furthermore, as described in equations in (3.59), one can determine a one-to-one relation between the chemical and hydrodynamic multipoles when the particles have a uniform surface mobility.

$$\mathbf{\Phi}^0_{j,1} = \frac{-2a_j^3 M_j}{3}\mathbf{C}^0_{j,1}; \qquad \mathbf{\Phi}^0_{j,q\geq 2} = \frac{q a_j^{q+2} M_j}{2}\mathbf{C}^0_{j,q} \tag{4.26}$$

$$\mathbf{P}^0_{j,q\geq 2} = q(2q-1)a_j^q M_j \mathbf{C}^0_{j,q} \quad \text{and,} \tag{4.27}$$

$$\mathbf{X}^0_{j,q\geq 1} = 0 \tag{4.28}$$

Note that $\mathbf{P}^0_{j,1} = 0$ and $\mathbf{X}^0_{j,1} = 0$ because the particle is both force- and torque-free. At reflection p, the drift velocity created by particle j on k is given by,

$$\mathbf{U}^p_k = \sum_{j\neq k}\sum_{s\geq 1}\left[\mathbf{\Phi}^{p-1}_{j,s} \overset{s}{\odot} \boldsymbol{\mathcal{F}}^{\mathbf{1}}{}_{jk}(1,s) - \mathbf{X}^{p-1}_{j,s} \overset{s}{\odot} \boldsymbol{\mathcal{F}}^{\mathbf{2}}{}_{jk}(1,s) + \mathbf{P}^{p-1}_{j,s} \overset{s}{\odot} \left(\boldsymbol{\mathcal{F}}^{\mathbf{3}}{}_{jk}(1,s) + \frac{a_k^2}{6}\boldsymbol{\mathcal{F}}^{\mathbf{1}}{}_{jk}(1,s)\right)\right], \tag{4.29}$$

$$\mathbf{\Omega}^p_k = -\frac{1}{2}\sum_{j\neq k}\sum_{s\geq 1}\left[\mathbf{P}^{p-1}_{j,s} \overset{s}{\odot} \boldsymbol{\mathcal{F}}^{\mathbf{2}}{}_{jk}(1,s) + s\mathbf{X}^{p-1}_{j,s} \overset{s}{\odot} \boldsymbol{\mathcal{F}}^{\mathbf{1}}{}_{jk}(1,s)\right], \tag{4.30}$$

where $\boldsymbol{\mathcal{F}}^1_{jk}$, $\boldsymbol{\mathcal{F}}^3_{jk}$ are given in Appendix D and can be expressed to evaluate the propulsion velocities as,

$$\boldsymbol{\mathcal{F}}^{\mathbf{1}}{}_{jk}(1,s) = \left[\nabla\left(\frac{\mathbf{r}_j \overset{s}{\otimes} \mathbf{r}_j}{r_j^{2s+1}}\right)\right]_{r_k=0} = O(\varepsilon^{s+2}), \quad \boldsymbol{\mathcal{F}}^{\mathbf{2}}{}_{jk}(1,s) = s\left[\frac{\mathbf{r}_j \overset{s-1}{\otimes} \mathbf{r}_j}{r_j^{2s+1}} \otimes (\boldsymbol{\varepsilon}\cdot\mathbf{r}_j)\right]_{r_k=0} = O(\varepsilon^{s+1}), \tag{4.31}$$

$$\boldsymbol{\mathcal{F}}^{\mathbf{3}}{}_{jk}(1,s) = \frac{1}{2(2s-1)}\left[\frac{\mathbf{r}_j \overset{s-1}{\otimes} \mathbf{r}_j}{r_j^{2s-1}} \otimes \left((2s-1)\frac{\mathbf{r}_j\mathbf{r}_j}{r_j^2} - (s-2)\mathbf{I}\right)\right]_{r_k=0} = O(\varepsilon^s) \tag{4.32}$$

4.4.2.1 Purely hydrodynamic interactions

If the particle is force-free, the mode corresponding to point force $\mathbf{P}^0_{k,1} = 0$. Additionally, since at the zeroth reflection $\mathbf{C}^0_{j,q\geq 1} = 0$, the non-swimming modes, $\mathbf{\Phi}^0_{k,q\geq 1} = \mathbf{P}^0_{k,q\geq 2} = \mathbf{X}^0_{k,q\geq 1} = 0$ i.e. the non-swimming modes are of zero strength. Thus, the particles does not produce any flow field around them, and hence, there are no purely hydrodynamic interactions between the particles.

4.4.2.2 Chemo-hydrodynamic interactions

Chemo-hydrodynamic interactions are multi-body interactions involving hydrodynamic interactions resulting *after* multiple chemical reflections between particles. After r reflections ($r > 1$), the relation between the modes of reflected chemical and hydrodynamic fields are

expressed as (see equation (3.59)),

$$\mathbf{\Phi}^0_{j,1} = a_j^3 M_j \sum_{r\geq 1} \mathbf{C}^r_{j,1}; \qquad \mathbf{\Phi}^0_{j,q\geq 2} = \frac{a_j^{q+2} M_j}{2} \sum_{r\geq 1} (2q+1)\mathbf{C}^r_{j,q} \tag{4.33}$$

$$\mathbf{P}^0_{j,q\geq 2} = a_j^q (2q-1) M_j \sum_{r\geq 1} (2q+1)\mathbf{C}^r_{j,q} \tag{4.34}$$

$$\mathbf{X}^0_{j,q\geq 1} = 0 \tag{4.35}$$

The leading-order value of the hydrodynamic coefficients is a potential dipole created after one reflection of chemical field and is given by,

$$\mathbf{\Phi}^0_{j,1} = a_j^3 M_j \mathbf{C}^1_{j,1} = a_j^3 M_j \sum_{l\neq j} C^0_{l,0}\, \boldsymbol{\mathcal{F}}^{\chi}_{lj}(1,0) = -M_j \sum_{l\neq j} \frac{A_l a_l a_j^4 \mathbf{e}_{lj}}{2 d_{lj}^2}; \tag{4.36}$$

which is of strength $O(\varepsilon^2)$. Similarly, at the next order, a stresslet and potential quadrupole are created from reflections of chemical source quadrupole which are of strengths $O(\varepsilon^3)$.

$$\mathbf{\Phi}^0_{j,2} = \frac{5a_j^4 M_j}{2} \mathbf{C}^1_{j,2} = \frac{-5a_j^4 M_j}{6} \sum_{l\neq j} \frac{A_l a_j^2 a_l}{d_{lj}^3} (\mathbf{I} - 3\mathbf{e}_{lj}\mathbf{e}_{lj}) \tag{4.37}$$

$$\mathbf{P}^0_{j,2} = 15 a_j^2 M_j \mathbf{C}^1_{j,2} = -5 a_j^2 M_j \sum_{l\neq j} \frac{A_l a_j^2 a_l}{d_{lj}^3} (\mathbf{I} - 3\mathbf{e}_{lj}\mathbf{e}_{lj}) \tag{4.38}$$

As before, the swimming velocity after first reflection can be determined using equation (4.29) as,

$$\mathbf{U}^1_k = \sum_{j\neq k} \underbrace{\mathbf{\Phi}^0_{j,1}}_{O(\varepsilon^2)} \cdot \underbrace{\boldsymbol{\mathcal{F}}^1_{jk}(1,1)}_{O(\varepsilon^3)} + \underbrace{\mathbf{\Phi}^0_{j,2}}_{O(\varepsilon^3)} \cdot \underbrace{\boldsymbol{\mathcal{F}}^1_{jk}(1,2)}_{O(\varepsilon^4)} + \underbrace{\mathbf{P}^0_{j,2}}_{O(\varepsilon^3)} : \left(\underbrace{\boldsymbol{\mathcal{F}}^3_{jk}(1,2)}_{O(\varepsilon^2)} + \underbrace{\frac{a_k^2}{6} \boldsymbol{\mathcal{F}}^1_{jk}(1,2)}_{O(\varepsilon^4)} \right) + O(\varepsilon^8) \tag{4.39}$$

Limiting to accuracy $O(\varepsilon^5)$,

$$\mathbf{U}^1_k = \sum_{j\neq k} \mathbf{\Phi}^0_{j,1} \cdot \boldsymbol{\mathcal{F}}^1_{jk}(1,1) + \mathbf{P}^0_{j,2} : \boldsymbol{\mathcal{F}}^3_{jk}(1,1) + O(\varepsilon^7) \tag{4.40}$$

Expanding using equations (4.32), the drift velocity of particle resulting from hydrodynamic field can be expressed as,

$$\mathbf{U}^{1,\text{free}}_k = \sum_{j\neq k} \sum_{l\neq j} -\frac{M_j}{2} \left(\frac{A_l a_l a_j^4}{d_{lj}^2 d_{jk}^3} \mathbf{e}_{lj} \cdot (\mathbf{I} - 3\mathbf{e}_{jk}\mathbf{e}_{jk}) + \frac{5 A_l a_j^4 a_l}{d_{lj}^3 d_{jk}^2} (\mathbf{I} - 3\mathbf{e}_{lj}\mathbf{e}_{lj}) : \mathbf{e}_{jk}\mathbf{e}_{jk}\mathbf{e}_{jk} \right) + O(\varepsilon^7) \tag{4.41}$$

Note that the hydrodynamic field is created by a first reflection of chemical field (and not self-generated as explained earlier) and hence, is a three-particle interaction with contribution of $O(\varepsilon^5)$.

Thus, the total propulsion velocity to $O(\varepsilon^5)$ from both chemical and hydrodynamic inter-

actions can be obtained by summing equations (4.24) and (4.41),

$$\mathbf{U}_k^{\text{free}} = \sum_{j\neq k} \frac{M_k A_j a_j a_k}{d_{jk}^2}\mathbf{e}_{jk} + \sum_{j\neq k}\sum_{l\neq j}\Bigg(\frac{A_j a_l a_j^3}{2d_{lj}^2 d_{jk}^3}(M_k a_k - M_j a_j)\mathbf{e}_{lj}\cdot(\mathbf{I}-3\mathbf{e}_{jk}\mathbf{e}_{jk}) - \frac{5M_j A_l a_j^4 a_l}{2d_{lj}^3 d_{jk}^2}(\mathbf{I}-3\mathbf{e}_{lj}\mathbf{e}_{lj}) : \mathbf{e}_{jk}\mathbf{e}_{jk}\mathbf{e}_{jk}\Bigg) + O(\varepsilon^7) \tag{4.42}$$

The global velocity of the system can be obtained from $\sum_{k=1}^{N}\mathbf{U}_k^{\text{free}}$. Noting that the first term is a pair-interaction which cancels out when summing over all particles, we find that the leading-order global velocity during the clustering phase is only $O(\varepsilon^5)$.

4.4.3 Hydrodynamic interactions: in a rigid cluster

Within a rigid cluster, the particles are not individually force-free; the cluster as a whole however remains force-free because it is still in the low Reynolds number regime. The forces originate from short-range steric interactions between the surfaces of the particles. The flow-field from any particle j is a linear superposition of two viz. flow driven by surface slip velocity on each particle and, flow-field due to external forcing $\mathbf{F}_j$. The former was evaluated in the previous section. Here we shall consider the case where the particles are rigidly bound to each other, i.e, their separation remains fixed.

Let a force $\mathbf{F}_j$ act on a *spherical* particle j. The sphere moves with a velocity

$$\mathbf{U}_j^{0,\text{forced}} = \frac{\mathbf{F}_j}{6\pi\eta a_j} \tag{4.43}$$

By satisfying the boundary condition on the surface of the particle, i.e. $\mathbf{u}_j|_{r_j=a_j} = \mathbf{U}_j$ one can write

$$\mathbf{u}_j^0 = \frac{\mathbf{F}_j}{8\pi\eta r_j}\cdot\left(\mathbf{I}+\frac{\mathbf{r}_j\mathbf{r}_j}{r_j^2}\right) + \frac{\mathbf{F}_j a_j^2}{24\pi\eta r_j^3}\cdot\left(\mathbf{I}-\frac{3\mathbf{r}_j\mathbf{r}_j}{r_j^2}\right) \tag{4.44}$$

which represents a Stokeslet and a potential dipole. Thus, by comparing equations (4.25) and (4.44), we observe that the coefficients representing strengths of the fields,

$$\mathbf{P}_{j,1}^0 = \frac{\mathbf{F}_j}{4\pi\eta}, \quad \mathbf{\Phi}_{j,1}^0 = \frac{\mathbf{F}_j a_j^2}{24\pi\eta} \tag{4.45}$$

Note that the strength of Stokeslet $\mathbf{P}_{j,1}^0 \neq 0$ in this case because the particles are not individually force-free. The drift velocity created by this field on another particle k is given by,

$$\mathbf{U}_k^{1,\text{forced}} = \sum_{j\neq k}\mathbf{\Phi}_{j,1}^0\cdot\boldsymbol{\mathcal{F}}_{jk}^1(1,1) + \mathbf{P}_{j,1}^0\cdot\left(\boldsymbol{\mathcal{F}}_{jk}^3(1,1)+\frac{a_k^2}{6}\boldsymbol{\mathcal{F}}_{jk}^1(1,1)\right) \tag{4.46}$$

$$= \frac{\mathbf{F}_j}{6\pi\eta a_j} + \sum_{j\neq k}\frac{a_j^2\mathbf{F}_j}{24\pi\eta d_{jk}^3}\cdot(\mathbf{I}-3\mathbf{e}_{jk}\mathbf{e}_{jk}) + \frac{\mathbf{F}_j}{8\pi\eta d_{jk}}\cdot\left[(\mathbf{I}+\mathbf{e}_{jk}\mathbf{e}_{jk}) + \frac{a_k^2}{3d_{jk}^2}(\mathbf{I}-3\mathbf{e}_{jk}\mathbf{e}_{jk})\right] \tag{4.47}$$

The total propulsion velocity is hence obtained from equations (4.43) and (4.48),

$$\mathbf{U}_k^{\text{forced}} = \frac{\mathbf{F}_j}{6\pi\eta a_j} + \sum_{j\neq k} \frac{\mathbf{F}_j}{8\pi\eta d_{jk}} \cdot (\mathbf{I} + \mathbf{e}_{jk}\mathbf{e}_{jk}) + \frac{(a_j^2 + a_k^2)\mathbf{F}_j}{24\pi\eta d_{jk}^3} \cdot (\mathbf{I} - 3\mathbf{e}_{jk}\mathbf{e}_{jk}) \tag{4.48}$$

The chemical and chemo-hydrodynamic interactions create slip velocity on the surface (force-free swimming) whereas purely hydrodynamic interactions result, in this case, due to particles being subjected to an external force

$$\mathbf{U} + \boldsymbol{\Omega} \times \mathbf{R}_k = \mathbf{U}_k^{\text{free}} + \mathbf{U}_k^{\text{forced}} \tag{4.49}$$

which can be formally written as,

$$\mathbf{U} + \boldsymbol{\Omega} \times \mathbf{R}_k = \mathbf{U}_k^{\text{free}} + \sum_j \mathbf{K}_{jk} \cdot \mathbf{F}_j \qquad \text{where,} \tag{4.50}$$

$$\mathbf{K}_{jj} = \frac{\mathbf{I}}{6\pi\eta a_j} \qquad \text{and,} \tag{4.51}$$

$$\mathbf{K}_{jk} = \frac{(\mathbf{I} + \mathbf{e}_{jk}\mathbf{e}_{jk})}{8\pi\eta d_{jk}} + \frac{(a_j^2 + a_k^2)}{24\pi\eta d_{jk}^3}(\mathbf{I} - 3\mathbf{e}_{jk}\mathbf{e}_{jk}) \tag{4.52}$$

The above linear system of equations can be closed by implementing the force- and torque-free boundary conditions on the cluster,

$$\sum_j \mathbf{F}_k = \sum_j \mathbf{R}_k \times \mathbf{F}_k = 0 \tag{4.53}$$

Unlike the case of free particles, here we observe that the global velocity, $\sum_{k=1}^{N} \mathbf{U}_k^{\text{forced}}$ is $O(\varepsilon^3)$ which is two orders of magnitude larger. This increase in global velocity is attributed to the forcing from steric interactions in the cluster.

4.4.4 Validation: Two homogeneous spheres of unequal radii

Consider two rigid spheres of unequal radii (a_1 and a_2 respt.), but identical surface activity A and mobility M. The distance between the particles may be represented by d in the direction $\mathbf{e}_{12} = -\mathbf{e}_{21} = \mathbf{e}$. If the particles are considered to be force-free,

$$\mathbf{U}_1^{\text{free}} = \frac{-AMa_2^2}{d^2}\left(1 + \frac{5a_1^2a_2}{d^3}\right)\mathbf{e}, \quad \mathbf{U}_2^{\text{free}} = \frac{AMa_1^2}{d^2}\left(1 + \frac{5a_1a_2^2}{d^3}\right)\mathbf{e} \tag{4.54}$$

$$\mathbf{K}_{11} = \frac{\mathbf{I}}{6\pi\eta a_1}, \quad \mathbf{K}_{22} = \frac{\mathbf{I}}{6\pi\eta a_2} \tag{4.55}$$

$$\mathbf{K}_{12} = \mathbf{K}_{21} = \frac{\mathbf{I} + \mathbf{ee}}{8\pi\eta d} + \frac{a_1^2 + a_2^2}{24\pi\eta d^3}(\mathbf{I} - 3\mathbf{ee}) \tag{4.56}$$

The system is axisymmetric and therefore $\boldsymbol{\Omega} = 0$, and all vectors are parallel to $\mathbf{e}$. The previous system can therefore be simplified into,

$$U - \frac{AMa_2^2}{d^2}\left(1 + \frac{5a_1^2a_2}{d^3}\right) = \frac{F_1}{6\pi\eta a_1} + \left(\frac{1}{4\pi\eta d} - \frac{a_1^2 + a_2^2}{12\pi\eta d^3}\right)F_2 \tag{4.57}$$

$$U + \frac{AMa_1^2}{d^2}\left(1 + \frac{5a_1a_2^2}{d^3}\right) = \frac{F_2}{6\pi\eta a_2} + \left(\frac{1}{4\pi\eta d} - \frac{a_1^2 + a_2^2}{12\pi\eta d^3}\right)F_1 \tag{4.58}$$

$$F_1 + F_2 = 0 \tag{4.59}$$

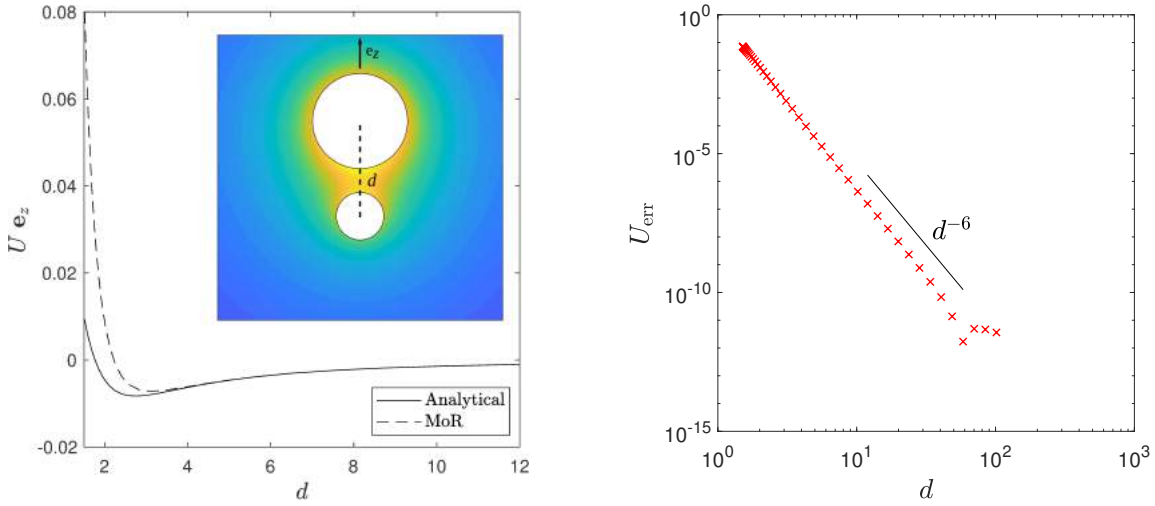

Figure 4.6: A two-sphere system, with particles of size raion 1 : 2 and the two particles are rigidly bound by an infinitely thin rod through their centers. The swimming velocity is computed as a function of the distance d between the particles. (right) The error in computing swimming velocity using MoR is checked against analytical solution.

4.4.5 Cluster of isotropic particles

For particles which are identical in size, activity and surface mobility, the equations simplify to

$$\mathbf{U} + \boldsymbol{\Omega} \times \mathbf{R}_k = \mathbf{U}_k^{\text{free}} + \sum_j \mathbf{K}_{jk} \cdot \mathbf{F}_j \qquad \text{where,} \tag{4.60}$$

$$\mathbf{U}_k^{\text{free}} = \sum_{j \neq k} \frac{MAa^2}{d_{jk}^2} \mathbf{e}_{jk} - \sum_{j \neq k} \sum_{l \neq j} \left(\frac{5MAa^5}{2d_{lj}^3 d_{jk}^2} (\mathbf{I} - 3\mathbf{e}_{lj}\mathbf{e}_{lj}) : \mathbf{e}_{jk}\mathbf{e}_{jk}\mathbf{e}_{jk} \right) \tag{4.61}$$

$$\mathbf{K}_{jj} = \frac{\mathbf{I}}{6\pi\eta a} \qquad \text{and,} \quad \mathbf{K}_{jk} = \frac{(\mathbf{I} + \mathbf{e}_{jk}\mathbf{e}_{jk})}{8\pi\eta d_{jk}} + \frac{a^2}{12\pi\eta d_{jk}^3} (\mathbf{I} - 3\mathbf{e}_{jk}\mathbf{e}_{jk}) \tag{4.62}$$

along with the force-free condition on the cluster $\sum_k \mathbf{F}_k = 0$. Comparison with BEM simulations for a translating 6-particle cluster is shown in figure.

4.5 Reduced-order modeling of the clustering phase

It is observed that for a given $N(> 5)$, the system can attain multiple final configurations depending on the initial arrangement of the particles. Each of the configurations would have a different global velocity due to difference in phoretic forcing. The type of configuration formed depends on the clustering phase and thus, this phase indirectly conditions the collective propulsion property of the system. If one were to understand the statistical properties of the system, i.e. the mean and most probable propulsion velocities, a good understanding and modelling of the clustering phase is necessary. While BEM is well suited to compute the dynamics accurately, it is prohibitively expensive for running thousands of simulations of the full temporal dynamics as needed for obtaining the probabilities of different cluster shapes starting from random initial positions. Motivated by the distinct features of the clustering and propelling phases identified in the previous section, our approach is therefore

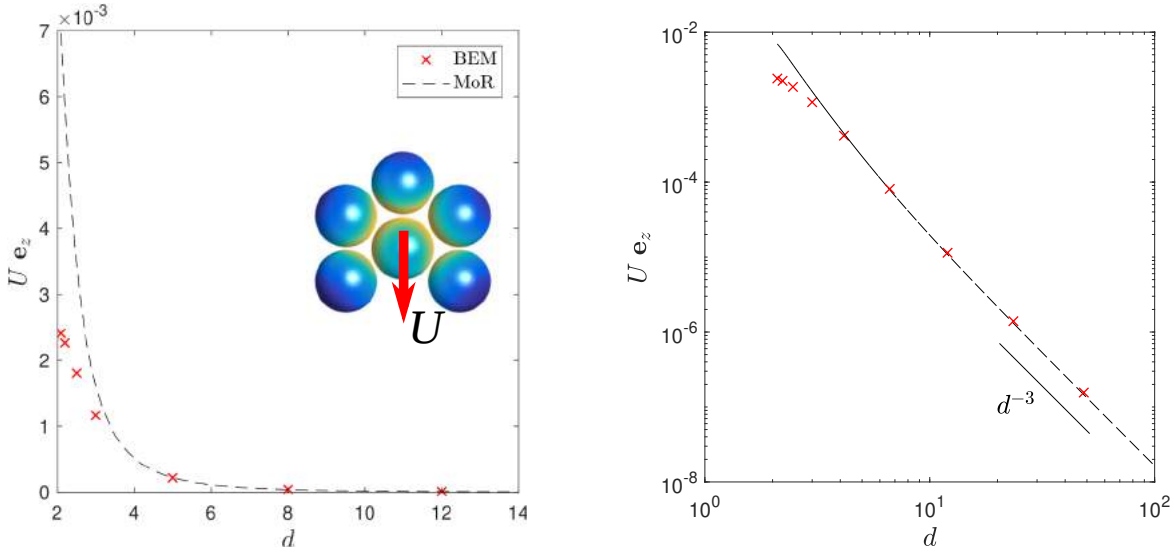

Figure 4.7: Left: Propulsion velocity of a rigid, symmetric 6-particle cluster as a function of the distance d between adjacent particles in a hexagonal lattice. MoR provides accurate predictions only when particle surfaces are more than a radii apart. Right: Scaling of the propulsion velocity of the cluster as d^{-3} when $a/d \ll 1$ as predicted by MoR (dashed line). Red cross represents results from BEM simulations.

to split the problem into two distinct parts: (i) determine the distribution of probabilities for the different cluster shapes using a reduced-order model of the clustering dynamics, and (ii) compute the exact propulsion velocity of each final cluster using regularized BEM.

4.5.1 Stable configurations of an N-particle cluster

A starting point to determine the propulsion statistics is to understand the various possible hexagonal lattice configurations that can be created from a given number of particles. This calculation can only be performed numerically. Restricting here our analysis to two-dimensional clusters, particles are arranged on a regular hexagonal lattice in their final configuration. For $N \leq 5$ particles, a single stable shape is obtained (see Figure 4.5), while for $N > 5$, the number of final distinct cluster configurations is finite but increases exponentially with N; for example: $N = 6$, $N = 8$ and $N = 10$ lead to 3, 9 and 35 distinct configurations, respectively.

4.5.2 Pairwise interaction model

The reduced-order model of the clustering phase required for the first part must be sufficiently accurate, both in the far-field and near-field limits, so that the final configuration is the same as that predicted by BEM, yet be sufficiently inexpensive computationally to be able to run a large number of simulations for each N. At leading order (i.e. far-field approximation), the relative velocity of the particles is determined as the superposition of symmetric interactions between pairs of particles. However, this method fails to provide accurate solutions when the separations between particles are small ($d_c < a$). The method of reflections detailed in Chapter 3, which provides iterative approximations of increasing accuracy, is an appealing alternative to full simulations as it can capture the multi-particle dynamics, but it is fundamentally restricted to distances greater than the size of the particle ($a/d < 1$) for numbers of reflections small enough for practical implementation.

Turning back to the two-particle case, an exact solution for the Laplace and Stokes problems was obtained in Section 4.2 which includes a full description of confinement and lubrication effects. We exploit this solution here to account for far- and near-field dynamics properly, by superimposing the pairwise phoretic drift velocities between the particles whilst retaining the exact analytical solution in Eq. (4.9) $U_a(d_{jk})$ (including the repulsive interaction that prevents particle overlap). In practice, the velocity of particle j is computed in this reduced-order model as

$$\frac{\mathrm{d}\mathbf{R}_j}{\mathrm{d}t} = \sum_{k \neq j} U_a(d_{jk}) \mathbf{e}_{jk}, \tag{4.63}$$

Note that a fundamental restriction of this superposition assumption is its inability to predict any collective propulsion: the velocity of the center of mass of the arrangement is identically zero by definition. Yet, we observed in the full dynamics that such center of mass motion is negligible during the clustering phase, so that this constraint has little physical implication in practice. It should further be emphasized that this superposition of pairwise solutions is not derived from first principles, but rather on its practical ability to capture correctly the leading order interactions both for near- and far-field limits, and its practical ability to match the BEM predictions with good accuracy.

The accuracy of this model needs to be checked in detail against BEM solutions. As test cases we shall study two situations:

1. when there are $N = 3$ particles clustering and the instantaneous dynamics predicted by the model are comparable to BEM
2. when $N = 6$ particles where we shall test if the system does in fact reproduce the same cluster configuration even for small changes in cluster configurations.

Figure 4.8 illustrates the clustering dynamics of $N = 3$ particles starting from arbitrary initial conditions and quantitatively compares the rate of change in relative distance at each time as predicted by the reduced-order model to that obtained using full BEM simulations. The model is observed to predict the clustering velocities with excellent accuracy except for the final stages of clustering where particles are already in contact but for two of them, and the final shape is already fully determined. A second validation of the ability of the reduced-order model to predict the final configuration correctly is proposed in Figure 4.9 where the evolution in time of three different initial arrangements of six particles ($N = 6$) are plotted.

Till the second panel, the interactions between particles are majorly far-field and it can be observed that these positions are accurately captured by the model. The stages of clustering where the particles transform into a particular configuration are set only once the particles are in close contact with each other i.e. it is the near field interactions that determine the final configuration. Thus, the model requires that these crucial near-field interactions be captured accurately. The method of reflections fails in this regard as a large number of reflections would be required to capture the confinement effects of the solute as well as the lubrication effect due to confinement of flow. The current pairwise modelling takes into account the confinement effects but with loss in accuracy because the multi-body influence is neglected; however, as explained in the section on MoR, these are sub-dominant compared to the pair interactions.

This reduced model is formally equivalent to the motion of N particles down the steepest gradient of a pairwise interaction potential $\mathcal{E}$:

$$\frac{\mathrm{d}\mathbf{R}_j}{\mathrm{d}t} = -\frac{\partial \mathcal{E}}{\partial \mathbf{R}_j}, \tag{4.64}$$

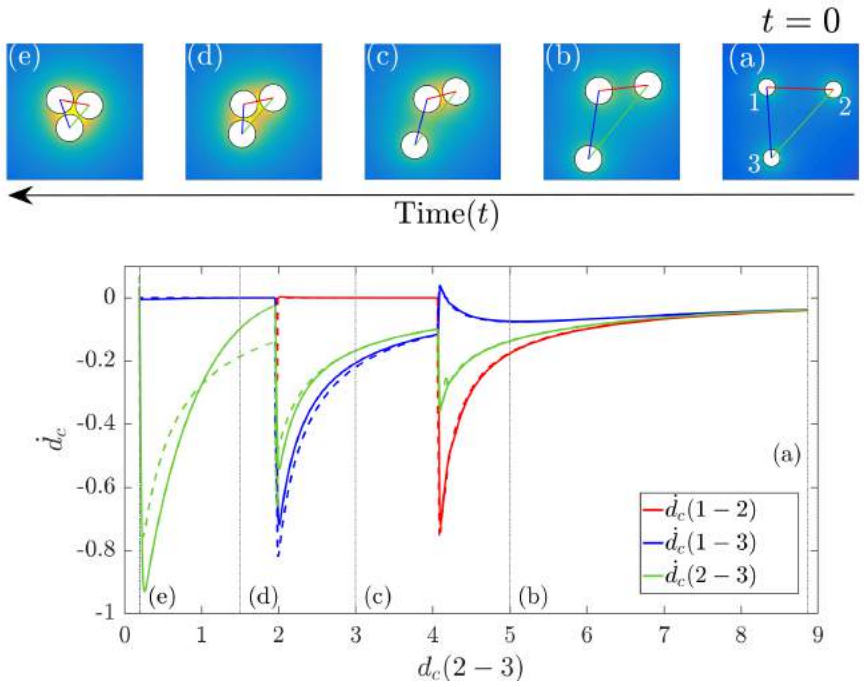

Figure 4.8: Top: from right to left, snapshots of the phoretic clustering in a system of $N = 3$ particles obtained using BEM. For visualization purposes, (a) is zoomed out; the coloured lines represent the distance between centers of different pairs of particles. Bottom: The rate of change of separation $(\dot{d}_c)$ between particles due to phoretic attraction predicted by the reduced model (dashed lines) and BEM (solid lines). The positions of the particles at each instant are set to that of the full BEM simulations. To avoid spurious repulsive velocities arising from slight differences in the equilibrium distance in the reduced model and BEM results and the stiffness of the repulsive model, the repulsive velocities in the reduced-order model are removed once two particles are in contact. The stages of clustering (a) to (e) are also shown (dashed-dotted lines).

with

$$\mathcal{E}(\mathbf{R}_1, ..., \mathbf{R}_n) = \sum_{k>1}^{k} \sum_{j=1} \mathcal{E}_{2p}(|\mathbf{R}_j - \mathbf{R}_k|), \quad \text{and} \quad \frac{\partial \mathcal{E}_{2p}}{\partial d} = -U_a(d). \tag{4.65}$$

Such a formalism is possible only if the interactions between particles are pairwise and hence rigorously holds only for the reduced order model and not for the full problem. The exact solution is *not* a simple pairwise interaction as there exists a non-zero global velocity (albeit small) during the clustering phase. Within the reduced-order model framework, particles arrange to minimize $\mathcal{E}$. As such, $\mathcal{E}$ can be understood as a measure of the cohesive interactions within and stability of a particular cluster shape.

4.6 Phoretic propulsion characteristics

Using the reduced-order clustering model described in the previous section (Phase I), a large number of simulations are performed, with random initial spatial arrangements of particles in order to obtain the probability of formation of the different cluster configurations through phoretic attractions. In a second step, the self-propulsion velocity of each cluster (Phase II)

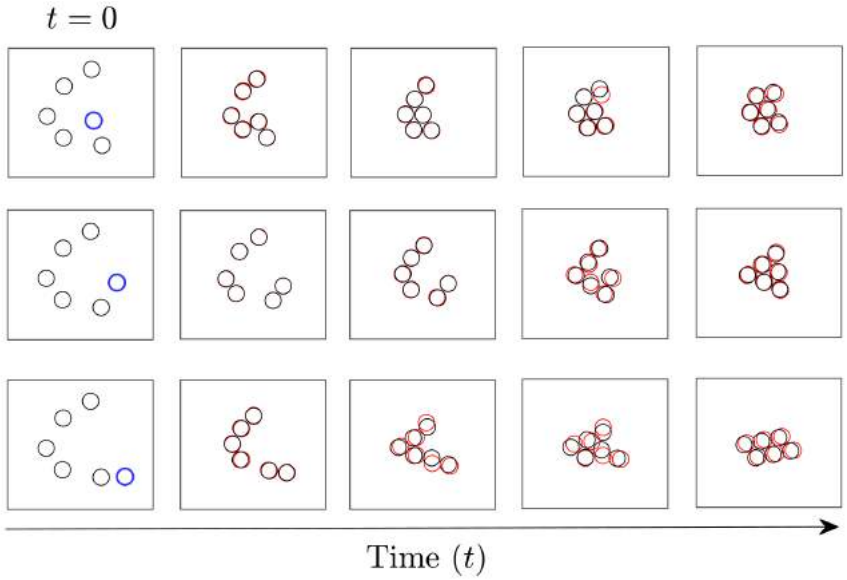

Figure 4.9: Comparison of the positions of the particles predicted by BEM (in black) and reduced model (in red) at various instances. The three different initial distributions of the particles, which differ only in the position of a single particle (in blue), lead to three different cluster shape using BEM, all of which are correctly captured by the reduced-order model.

is computed accurately using BEM and hence, the self-propulsion statistics are obtained for a given system of N particles. (i.e. maximum, mean and most probable velocities)

4.6.1 Probabilities of formation of stable rigid clusters

To distinguish one cluster from another we utilize the cluster potential, denoted by $\mathcal{E}_q$ for any cluster configuration q. If the particles were in thermal equilibrium (motion through purely stochastic process), the cluster formation would be driven solely by the stability of the final shape and so, a Boltzmann distribution would therefore be expected with the probability $\mathcal{P}_q^\sigma$ to obtain cluster q,

$$\mathcal{P}_q^\sigma = \frac{e^{-\mathcal{E}_q/(2\sigma^2)}}{\sum_m e^{-\mathcal{E}_m/(2\sigma^2)}}, \tag{4.66}$$

where σ^2 characterizes the background noise in the system: $\sigma = 0$ leads to $\mathcal{P}_q^0 = 1$ for the most stable cluster (i.e. that with maximum $\mathcal{E}_q$), and $\mathcal{P}_q^0 = 0$ for all others, while $\sigma = \infty$ results in all cluster shapes having the same probability.

Since the system is in a continuous state of non-equilibrium due to phoretic forcing on the particles, these statistics are expected to differ. To study the complete evolution of clustering of an N-particle system from zero interaction potential to a final cluster potential $\mathcal{E}_q$, the particles have to ideally begin from an infinite separation. For the practical purpose of simulations, the particles are initially distributed randomly within a large disk of radius R_{max}. It is ensured that R_{max} is sufficiently large that it does not significantly affect the probability statistics (Figure 4.10). For $N = 6$, which is the smallest value of N for which multiple stable configurations are obtained, probability values converge for $R_{max} \approx 20$ (see Figure 4.10), which corresponds to a density (area fraction of particles in the clustering plane) of 1.5%. For all $N \leq 12$, it is observed that this area fraction of 1.5% is sufficient to give accurate probability statistics.

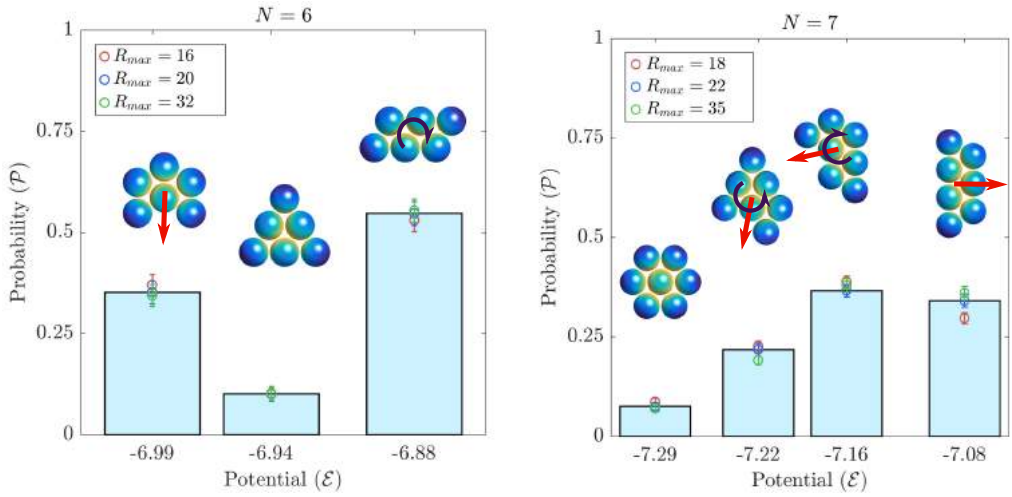

Figure 4.10: Stable 6-particle and 7-particle clusters and their probabilities obtained from 2000 independent trials. Bar graph shows probabilities when particles begin at different random locations within a circle of radius R_{max} for each trial (Histogram shown for $R_{max} = 20$ for 6-particle and $R_{max} = 22$ for 7-particle system respectively). Measurements are made for different R_{max} to show its influence. Range bars represent 2 standard deviation limits of probabilities computed from 50 such events.

The number of independent trials needed to determine the probabilities of configurations accurately increases with N. We found that for $N = 6$ and $N = 7$, 2000 distinct runs are sufficient and the resulting probability distributions and accuracy are shown in Figure 4.10. Clusters are labelled by their effective interaction potential $\mathcal{E}_q$, i.e. the most stable cluster is on the left. Interestingly, Figure 4.10 shows that the most stable cluster (i.e. that with least effective potential $\mathcal{E}_q$ in the reduced-order model) does not have the highest probability as one would expect in a stochastic process. The phoretic clustering described by Eq. (4.65) (i.e. down-gradient of the interaction potential) does not lead to an absolute but to a local minimum, as it depends on the detailed route followed in the configuration phase space during the clustering process. Less "stable" cluster shapes minimize the interaction potential only locally but may be wider attractors in the $(2N-3)$-dimensional phase space that characterizes the clustering motion. Because of the intimate link of cluster shape and velocity, this is expected to hold profound consequences on the collective self-propulsion properties of the N particles.

Once formed, a cluster cannot transition to another configuration without additional forcing (i.e. "energy" input). Even though the differences in the final potential between configurations ($\Delta\mathcal{E}_{pq} = |\mathcal{E}_p - \mathcal{E}_q|$) are relatively small in comparison to $|\mathcal{E}_q|$ and $|\mathcal{E}_p|$ (i.e. the change in potential from the initially-dispersed configuration to the final clustered shape), switching from one configuration to another requires overcoming a much larger potential barrier ($\Delta\mathcal{E}^{\text{barr}}_{p\to q}$). This is illustrated in Figure 4.11 in the case of $N = 6$ particles: changing the position of a single particle around the rest of the cluster allows the arrangement to describe all three possible stable configurations (identified as minima in effective potential $\mathcal{E}$).

While the difference in effective potential of the three stable configurations is small $\Delta\mathcal{E}_{pq} \sim O(0.01)$ ($\{p, q\} \subset \{A, B, C\}$) , transition from one configuration to another requires reaching intermediate stages representing a potential barrier typically an order of magnitude larger, $\Delta\mathcal{E}^{\text{barr}}_{p\to q} \sim O(0.1)$. Note also that the difference in effective potential between the pre-clustering state (ideally, $\mathcal{E} = 0$) and final configuration is yet an order of magnitude larger $|\mathcal{E}_q| \sim O(1)$.

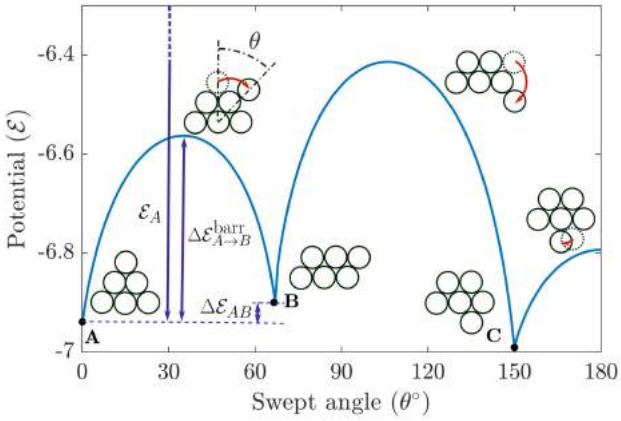

Figure 4.11: Evolution of the assembly potential while rolling a single particle around the cluster from an initial stable configuration A of potential $\mathcal{E}_A = -6.94$ in order to sample all configurations. Clusters A, B and C represent local minima of the effective interaction potential $\mathcal{E}$. $\Delta\mathcal{E}^{\text{barr}}_{A\to B} \approx 0.4$ represents the minimum gain in effective potential required to transition from cluster A to cluster B, while the actual potential difference between clusters is just $\Delta\mathcal{E}_{AB} \approx 0.05$. $|\mathcal{E}_A| \approx 7$ is the change in effective potential between the initial stage and final clustered configuration. The results for $180^\circ \leq \theta \leq 360^\circ$ are obtained by symmetry.

4.6.2 Propulsion velocities of rigid clusters

Geometrically-asymmetric phoretic systems self-propel with a global translation and/or rotation velocity determined only by the asymmetry of their geometric shape [177, 180]; in particular, this velocity is independent of the particles' size. As expected from symmetry arguments, configurations with a single mirror plane of symmetry cannot undergo any rotation. Configurations with rotational symmetry neither translate nor rotate (see Figure 4.10 for example).

As explained, in this clustered arrangement, the relative positions of the particles are fixed in a regular hexagonal lattice. For each N-particle system, the regularised Boundary Element Method detailed in Appendix C is used to compute the exact translational and angular velocities of propulsion (Phase II) of all possible cluster configurations. A list of the fastest propelling and rotating clusters, as well as the most probable ones are shown in Figure 4.12 for $9 \leq N \leq 12$. By defining the normalised effective potential for shape q for fixed N as $\mathcal{E}_r = (\mathcal{E}_q - \mathcal{E}_{\min})/(\mathcal{E}_{\max} - \mathcal{E}_{\min})$, we observe that the fastest propelling (translation or rotation) clusters are some of the least stable clusters with respect to the large effective potential $\mathcal{E}_r$. This is the result of their large geometric eccentricity, responsible for their larger propulsion velocity through the larger concentration gradients at their surface it creates. In contrast, the most probable clusters are characterized by their more compact and roughly symmetric arrangement around their geometric center (see Figure 4.12).

4.6.3 Statistics of clustering-induced self-propulsion velocities

Combining the results of the previous sections, the statistical properties of the collective self-propulsion of N isotropic particles resulting from their phoretic clustering are obtained here. Figure 4.13 shows the mean and maximum velocities of N-particle clusters. In particular, for a given N, noting $\mathcal{P}_q$ the probability and U_q the velocity magnitude (or equivalently,

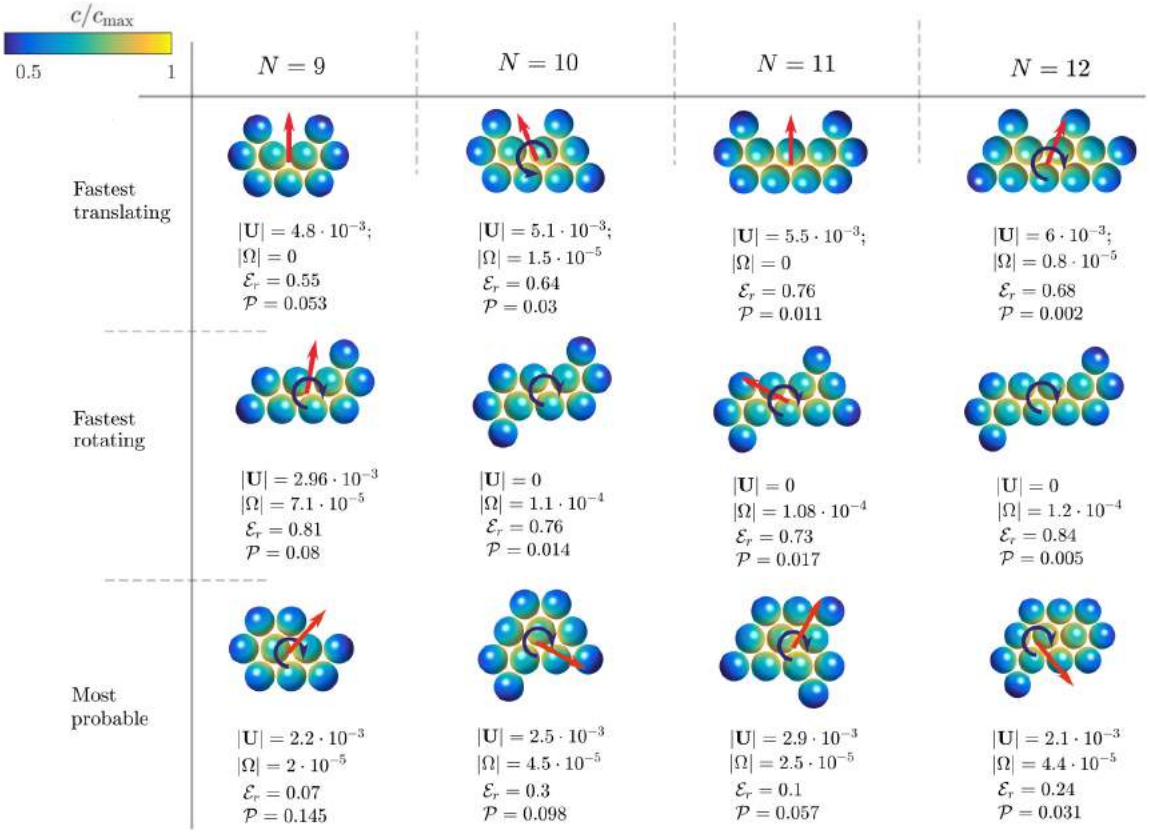

Figure 4.12: Fastest translating (top), fastest rotating (center) and most probable clusters (bottom) for $N = 9$ to 12. The relative surface concentration is shown in color for each cluster as well as its propulsion, stability and probability characteristics.

rotational velocity magnitude Ω_q) of cluster shape q, the mean velocity is defined as

$$U_{\text{mean}}(N) = \sum_q \mathcal{P}_q U_q, \quad \Omega_{\text{mean}}(N) = \sum_q \mathcal{P}_q \Omega_q, \tag{4.67}$$

with the sum carried out on all possible cluster shapes.

Because of the symmetry of the only existing final cluster, no self-propulsion is observed for $N \leq 4$. Note that for all $N > 5$, at least one non-propelling cluster (having rotational symmetry) is found; and therefore the minimum velocity for all $N > 5$ is strictly zero. The maximum propulsion velocity is observed to increase steadily with N as the larger number of particles allows for more eccentric shapes and larger phoretic forcing. However, the mean velocity $U_{\text{mean}}(N)$ is observed to saturate for larger values of N. Insight on this result as well as other statistical properties of importance such as the most probable velocity and the variance in propulsion velocities of large N-particle clusters is obtained by studying the probability distribution of the propulsion velocities (Figure 4.14).

The probability distributions of translational velocities of clusters with $N \geq 10$ show a prominent peak near the mean value of the distribution ($\approx 2 \times 10^{-3}$) indicating that clusters with this velocity are also the most likely to form. The most probable angular velocity, however, is lower than the mean value ($\approx 2.5 \times 10^{-5}$). As the maximum velocity (translation and rotation) increases with N, the graph spreads indicating an increase in variance of velocities between the various configurations. However, the fastest propelling configurations, which are also some of the most eccentric and elongated ones, have very low probability so that such clusters are only seldom observed for large N, and hence their contribution to the

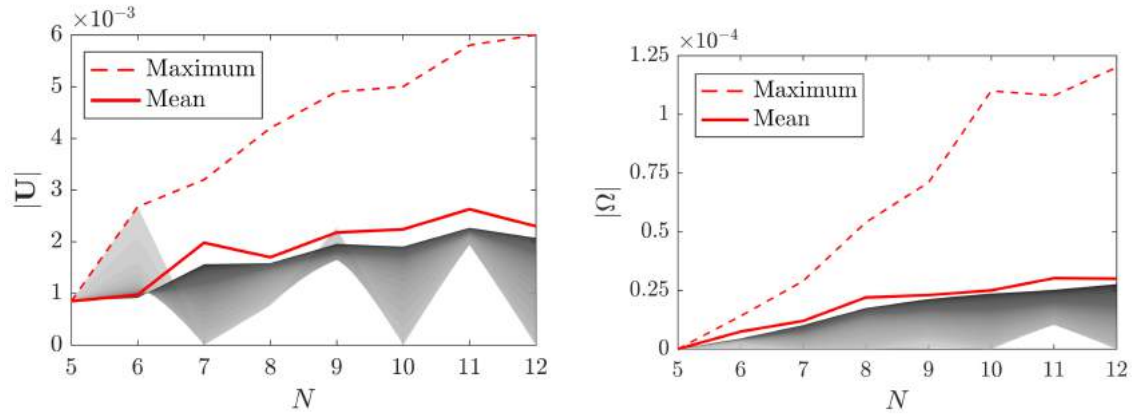

Figure 4.13: Magnitudes of maximum (dashed) and mean (solid) translational and rotational velocities of clusters obtained using BEM. The grey shading represents the mean velocity obtained through an equilibrium distribution, Eq. (4.66) with the noise level σ^2, increasing from zero to infinity as the intensity of shading gets darker.

mean velocity is minimal. For $N \geq 10$, most of the contribution to the mean properties is brought by clusters with an intermediate velocity which remains relatively fixed with N, leading to the saturation in the mean velocity as N grows. This can be qualitatively understood from the most dominant features of the most probable clusters as depicted in Figure 4.12: those clusters display more compact shapes with an asymmetry arising only from a small number of particles.

It was already emphasized above that the probability of formation of a given shape in the phoretic clustering process does not correlate with its effective potential $\mathcal{E}$ for the reduced-order model, as would be expected in a classical system at thermodynamic equilibrium, for which the probability of formation of various configurations follows a Boltzmann distribution, Eq. (4.66). Not unexpectedly, this has consequences for the collective propulsion properties: Figure 4.13 shows that the mean velocity resulting from phoretic interactions is systematically larger than it would be under the sole constraint of minimizing the effective interaction potential, regardless of the importance of noise in the process.

4.7 Effect of noise on clustering statistics

The previous sections focused on the clustering-induced collective dynamics of phoretic particles, *in purely deterministic systems*: for a given particles' arrangement at time t, the evolution of the particles' position in time is fully determined. Yet, in practice, all such systems which focus on microswimmers are subject to a variety of stochastic processes (including thermal noise) which continuously alter their motion. In the presence of background noise caused by temperature of the surrounding fluid, passive microscopic particles (or isolated isotropic phoretic swimmers) undergo Brownian motion characterized by zero mean displacement. Active particles however have a net displacement with continuous reorientation of the direction of propulsion, thus exhibiting diffusive behaviour in long time scales [181, 25]. Commonly employed minimal models for these *Active Brownian Particles* describe the essential dynamics involving overdamped motion (Langevin dynamics) as well as their thermal reorientation [182, 25].

Equivalently, in the case of isotropic phoretic particles, we describe the clustering process

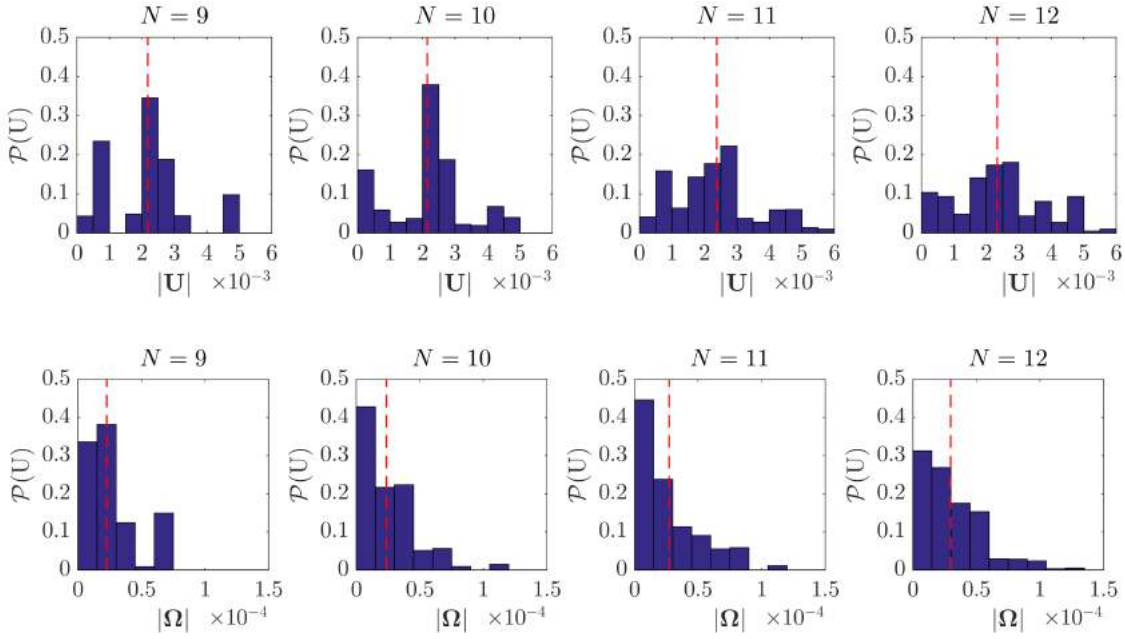

Figure 4.14: Probability distribution of (top) translational velocities $\mathbf{U}$ and (bottom) rotational velocities $\mathbf{\Omega}$ of N-particle clusters. The distribution mean is indicated by a dashed red line for each N.

by its reduced-order model (see Section 4.5.2) rather than using the full BEM simulations because of its versatility and reduced computational cost, as well as to maintain consistency with the rest of the manuscript. Hence, the deterministic dynamics of the particles corresponds to a collective minimization of the effective interaction potential $\mathcal{E}$ as defined in Eq. (4.65). The purpose of this section is therefore to provide some insight on the robustness of these deterministic results, i.e. how the results of self-propulsion statistics obtained in the previous sections are modified in the presence of background noise on the kinematics of individual particles.

In the absence of inertia, the evolution of the position $\mathbf{R}_j^{(b)}(t)$ of particle j under the effect of background noise is given by the overdamped Langevin equation:

$$\frac{\mathrm{d}\mathbf{R}_j^{(b)}(t)}{\mathrm{d}t} = \mathbf{U}_j(t) + \boldsymbol{\xi}_j(t), \tag{4.68}$$

where its deterministic velocity, $\mathbf{U}_j(t)$ is given by Eq. (4.65), and $\boldsymbol{\xi}_j(t)$ is a external Gaussian white noise, with zero mean and a variance, $\sigma^2\mathbf{I} =< \boldsymbol{\xi}_i(t)\ \boldsymbol{\xi}_j(t') >= 2D\delta(t-t')\delta_{ij}\mathbf{I}$, where D is the diffusivity of each particle in the fluid. Thus, the instantaneous displacement of particle j at any time t is

$$\mathrm{d}\mathbf{R}_j^{(b)}(t) = \mathbf{U}_j(t)\mathrm{d}t + \mathrm{d}\mathbf{W}_j, \tag{4.69}$$

where $\mathbf{W}_j$ is a Weiner process with zero mean and variance $\sigma^2 t\ \delta_{ij}\mathbf{I}$. Discretizing Eq. (4.69) by using Euler-Mayurama method gives

$$\mathbf{R}_j^{(b)}(t+\Delta t) = \mathbf{R}_j^{(b)}(t) + \mathbf{U}_j(t)\ \Delta t + \Delta\mathbf{W}_j, \tag{4.70}$$

$\Delta\mathbf{W}_j$ is also a zero mean Weiner process with variance $\sigma^2\Delta t\ \delta_{ij}\mathbf{I}$. Equation (4.70) is solved using an adaptive time stepping method.

A system of $N = 6$ particles is the smallest system that exhibits multiple clustered configura-

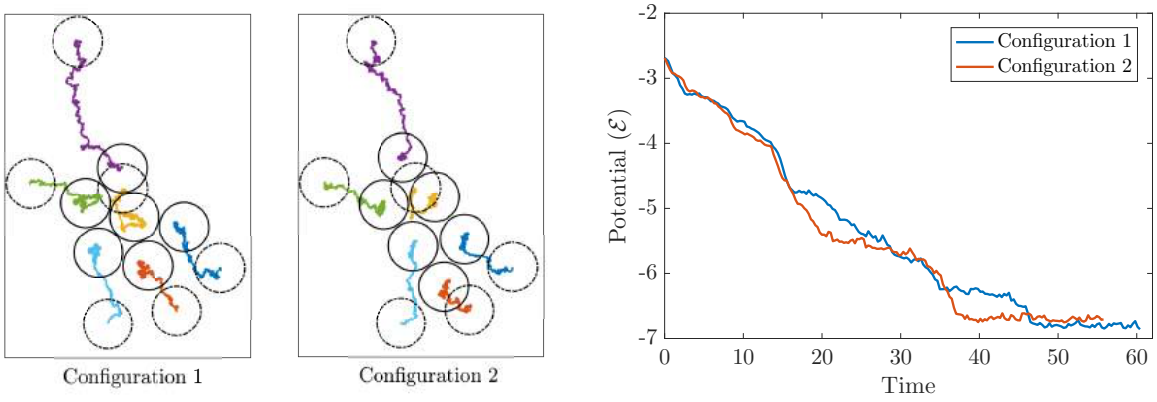

Figure 4.15: Formation of different clusters from the same initial positions of particles in the presence of noise of strength $\sigma^2 = 0.01$. Variation in potential of system with time during clustering for the cases shown.

tions, and for which the introduction of noise is expected to potentially introduce significant modification in the collective dynamics; we shall henceforth consider $N = 6$ as an example to illustrate the effect of noise on the clustering statistics and resulting propulsion properties. A direct result of the component of randomness in position of particle in Eq. (4.70), is the formation of multiple configurations from the same initial conditions of the system. For each set of initial conditions (typically a few hundreds), Eq. (4.70) is used to run about 100 simulations. If the strength of noise satisfies $\sigma^2 \sim |\mathcal{E}_q|$, background fluctuations are sufficient to break the formed clusters and redistribute the particles far apart. Hence, we restrict ourselves to the case where σ^2 is much smaller than the absolute cluster potential, $|\mathcal{E}_q|$ so that phoretic effects are still dominant and clustering occurs. In the following, two different behaviours are observed under the effect of noise, depending on its relative magnitude (σ^2) and the effective potential barrier $\Delta\mathcal{E}^{\text{barr}}_{p\to q}$ from configurations p to q (see Figure 4.11).

4.7.1 Low noise

Low noise conditions are characterised by $\sigma^2 \ll \Delta\mathcal{E}^{\text{barr}}$, which is not sufficient to change the configuration of a stable cluster once formed. However, it can influence the clustering dynamics by rearranging the particles as the system moves down the steepest gradient in interaction potential, as seen in Figure 4.15.

Its influence is particularly important when particles are far apart, i.e. when differences in $\mathcal{E}$ are small and of order σ^2. For this reason, one may wrongly presume that noise would change the probability statistics for the formation of cluster configurations. Instead, the probability statistics remain identical to that in the absence of noise (see Figure 4.16).

This result can be explained as follows: although a low background noise is expected to enable the system to explore neighboring routes in the configuration space to minimize the system's potential, $\mathcal{E}$, during the clustering phase, it is only effective in the initial stages where system has low $\mathcal{E}$; in the later stages, the magnitude of the noise becomes too small in front of the deterministic velocity (determined by $\nabla_{\mathbf{R}_i}\mathcal{E}$) to significantly alter the particles' trajectories. However, a lower potential during the initial stages does not ensure a low potential of the cluster thus formed (as observed in Figure 4.15). Thus, the noise just effectively redistributes the initial arrangement of the particles. But this randomness is already taken into account in the probability of formation of different clusters by considering

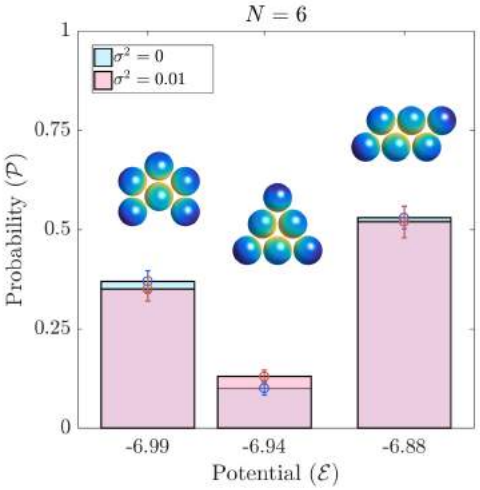

Figure 4.16: Comparison between probabilities of formation of 6 particle cluster configurations in the absence of noise and with low noise shows no significant difference in the statistics. The clustering was performed with $R_{max} = 16$ in both cases. In the case of low noise ($\sigma^2 = 0.025$), probabilities are computed from 200 random initial arrangements of particles with 100 trials per arrangement.

a large number of random initial positions. As a result the collective propulsion statistics in Figure 4.13 remain unmodified in low-noise conditions.

4.7.2 High noise

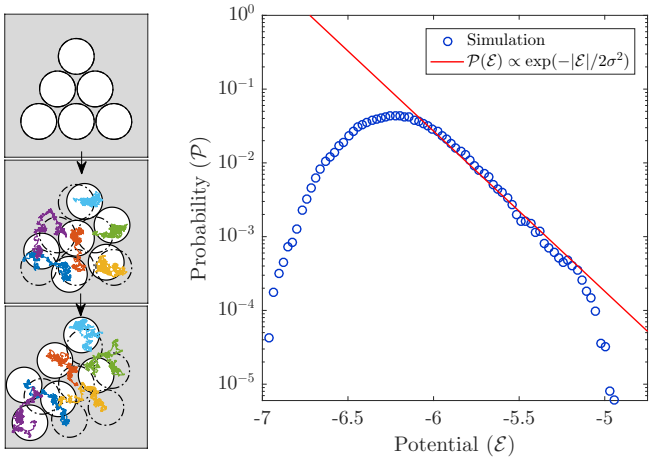

Figure 4.17: Formation of different cluster configurations by rearrangement of particles over time due to high noise, $\sigma^2 = 0.1$. Also shown is the probability distribution of various cluster configurations which follow a Boltzmann distribution. Since the average separation between particles are larger due to the continuous high noise, $\mathcal{E}$ takes larger values.

In the presence of sufficiently large noise, $\sigma^2 \sim O(\Delta\mathcal{E}^{\text{barr}}_{p\to q})$, a cluster, once formed, continuously transitions from one configuration to another without dislocating fully since the noise intensity remains much smaller than $|\mathcal{E}_q|$. This situation is in stark contrast with the low-noise dynamics for two main reasons: (i) it is not possible anymore to define a fixed cluster shape to the arrangement of the particles which continuously evolves in time and transi-

tions between all the available configurations, and (ii) the clustering dynamics does not play a significant role anymore. Indeed, since the particles' arrangement can be reconfigured, which cluster shape was reached in the first place is not relevant. Instead, how much time the particles spend in a particular configuration is now the significant information. This can be characterized as the probability to obtain a given configuration at any time, which is the result of the equilibrium between the background noise and the phoretic attraction. Not surprisingly, this probability now follows a Boltzmann distribution (Figure 4.17). However, since multiple intermediate configurations (with the same potential) exist, the probability of a particular stable configuration cannot be defined.

4.8 Conclusions

The results presented in this chapter therefore establish a fourth route to self-propulsion of active colloids. Unlike previously-identified strategies which relied either on an asymmetric design of the particle or the non-linear convective transport of solutes by the phoretic flows, self-propulsion of individually non-motile yet active particles is achieved here by non-symmetric interactions between multiple particles. Under the effect of attractive phoretic attractions and steric constraints, particles form geometrically-asymmetric clusters that are able to maintain the asymmetric concentration fields required for propulsion. The self-propulsion velocities are much lower (by at least an order of magnitude) than typical active Janus colloids, but lead nonetheless to a net migration of the particles.

Even though the governing dynamics of the particles (in the absence of external noise) are completely deterministic, multiple particle arrangements can be reached depending on the detailed dynamics of the cluster formation and balance between phoretic attraction and steric repulsion. Slightly different initial positions of the different particles may therefore lead in fundamentally different propulsion characteristics, thereby introducing an inherent stochasticity in the system. Focusing for simplicity on two-dimensional arrangements of the particles (the hydrodynamics and solute diffusion are three dimensional), the probability of formation of the different cluster shapes was determined for increasing N using Monte-Carlo simulations of the phoretic clustering for N particles with initially-random positions. These simulations were performed using a reduced-order model of the clustering process obtained by superimposing the velocity induced on a given particle by each of its neighbors as in a two-particle system, for which an analytical solution was first obtained.

Using these probabilities and the velocity of the different clusters computed numerically using a regularized Boundary Element Method, the statistics of the collective self-propulsion were obtained, namely the mean, maximum and most probable velocities, for both translation and rotation. The maximum attainable velocity was found to increase with N: for larger clusters, a greater degree of asymmetry can be achieved leading to larger velocities. The mean propulsion velocity on the other hand was found to saturate for increasing N: the most eccentric clusters with large velocity also become less and less probable as N increases, while the most probable clusters exhibit a more compact geometry with velocities close to the mean value.

The particles are continuously in a state of non-equilibrium. The lack of external noise to relax the system creates probability statistics of various configurations which are strikingly different from equilibrium statistics. This difference directly affects the velocity statistics and we observe a larger mean velocity compared to that expected from a purely equilibrium process. Yet thermal noise and Brownian motion can become important for smaller particles, and their impact on the present result was tested by introducing a Brownian component in

the motion of the active particles in addition to their deterministic phoretic clustering. Two different situations are observed depending on the magnitude of the noise with respect to the phoretic forces maintaining the cohesion of the formed clusters. The cluster probability and velocity statistics are found remarkably robust to low noise amplitude (i.e. thermal fluctuations that are unable to break or reconfigure a given cluster): such noise levels essentially redistribute the already random position of the particles in their initial state (before clustering). In contrast, higher levels of thermal noise can lead to cluster break-up or reconfiguration. In the latter, a given cluster undergoes continuous transition between different configurations, and the probability to find a given shape follows an equilibrium probability distribution. In that case, the group of N particles continuously reconfigure leading to changes in its translational and rotational velocity. This provides it with a self-propelled motion which is reminiscent in some regards to the run-and-tumble behaviour of bacteria where self-propulsion in a given configuration is followed by a geometric reorganization that modifies its swimming direction and velocity magnitude [183]. Although the process is quite different here, in particular because the relative length of a run is significantly smaller than for bacteria, it is expected to enhance transport by diffusion.

5

Conclusions and perspectives

In this chapter, we shall draw some final conclusions of the thesis and also provide some perspective applications of the MoR framework for modeling dynamics of autophoretic particles in complex environments and suspensions.

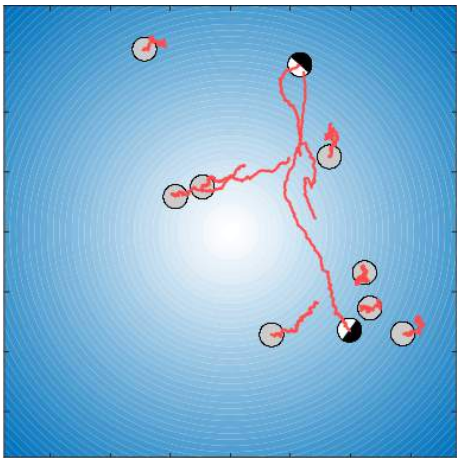

Dynamics of a mixture of active and passive spheres.

Contents

The goal of this thesis is, from a broad perspective, on modeling the physical interactions between active particles in a fluid suspension and, to study their resulting collective behaviour. The active particles considered here are phoretic colloids which "swim" in a fluid through gradients of a solute concentration field; the physico-chemical mechanism of propulsion is known as *diffusiophoresis*. This concentration field is self-generated through catalysis of a chemical reaction on the surface of each colloid. The particles influence each other through long-range chemical and hydrodynamic interactions, and short-range steric effects.

The fundamental reason for the collective behaviour is the thermodynamic non-equilibrium nature of the system which arises from continuous motion of the particles. Systems which are far from equilibrium exhibit much richer fluctuations and, pattern-forming behaviour than systems in equilibrium [7]. For example, in suspensions of active colloids, one can observe spontaneous formation of wave fronts and 'critters' [87, 22, 23]. Active colloidal suspensions also show non-equilibrium phase transitions due to collective interactions between the particles, such as complete coarsening, gas-like state, dynamic clusters, open-gel states [101, 87, 121] etc.. Hence, from a physical perspective, understanding the effect of the interactions between various active particles can give insight into these complex dynamics. Moreover, by modeling a system where the physico-chemical properties of the active elements can be appropriately tuned, one can even make comparison with organic swimming matter such as chemotactic bacteria to differentiate between the physical and psychological nature of the interactions [85].

From an engineering perspective, active colloids entail potential for controlled transport at microscopic scales for therapeutic and bio-medical applications [184]. The field of engineering at microscopic scales is still at a nascent stage, and characterizing the properties of active colloidal suspensions are critical in the field of material science and chemical engineering for development of active fluid suspensions with desired physical properties. Much progress is also being made in development of micro-machines using active colloids; the theoretical analysis presented in this thesis on the propulsion arising from spontaneous clustering of autophoretic colloids forms the simplest case of self-assembled colloidal micromotors that were developed recently [83]. Experimental research on the collective dynamics and interactions of these colloids with surroundings have gained immense attention over the last few decades since the possibility of manufacturing colloids with precisely tailored physico-chemical properties in very large numbers. A commonly used colloid is one which is composed of two different materials - known as a Janus particle; one material (such as Silica) forms the base colloid on which a reactive metal cap (such as Platinum) is added.

At the same time, theoretical investigations not only aim to aid in designing appropriate phoretic particles for a specific engineering task, but also give insight into effect of various physico-chemical interactions on the particles with itself and the surroundings which can provide a fundamental understanding of active systems [20]. Determining the exact (analytical) solutions to the multi-body dynamics of phoretic particles is not possible, unless full numerical simulations are performed using methods such as Boundary Element Methods, or Immersed Boundary Methods. However, these numerical techniques are limited by the computational cost involved, and more than a few tens of particles is the limit [137, 138, 130]. These are hence, currently not viable options for determining the dynamics of particles in large suspensions. Developing efficient and accurate models, capable of handling systems with a large number of particles, to predict their dynamics is a subject of intense research. Current modeling approaches involving a large number of particles rely on phenomenological models such as Phoretic Brownian Particle (PBP) model, or (Active Alingnment) AAA models [87] which consider only the chemotactic interaction as the alignment interaction between point particles. Physical models are currently restricted to far-field models which consider the particles as point source (or sink) of a solute and, a hydrodynamic stresslet

[185, 186, 124]. Such physical models are valid only in the dilute suspension limit. They have been extended to model the dynamics in the continuum limit; however, this mean-field approach cannot capture certain states of the system such as dynamical clustering [121, 101, 185].

Accurate theoretical models can thus not only shed light on the different interactions between phoretic particles and their dynamics at microscopic scales, but can also contribute significantly to understanding the macroscopic properties of their suspensions, which are otherwise difficult to determine [187, 188]. With limitations on computational times, physical models are the best means of determining the dynamics in a suspension containing large number of particles. Thus, there is currently a large body of scientific interest on developing detailed models that can be used to study phoretic suspensions. This thesis intends to contribute to this idea by using the classical *Method of Reflections* approach to develop a framework that determines an asymptotically more detailed model to determine the chemical and hydrodynamic interactions between the particles; a consequence of this more detailed approach is the identification of a new route to self-propulsion arising from spontaneous clustering of individually non-swimming isotropic phoretic colloids.

5.1 Summary and conclusions

The autophoretic particles have two physico-chemical properties: their surface activity and, their surface mobility. Their activity is their ability to emit or consume certain solute through chemical reactions on their surface. The gradients in solute concentration field create an effective slip velocity on the surface of the phoretic particle which propels them. The governing dynamics of the self-propulsion of these particles is thus based on physico-chemical hydrodynamics. For ease of analysis, we have considered a constant flux model, and in such a case, the velocity of the phoretic particle is independent of its size. Furthermore, we have considered only the case where the particles have uniform surface mobility. This is however not strictly the case in practical situations where a Janus particle, comprising of two different materials, are expected to have different surface properties.

The chemical field created by the particles was taken to be purely diffusive in nature and the flow field was considered to be viscous dominated (as is common in flows due to motion at microscopic scales). In this setting, the current physical models in literature consider only the far-field interactions i.e. these models consider the particles to be sufficiently far apart ($\varepsilon = a/d \ll 1$), they behave as point source of chemical and has a hydrodynamic stresslet signature at the leading-order. Although the higher-order fields decay much faster, at close ranges, which is expected in denser active suspensions, these interactions cannot be neglected. Moreover, the far-field models become inaccurate at short distances between particles because the non-zero size of the particles and the chemical patterning of surface activity are omitted in the analysis. Thus, to improve the accuracy in determining the interactions, one has to take into account both the higher-order chemical and hydrodynamic fields as well as the effect of size and orientation of the phoretic particles.

To this end, we have developed a unified framework based on the Method of Reflections (MoR) for both the chemical and hydrodynamic problems. The MoR framework is based on the idea of asymptotically approaching the prescribed chemical and hydrodynamic boundary conditions on the surface of the particles by compensating for the spurious effects created by the surrounding particles. Thus, this framework goes beyond the far-field model, which considers only point particles, by taking into account the non-zero surface area of the particles. It however needs to be noted that the framework presented here is valid only for spherical

particles. The chemical and hydrodynamic fields being harmonic in nature are decomposed into its spherical harmonic modes. The strength of each of the modes are corrected for, in powers of ε, at each *reflection* to satisfy the surface boundary conditions. Thus, MoR takes into account of the higher-order chemical and hydrodynamic modes. Despite its asymptotic nature and the fact that it is inherently not designed to represent near-contact dynamics such as lubrication effects, the method converges rapidly: an accuracy of $O(\varepsilon^5)$ in propulsion velocities were obtained using just a single reflection for the hydrodynamic problem and the chemical field. After p reflections, one can obtain an asymptotic order of accuracy of $O(\varepsilon^{3p+2})$. However, the possible combinations of reflected modes that need to be considered increase exponentially with the number of reflections; these reflections being cumbersome to compute from the general expressions provided in Chapter 3. Nonetheless, once an analytical expression is obtained, it is quite direct to be implemented. We have shown that the MoR framework, restricted to $O(\varepsilon^5)$ is sufficient to predict the velocity of particles to high accuracy even for inter-particle contact distances of the order of their radius.

The performance of the predictions using MoR are significantly better, qualitatively and quantitatively, than classical far-field models because by taking into account multiple reflections, one includes multi-body interactions which are neglected in the latter. So, far-field models can be seen as ε^2-truncations of the present framework. Such far-field models are widely used due to their simplicity [122, 125, 124]; yet, as they focus solely on pairwise particle interactions through the slowest-decaying hydrodynamic and chemical signatures, they fundamentally overlook more complex chemo-hydrodynamic interaction routes which result from many-body interactions. Additionally, the present framework in fact provides a unique opportunity to analyse rigorously the relative weight of different interaction routes, as each interaction type can be turned on or off easily in the model (a feature that is much more difficult to implement on a full numerical simulation for example). Furthermore, this framework well-suited for analysing the dynamics of a very large number of particles and of suspensions. with the number of particles N, with a $O(N^2)$-computational cost for large numbers of particles, which makes it a very compelling candidate to obtain quantitative insights in the behavior of large active suspensions. The computational costs are in par or better than current modeling approaches for low-Reynolds number swimmers [142, 189]

We have examined the collective dynamics in a special case of active fluid suspensions where the system comprises only of phoretic particles with homogeneous surface activity and mobility. In isolation, these particles do not self-propel from lack of phoretic forcing due to isotropy of the surface concentration field. By introducing an additional particles in the system, the symmetry of the field around each particle is broken by the external field created by the other; this introduces a forcing that pulls the particles towards each other, albeit with negligible global motion. However, remarkably, a global motion is observed once the particles form a rigid cluster. The MoR framework reveals that this property of collective self-propulsion of the system, arising from spontaneous clustering of the individually-non-swimming particles, is due to a complex coupling between chemical, hydrodynamic and steric interactions between them in the cluster.

This is the most fundamental example of what is now known as *modular swimmers* - those artificial micro-swimmers that achieve self-propulsion or enhanced transport from spontaneous formation of clusters [190, 183]. Modular swimmers are gaining popularity as means of tailoring micro-machines in-situ; this hence gives the flexibility of having their properties adjusted while in operation within the fluid [183, 83]. The simplest form of modular swimmers are those formed spontaneously from isotropic particles; these do infact show the versatility of creating clusters which can translate, rotate or both or neither depending on the arrangement of the individual particles.

In a system comprising of N isotropic particles, the propulsion velocities of the resulting cluster are stochastic in nature, not from any imposed background noise, but rather from

inherent possibilities of the system to form multiple cluster configurations based on the initial arrangement of particles. It has to be thus noted that these probability statistics are fundamentally different from equilibrium statistics. By computing the propulsion velocities using full numerical simulations with Boundary Element Methods (BEM), we elucidated the velocity statistics viz. the mean and maximum propulsion velocities in a system containing N particles (till $N = 12$ particles). The maximum propulsion velocity is noted to increase monotonically with increase in N while the mean velocity saturates to a value $\approx 2 \times 10^{-3}$ for large N. This is because the propulsion velocity is higher for oblong asymmetric clusters, and while this aspect ratio can be increased with increase in size of the cluster, the probability of formation of such clusters from initial random arrangement of particles. Thus, by identifying and characterising the clustering-induced self-propulsion of the isotropic phoretic particles, we have established the features of a new route of self-propulsion, arising not from individually tailored surface properties [58], or geometrical asymmetries [61], or from advective redistribution of solute [65], but rather from collective interactions. The swimming velocity of clusters are however computed to be an order of magnitude smaller than a true Janus particle. The velocity of clusters containing large number of particles are however yet to be understood.

The velocity calculations for large N are restricted by the availability of computational resource. An approximate value could be computed using MoR for large N, but would be accurate only when particles in the rigid cluster have large inter-particle surface separation. This is because solute confinement as well as hydrodynamic lubrication effects, which are strong a close separations, play a major role in determining the propulsion velocity of the cluster and these require a large number of reflections to be captured analytically. A qualitative idea of the propulsion velocity statistics could nonetheless be obtained using MoR.

5.2 Future perspectives: Some applications of MoR framework

The MoR framework is a versatile tool to study the dynamics of particles beyond the dilute limit in suspensions. The framework is generic in the sense that it is also applicable to study systems containing particles regardless of their physico-chemical properties; the varied properties of the colloids naturally lead to symmetry-breaking of the concentration field and could lead to self-assembly and propulsion of the clusters [62, 191]. Direct experimental evidence of the propulsion properties of self-assembled clusters within a mixture of active and passive particles have been observed [192]. As we have seen, the MoR framework, could be readily applied to predict this self-propulsion behaviour and also study the interaction dynamics of such clusters in more detail. This opens up the avenue for studying dynamics of dimer motors [193], suspension of particles with mixed activity and mobilities [191, 194].

To revel this perspective application, we shall hint on using the model to study the effect of active particles in the diffusion of passive tracers in their suspension. It is well known that passive particles immersed in an active fluid show enhanced diffusivities due to the interactions with the active particles such as bacteria in the suspension [195, 196, 197]. But how is this modified in the presence of chemical interactions? The passive particles considered here have no activity, but however posses a uniform surface mobility ($M = 1$) which drifts them towards a region of lower solute concentration i.e the particles are chemorepulsive; the active particles are also assumed here to have the same surface mobility. Situations involving interactions between active phoretic matter and their dynamics have

been studied previously, however in the light of chemo-attractive nature which naturally leads to their clustering [121]. Here, we seek to explore the effective diffusivity of the passive particles due to chemical and hydrodynamic interactions with the phoretic swimmers.

To prevent the self-swimming Janus particles from escaping to infinity they are immersed in a harmonic potential well; the passive particles are however not influenced by the well. In experiments, such the potential well is usually established with the aid of light using a mechanism known as *optical trapping* [198]. The focused laser beam creates the well, which is assumed here to be parabolic in nature [16]. The potential field is hence defined as

$$V(\mathbf{r}) = \frac{1}{2}kr^2 \tag{5.1}$$

where k is the *stiffness* of the well. For our simulations we use $k = 0.25$. For a Janus particle of unit radius with hemispherical surface activity, the self-propulsion velocity $U^{\text{self}} = 0.25$. The MoR approach for is validated for $O(\varepsilon^5)$ accuracy by comparing with analytical solution for the case of axisymmetrical configuration of a phoretic particle near a passive sphere (see Appendix B).

To compare the effect of active particles on the diffusivity of passive spheres, a background Brownian noise is added to the system. Their mean-squared displacement (MSD) in the presence of active particles are compared. All the particles, being of the same size and shape, have the same translational and rotational diffusivities (denoted by D_t and D_r respectively), taken in our simulations to be $D_t = 10^{-3}$ and $D_r = 10^{-2}$.

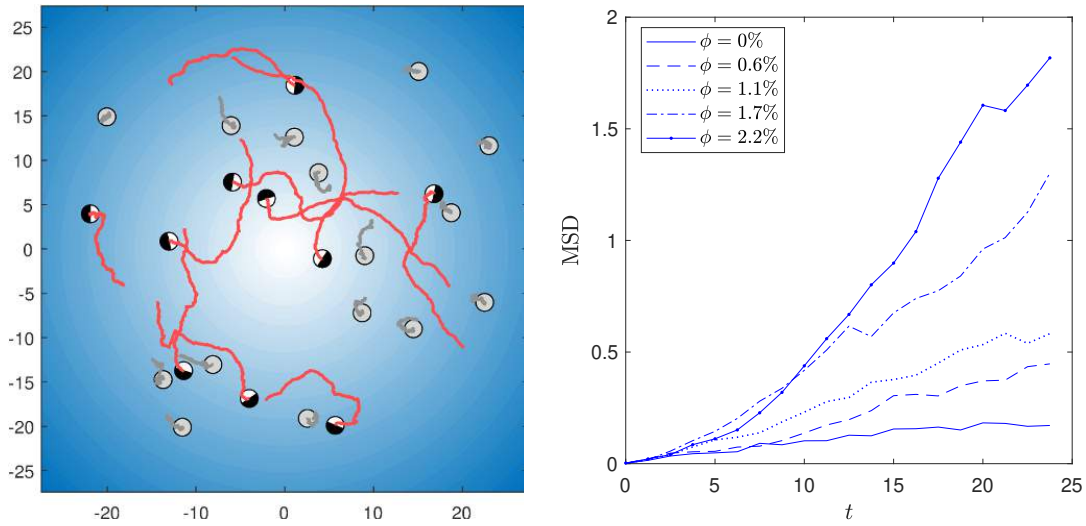

Figure 5.1: a) Trajectories of a system of active Janus particles occupying area fraction $\phi = 2\%$ and passive particles (in gray) of area fraction 2% over time $t = 100$. In isolation, each particle diffuses with translational diffusivity $D_t = 10^{-3}$ and rotational diffusivity $D_r = 10^{-2}$. The intensity of background colour is proportional to the magnitude of the radially inward force $\mathbf{F}$ on Janus particles due to the potential well. b) Mean-squared displacement of the passive particles as a function of time for various area fractions of Janus particles (ϕ).

It is observed from figure 5.1(b) that the MSD, in the absence of active swimmers i.e. $\phi = 0\%$, increases linearly with time as expected for a diffusive process. When the phoretic particles are introduced, the mean-squared displacement of the passive particles increases; this enhanced diffusivity is observed as the density of swimmers are increased. The nature of transport beyond area fraction of $\phi = 2\%$ however needs to be explored in detail as the displacement appears to be ballistic, as in the case of Janus particles, instead of diffusive.

Diffuivities when particles are distributed randomly in space, rather than initial restriction to a plane, is a possible future outlook to study diffusivity in 3D.

By making the passive sphere stationary, it becomes an obstacle to the motion of the Janus particle. Thus, the obstacle is not force- and torque-free and thus creates additional Stokeslet and rotlet flow fields (see Appendix B.2). But it is seen that the solute confinement and hydrodynamic effects from the wall play a major role in determining the dynamics of Janus particle near the obstacle [199]. This is especially true when the obstacle size is large compared to the particle ($a_{\text{obstacle}}/a_{\text{particle}} \gg 1$), and the wall effects by enforcing no slip and no penetration at the wall capture the phoretic particle. In this situation, MoR, within $O(\varepsilon^5)$ accuracy fails to predict the capture. It is expected that the *method of images* need to be implemented to obtain the wall effects on the particle [200, 112, 201]. Figure 5.2 shows the dynamics of a Janus particle near an obstacle of twice its size for various surface activity;the chemical and hydrodynamic interactions create a net change in the direction of the Janus particle.

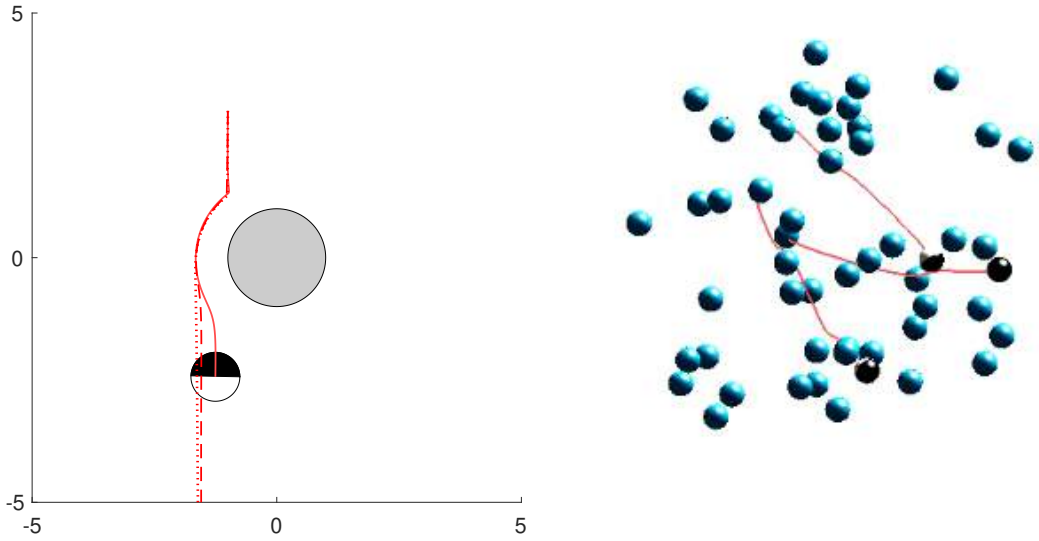

Figure 5.2: Trajectories of Janus particle (chemotactic with $M = -1$) with three different surfac coverage 0.5 (dotted), 0.75 (dashed) and 0.95 (solid) respectively near an obstacle. An example of the trajectories of three Janus particles which are chemo-repulsive ($M = 1$) through a forest of spherical obstacles (in blue) is shown on right.

For small obstacles these surface effects are considerably smaller and MoR is suitable; however, the influence of obstacle would also be significantly small. Nonetheless, MoR could be implemented to model motion of phoretic particles through complex environment like porous media with low area fraction of obstacles and small obstacle sizes; By taking into account the chemical and hydrodynamic interactions with the boundaries, MoR is expected to provide better estimate of the dynamics of phoretic particles in complex environments than ABP models which are being used currently [181, 25]. The above analyses was carried out by having the Janus particles initially positioned and oriented along a plane, which automatically restricts their dynamics to the said plane; the chemical and hydrodynamic interactions were however considered to be fully three-dimensional. This condition was imposed simply for the ease of comprehension of their dynamics. Nonetheless, the model can readily be applied for three-dimensional distributions and orientations (see figure 5.2 b). This can give a more realistic modelling of the dynamics of phoretic particles in suspensions and in porous media.

The current framework is based on the asymptotic a/d, a being the particle radius and being the center-center distance between the particles. However, one can imagine the strength of

each term to be quite small in the case of large boundaries, such as a wall, where d tends to infinity. This could pose difficulty in determining the dynamics of particles near walls accurately using the current framework as the convergence of the series would be slow i.e. a large number of reflections would be necessary to compensate for the weak asymptotics. A work-around can however be made by determining the appropriate images of the chemical and hydrodynamic field (self and reflected) that satisfy the surface boundary conditions exactly on the large boundary [202, 124, 200]

The simulations in the present thesis have only considered particles to have uniform surface mobility. However, the same modelling framework can be easily extended to case where there are particles of variable mobility. This would provide a more realistic modelling of the phoretic suspensions usually implemented in experiments. The proposed framework can nonetheless be immediately be applied to study a system with mixtures of spherical phoretic particles regardless of their size and surface properties. Thus, the MoR framework presents itself as a powerful tool to study the microscopic interactions and the long-term dynamics in a suspension containing a zoo of phoretic particles. The chosen phoretic mechanism and the modelling approach using MoR certainly explains the experimental observations of colloidal clustering and propulsion qualitatively. However, it should be perceived that to make a quantitative comparison to experimental observations, appropriate experimental conditions need to be met in the model as well, such as effect of boundaries, detailed colloidal surface properties and proper reaction kinetics need to be incorporated in the model.

APPENDICES

A

Analytical solution for two-sphere axisymmetric phoretic problem

An exact analytical solution can be obtained for the propulsion velocities of two moving spherical particles. The particles can be represented by fixed coordinates in a bispherical coordinate system. Here, we use this special coordinate system to compute the velocities of two axisymmetric Janus particles aligned along their common axis of symmetry (see Figure A.1). The analysis is presented here for two particles of identical radius a; even though we restrict the current analysis to two spheres of equal size for simplicity, the analysis using this coordinate system is flexible to evaluate both spheres of different sizes [61, 203].

In this coordinate system, the orthogonal coordinates (τ, ξ, ϕ) are related to the cylindrical coordinates (ρ, θ, z) through

$$\rho = \frac{\kappa\sqrt{1-\xi^2}}{\cosh\tau - \xi}, \qquad z = \frac{\kappa \sinh\tau}{\cosh\tau - \xi}. \tag{A.1}$$

The surface of two $\mathcal{S}_1$ and $\mathcal{S}_2$ can be represented by τ isosurfaces; for two size spheres of same radius a, one can describe their surfaces by $\tau = \pm\tau_0$ respectively . The radius, a and the distance between their centers, d are then given in this coordinate system by,

$$a = \kappa/|\sinh\tau_0| \quad \text{and,} \quad d = 2\kappa\coth\tau_0 \tag{A.2}$$

respectively. The expressions for radius and distance define κ and τ_0 uniquely.

A.1 Generalization

On the surface of each sphere, ξ varies monotonically from $\xi = -1$ (at the pole facing the other particle) to $\xi = 1$ (at the pole facing away from the other particle). Let $\xi = \xi_i^c$ demarcate the region of activity on the surface of a Janus particle i (i.e. let us suppose for our evaluation, the active regions are $[-1, \xi_1^c]$ for particle 1, and $[\xi_2^c, 1]$ for particle 2 shown in figure A.1 by white region).

Noting $\mathcal{S}_i^c$ the fraction of the particle surface that is chemically-active (e.g. coated with a catalyst):

$$\xi_1^c = \frac{1 + (2\mathcal{S}_i^c - 1)\cosh\tau_0}{\cosh\tau_0 + (2\mathcal{S}_1^c - 1)} \quad \text{and,} \tag{A.3}$$

$$\xi_2^c = \frac{1 - (2\mathcal{S}_i^c - 1)\cosh\tau_0}{\cosh\tau_0 - (2\mathcal{S}_2^c - 1)} \tag{A.4}$$

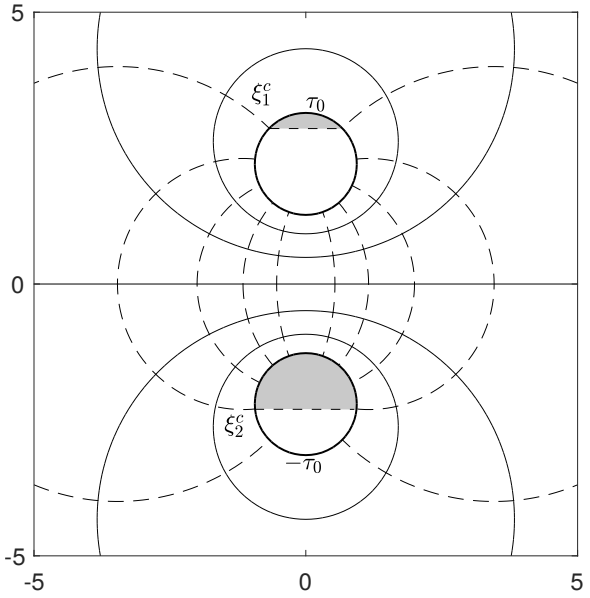

Figure A.1: Bispherical coordinate system with spheres $\pm\tau_0$ representing two particles of equal size. The two Janus particles have an active and passive parts demarcated by the coordinates ξ_1^c and ξ_2^c respectively. Although there is no inherent bias for shading, the shaded region is nonetheless regarded as the passive part for current analysis.

$\mathcal{S}_i^c = 1/2$ represents a Janus particle with hemispherical surface activity. Because of the particle structure of the bispherical coordinate system, ξ_i^c is also a function of the instantaneous distance between the particles.

The solute concentration field produced by the particles obeys the diffusion equation, equation (2.22), in bispherical coordinates,

$$\frac{\partial}{\partial\tau}\left(\frac{1}{\cosh\tau-\xi}\frac{\partial c}{\partial\tau}\right)+\frac{\partial}{\partial\xi}\left(\frac{1-\xi^2}{\cosh\tau-\xi}\frac{\partial c}{\partial\xi}\right)=0 \tag{A.5}$$

whose general far-field decaying solution is given by [204, 61]:

$$c(\tau,\xi)=\sqrt{\cosh\tau-\xi}\sum_{n=0}^{\infty}c_n(\tau)L_n(\xi)\quad\text{with,} \tag{A.6}$$

$$c_n(\tau)=a_n\exp((n+1/2)(\tau-\tau_0))+b_n\exp((n+1/2)(\tau+\tau_0)). \tag{A.7}$$

The normal flux boundary condition on the surface two particles,

$$\mathbf{e}_\tau\cdot\nabla c=\pm\frac{\cosh\tau-\xi}{\kappa}\frac{\partial c}{\partial\tau}\bigg|_{\tau=\pm\tau_0}=\pm A\,H(\xi,\xi^c_{i=1,2})\quad\text{where,} \tag{A.8}$$

$$H(\xi,\xi^c_{i=1,2})=\begin{cases}1 & l_1<\xi\le l_2\\ 0 & \text{otherwise}\end{cases}, \tag{A.9}$$

with, $l_1=-1$ and $l_2=\xi_1^c$ for particle 1 and $l_1=\xi_2^c$ and $l_2=1$ for particle 2. Equations (A.7)–(A.9) provide after projection along $L_n(\xi)$:

$$\frac{c_n(\pm\tau_0)\sinh(\tau_0)}{2(2n+1)}+\frac{c_n'(\pm\tau_0)\,\cosh(\pm\tau_0)}{2n+1}-\frac{(n+1)c_{n+1}'(\pm\tau_0)}{(2n+1)(2n+3)}-\frac{nc_{n-1}'(\pm\tau_0)}{(2n+1)(2n-1)}$$
$$=\pm\int_{l_1}^{l_2}\frac{A|\sinh\tau_0|L_n(\xi)d\xi}{2\sqrt{\cosh\tau_0-\xi}}. \tag{A.10}$$

Equations. (A.7) and (A.10) together provide a linear system for (a_n, b_n) whose solution determines the concentration field.

The surface concentration gradients induce an effective slip velocity along $\mathbf{e}_\xi$,

$$\tilde{u}_\xi(\pm\tau_0, \xi) = \frac{M\sqrt{1-\xi^2}}{\kappa}(\cosh\tau_0 - \xi)\frac{\partial c}{\partial \xi}\bigg|_{\tau=\pm\tau_0}. \tag{A.11}$$

To obtain the particles' velocities, the common strategy employed in low Reynolds hydrodynamics is to develop an auxiliary problem whose solution is known or can be computed easily (e.g. rigid body dynamics) and thereafter, use Lorentz reciprocal theorem to obtain velocity or forces of the original problem [169]. We consider here an auxiliary problem $(\mathbf{u}^*, \boldsymbol{\sigma}^*)$ corresponding to the flow field around the same particles considered here, with particle i translating rigidly with velocity $\mathbf{U}_i = U_i\mathbf{e}_z$ with a net hydrodynamic force $\mathbf{F}_i = F_i\mathbf{e}_z$. It satisfies

$$\nabla^2\mathbf{u}^* = \nabla p^*, \qquad \nabla\cdot\mathbf{u}^* = 0, \qquad \mathbf{u}^*(\mathbf{r}\to\infty)\to 0, \tag{A.12}$$

and $\mathbf{u} = \mathbf{U}_i^*$ and $\int_{\mathcal{S}_i}\boldsymbol{\sigma}^*\cdot\mathbf{n}\mathrm{d}S = \mathbf{F}_i^*$ on particle i. Applying Lorentz reciprocal theorem to this auxiliary problem and to the dynamics of the two Janus particles provide that for any (F_1^*, F_2^*)

$$F_1^*U_1 + F_2^*U_2 = -\int_{\mathcal{S}_1,\mathcal{S}_2}\tilde{\mathbf{u}}\cdot\boldsymbol{\sigma}^*\cdot\mathbf{n}\,\mathrm{d}S. \tag{A.13}$$

Applying this result for the particular choice of auxiliary problem with $F_1^* = F_2^*$ (resp. $F_2^* = -F_1^*$) provides the global velocity U_1+U_2 (resp. relative velocity U_1-U_2) and hence reconstruct the individual velocities of the particles.

In each case, the relation between the translation velocity of each sphere U_i^*, the total hydrodynamic force F_i^* and corresponding fluid stress tensor $\boldsymbol{\sigma}^*$ is well known [204], and we therefore only briefly summarize the main results. The auxiliary problem is axisymmetric and can be formulated in terms of a streamfunction ψ^*

$$\psi^*(\tau,\xi) = (\cosh\tau-\xi)^{-3/2}\sum_{n=1}^{\infty}(1-\xi^2)L_n'(\xi)\,V_n(\tau) \qquad \text{where} \tag{A.14}$$

$$V_n(\tau) = \alpha_n\cosh\left(n+\frac{3}{2}\right)\tau + \beta_n\sinh\left(n+\frac{3}{2}\right)\tau + \gamma_n\cosh\left(n-\frac{1}{2}\right)\tau + \delta_n\sinh\left(n-\frac{1}{2}\right)\tau. \tag{A.15}$$

The coefficients α_n, β_n, γ_n, and δ_n are computed from the no-slip boundary condition on the spheres, i.e $\mathbf{u}^* = U_i^*\mathbf{e}_z$ on particle i (i.e. $\tau = \pm\tau_0$) [204]. Once the coefficients are determined, one can evaluate the surface shear stress,

$$\sigma^*_{\tau,\xi}(\pm\tau_0,\xi) = \frac{\sqrt{1-\xi^2}}{\kappa}\left[\sum_{n\geq 1}L_n'(\xi)S_n - \cosh\tau_0 + \frac{\sinh^2\tau_0}{2(\cosh\tau_0-\xi)}\right] \quad \text{with,} \tag{A.16}$$

$$S_n = -(\cosh\tau_0-\xi)^{3/2}V_n''(\pm\tau_0) + \frac{\sqrt{\cosh\tau_0-\xi}}{2}(\pm V_n'(\pm\tau_0)\sinh\tau_0 + 3V_n(\pm\tau_0)\cosh\tau_0), \tag{A.17}$$

and the total hydrodynamic force on each sphere is then obtained as [204],

$$F_1^* = \frac{2\pi\sqrt{2}}{\kappa}\sum_{n\geq 1}n(n+1)(\alpha_n+\beta_n+\gamma_n+\delta_n) \quad \text{and} \quad F_2^* = \frac{2\pi\sqrt{2}}{\kappa}\sum_{n\geq 1}n(n+1)(\alpha_n-\beta_n+\gamma_n-\delta_n). \tag{A.18}$$

A.2 Special case: Isotropic particles

For isotropic particles $\mathcal{S}^c_{i=1,2} = 1$ which gives $\xi^c_{i=1,2} = \pm 1$. Since the particles are isotropic, each τ isosurface representing the particle has identical surface concentration for a given ξ,

$$c_n(\tau_0) = c_n(-\tau_0) \quad \text{which implies,} \quad a_n = b_n (= C_n/2, \text{say}) \tag{A.19}$$

Thus, the coefficient c_n for the case of isotropic particles can be expressed simply as,

$$c_n(\tau) = C_n \cosh\left[\left(n + \frac{1}{2}\right)\tau\right] \tag{A.20}$$

The integral in equation (A.10) is computed numerically. For isotropic particles, however, $\xi^c_1 = 1$ and $\xi^c_2 = -1$. Thus, the boundary condition in equation (A.9) has $H = 1 \quad \forall -1 \leq \xi \leq 1$. The integral limits are hence always between -1 and 1, and the above expression in equation (A.10) simplifies to:

$$\frac{\sinh\tau_0}{2} c_n(\tau_0) + c'_n(\tau_0)\cosh(\tau_0) - \frac{n+1}{2n+3} c'_{n+1}(\tau_0) - \frac{n}{2n-1} c'_{n-1}(\tau_0) = \kappa A\sqrt{2}\, e^{-(n+1/2)\tau_0} \tag{A.21}$$

Since we are interested in analysing the dynamics of clustering i.e. when $U_1 = -U_2 (= U)$, the dual problem that one should consider is when both the spheres are subjected to equal and opposite force F^* towards each other. Thus equation (A.13) becomes,

$$U = \frac{1}{2F^*} \int_{\mathcal{S}_1, \mathcal{S}_2} \tilde{\mathbf{u}} \cdot \boldsymbol{\sigma}^* \cdot \mathbf{n}\, \mathrm{d}S \tag{A.22}$$

The auxillary flow field for two spheres moving towards each other can be expressed as, with the streamfunction ψ^* given by [204, 61]

$$\frac{\psi^*(\tau,\mu)}{U^*} = (\cosh\tau - \mu)^{-3/2} \sum_{n=1}^{\infty} (1-\mu^2) L'_n(\mu) V_n(\tau) \quad \text{where,} \tag{A.23}$$

$$V_n(\tau) = \beta_n \sinh\left[\left(n + \frac{3}{2}\right)\tau\right] + \delta_n \sinh\left[\left(n - \frac{1}{2}\right)\tau\right]. \tag{A.24}$$

Note that two of the coefficients (α_n, γ_n) in the general equation (A.15) are zero due to the planar symmetry of the system. The no-slip boundary conditions on the spheres' surface write as

$$\psi^*(\tau_0,\mu) = -\frac{\alpha^2 U^*(1-\mu^2)}{(\cosh\tau_0 - \mu)^2}, \qquad \frac{\partial\psi^*}{\partial\tau}(\tau_0,\mu) = \frac{\alpha^2 U^*(1-\mu^2)\sinh\tau_0}{(\cosh\tau_0 - \mu)^3}, \tag{A.25}$$

and appropriate projections on the Legendre polynomials provide an explicit determination for β_n and δ_n. The shear stress distribution on the surface is then determined as [177]

$$\sigma^*_{\tau\mu}(\tau,\mu) = \frac{1}{\alpha^3\sqrt{1-\mu^2}} \frac{\partial}{\partial\tau}\left[(\cosh\tau - \mu)^3 \frac{\partial\psi^*}{\partial\tau}\right] - \frac{\sqrt{1-\mu^2}}{\alpha^3} \frac{\partial}{\partial\mu}\left[(\cosh\tau - \mu)^3 \frac{\partial\psi^*}{\partial\mu}\right], \tag{A.26}$$

and the hydrodynamic force on each sphere is obtained directly as [204, 61]

$$F^* = \frac{2\pi\sqrt{2}}{\alpha} \sum_{n=1}^{\infty} n(n+1)(\beta_n + \delta_n). \tag{A.27}$$

Two other special cases involving combination of active and passive particles is described in Appendix B

B

Mixture of active and passive particles

In this section we briefly describe the method of reflections approach applied to system comprising of active an passive particles. We shall consider two specific cases (i) where the passive particles have a uniform non-zero surface mobility and are free to move (ii) where the passive spheres are fixed and hence, behave as obstacle of motion of the active particle. The former case is considered to study the enhanced transport of passive phoretic spheres due to presence of self-propelling (active) phoretic particles. The latter case, where active particles move through a jungle of spherical passive obstacles, physically represents a situation of swimming through porous media.

B.1 Janus particle and passive tracer

The MoR framework described in Chapter 3 can directly be applied for particles with different surface activities. However, since we wish to study the long term influence of the particles on the transport of passive particles, we confined the Janus particles within a potential well. Thus, the active particle is no longer force- or torque-free. Additional interactions arise because of the point forcing exerted by the potential well on the Janus particle i.e. the spherical particle being dragged by an external force creates a stokeslet and a potential-dipole flow field which decays as $1/r$ and $1/r^3$ respectively. It has to be emphasized here that there are no additional chemical interactions (besides that detailed in Section 3.3.1 of Chapter 3) needed to be considered here; however, one has to take into account the additional hydrodynamic reflections arising from the stokeslet and potential dipole signature of each particle. Moreover, by restricting the computation of propulsion velocities to accuracy $O(\varepsilon^5)$, we observe that besides the drift from this stokeslet as well as the potential dipole, a first reflection of the stokeslet produces a reflected stresslet which creates a hydrodynamic drift of $O(\varepsilon^5)$ magnitude. Firstly, the flow field created by a spherical particle j subjected to a point force $\mathbf{F}$ at its center is given by

$$\mathbf{u}_j(\mathbf{r}_j) = \frac{\mathbf{F}_j}{8\pi\eta} \cdot \left(\frac{\mathbf{I}}{r_j} + \frac{\mathbf{r}_j \mathbf{r}_j}{r_j^3} \right) + \frac{\mathbf{F}_j a_j^2}{24\pi\eta} \cdot \left(\frac{\mathbf{I}}{r_j^3} - \frac{3\mathbf{r}_j \mathbf{r}_j}{r_j^5} \right) \tag{B.1}$$

which is a combination of a Stokeslet and a source dipole. This can be expressed in the form,

$$\mathbf{u}_j(\mathbf{r}_j) = \frac{\mathbf{P}_{j,1}^0}{2} \cdot \left(\mathbf{I} + \frac{\mathbf{r}_j \mathbf{r}_j}{r_j^3} \right) + \mathbf{\Phi}_{j,1}^0 \cdot \left(\frac{\mathbf{I}}{r_j^3} - \frac{3\mathbf{r}_j \mathbf{r}_j}{r_j^5} \right)$$

where, $\mathbf{P}_{j,1}^0 = \mathbf{F}_j / 4\pi\eta$ represents the strength of the Stokeslet and Potential dipole respectively. The drift velocity produced by this field is obtained using Faxén's laws and is given by

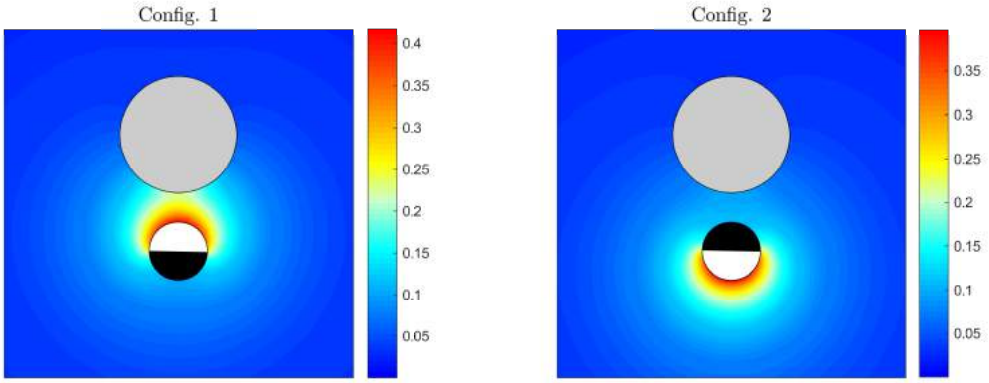

Figure B.1: Analytical solution for the solute concentration field created by two different configurations of Janus particles near an passive sphere determined using the Bispherical coordinate system approach in Section A.

$$\mathbf{U}_k^{h,r=1} = \sum_{j\neq k} \frac{1}{8\pi} \sum_{j\neq k} \frac{\mathbf{F}_j}{d_{jk}} \cdot (\mathbf{I} + \mathbf{e}_{jk}\mathbf{e}_{jk}) + \frac{(a_j^2 + a_k^2)\mathbf{F}_j}{3d_{jk}^3} \cdot (\mathbf{I} - 3\mathbf{e}_{jk}\mathbf{e}_{jk}) \tag{B.2}$$

$$\mathbf{\Omega}_k^{h,r=1} = -\frac{1}{2}\Big(\nabla \times \mathbf{u}_j(\mathbf{r}_j)\Big)_{r_k=0} \tag{B.3}$$

To maintain the accuracy of $O(\varepsilon^5)$ for the computed propulsion velocities, one has to include additional higher-order interactions that arise from hydrodynamic reflections of the Stokeslet and additional contribution to the source dipole. By listing out the various first reflections of the hydrodyanicm field,one can conclude that the only interaction that contributes to the drift velocity within an $O(\varepsilon^5)$ is that when the Stokelst produces a stresslet on the second particle which thereby influences the dynamics of the surrounding particles.

$$\begin{aligned}\text{Stokeslet}(\mathbf{P}_{l,1}^0) \xrightarrow{O(\varepsilon^2)} \text{Stresslet}(\mathbf{P}_{j,2}^1) \xrightarrow{O(\varepsilon^2),O(\varepsilon^3)} &\text{Drift velocity } \mathbf{U}_k\ O(\varepsilon^4) \\ &\text{Drift angular velocity } \mathbf{\Omega}_k\ O(\varepsilon^5)\end{aligned} \tag{B.4}$$

The strength of this stresslet is given by,

$$\mathbf{P}_{j,2}^1 = \sum_{l\neq j} \mathbf{P}_{l,1}^0 \cdot \boldsymbol{\mathcal{F}}_{\boldsymbol{lj}}^{\boldsymbol{\mathcal{P}}\rightarrow\boldsymbol{\mathcal{P}}}(2,1) = \frac{-5a_j^2}{6} \sum_{l\neq j} \mathbf{P}_{l,1}^0 \cdot \left[\underbrace{\boldsymbol{\mathcal{F}}_{lj}^3(2,1)}_{O(\varepsilon^2)} + \frac{a_j^2}{10}\underbrace{\boldsymbol{\mathcal{F}}_{lj}^1(2,1)}_{O(\varepsilon^4)}\right] \tag{B.5}$$

As the $O(\varepsilon^4)$ term in the above expression creates a drift of $O(\varepsilon^6)$ (in equation B.4), we shall exclude it from the analysis.

$$\boldsymbol{\mathcal{F}}_{lj}^3(1,2) = \frac{1}{2}\left[\overline{\nabla\left(\frac{\mathbf{I}}{r_l} + \frac{\mathbf{r}_l\mathbf{r}_l}{r_l^3}\right)}\right]_{r_j=0} = \frac{1}{2d_{lj}^2}[\mathbf{e}_{lj}\mathbf{I} + (\mathbf{e}_{lj}\mathbf{I})^{T_{12}} + (\mathbf{e}_{lj}\mathbf{I})^{T_{13}} - 5\mathbf{e}_{lj}\mathbf{e}_{lj}\mathbf{e}_{lj}] \tag{B.6}$$

The overbracket symbolizes the matrix which is symmetric and deviatoric with respect to the last two indices. Substituting the above equation in equation (B.5), the strength of the stresslet that is created at the first reflection

$$\mathbf{P}^1_{j,2} = \sum_{l\neq j} \frac{-5a_j^2}{48\pi\eta d_{lj}^2}[(\mathbf{F}_l\cdot\mathbf{e}_{lj})(\mathbf{I}-5\mathbf{e}_{lj}\mathbf{e}_{lj}) + (\mathbf{F}_l\mathbf{e}_{lj})^T + (\mathbf{F}_l\mathbf{e}_{lj})] \tag{B.7}$$

The drift produced by this reflected stresslet from a particle j on a particle k,

$$\mathbf{U}_k^{h,r=2} = \sum_{j\neq k}\mathbf{P}^1_{j,2} : \boldsymbol{\mathcal{F}}^3_{jk}(1,2) = \sum_{j\neq k}\mathbf{P}^1_{j,2} : \frac{\mathbf{e}_{jk}\mathbf{e}_{jk}\mathbf{e}_{jk}}{2d_{jk}^2} \tag{B.8}$$

$$= \frac{-5}{96\pi}\sum_{j\neq k}\sum_{l\neq j}\frac{a_j^2a_l^2}{d_{lj}^2d_{jk}^2}[(\mathbf{F}_l\cdot\mathbf{e}_{lj})(\mathbf{I}-5\mathbf{e}_{lj}\mathbf{e}_{lj}) + (\mathbf{F}_l\mathbf{e}_{lj})^T + (\mathbf{F}_l\mathbf{e}_{lj})] : \mathbf{e}_{jk}\mathbf{e}_{jk}\mathbf{e}_{jk} \tag{B.9}$$

$$\boldsymbol{\Omega}_k^{h,r=2} = -\frac{1}{2}\sum_{j\neq k}\mathbf{P}^1_{j,2} : \boldsymbol{\mathcal{F}}^2_{jk}(1,2) \tag{B.10}$$

Note that the stresslet produced by the potential dipole component is of $O(\varepsilon^6)$ is is neglected.

B.2 Janus particle near an obstacle

An obstacle is considered here to be a stationary spherical passive particle. Here we shall however not consider any potential well that restricts the Janus particle. Thus, the phoretic particle is individually force- and torque-free.

In the development using MoR, we find that here again, there are no additional chemical interactions (besides that detailed in Section 3.3.1 of Chapter 3) to be considered. There is however an additional contribution to the drift velocity of the particle arising from the immobile nature of the obstacle; the obstacle resists drifting due to external flow field in the form of a point force at its center. This creates a stokeslet flow-field which interacts with the active particle. This interaction is a 3-particle hydrodynamic interaction and the drift velocities created by them are $O(\varepsilon^5)$. If the obstacle were to have a non-zero uniform mobility, additional chemo-hydrodynamic interactions would have to be included.

If a force prevents the drift of an obstacle j (with a velocity $\mathbf{U}_j$) due to disturbance flow from the phoreticparticle, the stokeslet flow field is given by

$$\mathbf{u}_j^{\text{stk}} = \frac{-3a_j}{4r_j}\mathbf{U}_j\cdot\left(\mathbf{I}+\frac{\mathbf{r}_j\mathbf{r}_j}{r_j^2}\right) \tag{B.11}$$

This *apparent* drift velocity $\mathbf{U}_j$ of the obstacle is due to force dipole, force quadrupole and force octupole (scales as ε^2, ε^3, ε^4 respt.) created by the phoretic particle. The obstacle creates a point force of strength $6\pi\eta U_j$ that prevents the drift of the obstacle. The flow field created by this point force on the obstacle produces a stokeslet flow field, which creates a drift on the neighbouring phoretic particles. This drift velocity is obtained from Faxén's law

$$\mathbf{U}_k = \sum_{j\neq k}\mathbf{U}_j\cdot(\mathbf{I}+\mathbf{e}_{jk}\mathbf{e}_{jk}) + \frac{a_j^3\mathbf{U}_j}{2d_{jk}^3} \tag{B.12}$$

At the leading order, $\mathbf{U}_j$ is the drift due to a stresslet which scales as $O(\varepsilon^2)$. A rotlet flow-field due to a point torque $\mathbf{L}$ is given by

$$\mathbf{u}_j^{\text{rot}} = \frac{-1}{8\pi\eta r_j^3}\mathbf{L}_j\cdot(\mathbf{I}\times r_j) \tag{B.13}$$

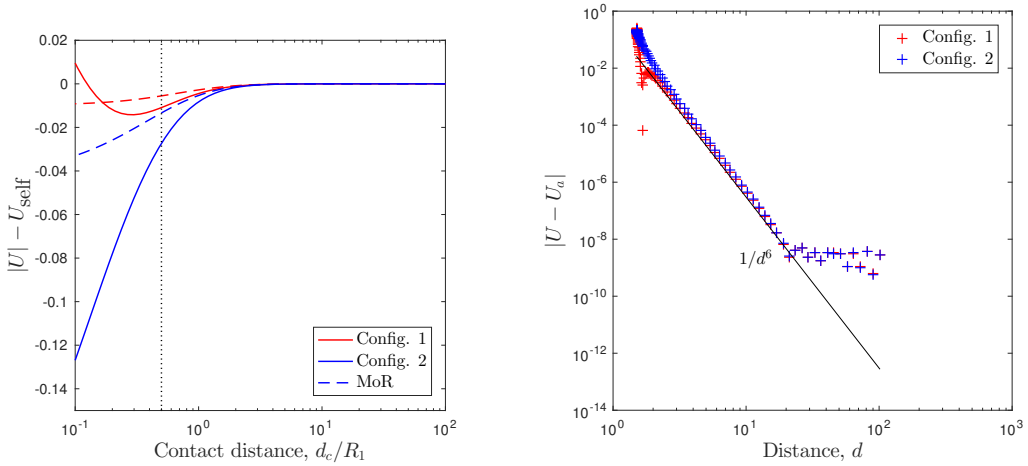

Figure B.2: Analytically determined propulsion velocity of the acitve particle (left) as a function of separation distance with the obstacle. (right) ε^6 scaling of error obtained from MoR calculations. The bispherical coordinate system used here is exactly the same as that mentioned in the above section B.1. The two configurations are as shown in figure B.1. Note that lubrication and solute confinement effects play a major role in determining the velocities of the Janus particles.

The drift velocity induced by the rotlet from the obstacle on the surrounding particles is similarly obtained as

$$\mathbf{U}_k = \sum_{j \neq k} \frac{a_j^2}{d_{jk}^2} \mathbf{e}_{jk} \times \mathbf{\Omega}_j \tag{B.14}$$

where $\mathbf{\Omega}_j$ is the angular velocity of the obstacle that is prevented by the torque $\mathbf{L}_j$. At the leading order $\mathbf{\Omega}_j$ is of $O(\varepsilon^3)$ and comes from the stresslet produced by the phoretic particles; the translational drift on the phoretic particle is thus $O(\varepsilon^5)$. However, for an apparent drift velocity $\mathbf{U}_j$ prevented by the obstacle, the contribution to rotational velocity $\mathbf{\Omega}_k$ of the phoretic particles comes from both stresslet and force quadrupole.

$$\mathbf{\Omega}_k = \sum_{j \neq k} \frac{-3a_k^2}{8d_{jk}^2} \mathbf{e}_{jk} \times \mathbf{U}_j \tag{B.15}$$

Note that the rotlet needed to prevent rotation of the obstacle creates only translation and no rotation of the phoretic particle within the $O(\varepsilon^5)$ accuracy.

C

Regularized Boundary Element Method

C.1 Regularized boundary integral formulation

Since the Green's functions for both the chemical and hydrodynamic problem scales as $1/r$ (for Stokeslet as well as point chemical source), both the velocity and the concentration field on a planar surface in 3-dimensions (and points in 2 dimensions) are integrable over the surface and are bounded. Nonetheless, the classical Boundary Integral formulation for Laplace and Stokes problems (discussed in Section 2.6) involve singular kernels which require a separate analytical treatment of the singular contributions and precise quadrature techniques. To avoid the singular nature of the kernals, one can smoothen the function by replacing it with a approximated blob function. Such a regularization has been found useful in multiple applications of Stokes flows [179, 167]. The commonly used blob function in literature is [179, 167, 137, 205],

$$\phi^{\epsilon}(\mathbf{x}, \mathbf{x}_0) = \frac{15\epsilon^4}{8\pi r_{\epsilon}^7} \tag{C.1}$$

where $r_{\epsilon}^2 = r^2 + \epsilon^2$ and $r = |\mathbf{x} - \mathbf{x}_0|$. The associated kernels are then given by,

$$J^{\epsilon}(\mathbf{x}, \mathbf{x}_0) = -\frac{(2r^2 + 3\epsilon^2)}{8\pi r_{\epsilon}^3}, \qquad K_j^{\epsilon}(\mathbf{x}, \mathbf{x}_0) = r_j \frac{2r^2 + 5\epsilon^2}{8\pi r_{\epsilon}^5}, \tag{C.2}$$

Using the above regularized kernals to develop the integrals equations as described in Section (2.6), we obtain a regularized form of the boundary integral formulations [179, 205]. Here, we shall simply list out some of the important expressions for determining the surface concentration and velocities on the phoretic particle. The *regularized* boundary integral equation for the concentration field (equivalent to the singular integral equation (C.3)) in response to the flux forcing on the active particles [137]

$$\lambda^{\epsilon} c(\mathbf{x}_0) = \int_{\mathcal{S}} \Big[c(\mathbf{x})\, \mathbf{K}^{\epsilon}(\mathbf{x}, \mathbf{x}_0) \cdot \mathbf{n}(\mathbf{x}) - \frac{\partial c(\mathbf{x})}{\partial n}\, J^{\epsilon}(\mathbf{x}, \mathbf{x}_0) \Big] \mathrm{d}\mathcal{S}_{\mathbf{x}} \tag{C.3}$$

where, on the surface of the particle, one can determine [137, 138]

$$\lambda^{\epsilon} = \left(\frac{1}{2} + \frac{\epsilon\kappa}{4} \right) + \frac{\epsilon}{4} \frac{\partial c}{\partial n}(\mathbf{x}_0) + O(\epsilon^2) \tag{C.4}$$

with κ the mean local curvature of the particle surface ($\kappa = 1$ for spherical particles). $O(\epsilon)$ thus accounts for the the regularization with i) the local curvature of the surface and ii) the gradient of c. Once the surface concentration field has been obtained, the surface slip velocity, $\tilde{\mathbf{u}}$, is computed from the particle's phoretic mobility property. The boundary integral formulation of the Stokes flow problem and force- and torque-free condition on each

particle is then solved for the flow traction and translation and rotation velocities $\mathbf{U}_j$ and $\mathbf{\Omega}_j$ of the different particles using [179, 137]

$$\lambda^{\epsilon} u_j(\mathbf{x}_0) = \frac{1}{8\pi} \int_{\mathcal{S}} \Big[G^{\epsilon}_{ij}(\mathbf{x}, \mathbf{x}_0)\ f_i(\mathbf{x}) - u_i(\mathbf{x})\ T^{\epsilon}_{ijk}(\mathbf{x}, \mathbf{x}_0)\ n_k(\mathbf{x}) \Big] \mathrm{d}\mathcal{S}_{\mathbf{x}}$$

where $\mathbf{f}$ is the surface traction. The regularized Greeen's functions in the above equation are given by

$$G^{\epsilon}_{ij}(\mathbf{x}, \mathbf{x}_0) = \frac{(r^2 + 2\epsilon^2)\delta_{ij} + r_i r_j}{r^3_{\epsilon}}, \tag{C.5}$$

$$T^{\epsilon}_{ijk}(\mathbf{x}, \mathbf{x}_0) = \frac{-6 r_i r_j r_k - 3\epsilon^2 (r_i \delta_{jk} + r_j \delta_{ik} + r_k \delta_{ij})}{r^5_{\epsilon}}. \tag{C.6}$$

Substituting the flow velocity at the surface, $\mathbf{u} = \tilde{\mathbf{u}} + \mathbf{U} + \mathbf{\Omega} \times \mathbf{x}$ in the above equation gives,

$$\lambda^{\epsilon} \widetilde{u}_j(\mathbf{x}_0) + \int_{\mathcal{S}} \widetilde{u}_i(\mathbf{x}_0) T^{\epsilon}_{ijk}(\mathbf{x}, \mathbf{x}_0) n_k(\mathbf{x}) \mathrm{d}\mathcal{S}_{\mathbf{x}} = \int_{\mathcal{S}} \Big[G^{\epsilon}_{ij}(\mathbf{x}, \mathbf{x}_0)\ f_i(\mathbf{x}) - \left[U_i(\mathbf{x}) + \Omega \times (\mathbf{x}_0 - \mathbf{x}_c) \right] T^{\epsilon}_{ijk}(\mathbf{x}, \mathbf{x}_0)\ n_k(\mathbf{x}) \Big] \mathrm{d}\mathcal{S}_{\mathbf{x}} \tag{C.7}$$

The surface slip velocity $\widetilde{\mathbf{u}}$ is determined from the local surface concentration gradient

$$\widetilde{u}_j(\mathbf{x}_0) = M(\delta_{ij} - n_i n_j) \frac{\partial}{\partial x_i} c(\mathbf{x}_0) \tag{C.8}$$

And finally, the matrix set of equations are closed using the force and torque-free boundary conditions

$$\int_{\mathcal{S}} \mathbf{f}(\mathbf{x}) \mathrm{d}\mathcal{S}_{\mathbf{x}} = 0 \quad \text{and} \quad \int_{\mathcal{S}} (\mathbf{x} - \mathbf{x}_c) \times \mathbf{f}(\mathbf{x}) \mathrm{d}\mathcal{S}_{\mathbf{x}} = 0 \tag{C.9}$$

The surface distribution of concentration and velocity may be used to compute their bulk distribution, using the fundamental integral representations. The regularization parameter ϵ must be chosen small enough to approach the true solution but large enough to avoid a singular behaviour of the integral equation; a value of 0.005 and 0.01 is typically used.

There are only a few special cases where the boundary integrals have a closed form solutions; these are not applicable in most cases of practical importance where the bodies have complex shapes and/or boundary conditions. A numerical scheme for the integrals are known as the *Boundary Element Methods* (BEM), where the velocities and forces are discretized over the surface of the body. We follow the computational framework of regularised BEM developed for phoretic problems by Montenegro-Johnson *et al.* [137] to generate mesh and quadrature routines for evaluation of surface integrals. In general, the Boundary Element Methods (BEM) traces the listed steps.

C.2 Details of simulation using BEM

Boundary Element Method (BEM) is the discretized version of the boundary integral formulation described in the previous section. Method of Regularized Stokeslet has been used for determining the dynamic of micro-organisms swimming in low Reynolds number [205, 129]. We follow the same spirit in modeling the dynamics of artificial phoretic swimmers. An approximation of the surface of the particle is first generated by discretizing the surface profile

using nodes. Normally, a planar surface discretization is sufficient; however, to capture the curved surface of the particles, a quadratic representation is used here; this allows one to create the spherical geometry of the particles with less elements [137]. For our problem, two discretizations, depending on the desired accuracy are used: i) A rough mesh, with 512 elements and 2) a fine mesh with 2048 elements. The surface unknowns (i.e. solute concentration, flow velocities and traction) on the surface of the body are expanded as truncated polynomial series about each node. The coefficient of each term in the series is known as the *local basis function* [153]. In most BEM simulations in literature, the values of surface unknowns are kept constant within each element. However, for phoretic problems, since the prediction of the propulsion velocity depends on the accuracy in prediction of concentration gradients, one also has to include the linear variation of the fields within each element. In considering the linear variation, compared to the case of constant element method where each point is dependent on the three neighbouring values, here, each node is shared by six others, thus reducing the size of the linear system by a factor 1/8. The local expansion is substituted in the integral equations to obtain the coefficients of expansion of single and double layer potential. The integration is performed on quadrature points which are projected from planar elements to quadratic elements; this is separate from element-based discretization of the field. Thus, in this manner, one decouples this solution space from the quadrature space used to evaluate surface integrals. A Fekete quadrature routine is then implemented on the quadrature points to evaluate the surface integral of the Green's functions [137]. For the simulations of phoretic particles in our simulations, 1026 quadratic nodes for rough mesh and 4098 nodes for a fine mesh were used. The system of linear equations one obtains is finally solved for using Gauss elimination, which is suitable for large linear systems.

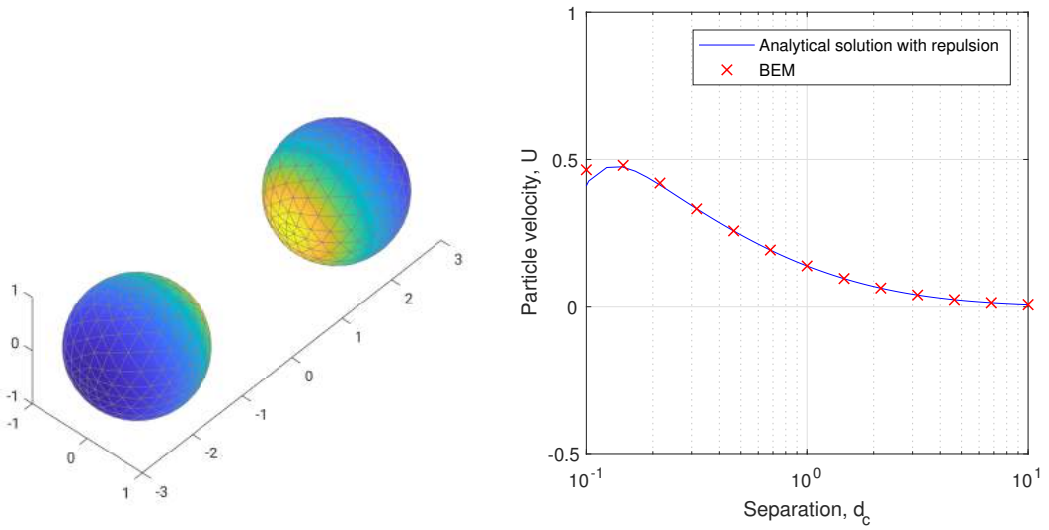

Figure C.1: Regularized mesh (rough mesh with 512 elements) for determining clustering velocity of each of the 2 identical isotropic phoretic particles due to mutual symmetry-breaking of concentration field. (right) Comparison of clustering velocity computed using BEM with that of analytical solution derived in Chapter 4, Section 4.2.2

The solutions to boundary integral equations have been shown to exhibit regular behaviour, except in situations such as sharp corners or singular points (such as near a contact line), where the solutions can display oscillatory behaviour and slow convergence. The accuracy of BEM also depends on the shape of the distribution of elements and the order of the approximation function. In general, there are two types of errors one can expect in using regularized BEM: 1) Regularization error 2) Discretization error [205]. The discretization error can be reduced by reducing the size of the elements; the quadratic surface approximation used here

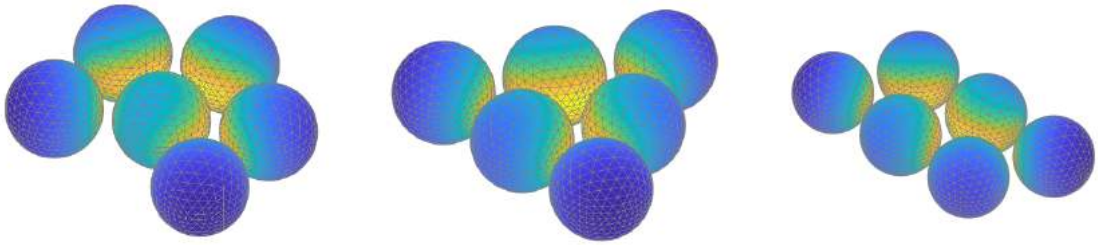

Figure C.2: The possible cluster configurations of 6-particle system of isotropic particles is shown. The computed propulsion velocities are (a) $U = 2.8 \times 10^{-4}$, $\Omega = 0$ and (b) $U = 10^{-13}$, $\Omega = 10^{-11}$ and (c)$U = 10^{-13}$, $\Omega = 1.46 \times 10^{-5}$.

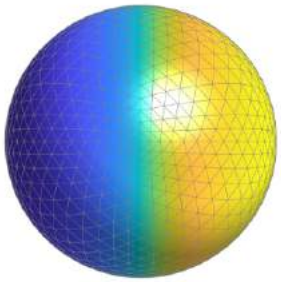

Figure C.3: Meshing for computing propulsion velocity of Janus particle. The computed velocity of an isolated Janus particle, having half of its surface active, was found to be accurate to 10^{-8}.

also reduces the discretization error as it represents the curved geometry more faithfully. Additionally, for phoretic problems the accuracy of the computed propulsion velocities depend on the surface concentration gradients and so, the computation of gradients require finer meshing as well. For example: To compute the propulsion velocity of Janus particle one has to make finer discretization near the sharp region where the surface transitions from active to passive. Another example is the case for computing the propulsion velocities of clusters of phoretic particles; In this case, the region where the particles are closest to each other (at the expected contact points of particles in the cluster) require much finer mesh to capture the sharp gradients created by the curved interfaces.

The BEM framework that we use for our simulations were validated in Montenegro-Johnson *et.al.* for both isotropic as well as Janus particles [137]. In Chapter 4, where we study the dynamics of isotropic particles, full numerical simulations for 5 particles were performed using this framework. For the clustering phase which requires time-stepping computations, a regular meshing comprising of 512 elements per particle (i.e. the rough mesh) was found to be sufficient. An example of this mesh is shown in figure C.1.

However for computing the propulsion velocities of clusters, a higher precision is required. In addition to using the fine mesh with 2048 elements, additional refinement of the mesh is made near contact points with other particles. Since the particles are known to form a cluster within a hexagonal lattice, the refinement is made at these hexagonal locations. Example of this meshing for 6 particle is shown in figure C.2. The zero propulsion velocities of the symmetric configuration validates the form of mesh used for computing the translational and rotational velocities of clusters.

For Janus particles, a regular mesh with refinement at the equator was necessary to capture sharp concentration gradients in this region. For simulating the dynamics of multiple Janus

particles, the mesh had to be reconstructed at each time step to align with the orientation of the particle.

D

Solution of the hydrodynamic reflection problem

D.1 Spherical harmonics decomposition

The first step in solving the hydrodynamic reflection problem (i.e. finding the flow field $\mathbf{u}_k^p$ for $p \geq 1$) is to determine the intensity of the flow singularities involved in equation (3.51) as a function of the velocity gradients generated near particle k at the previous reflection. To this end, using the expression for the surface velocity $\mathbf{v}_k^p$, equation (3.59), the normal velocity, surface divergence and surface vorticity are first obtained as

$$\mathbf{v}_k^p \cdot \mathbf{n}_k = -\sum_{q\geq 1} \left[\sum_{j\neq k} \frac{a_k^{q-1}}{(q-1)!} \overset{q-1}{\nabla} \mathbf{u}_j^{p-1} \Big|_{r_k=0} \right] \overset{q}{\odot} [\mathbf{n}_k \overset{q}{\otimes} \mathbf{n}_k] \tag{D.1}$$

$$-a_k \nabla_s \cdot \mathbf{v}_k^p = -\sum_{q\geq 1} (q-1) \left[\sum_{j\neq k} \frac{a_k^{q-1}}{(q-1)!} \overset{q-1}{\nabla} \mathbf{u}_j^{p-1} \Big|_{r_k=0} \right] \overset{q}{\odot} [\mathbf{n}_k \overset{q}{\otimes} \mathbf{n}_k] \tag{D.2}$$

$$a_k \mathbf{n}_k \cdot [\nabla_s \times \mathbf{v}_k^p] = -\sum_{q\geq 1} \left[\sum_{j\neq k} \frac{a_k^q}{q!} \overset{q-1}{\nabla} \boldsymbol{\omega}_j^{p-1} \Big|_{r_k=0} \right] \overset{q}{\odot} [\mathbf{n}_k \overset{q}{\otimes} \mathbf{n}_k] \tag{D.3}$$

Identifying the singularities' intensity using Eqs. (3.52)–(3.54) requires decomposing these three functions into spherical harmonics along the particle's surface as in equation (2.69). The $(q-1)$-th gradient of the flow field can first be decomposed by isolating its symmetric part with respect to all indices:

$$\overset{q-1}{\nabla} \mathbf{u}_j^{p-1} = \frac{1}{q} \sum_{s=1}^{q} (\overset{q-1}{\nabla} \mathbf{u}_j^{p-1})^{T_{1s}} + \Big[\overset{q-1}{\nabla} \mathbf{u}_j^{p-1} - \frac{1}{q} \sum_{s=1}^{q} (\overset{q-1}{\nabla} \mathbf{u}_j^{p-1})^{T_{1s}} \Big], \tag{D.4}$$

where the terms in bracket do not contribute to equation (D.1), where it is contracted with a fully-symmetric tensor, $\mathbf{n}_k \overset{q}{\otimes} \mathbf{n}_k$. Here, $\mathbf{A}^{T_{1s}}$ corresponds to the transpose of $\mathbf{A}$ with respect to indices 1 and s. When $q \geq 3$, the first part (i.e. the symmetric part) is not necessarily trace-free with respect to any pair of the last $q-1$ indices and must therefore be further decomposed as

$$\begin{aligned} \overbrace{\frac{1}{q} \sum_{s=1}^{q} (\overset{q-1}{\nabla} \mathbf{u}_j^{p-1})^{T_{1s}}}^{\overset{q-1}{\nabla} \mathbf{u}_j^{p-1}} = \overbrace{\frac{1}{q} \sum_{s=1}^{q} (\overset{q-1}{\nabla} \mathbf{u}_j^{p-1})^{T_{1s}} - \frac{q-2}{q(2q-1)} \sum_{1\leq l<m\leq q} \Big[\overset{q-3}{\nabla} (\mathbf{I} \otimes \nabla^2 \mathbf{u}_j^{p-1}) \Big]^{T_{1l},T_{2m}}}^{} \\ + \frac{q-2}{q(2q-1)} \sum_{1\leq l<m\leq q} \Big[\mathbf{I} \otimes \overset{q-3}{\nabla} (\nabla^2 \mathbf{u}_j^{p-1}) \Big]^{T_{1l},T_{2m}}, \end{aligned} \tag{D.5}$$

and the first part is the fully symmetric and deviatoric part of $\overset{q-1}{\nabla}\mathbf{u}_j^{p-1}$. Then, noting that the last terms includes $q(q-1)/2$ different terms contributing identically once contracted with $\mathbf{n}_k \overset{q}{\otimes} \mathbf{n}_k$,

$$\sum_{q\geq 1}\left[\frac{a_k^{q-1}}{(q-1)!}\overset{q-1}{\nabla}\mathbf{u}_j^{p-1}\right]\overset{q}{\odot}[\mathbf{n}_k\overset{q}{\otimes}\mathbf{n}_k] = \sum_{q\geq 1}\left[\frac{a_k^{q-1}}{(q-1)!}\overline{\overset{q-1}{\nabla}\mathbf{u}_j^{p-1}}\right]\overset{q}{\odot}[\mathbf{n}_k\overset{q}{\otimes}\mathbf{n}_k]+ \tag{D.6}$$

$$\sum_{q\geq 3}\frac{1}{2(2q-1)}\frac{a_k^{q-1}}{(q-3)!}\overset{q-3}{\nabla}\left(\nabla^2\mathbf{u}_j^{p-1}\right)\overset{q-2}{\odot}[\mathbf{n}_k\overset{q-2}{\otimes}\mathbf{n}_k]$$

$$= \sum_{q\geq 1}\left[\frac{a_k^{q-1}}{(q-1)!}\left(1+\frac{a_k^2}{2(2q+3)}\nabla^2\right)\overline{\overset{q-1}{\nabla}\mathbf{u}_j^{p-1}}\right]\overset{q}{\odot}[\mathbf{n}_k\overset{q}{\otimes}\mathbf{n}_k] \tag{D.7}$$

since $\overset{q-1}{\nabla}\left(\nabla^2\mathbf{u}_j^{p-1}\right)$ is traceless with respect to any pair of its indices. equations (D.2) and (D.3) can be decomposed similarly, noting that $\overset{q-1}{\nabla}\boldsymbol{\omega}_j^{p-1}$ is already fully deviatoric, and lead to equations (3.60)–(3.62).

D.2 Recursive relations

From Eqs. (3.64)–(3.66), obtaining recursive relations in p between the three sets of tensors $\boldsymbol{\Phi}_{k,q}^p$, $\mathbf{P}_{k,q}^p$ and $\mathbf{X}_{k,q}^p$ therefore requires determining $\overset{q-1}{\nabla}\mathbf{u}_j^{p-1}$, $\overset{q-1}{\nabla}\boldsymbol{\omega}_j^{p-1}$ and $\nabla^2(\overset{q-1}{\nabla}\mathbf{u}_j^{p-1}) = \overset{q}{\nabla}p_j^{p-1}$ associated with each singularity at reflection $p-1$ at the center of particle k. Rewriting equation (3.51) in terms of the set of tensors $\boldsymbol{\Phi}_{k,q}^p$, $\mathbf{P}_{k,q}^p$ and $\mathbf{X}_{k,q}^p$:

$$\mathbf{u}_j^{p-1} = \sum_{s=1}^{\infty}\left\{\boldsymbol{\Phi}_{j,s}^{p-1}\overset{s}{\odot}\nabla\left(\frac{\mathbf{r}_j\overset{s}{\otimes}\mathbf{r}_j}{r_j^{2s+1}}\right) - \mathbf{X}_{j,s}^{p-1}\overset{s}{\odot}\left[s\left(\frac{\mathbf{r}_j\overset{s-1}{\otimes}\mathbf{r}_j}{r_j^{2s+1}}\right)\otimes(\boldsymbol{\varepsilon}\cdot\mathbf{r}_j)\right]\right.$$

$$\left.+\frac{\mathbf{P}_{j,s}^{p-1}}{2(2s-1)}\overset{s}{\odot}\left[\frac{\mathbf{r}_j\overset{s-1}{\otimes}\mathbf{r}_j}{r_j^{2s-1}}\otimes\left((2s-1)\frac{\mathbf{r}_j\mathbf{r}_j}{r_j^2}-(s-2)\mathbf{I}\right)\right]\right\}, \tag{D.8}$$

the required gradients are computed as

$$\overset{q-1}{\nabla}\mathbf{u}_j^{p-1} = \sum_{s=1}^{\infty}\left\{\boldsymbol{\Phi}_{j,s}^{p-1}\overset{s}{\odot}\overset{q}{\nabla}\left(\frac{\mathbf{r}_j\overset{s}{\otimes}\mathbf{r}_j}{r_j^{2s+1}}\right) - \mathbf{X}_{j,s}^{p-1}\overset{s}{\odot}\overset{q-1}{\nabla}\left[s\left(\frac{\mathbf{r}_j\overset{s-1}{\otimes}\mathbf{r}_j}{r_j^{2s+1}}\right)\otimes(\boldsymbol{\varepsilon}\cdot\mathbf{r}_j)\right]\right.$$
$$\left. + \frac{\mathbf{P}_{j,s}^{p-1}}{2(2s-1)}\overset{s}{\odot}\overset{q-1}{\nabla}\left[\frac{\mathbf{r}_j\overset{s-1}{\otimes}\mathbf{r}_j}{r_j^{2s-1}}\otimes\left((2s-1)\frac{\mathbf{r}_j\mathbf{r}_j}{r_j^2} - (s-2)\mathbf{I}\right)\right]\right\}, \quad \text{(D.9)}$$

$$\overset{q-1}{\nabla}\boldsymbol{\omega}_j^{p-1} = \sum_{s=1}^{\infty}\overset{q-1}{\nabla}\left(-s\nabla\chi_{j,s}^{p-1} + \frac{1}{s}\nabla p_{j,s}^{p-1}\times\mathbf{r}_j\right)$$
$$= \sum_{s=1}^{\infty}\left\{-s\mathbf{X}_{j,s}^{p-1}\overset{s}{\odot}\overset{q}{\nabla}\left[\frac{\mathbf{r}_j\overset{s}{\otimes}\mathbf{r}_j}{r_j^{2s+1}}\right] - \mathbf{P}_{j,s}^{p-1}\overset{s}{\odot}\overset{q-1}{\nabla}\left[\frac{\mathbf{r}_j\overset{s-1}{\otimes}\mathbf{r}_j}{r_j^{2s+1}}\otimes(\boldsymbol{\varepsilon}\cdot\mathbf{r}_j)\right]\right\} \quad \text{(D.10)}$$

$$\nabla^2(\overset{q-1}{\nabla}\mathbf{u}_j^{p-1}) = \sum_{s=1}^{\infty}\mathbf{P}_{j,s}^{p-1}\overset{s}{\odot}\overset{q}{\nabla}\left[\frac{\mathbf{r}_j\overset{s}{\otimes}\mathbf{r}_j}{r_j^{2s+1}}\right] \quad \text{(D.11)}$$

Using these results, the transfer functions between two successive orders of reflections are obtained as

$$\mathbf{U}_k^p = \sum_{j\neq k}\sum_{s\geq 1}\left[\boldsymbol{\Phi}_{j,s}^{p-1}\overset{s}{\odot}\boldsymbol{\mathcal{F}}_{\boldsymbol{jk}}^{\mathbf{1}}(1,s) - \mathbf{X}_{j,s}^{p-1}\overset{s}{\odot}\boldsymbol{\mathcal{F}}_{\boldsymbol{jk}}^{\mathbf{2}}(1,s) + \mathbf{P}_{j,s}^{p-1}\overset{s}{\odot}\left(\boldsymbol{\mathcal{F}}_{\boldsymbol{jk}}^{\mathbf{3}}(1,s) + \frac{a_k^2}{6}\boldsymbol{\mathcal{F}}_{\boldsymbol{jk}}^{\mathbf{1}}(1,s)\right)\right], \quad \text{(D.12)}$$

$$\boldsymbol{\Omega}_k^p = -\frac{1}{2}\sum_{j\neq k}\sum_{s\geq 1}\left[\mathbf{P}_{j,s}^{p-1}\overset{s}{\odot}\boldsymbol{\mathcal{F}}_{\boldsymbol{jk}}^{\mathbf{2}}(1,s) + s\mathbf{X}_{j,s}^{p-1}\overset{s}{\odot}\boldsymbol{\mathcal{F}}_{\boldsymbol{jk}}^{\mathbf{1}}(1,s)\right], \quad \text{(D.13)}$$

$$\boldsymbol{\Phi}_{j,1}^p = -\frac{a_k^5}{30}\sum_{j\neq k}\sum_{s\geq 1}\left[\mathbf{P}_{j,s}^{p-1}\overset{s}{\odot}\boldsymbol{\mathcal{F}}_{\boldsymbol{jk}}^{\mathbf{1}}(1,s)\right] \quad \text{(D.14)}$$

with

$$\boldsymbol{\mathcal{F}}_{\boldsymbol{jk}}^{\boldsymbol{\Phi}\to\boldsymbol{\Phi}}(q,s) = -\frac{(2q-1)a_k^{2q+1}}{2(q+1)(q-1)!}\boldsymbol{\mathcal{F}}_{\boldsymbol{jk}\,\boldsymbol{jk}}^{\mathbf{1}}(q,s), \quad \text{(D.15)}$$

$$\boldsymbol{\mathcal{F}}_{\boldsymbol{jk}}^{\boldsymbol{X}\to\boldsymbol{\Phi}}(q,s) = \frac{(2q-1)a_k^{2q+1}}{2(q+1)(q-1)!}\boldsymbol{\mathcal{F}}_{\boldsymbol{jk}}^{\mathbf{2}}(q,s) \quad \text{(D.16)}$$

$$\boldsymbol{\mathcal{F}}_{\boldsymbol{jk}}^{\boldsymbol{P}\to\boldsymbol{\Phi}}(q,s) = -\frac{(2q-1)a_k^{2q+1}}{2(q+1)(q-1)!}\left[\boldsymbol{\mathcal{F}}_{\boldsymbol{jk}}^{\mathbf{3}}(q,s) + \frac{(2q+1)a_k^2}{2(2q-1)(2q+3)}\boldsymbol{\mathcal{F}}_{\boldsymbol{jk}}^{\mathbf{1}}(q,s)\right] \quad \text{(D.17)}$$

$$\boldsymbol{\mathcal{F}}_{\boldsymbol{jk}}^{\boldsymbol{\Phi}\to\boldsymbol{P}}(q,s) = -\frac{(2q+1)a_k^{2q-1}}{2(q+1)(q-1)!}\boldsymbol{\mathcal{F}}_{\boldsymbol{jk}}^{\mathbf{1}}(q,s), \quad \text{(D.18)}$$

$$\boldsymbol{\mathcal{F}}_{\boldsymbol{jk}}^{\boldsymbol{X}\to\boldsymbol{P}}(q,s) = \frac{(2q+1)a_k^{2q-1}s}{2(q+1)(q-1)!}\boldsymbol{\mathcal{F}}_{\boldsymbol{jk}}^{\mathbf{2}}(q,s) \quad \text{(D.19)}$$

$$\boldsymbol{\mathcal{F}}_{\boldsymbol{jk}}^{\boldsymbol{P}\to\boldsymbol{P}}(q,s) = -\frac{(2q+1)a_k^{2q-1}}{2(q+1)(q-1)!}\left[\boldsymbol{\mathcal{F}}_{\boldsymbol{jk}}^{\mathbf{3}}(q,s) + \frac{a_k^2}{2(2q+1)}\boldsymbol{\mathcal{F}}_{\boldsymbol{jk}}^{\mathbf{1}}(q,s)\right] \quad \text{(D.20)}$$

$$\boldsymbol{\mathcal{F}}_{\boldsymbol{jk}}^{\boldsymbol{\Phi}\to\boldsymbol{X}}(q,s) = 0, \qquad \boldsymbol{\mathcal{F}}_{\boldsymbol{jk}}^{\boldsymbol{P}\to\boldsymbol{X}}(q,s) = \frac{a_k^{2q+1}}{q(q+1)\times q!}\boldsymbol{\mathcal{F}}_{\boldsymbol{jk}}^{\mathbf{2}}(q,s), \quad \text{(D.21)}$$

$$\boldsymbol{\mathcal{F}}_{\boldsymbol{jk}}^{\boldsymbol{X}\to\boldsymbol{X}}(q,s) = \frac{a_k^{2q+1}s}{q(q+1)\times q!}\boldsymbol{\mathcal{F}}_{\boldsymbol{jk}}^{\mathbf{1}}(q,s) \quad \text{(D.22)}$$

where the following $(q+s)$-order tensors, which are fully-symmetric and deviatoric with respect to their last q indices, have been defined (with their respective order in $\varepsilon = a/d$

shown):

$$\boldsymbol{\mathcal{F}}^{\mathbf{1}}_{\boldsymbol{jk}}(q,s) = \left[\overset{q}{\nabla}\left(\frac{\mathbf{r}_j \overset{s}{\otimes} \mathbf{r}_j}{r_j^{2s+1}}\right)\right]_{r_k=0} = O(\varepsilon^{s+q+1}), \tag{D.23}$$

$$\boldsymbol{\mathcal{F}}^{\mathbf{2}}_{\boldsymbol{jk}}(q,s) = s\left[\overbrace{\overset{q-1}{\nabla}\left(\frac{\mathbf{r}_j \overset{s-1}{\otimes} \mathbf{r}_j}{r_j^{2s+1}} \otimes (\boldsymbol{\varepsilon}\cdot\mathbf{r}_j)\right)}^{q}\right]_{r_k=0} = O(\varepsilon^{s+q}), \tag{D.24}$$

$$\boldsymbol{\mathcal{F}}^{\mathbf{3}}_{\boldsymbol{jk}}(q,s) = \frac{1}{2(2s-1)}\left[\overbrace{\overset{q-1}{\nabla}\left(\frac{\mathbf{r}_j \overset{s-1}{\otimes} \mathbf{r}_j}{r_j^{2s-1}} \otimes \left((2s-1)\frac{\mathbf{r}_j\mathbf{r}_j}{r_j^2} - (s-2)\mathbf{I}\right)\right)}^{q}\right]_{r_k=0} = O(\varepsilon^{s+q-1}) \tag{D.25}$$

Bibliography

[1] A. Bricard, J.-B. Caussin, N. Desreumaux, O. Dauchot, and D. Bartolo. Emergence of macroscopic directed motion in populations of motile colloids. *Nature*, 503(5834):95, 2013.

[2] C. Reichhardt and C. J. Olson Reichhardt. Active matter transport and jamming on disordered landscapes. *Phys. Rev. E*, 90:012701, Jul 2014.

[3] W. J. Thomson. *Introduction to transport phenomenon.* Prentice Hall, 2000.

[4] S.R. Groot and P. Mazur. *Non-equilibrium thermodynamics.* North-Holland and Publishing Company, 1962.

[5] R Piazza and A Parola. Thermophoresis in colloidal suspensions. *Journal of Physics: Condensed Matter*, 20(15):153102, mar 2008.

[6] L. Gary Leal. *Advanced Transport Phenomena: Fluid Mechanics and Convective Transport Processes.* Cambridge Series in Chemical Engineering. Cambridge University Press, 2007.

[7] Michael Cross and Henry Greenside. *Pattern Formation and Dynamics in Nonequilibrium Systems.* Cambridge University Press, 2009.

[8] M. C. Cross and P. C. Hohenberg. Pattern formation outside of equilibrium. *Rev. Mod. Phys.*, 65:851–1112, Jul 1993.

[9] Salma Jalal, Shidong Shi, Vidhyalakshmi Acharya, Ruby Yun-Ju Huang, Virgile Viasnoff, Alexander D. Bershadsky, and Yee Han Tee. Actin cytoskeleton self-organization in single epithelial cells and fibroblasts under isotropic confinement. *Journal of Cell Science*, 132(5), 2019.

[10] H. P. Zhang, Avraham Be'er, E.-L. Florin, and Harry L. Swinney. Collective motion and density fluctuations in bacterial colonies. *Proceedings of the National Academy of Sciences*, 107(31):13626–13630, 2010.

[11] Peter Galajda, Juan Keymer, Paul Chaikin, and Robert Austin. A wall of funnels concentrates swimming bacteria. *Journal of Bacteriology*, 189(23):8704–8707, 2007.

[12] J. Palacci, S. Sacanna, A. P. Steinberg, D. J. Pine, and P. M. Chaikin. Living crystals of light-activated colloidal surfers. *Science*, 339:936–940, 2013.

[13] R. Singh and R. Adhikari. Generalized stokes laws for active colloids and their applications. *J. Phys. Commun.*, 2(2):025025, 2018.

[14] Ivo Buttinoni, Julian Bialké, Felix Kümmel, Hartmut Löwen, Clemens Bechinger, and Thomas Speck. Dynamical clustering and phase separation in suspensions of self-propelled colloidal particles. *Phys. Rev. Lett.*, 110:238301, Jun 2013.

[15] Sambeeta Das, Astha Garg, Andrew I. Campbell, Jonathan Howse, Ayusman Sen, Darrell Velegol, Ramin Golestanian, and Stephen J. Ebbens. Boundaries can steer active janus spheres. *Nature Communications*, 65:851–1112, 2015.

[16] C. Bechinger, R. Di Leonardo, H. Löwen, C. Reichhardt, G. Volpe, and G. Volpe. Active particles in complex and crowded environments. *Rev. Mod. Phys.*, 88:045006, 2016.

[17] W. E. Uspal, M. N. Popescu, S. Dietrich, and M. Tasinkevych. Self-propulsion of a catalytically active particle near a planar wall: from reflection to sliding and hovering. *Soft Matter*, 11:434–438, 2015.

[18] S. J. Ebbens. Active colloids: progress and challenges towards realising autonomous applications. *Curr. Opin. Colloid Interface Sci.*, 21:14–23, 2016.

[19] P. Illien, R. Golestanian, and A. Sen. 'fuelled' motion: phoretic motility and collective behaviour of active colloids. *Chem. Soc. Rev.*, 46:1, 2017.

[20] J. L. Moran and J. D. Posner. Phoretic self-propulsion. *Ann. Rev. of Fluid Mech.*, 49(1):511–540, 2017.

[21] A. Kaiser, A. Snezhko, and I. S. Aranson. Flocking ferromagnetic colloids. *Sci. Adv.*, 3(2), 2017.

[22] A. Bricard, J-B. Caussin, D. Das, C. Savoie, V. Chikkadi, K. Shitara, O. Chepizhko, F. Peruani, D. Saintillan, and D. Bartolo. Emergent vortices in populations of colloidal rollers. *Nat. Comm.*, 6, 2015.

[23] M. Driscoll, B. Delmotte, S. Sacanna, A. Donev, and P. Chaikin. Unstable fronts and motile structures formed by microrollers. *Nature*, 375(13), 2016.

[24] I. Theurkauff, C. Cottin-Bizonne, J. Palacci, C. Ybert, and Bocquet. L. Dynamic clustering in active colloidal suspensions with chemical signaling. *Phys. Rev. Lett*, 108:268303, 2012.

[25] C. Bechinger, R. Di Leonardo, H. Löwen, C. Reichhardt, G. Volpe, and G. Volpe. Active particles in complex and crowded environments. *Rev. Mod. Phys.*, 88:1, 2016.

[26] T. B. Jones. Quincke rotation of spheres. *IEEE Transactions on Industry Applications*, IA-20(4):845–849, July 1984.

[27] Filip Petersson, Lena Ãberg, Ann-Margret SwÃrd-Nilsson, and Thomas Laurell. Free flow acoustophoresis:â microfluidic-based mode of particle and cell separation. *Analytical Chemistry*, 79(14):5117–5123, 2007. PMID: 17569501.

[28] J. R. Howse, R. A. L. Jones, A. J. Ryan, T. Gough, R. Vafabakhsh, and R. Golestanian. Self-Motile Colloidal Particles: From Directed Propulsion to Random Walk. *Phys. Rev. Lett.*, 99(4):048102, 2007.

[29] Knut Drescher, Raymond E. Goldstein, Nicolas Michel, Marco Polin, and Idan Tuval. Direct measurement of the flow field around swimming microorganisms. *Phys. Rev. Lett.*, 105:168101, Oct 2010.

[30] Julius B. Kirkegaard, Alan O. Marron, and Raymond E. Goldstein. Motility of colonial choanoflagellates and the statistics of aggregate random walkers. *Phys. Rev. Lett.*, 116:038102, Jan 2016.

[31] F. Jülicher, K. Kruse, J. Prost, and J.-F. Joanny. Active behavior of the cytoskeleton. *Phys. Rep.*, 449(1):3 – 28, 2007.

[32] Bradley J. Nelson, Ioannis K. Kaliakatsos, and Jake J. Abbott. Microrobots for minimally invasive medicine. *Annual Review of Biomedical Engineering*, 12(1):55–85, 2010. PMID: 20415589.

[33] Carlo Marangoni. Sull'espansione delle goccie d'un liquido galleggianti sulla superfice di altro liquido. *Pavia tipografia dei Fratelli Fusi*, 1865.

[34] V G Levich and V S Krylov. Surface-tension-driven phenomena. *Annual Review of Fluid Mechanics*, 1(1):293–316, 1969.

[35] C. V. Sternling and L. E. Scriven. Interfacial turbulence: Hydrodynamic instability and the marangoni effect. *AIChE Journal*, 5(4):514–523, 1959.

[36] S. Thutupalli, R. Seemann, and S. Herminghaus. Swarming behavior of simple model squirmers. *New J. Phys.*, 13(073021), 2011.

[37] S. Herminghaus, C. C. Maass, C. KrÃÅger, S. Thutupalli, L. Goehring, and C. Bahr. Interfacial mechanisms in active emulsions. *Soft Matter*, 10:7008–7022, 2014.

[38] Eli Ruckenstein. Can phoretic motions be treated as interfacial tension gradient driven phenomena? *Journal of Colloid and Interface Science*, 83(1):77 – 81, 1981.

[39] Peter O Staffeld and John A Quinn. Diffusion-induced banding of colloid particles via diffusiophoresis: 1. electrolytes. *Journal of Colloid and Interface Science*, 130(1):69 – 87, 1989.

[40] J. L. Anderson. Colloidal transport by interfacial forces. *Annu. Rev. Fluid Mech*, 21:61–99, 1989.

[41] B.V. Derjaguin, G.P. Sidorenkov, E.A. Zubashchenkov, and E.V. Kiseleva. Kinetic phenomena in boundary films of liquids. *Kolloidn. Zh.*, 9, 01 1947.

[42] G Gerisch. Chemotaxis in dictyostelium. *Annual Review of Physiology*, 44(1):535–552, 1982. PMID: 6280593.

[43] Jaime Agudo-Canalejo, Pierre Illien, and Ramin Golestanian. Phoresis and enhanced diffusion compete in enzyme chemotaxis. *Nano Letters*, 18(4):2711–2717, 2018. PMID: 29552886.

[44] Samudra Sengupta, Krishna K. Dey, Hari S. Muddana, Tristan Tabouillot, Michael E. Ibele, Peter J. Butler, and Ayusman Sen. Enzyme molecules as nanomotors. *Journal of the American Chemical Society*, 135(4):1406–1414, 2013. PMID: 23308365.

[45] Henry Hess, George D. Bachand, and Viola Vogel. Powering nanodevices with biomolecular motors. *Chemistry â A European Journal*, 10(9):2110–2116, 2004.

[46] J. L. Anderson, M. E. Lowell, and D. C. Prieve. Motion of a particle generated by chemical gradients part 1. non-electrolytes. *Journal of Fluid Mechanics*, 117:107â121, 1982.

[47] P.O Staffeld and J. A. Quinn. Diffusion-induced banding of colloid particles via diffusiophoresis: 2. non-electrolytes. *Journal of Colloid and Interface Science*, 130(1):88 – 100, 1989.

[48] F.A Morrison. Electrophoresis of a particle of arbitrary shape. *Journal of Colloid and Interface Science*, 34(2):210 – 214, 1970.

[49] D A Saville. Electrokinetic effects with small particles. *Annual Review of Fluid Mechanics*, 9(1):321–337, 1977.

[50] S. Ebbens, M.-H. Tu, J. R. Howse, and R. Golestanian. Size dependence of the propulsion velocity for catalytic janus-sphere swimmers. *Phys. Rev. E*, 85:020401(R), 2012.

[51] J. Newman and K.E. Thomas-Alyea. *Electrochemical systems*. Wiley and sons, 1973.

[52] J. P. Ebel, John L. Anderson, and D. C. Prieve. Diffusiophoresis of latex particles in electrolyte gradients. *Langmuir*, 4(2):396–406, 1988.

[53] Mitchell M.-J Lin and Dennis C Prieve. Electromigration of latex induced by a salt gradient. *Journal of Colloid and Interface Science*, 95(2):327 – 339, 1983.

[54] Hong-Ren Jiang, Natsuhiko Yoshinaga, and Masaki Sano. Active motion of a janus particle by self-thermophoresis in a defocused laser beam. *Phys. Rev. Lett.*, 105:268302, Dec 2010.

[55] Leopold Kremser, Dieter Blaas, and Ernst Kenndler. Capillary electrophoresis of biological particles: Viruses, bacteria, and eukaryotic cells. *ELECTROPHORESIS*, 25(14):2282–2291, 2004.

[56] C. C. Maass, C. Krüger, S. Herminghaus, and C. Bahr. Swimming droplets. *Annu. Rev. Condens. Matter Phys.*, 7:171–193, 2016.

[57] S. Michelin and E. Lauga. Phoretic self-propulsion at finite Péclet numbers. *J. Fluid Mech.*, 747:572–604, 2014.

[58] R. Golestanian, T. B. Liverpool, and A. Ajdari. Designing phoretic micro- and nano-swimmers. *N. J. Phys.*, 9(5):126, 2007.

[59] Randall M. Erb, Nathan J. Jenness, Robert L. Clark, and Benjamin B. Yellen. Towards holonomic control of janus particles in optomagnetic traps. *Advanced Materials*, 21(47):4825–4829, 2009.

[60] Leonardo F. Valadares, Yu-Guo Tao, Nicole S. Zacharia, Vladimir Kitaev, Fernando Galembeck, Raymond Kapral, and Geoffrey A. Ozin. Catalytic nanomotors: Self-propelled sphere dimers. *Small*, 6(4):565–572, 2010.

[61] S. Michelin and E. Lauga. Autophoretic locomotion from geometric asymmetry. *Eur. Phys. J. E*, 38(7), 2015.

[62] R. Soto and R. Golestanian. Self-assembly of catalytically-active colloidal molecules: tailoring activity through surface chemistry. *Phys. Rev. Lett.*, 112:068301, 2014.

[63] Sébastien Michelin and Eric Lauga. A reciprocal theorem for boundary-driven channel flows. *Physics of Fluids*, 27(11):111701, 2015.

[64] Sergey Shklyaev, John F. Brady, and Ubaldo M. CÃ^3*rdova* − *Figueroa*. *Non* − *sphericalosmoticmotor* : *chemicalsailing*. *JournalofFluidMechanics*, 748 : 488â520, 2014.

[65] Sébastien Michelin, Eric Lauga, and Denis Bartolo. Spontaneous autophoretic motion of isotropic particles. *Physics of Fluids*, 25(6):061701, 2013.

[66] Ziane Izri, Marjolein N. van der Linden, Sébastien Michelin, and Olivier Dauchot. Self-propulsion of pure water droplets by spontaneous marangoni-stress-driven motion. *Phys. Rev. Lett.*, 113:248302, Dec 2014.

[67] Matvey Morozov and Sébastien Michelin. Nonlinear dynamics of a chemically-active drop: From steady to chaotic self-propulsion. *The Journal of Chemical Physics*, 150(4):044110, 2019.

[68] Wei Wang, Wentao Duan, Suzanne Ahmed, Ayusman Sen, and Thomas E. Mallouk. From one to many: Dynamic assembly and collective behavior of self-propelled colloidal motors. *Accounts of Chemical Research*, 48(7):1938–1946, 2015. PMID: 26057233.

[69] Wei Gao, Allen Pei, Renfeng Dong, and Joseph Wang. Catalytic iridium-based janus micromotors powered by ultralow levels of chemical fuels. *Journal of the American Chemical Society*, 136(6):2276–2279, 2014. PMID: 24475997.

[70] Yiying Hong, Misael Diaz, Ubaldo M. Córdova-Fteueroa, and Ayusman Sen. Light-driven titanium-dioxide-based reversible microfireworks and micromotor/micropump systems. *Advanced Functional Materials*, 20(10):1568–1576, 2010.

[71] Ryan A. Pavlick, Samudra Sengupta, Timothy McFadden, Hua Zhang, and Ayusman Sen. A polymerization-powered motor. *Angewandte Chemie International Edition*, 50(40):9374–9377, 2011.

[72] Giovanni Volpe, Ivo Buttinoni, Dominik Vogt, Hans-JÃ$\frac{1}{4}$rgen KÃ$\frac{1}{4}$mmerer, and Clemens Bechinger. Microswimmers in patterned environments. *Soft Matter*, 7:8810–8815, 2011.

[73] Alois Würger. Thermophoresis in colloidal suspensions driven by marangoni forces. *Phys. Rev. Lett.*, 98:138301, Mar 2007.

[74] A. Ghosh and P. Fischer. Controlled propulsion of artificial magnetic nanostructured propellers. *Nano Lett.*, 9(6):2243–2245, 2009. PMID: 19413293.

[75] Soichiro Tottori, Li Zhang, Famin Qiu, Krzysztof K. Krawczyk, Alfredo Franco-Obregon, and Bradley J. Nelson. Magnetic helical micromachines: Fabrication, controlled swimming, and cargo transport. *Advanced Materials*, 24(6):811–816.

[76] Eric E. Keaveny and Martin R. Maxey. Interactions between comoving magnetic microswimmers. *Phys. Rev. E*, 77:041910, Apr 2008.

[77] L. Baraban, M. Tasinkevych, M. N. Popescu, S. Sanchez, S. Dietrich, and O. G. Schmidt. Transport of cargo by catalytic janus micro-motors. *Soft Matter*, 8:48–52, 2012.

[78] Shakuntala Sundararajan, Paul E. Lammert, Andrew W. Zudans, Vincent H. Crespi, and Ayusman Sen. Catalytic motors for transport of colloidal cargo. *Nano Letters*, 8(5):1271–1276, 2008. PMID: 18416540.

[79] R Dreyfus, Jean Baudry, Marcus L. Roper, Marc Fermigier, Howard A. Stone, and JÃ©rÃ´me Bibette. Magnetic microswimmer. *Nature*, 108:038303, Jan 2005.

[80] C.J. Olson Reichhardt and C. Reichhardt. Ratchet effects in active matter systems. *Annual Review of Condensed Matter Physics*, 8(1):51–75, 2017.

[81] R. Di Leonardo, L. Angelani, D. Dell'Arciprete, G. Ruocco, V. Iebba, S. Schippa, M. P. Conte, F. Mecarini, F. De Angelis, and E. Di Fabrizio. Bacterial ratchet motors. *Proceedings of the National Academy of Sciences*, 107(21):9541–9545, 2010.

[82] Claudio Maggi, Juliane Simmchen, Filippo Saglimbeni, Jaideep Katuri, Michele Dipalo, Francesco De Angelis, Samuel Sanchez, and Roberto Di Leonardo. Self-assembly of micromachining systems powered by janus micromotors. *Small*, 12(4):446–451, 2016.

[83] Antoine Aubret, Mena Youssef, Stefano Sacanna, and JÃ©rÃ©mie Palacci. Targeted assembly and synchronization of self-spinning microgears. *Nature Physics*, 14, 2018.

[84] S. Saha, R. Golestanian, and S. Ramaswamy. Clusters, asters, and collective oscillations in chemotactic colloids. *Phys. Rev. E*, 89:062316, 2014.

[85] M. Tătulea-Codrean and E. Lauga. Artificial chemotaxis of phoretic swimmers: instantaneous and long-time behaviour. *J. Fluid Mech.*, 856:921–957, 2018.

[86] Oliver Pohl and Holger Stark. Dynamic clustering and chemotactic collapse of self-phoretic active particles. *Phys. Rev. Lett.*, 112:238303, Jun 2014.

[87] B. Liebchen, D. Marenduzzo, and M. E. Cates. Phoretic interactions generically induce dynamic clusters and wave patterns in active colloids. *Phys. Rev. Lett.*, 118:268001, 2017.

[88] Mingcheng Yang and Marisol Ripoll. A self-propelled thermophoretic microgear. *Soft Matter*, 10:1006–1011, 2014.

[89] Galien Grosjean, Maxime Hubert, Guillaume Lagubeau, and Nicolas Vandewalle. Realization of the najafi-golestanian microswimmer. *Phys. Rev. E*, 94:021101, Aug 2016.

[90] Andreas Zöttl and Holger Stark. Hydrodynamics determines collective motion and phase behavior of active colloids in quasi-two-dimensional confinement. *Phys. Rev. Lett.*, 112:118101, Mar 2014.

[91] Enkeleida Lushi, Hugo Wioland, and Raymond E. Goldstein. Fluid flows created by swimming bacteria drive self-organization in confined suspensions. *Proceedings of the National Academy of Sciences*, 111(27):9733–9738, 2014.

[92] Enkeleida Lushi, Raymond E. Goldstein, and Michael J. Shelley. Collective chemotactic dynamics in the presence of self-generated fluid flows. *Phys. Rev. E*, 86:040902, Oct 2012.

[93] I. Theurkauff, C. Cottin-Bizonne, J. Palacci, C. Ybert, and Bocquet. L. Dynamic clustering in active colloidal suspensions with chemical signaling. *Phys. Rev. Lett*, 108:268303, 2012.

[94] Dhruv P. Singh, Udit Choudhury, Peer Fischer, and Andrew G. Mark. Non-equilibrium assembly of light-activated colloidal mixtures. *Advanced Materials*, 29(32):1701328, 2017.

[95] Mallouk T. Ibele, M. and A. Sen. Schoolingbehaviour of light-powered micromotor. *Phys. Rev. Lett.*, 110:238301, Jun 2013.

[96] R. Di Leonardo, F. Ianni, and G. Ruocco. Colloidal attraction induced by a temperature gradient. *Langmuir*, 25(8):4247–4250, 2009. PMID: 19265405.

[97] Daniel Kagan, Shankar Balasubramanian, and Joseph Wang. Chemically triggered swarming of gold microparticles. *Angewandte Chemie International Edition*, 50(2):503–506.

[98] Thomas Bickel, Guillermo Zecua, and Alois Würger. Polarization of active janus particles. *Phys. Rev. E*, 89:050303, May 2014.

[99] Michael E. Cates and Julien Tailleur. Motility-induced phase separation. *Annual Review of Condensed Matter Physics*, 6(1):219–244, 2015.

[100] Christopher Dombrowski, Luis Cisneros, Sunita Chatkaew, Raymond E. Goldstein, and John O. Kessler. Self-concentration and large-scale coherence in bacterial dynamics. *Phys. Rev. Lett.*, 93:098103, Aug 2004.

[101] N Yoshinaga and T. B. Liverpool. From hydrodynamic lubrication to many-body interactions in dense suspensions of active swimmers. *arXiv:1901.04311*, 2018.

[102] T. Ishikawa, J. T. Locsei, and T. J. Pedley. Development of coherent structures in concentrated suspensions of swimming model micro-organisms. *J. Fluid Mech.*, 615:401–431, 2008.

[103] F. Alarcòn and I. Pagonabarraga. Spontaneous aggregation and global polar ordering in squirmer suspensions. *J. Mol. Liq.*, 185:56–61, 2013.

[104] B. Delmotte, E. E. Keaveny, F. Plouraboué, and E. Climent. Large-scale simulation of steady and time-dependent active suspensions with the force-coupling method. *J. Comp. Phys.*, 302:524–547, 2015.

[105] R. Aditi Simha and Sriram Ramaswamy. Hydrodynamic fluctuations and instabilities in ordered suspensions of self-propelled particles. *Phys. Rev. Lett.*, 89:058101, Jul 2002.

[106] David Saintillan and Michael J. Shelley. Orientational order and instabilities in suspensions of self-locomoting rods. *Phys. Rev. Lett.*, 99:058102, Jul 2007.

[107] Knut Drescher, Kyriacos C. Leptos, Idan Tuval, Takuji Ishikawa, Timothy J. Pedley, and Raymond E. Goldstein. Dancing volvox: Hydrodynamic bound states of swimming algae. *Phys. Rev. Lett.*, 102:168101, Apr 2009.

[108] Jörn Dunkel, Sebastian Heidenreich, Knut Drescher, Henricus H. Wensink, Markus Bär, and Raymond E. Goldstein. Fluid dynamics of bacterial turbulence. *Phys. Rev. Lett.*, 110:228102, May 2013.

[109] Christopher J. Miles, Arthur A. Evans, Michael J. Shelley, and Saverio E. Spagnolie. Active matter invasion of a viscous fluid: Unstable sheets and a no-flow theorem. *Phys. Rev. Lett.*, 122:098002, Mar 2019.

[110] Mu-Jie Huang, Jeremy Schofield, and Raymond Kapral. Chemotactic and hydrodynamic effects on collective dynamics of self-diffusiophoretic janus motors. *New Journal of Physics*, 19(12):125003, dec 2017.

[111] Vasily Kantsler, Jörn Dunkel, Marco Polin, and Raymond E. Goldstein. Ciliary contact interactions dominate surface scattering of swimming eukaryotes. *Proceedings of the National Academy of Sciences*, 110(4):1187–1192, 2013.

[112] S. E. Spagnolie and E. Lauga. Hydrodynamics of self-propulsion near a boundary: predictions and accuracy of far-field approximations. *J. Fluid Mech.*, 700:105–147, 2012.

[113] T. Vicsek, A. Czirók, E. Ben-Jacob, I. Cohen, and O. Shochet. Novel type of phase transition in a system of self-driven particles. *Phys. Rev. Lett.*, 75:1226–1229, 1995.

[114] J. Toner and Y. Tu. Long-range order in a two-dimensional dynamical XY model: How birds fly together. *Phys. Rev. Lett.*, 75:4326–4329, 1995.

[115] J. Toner and Y. Tu. Flocks, herds, and schools: A quantitative theory of flocking. *Phys. Rev. E*, 58:4828–4858, 1998.

[116] B. Liebchen and H. Löwen. Synthetic chemotaxis and collective behavior in active matter. *Acc. Chem. Res.*, 51(12), 2018.

[117] Yaouen Fily and M. Cristina Marchetti. Athermal phase separation of self-propelled particles with no alignment. *Phys. Rev. Lett.*, 108:235702, 2012.

[118] Joakim Stenhammar, Adriano Tiribocchi, Rosalind J. Allen, Davide Marenduzzo, and Michael E. Cates. Continuum theory of phase separation kinetics for active brownian particles. *Phys. Rev. Lett.*, 111:145702, Oct 2013.

[119] Julian Bialké, Hartmut LÃ¶wen, and Thomas Speck. Microscopic theory for the phase separation of self-propelled repulsive disks. *EPL (Europhysics Letters)*, 103(3):30008, aug 2013.

[120] G. S. Redner, M. F. Hagan, and A. Baskaran. Structure and dynamics of a phase-separating active colloidal fluid. *Phys. Rev. Lett.*, 110:055701, 2013.

[121] Holger Stark. Artificial chemotaxis of self-phoretic active colloids: Collective behavior. *Accounts of Chemical Research*, 51(11):2681–2688, 2018.

[122] B. Liebchen and H. Löwen. Which interactions dominate in active colloids? *J. Chem. Phys.*, 150(6):061102, 2019.

[123] K. Drescher, J. Dunkel, L. H. Cisneros, S. Ganguly, and R. E. Goldstein. Fluid dynamics and noise in bacterial cell–cell and cell–surface scattering. *Proc. Natl. Acad. Sci. USA*, 108(27):10940–10945, 2011.

[124] E. Kanso and S. Michelin. Phoretic and hydrodynamic interactions of weakly confined autophoretic particles. *J. of Chem. Phys.*, 150(4):044902, 2019.

[125] A. Zöttl and H. Stark. Emergent behavior in active colloids. *J. Phys. Condens. Matter*, 28(25):253001, 2016.

[126] M. Leoni and T. B. Liverpool. Dynamics and interactions of active rotors. *EPL*, 92:64004, 2010.

[127] B. Nasouri and G. J. Elfring. Higher-order force moments of active particles. *Phys. Rev. Fluids*, 3:044101, 2018.

[128] N. Yoshinaga and T. B. Liverpool. Hydrodynamic interactions in dense active suspensions: From polar order to dynamical clusters. *Phys. Rev. E*, 96:020603, 2017.

[129] T. Ishikawa, M. P. Simmonds, and T. J. Pedley. Hydrodynamic interaction of two swimming model micro-organisms. *J. Fluid Mech.*, 568:119–160, 2006.

[130] T. Ishikawa and T. J. Pedley. Coherent structures in monolayers of swimming particles. *Phys. Rev. Lett.*, 100:088103, 2008.

[131] Shiyi Chen and Gary D. Doolen. Lattice boltzmann method for fluid flows. *Annual Review of Fluid Mechanics*, 30(1):329–364, 1998.

[132] G. Gompper, T. Ihle, D. M. Kroll, and R. G. Winkler. *Multi-Particle Collision Dynamics: A Particle-Based Mesoscale Simulation Approach to the Hydrodynamics of Complex Fluids*. Springer Berlin Heidelberg, Berlin, Heidelberg, 2009.

[133] Raymond Kapral. *Multiparticle Collision Dynamics: Simulation of Complex Systems on Mesoscales*. John Wiley Sons, Ltd, 2008.

[134] Rajat Mittal and Gianluca Iaccarino. Immersed boundary methods. *Annual Review of Fluid Mechanics*, 37(1):239–261, 2005.

[135] J. Zhang, P. C. Johnson, and A. S. Popel. An immersed boundary lattice boltzmann approach to simulate deformable liquid capsules and its application to microscopic blood flows. *Phys. Biol.*, 4(4):285–295, 2007.

[136] Charles S. Peskin. The immersed boundary method. *Acta Numerica*, 11:479â517, 2002.

[137] T. D. Montenegro-Johnson, S. Michelin, and E. Lauga. A regularised singularity approach to phoretic problems. *Eur. Phys. J. E*, 38:139, 2015.

[138] A. Varma, T. D. Montenegro-Johnson, and S. Michelin. Clustering-induced self-propulsion of isotropic autophoretic particles. *Soft Matter*, 14:7155–7173, 2018.

[139] J. W. Swan, J. F. Brady, and R. S. Moore. Modeling hydrodynamic self-propulsion with stokesian dynamics. or teaching stokesian dynamics to swim. *Phys. Fluids*, 23(7):071901, 2011.

[140] L. Durlofsky, J. F. Brady, and G. Bossis. Dynamic simulation of hydrodynamically interacting particles. *J. Fluid Mech.*, 180:21–49, 1987.

[141] S. Lomholt and M. R. Maxey. Force-coupling method for particulate two-phase flow: Stokes flow. *J. Comp. Phys.*, 184(2):381 – 405, 2003.

[142] R. Singh, R. Adhikari, and M. E. Cates. Competing chemical and hydrodynamic effects in autophoretic colloidal suspensions. *arXiv:1811.04658*, 2019.

[143] A. G. Mark, J. G. Gibbs, T-C. Lee, and P. Fischer. Hybrid nanocolloids with programmed three-dimensional shape and material composition. *Nat. Materials*, 12, 2015.

[144] Z. Izri, M. N. van der Linden, S. Michelin, and O. Dauchot. Self-propulsion of pure water droplets by spontaneous marangoni-stress-driven motion. *Phys. Rev. Lett.*, 113:248302, 2014.

[145] E. Lauga and T. R. Powers. The hydrodynamics of swimming microorganisms. *Rep. Prog. Phys.*, 72(096601), 2009.

[146] Wilfred Stein. *Transport And Diffusion Across Cell Membranes.* Elsevier, 1986.

[147] Adolf Fick. Ueber diffusion. *Annalen der Physik*, 170(1):59–86, 1855.

[148] Robert Brown. Xxvii. a brief account of microscopical observations made in the months of june, july and august 1827, on the particles contained in the pollen of plants; and on the general existence of active molecules in organic and inorganic bodies. *The Philosophical Magazine*, 4(21):161–173, 1828.

[149] William Sutherland. Lxxv. a dynamical theory of diffusion for non-electrolytes and the molecular mass of albumin. *The London, Edinburgh, and Dublin Philosophical Magazine and Journal of Science*, 9(54):781–785, 1905.

[150] A. Einstein. Ãber die von der molekularkinetischen theorie der wÃrme geforderte bewegung von in ruhenden flÃ$\frac{1}{4}$ssigkeiten suspendierten teilchen. *Annalen der Physik*, 322(8):549–560, 1905.

[151] M. von Smoluchowski. Zur kinetischen theorie der brownschen molekularbewegung und der suspensionen. *Annalen der Physik*, 326(14):756–780, 1906.

[152] E. M. Purcell. Life at low reynolds number. *Am. J. Phys.*, 45:3, 1977.

[153] C. Pozrikidis. *Boundary Integral and Singularity Methods for Linearized Viscous Flow.* Cambridge University Press, 1992.

[154] J. Happel and H. Brenner. *Low Reynolds number hydrodynamics.* Springer, 1965.

[155] Geoffrey Ingram Taylor. Analysis of the swimming of microscopic organisms. *Proceedings of the Royal Society of London. Series A. Mathematical and Physical Sciences*, 209(1099):447–461, 1951.

[156] T. J. Pedley, D. R. Brumley, and R. E. Goldstein. Squirmers with swirl: a model for volvox swimming. *Journal of Fluid Mechanics*, 798:165â186, 2016.

[157] S. Kim and S. J. Karrila. *Microhydrodynamics: Principles and Selected Applications*. Butterworth-Heinemann, 1991.

[158] Yi Man, Lyndon Koens, and Eric Lauga. Hydrodynamic interactions between nearby slender filaments. *EPL (Europhysics Letters)*, 116(2):24002, oct 2016.

[159] Batchelor G. K. *An Introduction to Fluid Dynamics)*. Springer, 2015.

[160] M. J. Lighthill. On the squirming motion of nearly spherical deformable bodies through liquids at very small reynolds numbers. *Communications on Pure and Applied Mathematics*, 5(2):109–118, 1952.

[161] J. R. Blake. A spherical envelope approach to ciliary propulsion. *J. Fluid Mech.*, 46(1):199–208, 1971.

[162] O. S. Pak and E. Lauga. Generalized squirming motion of a sphere. *J. Eng. Math.*, 88(1):1–28, 2014.

[163] SÃ©bastien Michelin and Eric Lauga. Efficiency optimization and symmetry-breaking in a model of ciliary locomotion. *Physics of Fluids*, 22(11):111901, 2010.

[164] H. A. Stone and A. D. T. Samuel. Propulsion of microorganisms by surface distortions. *Phys. Rev. Lett*, 77:4102, 1996.

[165] Emily E. Riley and Eric Lauga. Enhanced active swimming in viscoelastic fluids. *EPL (Europhysics Letters)*, 108(3):34003, nov 2014.

[166] H. Lamb. *Hydrodynamics*. Dover, New York, 6th edition, 1932.

[167] R. Cortez, L. Fauci, and Alexei Medovikov. The method of regularized stokeslets in three dimensions: Analysis, validation, and application to helical swimming. *Phys. Fluids*, 17:031504, 2005.

[168] M. Smoluchowski. On the mutual action of spheres which move in a viscous liquid. *Bull. Acad. Sci. Cracovie A*, 1:28–39, 1911.

[169] H. A. Stone and A. D. T. Samuel. Propulsion of microorganisms by surface distortions. *Phys. Rev. Lett*, 77:4102, 1996.

[170] M. Lisicki, S. Y. Reigh, and E. Lauga. Autophoretic motion in three dimensions. *Soft Matter*, 14:3304–3314, 2018.

[171] E. Yariv. Wall-induced self-diffusiophoresis of active isotropic colloids. *Phys. Rev. Fluids*, 1:032101, 2016.

[172] N. Sharifi-Mood, A. Mozaffari, and U. M. Cordova-Figueroa. Pair interaction of catalytically active colloids: from assembly to escape. *J. Fluid Mech.*, 798:910–954, 2016.

[173] G. M. Golusin. Auflösung eines ebenen wärmeleitungsproblems in einem von isolierender schichte umgebenen mehrfachzusammenhängenden kreisbereiche. *Mat. Sb.*, 42, 1935.

[174] J. H. C. Luke. Convergence of a multiple reflection method for calculating stokes flow in a suspension. *SIAM J. Appl. Math.*, 49(6):1635–1651, 1989.

[175] K. Ichiki and J. F. Brady. Many-body effects and matrix inversion in low-reynolds-number hydrodynamics. *Physics of Fluids*, 13(1):350–353, 2001.

[176] S. Shklyaev, J. F. Brady, and U. M. Cordova-Figueroa. Non-spherical osmotic motor: chemical sailing. *J. Fluid Mech.*, 748:488–520, 2014.

[177] S. Michelin and E. Lauga. Autophoretic locomotion from geometric asymmetry. *Eur. Phys. J. E*, 38:7, 2015.

[178] Alvaro Dominguez, P. Malgaretti, M. N. Popescu, and S. Dietrich. Collective dynamics of chemically active particles trapped at a fluid interface. *Soft Matter*, 12:8398–8406, 2016.

[179] R. Cortez. The method of regularized stokeslets. *SIAM J. Sci. Comput.*, 23(4):1204–1225, 2001.

[180] S. Shklyaev. Janus droplet as a catalytic micromotor. *Europhys. Letters*, 110(5):54002, 2015.

[181] G. Volpe, S. Gigan, and G. Volpe. Simulation of the active brownian motion of a microswimmer. *Am. J. Phys.*, 82:659, 2014.

[182] A. Zöttl and H. Stark. Emergent behavior in active colloids. *J. Phys.: Condens. Matter*, 28(25):253001, 2016.

[183] Megan S. Davies Wykes, Jeremie Palacci, Takuji Adachi, Leif Ristroph, Xiao Zhong, Michael D. Ward, Jun Zhang, and Michael J. Shelley. Dynamic self-assembly of microscale rotors and swimmers. *Soft Matter*, 12:4584–4589, 2016.

[184] S.J. Ebbens and D. A. Gregory. Catalytic janus colloids: Controlling trajectories of chemical microswimmers. *Acc. Chem. Res.*, 51(9), 2018.

[185] Enkeleida Lushi, Raymond E. Goldstein, and Michael J. Shelley. Nonlinear concentration patterns and bands in autochemotactic suspensions. *Phys. Rev. E*, 98:052411, Nov 2018.

[186] Suropriya Saha, Sriram Ramaswamy, and Ramin Golestanian. Pairing, waltzing and scattering of chemotactic active colloids. *New Journal of Physics*, 21(6):063006, jun 2019.

[187] F. B. Usabiaga, B. Kallemov, A. P. Singh Bhalla B. Delmotte, B. E. Griffith, and A. Donev. Hydrodynamics of suspensions of passive and active rigid particles: a rigid multiblob approach. *Comp. App. Math and Comp. Sci.*, 11:217–296, 2016.

[188] Thanh N. Phung, John F. Brady, and Georges Bossis. Stokesian dynamics simulation of brownian suspensions. *Journal of Fluid Mechanics*, 313:181â207, 1996.

[189] J. F Brady. Particle motion driven by solute gradients with application to autonomous motion: continuum and colloidal perspectives. *J. Fluid Mech.*, 667:216–259, 2011.

[190] Benno Liebchen, Ran Niu, Thomas Palberg, and Hartmut Löwen. Unraveling modular microswimmers: From self-assembly to ion-exchange-driven motors. *Phys. Rev. E*, 98:052610, Nov 2018.

[191] Bhargav Rallabandi, Fan Yang, and Howard A. Stone. Motion of hydrodynamically interacting active particles. *arXiv e-prints*, page arXiv:1901.04311, Jan 2019.

[192] Falko Schmidt, Benno Liebchen, Hartmut LÃ¶wen, and Giovanni Volpe. Light-controlled assembly of active colloidal molecules. *The Journal of Chemical Physics*, 150(9):094905, 2019.

[193] Popescu, M. N., Tasinkevych, M., and Dietrich, S. Pulling and pushing a cargo with a catalytically active carrier. *EPL*, 95(2):28004, 2011.

[194] Rodrigo Soto and Ramin Golestanian. Self-assembly of catalytically active colloidal molecules: Tailoring activity through surface chemistry. *Phys. Rev. Lett.*, 112:068301, Feb 2014.

[195] Kyriacos C. Leptos, Jeffrey S. Guasto, J. P. Gollub, Adriana I. Pesci, and Raymond E. Goldstein. Dynamics of enhanced tracer diffusion in suspensions of swimming eukaryotic microorganisms. *Phys. Rev. Lett.*, 103:198103, Nov 2009.

[196] Levke Ortlieb, Salima Rafaï, Philippe Peyla, Christian Wagner, and Thomas John. Statistics of colloidal suspensions stirred by microswimmers. *Phys. Rev. Lett.*, 122:148101, Apr 2019.

[197] Blaise Delmotte, Eric E Keaveny, Eric Climent, and Franck PlourabouÃ©. Simulations of Brownian tracer transport in squirmer suspensions. *IMA Journal of Applied Mathematics*, 83(4):680–699, 07 2018.

[198] Onofrio M. Maragó, Philip H. Jones, Pietro G. Gucciardi, Giovanni Volpe, and Andrea C. Ferrari. Optical trapping and manipulation of nanostructures. *Nature Nanotechnology*, 807(8):514–523, 2013.

[199] Nima Sharifi-Mood, Pablo G. Díaz-Hyland, and Ubaldo M. Córdova-Figueroa. Dynamics of a microswimmer near a curved wall: guided and trapped locomotions. *arXiv e-prints*, page arXiv:1710.10578, Oct 2017.

[200] Y. Ibrahim and T.B. Liverpool. How walls affect the dynamics of self-phoretic microswimmers. *The European Physical Journal Special Topics*, 225(8):1843–1874, Oct 2016.

[201] Alexander Chamolly, Takuji Ishikawa, and Eric Lauga. Active particles in periodic lattices. *New Journal of Physics*, 19(11):115001, nov 2017.

[202] Parvin Bayati, Mihail N. Popescu, William E. Uspal, S. Dietrich, and Ali Najafi. Dynamics near planar walls for various model self-phoretic particles. *Soft Matter*, 15:5644–5672, 2019.

[203] Shang Yik Reigh and Raymond Kapral. Catalytic dimer nanomotors: continuum theory and microscopic dynamics. *Soft Matter*, 11:3149–3158, 2015.

[204] M. Stimson and G. B. Jeffery. The motion of two spheres in a viscous fluid. *Proc. Royal Soc. Lond. A*, 111:757, 1926.

[205] D. J. Smith. A boundary element regularized stokeslet method applied to cilia- and flagella-driven flow. *Proceedings of the Royal Society A: Mathematical, Physical and Engineering Sciences*, 465:068301, 2009.

université PARIS-SACLAY
ÉCOLE DOCTORALE
Sciences mécaniques et énergétiques, matériaux et géosciences (SMEMAG)

Titre : Fluides actifs - Interactions et dynamiques collectives dans les suspensions phorétique

Mots clés : fluid actifs, autopropulsion, interactions chimiques et hydrodynamiques, comportement collectif

Résumé : La phorése est un mécanisme physico-chimique par lequel certains collo¨ides microscopiques dérivent à travers les gradients d'un champ de concentration de soluté dans un fluide. Ce mécanisme est exploité par des particules autophorétiques, qui sont des collo¨ides synthétiques chimiquement actifs, pour réaliser une autopropulsion. Ces particules influencent les mouvements des uns et des autres par le biais d'interactions chimiques et hydrodynamiques et sont donc connues pour leur comportement collectif. La modélisation de ces interactions a fait l'objet d'intenses recherches au cours des derniéres décennies, à la fois d'un point de vue physique pour comprendre les mécanismes précis des interactions, et pour expliquer les observations de la formation de structures cohérentes à grande échelle. Cependant, une modélisation exacte de est difficile en raison des interactions multi-corps et des effets de surface. Jusqu'a présent, la plupart des efforts reposent sur la superposition d'approximations de champ lointain pour la signature de chaque particule, qui ne sont valides que de maniére asymptotique dans la limite de suspension diluée. Un cadre analytique systématique et unifié basé sur la methode classique de reflexion (MoR) est developpe ici pour les problémes de Laplace et de Stokes afin d'obtenir les interactions multicorps et les vitesses résultantes des particules phorétiques, jusqu'a un ordre de précision du rayon rapport à distance des particules ε . Un systéme comprenant uniquement des particules autophorétiques chimiquement et geometriquement isotropes est ensuite considéré en détail. On sait que de telles particules isotropes ne peuvent se propulser seules; cependant, en présence d'autres particules identiques, la symétrie du champ de concentration est brisée et les particules forment spontanément des amas tassés. Remarquablement, ces grappes s'auto-propulsent en fonction de leur disposition géométrique. Ce résultat identifie donc une nouvelle voie pour briser la symétrie pour le champ de concentration et pour l'ˆaauto-propulsion, qui ne repose pas sur une conception anisotrope, mais sur les interactions collectives de particules actives identiques et homogénes. De plus, en utilisant des simulations numériques complétes et un modéle théorique pour la classification, nous caractérisons les propriétés statistiques de l'autopropulsion du systéme.

Title : Active fluids - Interactions and collective dynamics in phoretic suspensions

Keywords : Active fluids, self-propulsion, chemo-hydrodynamic interactions, modeling phoretic suspension, collective dynamics

Abstract : *Diffusiophoresis* is a physico-chemical mechanism by which certain microscopic colloids drift in gradients of a solute concentration field in a fluid. This mechanism is exploited by autophoretic particles, which are chemically active synthetic colloids, to achieve self-propulsion. These particles influence each others' motion through chemical and hydrodynamic interactions and are hence known to exhibit collective behaviour. Modeling these interactions is a subject of intense research over the past decades to understand the precise mechanisms of the interactions, as well as to explain the observations of formation of coherent large-scale structures. However, an exact modelling of is difficult due to multi-body interactions. Most efforts so far rely on the superposition of far-field approximations for each particle's signature, which are only valid asymptotically in the dilute suspension limit. A systematic and unified analytical framework based on the classical Method of Reflections (MoR) is developed here for both Laplace and Stokes' problems to obtain the multi-body interactions and the resulting velocities of phoretic particles, up to any order of accuracy in the radius-to-distance ratio ε of the particles. A system comprising only of chemically- and geometrically-isotropic autophoretic particles is then considered in detail. It is known that such isotropic particles cannot self-propel in isolation; however, in the presence of other identical particles, the symmetry of the concentration field is broken and the particles spontaneously form close packed clusters. Remarkably, these clusters are observed to self-propel based on their geometric arrangement. This result thus identifies a new route to symmetry-breaking for the concentration field and to self-propulsion, that is not based on an anisotropic design, but on the collective interactions of identical and homogeneous active particles. Furthermore, using full numerical simulations and theoretical model for clustering, we characterize the statistical properties of self-propulsion of the system.

Université Paris-Saclay
Espace Technologique / Immeuble Discovery
Route de l'Orme aux Merisiers RD 128 / 91190 Saint-Aubin, France